Bond-Selective Nonlinear Optical Microscopy: From Live Cells to Single-Molecule Imaging

Thesis by

Dongkwan Lee

In Partial Fulfillment of the Requirements for

the degree of

Doctor of Philosophy

CALIFORNIA INSTITUTE OF TECHNOLOGY

Pasadena, California

2025

(Defended Jan 31, 2025)

Dongkwan Lee
ORCID: 0000-0001-6091-1349

ACKNOWLEDGEMENTS

First and foremost, I want to thank my advisor, Prof. Lu Wei. It was a huge privilege to be one of her first three students and to participate in building a new lab from scratch. Throughout my times in her lab, I was inspired by her optimism, love for science, perseverance, and scientific excellence, which will always stay with me as I continue my scientific career. She deeply cares about the best interests of her students. I have immense respect for her as a scientific and life mentor.

I would like to express my heartfelt gratitude to my committee members, Prof. Lihong Wang, Prof. David Tirrell, and Prof. Mikhail Shapiro. Prof. Wang's course on biomedical optics laid the foundation of my understanding in optics and imaging. I am especially grateful to him for giving me the opportunity to collaborate with Dr. Lei Li on the photoswitchable project, where we developed DrBphP-PCM NIR fluorescent protein as a genetically encodable photoswitchable stimulated Raman probe. This work was selected as Editor's Choice 2021 for its innovation and impact in chemical physics and was also featured in *JCP*, which would have not been possible without his help. I am also thankful to Prof. Tirrell for his insightful suggestions during my candidacy, which were helpful throughout my PhD career, and for his encouragement, advice, and willingness to read my proposals. Finally, I want to thank Prof. Shapiro. Working as a TA with him for two quarters was an inspiring experience, as I admired his ability to communicate science so effectively. His energy, approachability, and quick email responses have left a lasting impression on me. I am grateful for his advice and encouragement during our meetings.

I want to thank the BonFIRE team: Haomin Wang, Phil Kocheril, Ryan Leighton, and Noor Naji. I feel fortunate to have worked alongside them and learned so much through our daily interactions. I especially appreciated the discussions, which turned long experiment hours and setbacks into enjoyable and memorable experiences. I also want to thank the rest of the Wei Lab members: Chenxi Qian, Jiajun Du, Kun Miao, Xiaotian Bi, Li-en Lin, Adrian Colazo, R.J. Chandra, Ziguang Yang, and Joe Ambarian. I am particularly grateful to Jiajun and Chenxi for their help with the glycogen and photoswitchable projects, and to Xiaotian for her support with the neuron and cell samples.

I want to thank my mentors at UIUC. In the lab of Prof. Rohit Bhargava, I discovered the excitement of optics, spectroscopy, and imaging. Under the guidance of my mentors Kevin Yeh and Seth Kenkel, I gained early experience in building custom microscopes and learned to work independently. I also want to thank Steve Doonan for his mentorship and Prof. Ryan Bailey. I was devastated as an undergraduate when Prof. Bailey decided to move to the University of Michigan, but this transition allowed me to join another lab and discover my passion for optics, imaging, and microscopy. It was a valuable reminder that you can only connect the dots looking backward.

I want to thank my friends at Caltech for the enjoyable times and memories we've shared. My cohort, the Korean cohort from my year and the year below, the tennis crew, and the weightlifting crew have all been an important part of my journey. I also want to thank Sola

for the wonderful moments we have shared at Caltech and beyond.

Finally, I want to thank my sister and parents for their unwavering support and love over the past years. None of this would have been possible without them. This thesis is dedicated to them.

ABSTRACT

Advances in optical microscopy have revolutionized cell biology, transforming our understanding of cellular processes from static structural observations to dynamic temporal and spatial insights at the single-molecule level. While fluorescence imaging remains the gold standard due to its high sensitivity, specificity, and versatile toolbox, it faces significant limitations, particularly in imaging small molecules that are not inherently fluorescent. Attaching fluorescent tags to these molecules often disrupts their physicochemical properties, highlighting the need for minimally invasive and intrinsic-contrast-based approaches.

Vibrational spectro-microscopy, which probes the intrinsic vibrational frequencies of chemical bonds, offers a promising solution. Stimulated Raman scattering (SRS) microscopy, a well-established vibrational imaging technique, enhances vibrational excitation by up 10^8 -fold through stimulated emission amplification, enabling rapid, label-free imaging of biological samples with high specificity.

In the first half of this thesis, we advance SRS microscopy to tackle specific biological challenges and explore new methodological possibilities. To visualize glycogen metabolism, we combined a stable isotope labeling strategy with SRS imaging, achieving high-specificity imaging of glycogen in live cells. This approach was further applied to metabolic phenotyping of patient-derived melanoma cell lines. Additionally, we investigated strategies to photoswitch electronic pre-resonance (epr) SRS probes, which are typically photostable. By inducing electronic transitions that modulate electronic-vibrational coupling, we developed the first genetically encodable photoswitchable epr-SRS probe using a near-infrared fluorescent protein, unlocking new possibilities in Raman imaging.

In the second half of this thesis, we address the limitations of SRS microscopy by developing a novel bond-selective nonlinear optical microscopy technique called bond-selective fluorescence-detected infrared-excited (BonFIRE). BonFIRE introduces a vibration-state-mediated two-photon process as a new vibrational contrast mechanism, overcoming key limitations in sensitivity and speed associated with SRS. By combining the high sensitivity and specificity of fluorescence with the rich chemical information provided by IR absorption-based vibrational contrast, BonFIRE offers a powerful platform for multidimensional insights into biological systems. We envision BonFIRE as a tool to tackle unique challenges that current technologies cannot address, representing a significant step forward in understanding the complex processes that define life.

PUBLISHED CONTENT AND CONTRIBUTIONS

Lee, D., Wang, H., Kocheril, P. A., Bi, X., Naji, N. & Wei, L. Wide-field bond-selective fluorescence imaging: From single-molecule to cellular imaging beyond video-rate. *Optica* (accepted). https://doi.org/10.1101/2024.07.05.601986

DL participated in the study design, experiments, data analysis, and writing.

Wang, H.†, **Lee, D**.†, Cao, Y., Bi, X., Du, J., Miao, K. & Wei, L. Bond-selective fluorescence imaging with single-molecule sensitivity. *Nat. Photonics* **17**, 846–855 (2023). https://doi.org/10.1038/s41566-023-01243-8. † Equal contribution.

DL participated in the study design, experiments, data analysis, and writing.

Lee, D., Qian, C., Wang, H., Li, L., Miao, K., Du, J., Shcherbakova, D. M., Verkhusha, V. V., Wang, L. V. & Wei, L. Toward photoswitchable electronic pre-resonance stimulated Raman probes. *J. Chem. Phys.* **154**, 135102 (2021). https://doi.org/10.1063/5.0043791.

DL participated in the study design, experiments, data analysis, and writing.

Lee, D., Du, J., Yu, R., Su, Y., Heath, J. R. & Wei, L. Visualizing subcellular enrichment of glycogen in live cancer cells by stimulated Raman scattering. *Anal. Chem.* **92**, 13182–13191 (2020). https://doi.org/10.1021/acs.analchem.0c02348.

DL participated in the study design, experiments, data analysis, and writing.

Kocheril, P. A., **Lee, D.**, Naji, N., Chadha, R. S., Leighton, R.E., Wang, H. & Wei, L. Vibrational thermometry with single-molecule sensitivity. *Manuscript submitted.*

DL assisted in experimental and manuscript editing.

Wang, H., **Lee, D**. & Wei, L. Toward the next frontiers of vibrational bioimaging. *Chem. Biomed. Imaging* **1**, 3–17 (2023). https://doi.org/10.1021/cbmi.3c00004

DL contributed to the conceptualization and writing of the manuscript.

Kocheril, P. A., Wang, H., **Lee, D.**, Naji, N. & Wei, L. Nitrile vibrational lifetimes as probes of local electric fields. *J. Phys. Chem. Lett.* **15**, 5306–5314 (2024). https://doi.org/10.1021/acs.jpclett.4c00597.

DL assisted in experimental and manuscript editing.

Wang, H., Du, J., **Lee, D**. & Wei, L. Stimulated Raman scattering imaging with small vibrational probes. In *Stimulated Raman Scattering Microscopy* (eds Cheng, J.-X., Min, W., Ozeki, Y. & Polli, D.) 289–310 (Elsevier, 2022). https://doi.org/10.1016/B978-0-323-85158-9.00023-3.

DL contributed to literature analysis and manuscript preparation.

Wang, H., Kocheril, P. A., Yang, Z., **Lee, D.,** Naji, N., Du, J., Lin, L.-E. & Wei, L. Room-temperature single-molecule infrared imaging and spectroscopy through bond-selective fluorescence. *Angew. Chem. Int. Ed.* **63**, e202413647 (2024). https://doi.org/10.1002/anie.202413647.

DL assisted in experimental and manuscript editing.

Kocheril, P. A.; Wang, H.; Leighton, R. E.; **Lee, D.**; Naji, N.; Du, J.; Wei, L. Two-Dimensional Vibronic Fluorescence Spectroscopy: Vibronic Multiplexing, Violations of the Resonance Condition, and Vibrational Cooling Rate Dispersion. *Manuscript submitted.*

DL participated in the experimental and manuscript editing.

Du, J., Su, Y., Qian, C., Yuan, D., Miao, K., **Lee, D.**, Ng, A. H. C., Wijker, R. S., Ribas, A., Levine, R. D., Heath, J. R. & Wei, L. Raman-guided subcellular pharmaco-metabolomics for metastatic melanoma cells. *Nat. Commun.* **11**, 4830 (2020). https://doi.org/10.1038/s41467-020-18376-x.

DL assisted in experimental and manuscript editing.

TABLE OF CONTENT

Chapter 1

INTRODUCTION

1.1 From fluorescence to bond-selective nonlinear optical microscopy

Advances in optical microscopy have been instrumental in shaping our understanding of biology[1–4]. From Robert Hooke's first observation of cells using a compound microscope in 1665 to the advent of single-molecule fluorescence and super-resolution microscopy, our ability to study cells has transformed dramatically. Initially limited to structural observations, modern microscopy now reveals dynamic temporal and spatial information at the single-molecule level. In contrast, many end-point biochemical assays treat cells as static entities, failing to capture the stochastic and dynamic nature of diverse molecular mechanisms often hidden in ensemble measurements[5]. Optical microscopy uniquely provides real-time insights into cellular dynamics[6,7], offering a window into the processes that define life itself.

Among the various optical microscopy techniques, fluorescence imaging has emerged as the gold standard, offering high sensitivity, specificity, and a versatile toolbox. These include diverse labeling strategies, genetically encoded proteins, and advanced techniques such as light-sheet and super-resolution microscopy. This versatility has made fluorescence imaging indispensable for addressing many complex biological challenges. However, a significant limitation is that small molecules within cells—crucial for regulation, signaling, and other intricate processes—are not inherently fluorescent. Attaching bulky fluorescent tags to these molecules can disrupt their physicochemical properties, altering their natural behavior. This raises a critical question: how can we image small molecules within cells without the use of fluorescent tags?

One promising solution lies in imaging the intrinsic properties of small molecules themselves—specifically, their chemical bonds. Chemical bonds form the fundamental building blocks of molecules, each characterized by a unique vibrational frequency determined by quantum mechanics. These vibrational frequencies can be probed through light-matter interactions, forming the basis of vibrational spectro-microscopy. A well-established vibrational imaging technique is stimulated Raman scattering (SRS) microscopy[8–10]. Unlike spontaneous Raman scattering, which uses a single light frequency, SRS employs two beams—a Stokes beam and a pump beam. When the energy difference between the two beams matches the vibrational frequency of a chemical bond, the vibrational excitation is enhanced by up to 10^8-fold due to stimulated emission amplification[11–13]. The classical description stimulated Raman process is detailed in the **Appendix** of the thesis, as it provides intuitive understanding of the process. This increased sensitivity enables rapid, label-free imaging of biological samples, producing spatial maps of chemical bonds with high specificity in live cells and tissues[12,14–17].

In this thesis, we build on the advancements in SRS microscopy to extend its capabilities in generating multidimensional information. We enhance stimulated Raman scattering (SRS) microscopy in the effort to address specific biological problems that are

challenging to resolve with current imaging techniques[18,19]. Then beyond SRS, we develop a novel bond-selective nonlinear optical microscopy technique called bond-selective fluorescence-detected infrared-excited (BonFIRE)[20,21]. BonFIRE employs a unique vibrational contrast mechanism, vibration-state-mediated two-photon process, to overcome key limitations of SRS, which are restricted sensitivity and speed. By integrating the strengths of fluorescence and vibrational imaging, BonFIRE is designed to provide comprehensive multidimensional insights into biological systems[22,23], enabling the study of unique problems that remain inaccessible with existing technologies. The remaining sections of Chapter 1 introduce the thesis work, provide the necessary background on foundational concepts, and discuss the seminal works that provide context.

1.2 **Development of an SRS imaging strategy to visualize glycogen in live cancer cells**

Metabolic reprogramming is a hallmark of cancer cells, enabling them to meet the unique energy demands required for rapid growth and proliferation[24–27]. While traditionally viewed as a simple glucose storage reservoir, emerging research has revealed that glycogen metabolism plays critical roles in glycogen mobilization, tumor progression, and the modulation of the tumor microenvironment[28–31]. However, current technologies (e.g. transmission electron microscopy, mass spectrometry-based imaging, and fluorescence microscopy) for specifically visualizing subcellular glycogen and its metabolism in live cells remain highly limited due to their destructive and perturbative nature[31].

Small molecule imaging using SRS microscopy. To address this problem, we developed a new imaging strategy using SRS microscopy to visualize glycogen metabolism in live cancer cells[18]. Imaging small molecules with SRS can be achieved through several approaches[14,32]. The first approach is label-free imaging, which detects intrinsic chemical bonds such as O-H, C-H, C=C, C=O, S=O, and O=P=O, commonly found in biomolecules like water, lipids, proteins, and nucleotides. These bonds are primarily located in the fingerprint region (600–1800 cm^{-1}) of the Raman spectrum. However, overlapping Raman signals within this region often reduce specificity, and their sensitivity is limited to millimolar concentrations[9,11]. Moreover, label-free imaging of endogenous molecules provides information only on the steady-state composition of cells[15], failing to capture the temporal dynamics that are a hallmark of metabolism. As a result, this approach cannot provide specific imaging of glycogen or its metabolic turnover.

The second approach leverages triple-bond tagging, where biomolecules are labeled with triple bonds such as alkynes (C≡C), nitriles (C≡N), or isonitriles (N≡C), enabling their incorporation into cellular processes through metabolic labeling. Triple bonds produce sharp and distinct Raman peaks in the cell-silent region[33], free from interference by endogenous molecules, thereby enhancing sensitivity and specificity. This method has been successfully applied in metabolic labeling, such as incorporating alkyne-tagged nucleosides into DNA and RNA to track nucleic acid biosynthesis or using alkyne-tagged fatty acids to monitor lipid metabolism[33]. However, the use of triple-bond-tagged glucose analogs like 3-O-propargyl-d-glucose (3-OPG) is limited because 3-OPG cannot be metabolized[34], restricting its application to glucose uptake tracing.

Development of SRS imaging strategy to visualize glycogen in live cancer cells. To address the limitations of the first two approaches, we utilized stable isotope labeling, in which atoms in a target molecule are substituted with isotopes, such as replacing hydrogen with deuterium. This substitution shifts vibrational frequencies into the cell-silent region, allowing high chemical specificity without interference from cellular background signals[35–38]. Unlike triple-bond tagging, isotope labeling minimally perturbs the biochemical properties of molecules, preserving their native structure and function.

To label glycogen with C-D bonds, we incubated cancer cells with deuterated glucose, which retains nearly identical physicochemical properties to regular glucose. This enables deuterated glucose to be incorporated into the glycogen chain. The C-D signal from glycogen was distinguished from C-D labeled lipids and proteins using their distinct spectra in the cell-silent region[39] and employing linear unmixing techniques. After validating the specificity and robustness of this glycogen imaging strategy, we applied the technique to perform metabolic phenotyping of patient-derived melanoma cell lines with varying dedifferentiation states, which likely exhibit different metabolic patterns. Our observations revealed evidence supporting a role for glycogen as a metabolic buffer, enabling cancer cells to tolerate stress conditions. This work is discussed in detail in **Chapter 2**.

1.3. Development of photoswitchable electronic pre-resonance SRS probes

One key advantage of SRS microscopy is its high sensitivity, enabled by stimulated emission amplification, which enhances the Raman cross-section by up to 10^8-fold compared to spontaneous Raman scattering[11–13]. Despite this amplification, the sensitivity of SRS microscopy remains limited to the micromolar to millimolar range[15], leaving many low-concentration biomolecules inaccessible.

Pre-resonance enhancement effect. One way to further increase sensitivity is by utilizing the pre-resonance (epr) effect. When the pump wavelength is close to the electronic absorption maximum of a molecule, the vibrational transition is amplified by up to 10^5-fold due to electronic-vibrational coupling[40,41]. The Raman cross-section, as a function of the detuning between the absorption maximum and the pump wavelength, is described by the Albrecht A-term pre-resonance approximation[41–43], where the cross-section decreases with detuning $(\omega_0 - \omega_{pump})$ to the fourth power.

$$\sigma_{Raman} = K\omega_{pump}\left(\omega_{pump} - \omega_{vib}\right)^3 \left[\frac{\omega_{pump}^2 + \omega_0^2}{(\omega_0^2 - \omega_{pump}^2)^2}\right]^2$$

where ω_{vib} is the vibrational transition energy, ω_0 is the electronic absorption energy, ω_{pump} is the pump photon energy, and K is a collection of frequency-independent factors of the Raman dyes. While on-resonance excitation provides the highest signal, it also generates severe background from other four-wave mixing processes[44]. To address this, pre-resonance involves detuning the pump wavelength from the absorption maximum, which improves the signal-to-background ratio. This is possible because the decay of electronic absorption is faster than that of the Raman signal, reducing background while

maintaining a sufficiently strong Raman signal[41]. The electronic-vibrational coupling is related to the distance between the equilibrium positions of the vibrational modes[45]. As the vibrational mode displacement increases, the coupling strength grows, since electronic transitions result in larger vibrational mode shifts. Stronger coupling influences the molecule's polarizability, thereby enhancing the Raman signal.

Multiplexed imaging using epr-SRS probes. Leveraging the narrow linewidths of nitriles (~11 cm^{-1}), a palette of epr-enhanced dyes has been developed, enabling super-multiplexed imaging with up to 24-color visualization of biological targets[40]. However, the signals from nitrile bonds remain constant due to their inert nature, limiting their functionality in dynamic imaging applications. To expand the capabilities of SRS microscopy, we aimed to develop photoswitchable SRS probes for functional imaging with high spatial and temporal resolution, as well as for potential super-resolution SRS microscopy applications.

Development of photoswitchable electronic pre-resonance SRS probes. Building on our understanding of the pre-resonance effect, which arises from the coupling between electronic transitions and vibrational modes, we explored whether SRS signals that are typically photostable could be photoswitched by inducing different electronic transitions using light that modulate electronic-vibrational coupling[19]. One way this was achieved was by utilizing a photoswitchable near-infrared (NIR) fluorescent protein DrBphP-PCM[46], which shifts its absorption maximum depending on the conformation of its biliverdin chromophore. Light-induced switching of the chromophore conformation alters the pre-resonance effect, effectively turning the SRS signal on and off. This work is detailed in **Chapter 3**.

1.4 Development of BonFIRE to overcome the sensitivity and speed limit for SRS microscopy

Improving sensitivity has been a persistent challenge in Raman spectroscopy since its discovery in 1928 by C.V. Raman. The advent of SRS significantly enhanced the effective Raman cross-section, increasing it by approximately 10^8-fold to ~10^{-22} cm^2 [11]. The pre-resonance effect further amplifies the cross-section by an additional 10^5-fold boost, resulting in a cross-section of ~10^{-17} cm^2 [41], which corresponds to approximately 30-40 molecules. This value approaches the absorption cross-section of a typical fluorophore (~10^{-15} - 10^{-16} cm^2)[46]. Despite these substantial improvements, the Raman cross-section remains insufficient to achieve single-molecule sensitivity. This limitation arises from the fundamental heterodyne nature of SRS signal detection[13]. The SRS signal, which manifests as stimulated Raman loss (ΔI_P) or stimulated Raman gain (ΔI_S), is measured against the intense pump (I_P) and Stokes (I_S) laser beams. Consequently, the shot noise of the laser ultimately limits the sensitivity of the SRS signal[11,47].

Development of BonFIRE. To address the fundamental limitations of SRS microscopy, we explored an alternative contrast mechanism beyond Raman scattering. Specifically, we leveraged infrared (IR) absorption as the contrast mechanism, taking advantage of its significantly larger cross-sections compared to those of SRS. To circumvent the issue of laser noise, we adopted a secondary readout approach, utilizing fluorescence for highly

sensitive detection[48,49]. In this method, a molecule is first excited to a higher vibrational level via IR absorption of mid-infrared (MIR) light. It is then upconverted to the first electronic excited state using near-infrared (NIR) light, resulting in fluorescence emission, which serves as the detected signal. Molecules that do not absorb MIR light lack the energy ladder necessary to reach the electronic excited state and fluoresce. Thus, the fluorescence intensity is directly proportional to the vibrational population, effectively encoding vibrational information into the fluorescence signal. We termed this technique bond-selective fluorescence-detected infrared-excited (BonFIRE) microscopy[20]. Using BonFIRE, we achieved single-molecule imaging and biological imaging with MIR absorption as the vibrational contrast mechanism, surpassing the capabilities of epr-SRS. A detailed discussion of this work is provided in **Chapter 4**.

Development of wide-field BonFIRE imaging. Despite its improved sensitivity, the imaging speed of the first-generation BonFIRE microscope was constrained by sequential pixel scanning using a slow translational stage. To overcome this limitation, we introduced wide-field illumination combined with parallel pixel detection using a camera[21]. This advancement enabled imaging speeds surpassing video rates while preserving single-molecule sensitivity. Compared to SRS microscopy, which is limited by point-scanning and lower sensitivity, this innovation marks a significant step forward in imaging speed for bond-selective imaging. A detailed discussion of this work is presented in **Chapter 5**.

1.5 Future outlook

The advancement of optical imaging tools has been deeply intertwined with progress in our understanding of biology. BonFIRE merges the strengths of fluorescence microscopy and IR spectro-microscopy, combining the high sensitivity and specificity of fluorescence with the rich chemical information provided by IR absorption-based vibrational contrast. By integrating these complementary capabilities, BonFIRE has the potential to deliver multidimensional insights beyond those offered by traditional fluorescence imaging, paving the way for the exploration of novel biological questions.

Multiplexed super-resolution imaging. Multiplexed imaging is crucial for addressing the complexity of biological systems, where a deeper understanding requires analyzing the spatial interactions and context of diverse biomolecules. The small size of biomolecules further underscores the need for multiplexed super-resolution microscopy. However, achieving this remains challenging in fluorescence microscopy due to its inherently broad absorption and emission spectra, which result in significant spectral cross-talk. Sequential imaging approaches have been developed to enable highly multiplexed super-resolution imaging of proteins[50,51], but these methods often involve washing steps between imaging rounds, making them time-intensive and potentially disruptive to delicate samples. BonFIRE offers a promising solution, with its narrow linewidths, wide-field imaging capabilities, and high sensitivity, addressing the limitations of traditional fluorescence microscopy.

Local environment sensing. Another promising application for BonFIRE is local environmental sensing within cells. Cellular environments are highly dynamic, with

significant variations in pH, ion concentrations, electric fields, and hydrophobicity. Understanding these variations is critical for uncovering how cells function and respond to external stimuli. Among these factors, local electric fields play a particularly important role in stabilizing protein structures and mediating enzymatic activity[52,53]. The electronic Stark effect has traditionally been used to measure electric fields by detecting shifts in electronic energy levels in response to applied fields. However, despite its utility in qualitatively characterizing intracellular electric fields, the electronic Stark effect is limited by the non-linear and unpredictable response of fluorescent emission profiles to applied fields, making quantitative measurements in biological systems challenging[54–56]. In contrast, our work demonstrates that the BonFIRE vibrational lifetime of nitriles exhibits a strong linear correlation with hydrogen bonding and electric fields[20,22]. This enables local environmental sensing at high sensitivity, providing a tool for investigating the intricate molecular landscapes within cells and uncovering new insights into biological processes.

1.6 References

1. Yang, W. & Yuste, R. In vivo imaging of neural activity. *Nat Methods* **14**, 349–359 (2017).
2. Balasubramanian, H., Hobson, C. M., Chew, T.-L. & Aaron, J. S. Imagining the future of optical microscopy: everything, everywhere, all at once. *Commun Biol* **6**, 1–12 (2023).
3. Huang, Q. *et al.* The frontier of live tissue imaging across space and time. *Cell Stem Cell* **28**, 603–622 (2021).
4. Bon, P. & Cognet, L. On Some Current Challenges in High-Resolution Optical Bioimaging. *ACS Photonics* **9**, 2538–2546 (2022).
5. Liu, Z., Lavis, L. D. & Betzig, E. Imaging Live-Cell Dynamics and Structure at the Single-Molecule Level. *Molecular Cell* **58**, 644–659 (2015).
6. Verweij, F. J. *et al.* The power of imaging to understand extracellular vesicle biology in vivo. *Nat Methods* **18**, 1013–1026 (2021).
7. Ruiz-Rodado, V., Lita, A. & Larion, M. Advances in measuring cancer cell metabolism with subcellular resolution. *Nat Methods* **19**, 1048–1063 (2022).
8. Ploetz, E., Laimgruber, S., Berner, S., Zinth, W. & Gilch, P. Femtosecond stimulated Raman microscopy. *Appl. Phys. B* **87**, 389–393 (2007).
9. Freudiger, C. W. *et al.* Label-Free Biomedical Imaging with High Sensitivity by Stimulated Raman Scattering Microscopy. *Science* **322**, 1857–1861 (2008).
10. Nandakumar, P., Kovalev, A. & Volkmer, A. Vibrational imaging based on stimulated Raman scattering microscopy. *New J. Phys.* **11**, 033026 (2009).
11. Min, W., Freudiger, C. W., Lu, S. & Xie, X. S. Coherent Nonlinear Optical Imaging: Beyond Fluorescence Microscopy. *Annual Review of Physical Chemistry* **62**, 507–530 (2011).
12. Cheng, J.-X. & Xie, X. S. Vibrational spectroscopic imaging of living systems: An emerging platform for biology and medicine. *Science* **350**, (2015).
13. Cheng, J.-X. & Xie, X. S. *Coherent Raman Scattering Microscopy*. (CRC press, Boca Raton (Fla.), 2013).
14. Shen, Y., Hu, F. & Min, W. Raman Imaging of Small Biomolecules. *Annual Review of Biophysics* **48**, 347–369 (2019).

15. Hu, F., Shi, L. & Min, W. Biological imaging of chemical bonds by stimulated Raman scattering microscopy. *Nature Methods* **16**, 830–842 (2019).
16. Tipping, W. J., Lee, M., Serrels, A., Brunton, V. G. & Hulme, A. N. Stimulated Raman scattering microscopy: an emerging tool for drug discovery. *Chem. Soc. Rev.* **45**, 2075–2089 (2016).
17. Lee, H. J. & Cheng, J.-X. Imaging chemistry inside living cells by stimulated Raman scattering microscopy. *Methods* **128**, 119–128 (2017).
18. Lee, D. *et al.* Visualizing Subcellular Enrichment of Glycogen in Live Cancer Cells by Stimulated Raman Scattering. *Anal. Chem.* **92**, 13182–13191 (2020).
19. Lee, D. *et al.* Toward photoswitchable electronic pre-resonance stimulated Raman probes. *J. Chem. Phys.* **154**, 135102 (2021).
20. Wang, H. *et al.* Bond-selective fluorescence imaging with single-molecule sensitivity. *Nat. Photon.* **17**, 846–855 (2023).
21. Lee, D. *et al.* Wide-field bond-selective fluorescence imaging: from single-molecule to 2 cellular imaging beyond video-rate. *Optica*.
22. Kocheril, P. A., Wang, H., Lee, D., Naji, N. & Wei, L. Nitrile Vibrational Lifetimes as Probes of Local Electric Fields. *J. Phys. Chem. Lett.* 5306–5314 (2024) doi:10.1021/acs.jpclett.4c00597.
23. Wang, H. *et al.* Room-Temperature Single-Molecule Infrared Imaging and Spectroscopy through Bond-Selective Fluorescence. *Angewandte Chemie International Edition* **n/a**, e202413647.
24. DeBerardinis, R. J., Lum, J. J., Hatzivassiliou, G. & Thompson, C. B. The Biology of Cancer: Metabolic Reprogramming Fuels Cell Growth and Proliferation. *Cell Metabolism* **7**, 11–20 (2008).
25. Lunt, S. Y. & Vander Heiden, M. G. Aerobic Glycolysis: Meeting the Metabolic Requirements of Cell Proliferation. *Annual Review of Cell and Developmental Biology* **27**, 441–464 (2011).
26. Yan, L., Raj, P., Yao, W. & Ying, H. Glucose Metabolism in Pancreatic Cancer. *Cancers (Basel)* **11**, (2019).
27. Heiden, M. G. V., Cantley, L. C. & Thompson, C. B. Understanding the Warburg Effect: The Metabolic Requirements of Cell Proliferation. *Science* **324**, 1029–1033 (2009).
28. Khan, T. *et al.* Revisiting Glycogen in Cancer: A Conspicuous and Targetable Enabler of Malignant Transformation. *Front. Oncol.* **10**, (2020).
29. Dauer, P. & Lengyel, E. New Roles for Glycogen in Tumor Progression. *Trends in Cancer* **5**, 396–399 (2019).
30. Thwe, P. M. *et al.* Cell-Intrinsic Glycogen Metabolism Supports Early Glycolytic Reprogramming Required for Dendritic Cell Immune Responses. *Cell Metabolism* **26**, 558-567.e5 (2017).
31. Zois, C. E. & Harris, A. L. Glycogen metabolism has a key role in the cancer microenvironment and provides new targets for cancer therapy. *J Mol Med* **94**, 137–154 (2016).
32. Wang, H., Du, J., Lee, D. & Wei, L. Chapter 20 - Stimulated Raman scattering imaging with small vibrational probes. in *Stimulated Raman Scattering Microscopy* (eds. Cheng,

J.-X., Min, W., Ozeki, Y. & Polli, D.) 289–310 (Elsevier, 2022). doi:10.1016/B978-0-323-85158-9.00023-3.

33. Wei, L. *et al.* Live-cell imaging of alkyne-tagged small biomolecules by stimulated Raman scattering. *Nature Methods* **11**, 410–412 (2014).
34. Hu, F. *et al.* Vibrational Imaging of Glucose Uptake Activity in Live Cells and Tissues by Stimulated Raman Scattering. *Angewandte Chemie International Edition* **54**, 9821–9825 (2015).
35. Hu, F., Wei, L., Zheng, C., Shen, Y. & Min, W. Live-cell vibrational imaging of choline metabolites by stimulated Raman scattering coupled with isotope-based metabolic labeling. *Analyst* **139**, 2312–2317 (2014).
36. Zhang, D., Slipchenko, M. N. & Cheng, J.-X. Highly Sensitive Vibrational Imaging by Femtosecond Pulse Stimulated Raman Loss. *J. Phys. Chem. Lett.* **2**, 1248–1253 (2011).
37. García, A. A., Pfisterer, S. G., Riezman, H., Ikonen, E. & Potma, E. O. D38-cholesterol as a Raman active probe for imaging intracellular cholesterol storage. *JBO* **21**, 061003 (2015).
38. Li, J. & Cheng, J.-X. Direct Visualization of De novo Lipogenesis in Single Living Cells. *Sci Rep* **4**, 6807 (2014).
39. Zhang, L. *et al.* Spectral tracing of deuterium for imaging glucose metabolism. *Nat Biomed Eng* **3**, 402–413 (2019).
40. Wei, L. *et al.* Super-multiplex vibrational imaging. *Nature* **544**, 465–470 (2017).
41. Wei, L. & Min, W. Electronic Preresonance Stimulated Raman Scattering Microscopy. *J. Phys. Chem. Lett.* **9**, 4294–4301 (2018).
42. Albrecht, A. C. & Hutley, M. C. On the Dependence of Vibrational Raman Intensity on the Wavelength of Incident Light. *J. Chem. Phys.* **55**, 4438–4443 (1971).
43. Asher, S. A. UV Resonance Raman Studies of Molecular Structure and Dynamics: Applications in Physical and Biophysical Chemistry. 54.
44. Shi, L. *et al.* Electronic Resonant Stimulated Raman Scattering Micro-Spectroscopy. *J. Phys. Chem. B* **122**, 9218–9224 (2018).
45. Du, J., Tao, X., Begušić, T. & Wei, L. Computational Design of Molecular Probes for Electronic Preresonance Raman Scattering Microscopy. *J. Phys. Chem. B* **127**, 4979–4988 (2023).
46. Kastrup, L. & Hell, S. W. Absolute Optical Cross Section of Individual Fluorescent Molecules. *Angewandte Chemie International Edition* **43**, 6646–6649 (2004).
47. Rigneault, H. & Ozeki, Y. Sensitivity and noise in SRS microscopy. in *Stimulated Raman Scattering Microscopy* 21–40 (Elsevier, 2022). doi:10.1016/B978-0-323-85158-9.00010-5.
48. Laubereau, A., Seilmeier, A. & Kaiser, W. A new technique to measure ultrashort vibrational relaxation times in liquid systems. *Chemical Physics Letters* **36**, 232–237 (1975).
49. Whaley-Mayda, L., Penwell, S. B. & Tokmakoff, A. Fluorescence-Encoded Infrared Spectroscopy: Ultrafast Vibrational Spectroscopy on Small Ensembles of Molecules in Solution. *J. Phys. Chem. Lett.* **10**, 1967–1972 (2019).
50. Unterauer, E. M. *et al.* Spatial proteomics in neurons at single-protein resolution. *Cell* **187**, 1785-1800.e16 (2024).

51. Schueder, F. *et al.* Unraveling cellular complexity with transient adapters in highly multiplexed super-resolution imaging. *Cell* **187**, 1769-1784.e18 (2024).
52. Zheng, C., Ji, Z., Mathews, I. I. & Boxer, S. G. Enhanced active-site electric field accelerates enzyme catalysis. *Nat. Chem.* **15**, 1715–1721 (2023).
53. Suydam, I. T., Snow, C. D., Pande, V. S. & Boxer, S. G. Electric Fields at the Active Site of an Enzyme: Direct Comparison of Experiment with Theory. *Science* **313**, 200–204 (2006).
54. Lazzari-Dean, J. R., Gest, A. M. & Miller, E. W. Optical estimation of absolute membrane potential using fluorescence lifetime imaging. *eLife* **8**, e44522 (2019).
55. Hou, J. H., Venkatachalam, V. & Cohen, A. E. Temporal Dynamics of Microbial Rhodopsin Fluorescence Reports Absolute Membrane Voltage. *Biophysical Journal* **106**, 639–648 (2014).
56. Ratcliff, L. E. *et al.* Challenges in large scale quantum mechanical calculations. *WIREs Computational Molecular Science* **7**, e1290 (2017).

Chapter 2

VISUALIZING SUBCELLULAR ENRICHMENT OF GLYCOGEN IN LIVE CANCER CELLS BY STIMULATED RAMAN SCATTERING

Sections of this chapter have been adapted from:
Lee, D.; Du, J.; Yu, R.; Su, Y.; Heath, J. R.; Wei, L. Visualizing Subcellular Enrichment of Glycogen in Live Cancer Cells by Stimulated Raman Scattering. Anal. Chem. 2020, 92 (19), 13182–13191. https://doi.org/10.1021/acs.analchem.0c02348.

2.1 Abstract

Glycogen, a branched glucose polymer, helps regulate glucose homeostasis through immediate storage and release of glucose. Reprogramming of glycogen metabolism has recently been suggested to play an emerging role in cancer progression and tumorigenesis. However, regulation of metabolic rewiring for glycogen synthesis and breakdown in cancer cells remains less understood. Despite the availability of various glycogen detection methods, selective visualization of glycogen in living cells with high spatial resolution has proven to be highly challenging. Here, we present an optical imaging strategy to visualize glycogen in live cancer cells with minimal perturbation by combining stimulated Raman scattering microscopy with metabolic incorporation of deuterium-labeled glucose. We revealed the subcellular enrichment of glycogen in live cancer cells and achieved specific glycogen mapping through distinct spectral identification. Using this method, different glycogen metabolic phenotypes were characterized in a series of patient-derived BRAF-mutant melanoma cell-lines. Our results indicate that cell-lines manifesting high glycogen storage level showed increased tolerance to glucose deficiency among the studied melanoma phenotypes. This method opens up the possibility for non-invasive study of complex glycogen metabolism at subcellular resolution and may help reveal new features of glycogen regulation in cancer systems.

2.2 Introduction

Cancer cells undergo significant metabolic reprogramming to meet their high energy and anabolic demands[1]. Numerous studies have revealed that metabolic pathways that branch from glycolysis, including glycogenesis, tricarboxylic acid (TCA) cycle, pentose phosphate pathway (PPP), serine biosynthesis, and fatty acid synthesis, can be altered to promote tumorigenesis and cancer cell survival[2–4]. Although in-depth understandings have been achieved for many of these metabolic pathways, valuable insights have only started to emerge on the role of rewired glycogen metabolism in cancer-cell pathophysiology[5,6]. Glycogen, in the form of branched polysaccharides of glucose residues, has mostly been regarded as the glucose storage site in mammalian tissues (e.g. liver, muscle, kidney, brain, and lungs)[6]. Yet more recently, it has been suggested that glycogen metabolism is upregulated in cancer cells in response to hypoxia as a sign of metabolic adaptation[7]. In

addition, the shuttling of glycogen was found in metastasizing ovarian cancer cells co-cultured with cancer-associated fibroblasts[8]. With increasing evidence demonstrating the importance of cell-type and organelle specific glycogen metabolism in cancer systems[8,9], a live-cell imaging platform for investigating the glycogen activities and tracking the mobile glycogen dynamics[10–12] with good selectivity, subcellular resolution, and fast temporal acquisition is in high demand.

However, subcellular interrogation of glycogen in live cancer cells remains challenging due to limitations of existing methods[6]. Commonly used glycogen biochemical assays require extensive post-processing and lack spatial information[13]. Magnetic resonance imaging (MRI) with isotope-labeled (i.e. ^{13}C) glucose and positron emission tomography (PET) with radiotracer are powerful for *in vivo* glycogen imaging but are limited to millimeter resolution[14,15]. Fourier transform infrared (FTIR) has recently been adopted for label-free imaging of glycogen in brain tissues but lacks subcellular resolution[16]. Chemical staining and imaging (e.g. periodic acid-Schiff) provides subcellular information but requires sample fixation, which is known to lose more than 70% of glycogen[6]. Mass spectrometry-based methods such as nano secondary ion mass spectrometry (nano SIMS) or transmission electron microscopy (TEM) are sample-destructive and not compatible for live-cell studies. Fluorescence imaging of 2-NBDG, a popular fluorescent glucose analog, offers subcellular and live-cell visualization[17,18] but has a few limitations from the fluorophore labeling. First, 2-NBDG is significantly more hydrophobic compared to regular glucose[19], which can yield an affinity to lipids that decreases the specificity of 2-NBDG labeling of glycogen[20,21]. Second, 2-NBDG is non-metabolizable after phosphorylation and may not provide downstream metabolic information[22].

In this study, we report a strategy of stimulated Raman scattering (SRS) imaging with deuterated glucose (d_7-glucose) labeling for visualizing subcellular glycogen in living cancer cells. We also demonstrate simultaneous metabolic phenotyping of glycogen together with glucose-derived proteins and lipids. By incubating cells in d_7-glucose containing medium and targeting carbon-deuterium (C-D) vibrations using SRS, we visualized the incorporation of C-D bonds into subcellular glycogen. Taking advantage of the characteristic C-D Raman peaks of various types of macromolecules[23], we then constructed concentration maps of C-D labeled glycogen, lipids, and proteins using a robust linear combination algorithm in live HeLa and U87 cells. After validating the detection specificity of glycogen, we applied our technique to quantitatively study the subcellular accumulation of glycogen in a series of melanoma cancer cells that share the same BRAF-mutation but have different phenotypes. Our glycogen phenotyping results show consistent trend with gene expression profiles of glycogen metabolic enzymes. Guided by our observations, we further uncovered a previously unknown metabolic feature of increased resistance for glucose deficiency for one melanoma subtype. This imaging strategy sheds light on the role of glycogen and furthers our understanding of complex metabolic dynamics in cancer cells.

2.3 Methods

Cell-lines and cell culture

U87 and HeLa cells were cultured in DMEM (Gibco), supplemented with 10% fetal bovine serum (Corning, 35-015-CV), and 1% penicillin-streptomycin (Sigma-Aldrich). Patient-derived melanoma cell lines used in this study were generated under UCLA IRB approval # 11–003254. Melanoma cells were cultured in RPMI 1640 (Gibco, 11875119), supplemented with 10% fetal bovine serum (Corning, 35-015-CV), and 0.2% MycoZap Plus-CL antibiotics (Lonza, VZA-2011). Cultures were incubated in a water-saturated incubator at 37°C with 5% CO_2. Cells were passaged 3-5 days once confluence reached 80%.

Spontaneous Raman spectra

Fixed cell pellets were washed twice with pure water and then resuspended in water to form a cell solution, avoiding the influence of salt crystals after drying. The cell solution containing 5k cells was added dropwise on a glass slide. After air dry, glass slides with cells were then used to take Raman spectra. Spontaneous Raman spectra were acquired using an upright confocal Raman spectrometer (Horiba Raman microscope; Xplora plus). A 532 nm YAG laser is used to illuminate the sample with a power of 12 mW on sample through a 100 x, N.A. 0.9 objective (MPLAN N; Olympus) with slit 100 μm and hole 500 μm. Spectro/Raman shift center was set to be 2000.04 cm^{-1}. With a 1200 grating (750 nm), Raman shift ranges from 690.81 cm^{-1} to 3141.49 cm^{-1} was acquired to cover whole cellular Raman peaks. Acquisition time for one spectrum was set to be 5 s, and then averaged for 5 times. The target cell was chosen randomly and spectra of five points (center, top, bottom, left, right) on the cell were acquired. The acquired spectra were processed by the LabSpec 6 software for baseline correction.

Stimulated Raman scattering microscopy

Fig. 1B illustrates the SRS microscopy system used in this study. A picoEMERALD (Applied Physics and Electronics) system provided the pump (770-990 nm wavelength, 2 ps pulse width, 80 MHz repetition rate) and Stokes (1032 nm wavelength, 2 ps pulse width, 80 MHz repetition rate). Stokes beam was modulated by a built-in electro-optic modulator (EOM) at 20 MHz. The pump and Stokes beams were spatially and temporally overlapped within picoEMERALD. To fill the back aperture of a 25X water objective (XLPLN25XWMP, 1.05 N.A., Olympus), the two beams were expanded using a telescope and were guided into an inverted multiphoton laser scanning microscopy (FV3000, Olympus). The beams were aligned to maximize SRS signal of deuterium oxide (99.9 at% D, 151882 ALDRICH). The beams transmitted through the sample were collected using a high-NA condenser (oil immersion, 1.4 N.A., Olympus). Before detection of stimulated Raman loss using a large area (10×10 mm) Si photodiode (S3590-09, Hamamatsu), the Stokes beam was blocked out using a bandpass filter (893/209 BrightLine, 25 mm, AVR Optics) to filter out the Stokes beam. 64 V DC voltage was used on the photodiode to increase saturation threshold and reduce response time. The output current is terminated by a 50 Ω terminator and pre-filtered by a 19.2-23.6-MHz band-pass filter (BBP-21.4+, Mini-Circuits) to reduce laser and scanning noise. A lock-in amplifier (SR844, Stanford Research Systems) demodulated the signal at shot-noise-limited detection sensitivity. The in-phase X output of the lock-in amplifier was sent to analog channel of the FV1200 software (FV30-ANALOG).

Image acquisition speed is limited by 30 µs time constant set for the lock-in amplifier. Correspondingly, we use 80 µs pixel dwell time, which gives a speed of 8.5 s/frame for a 320-by-320-pixel field of view. For unmixing, 3 images at channels 2123 cm^{-1}, 2151 cm^{-1} and 2192 cm^{-1} are required, which leads to total acquisition time of approximately 1 min. The total acquisition to record an SRS spectral data cube (37 images) was approximately 9 minutes including image acquisition and wavelength tuning. For 2151 cm^{-1} (C-D, d_7-glucose), 2845 cm^{-1} (CH_2) and 2940 cm^{-1} (CH_3), the wavelengths of Pump laser are 844, 797.3, and 791.3 nm, respectively. Laser powers on sample are measured to be 30 mW for modulated Stokes beam and 160 mW for Pump beam. Laser powers are monitored through image acquisition by an internal power meter and power fluctuation are controlled within 5% by the laser system. 16-bit grey scale images are acquired by Fluoview software. SRS spectra were acquired by fixing the Stokes beam at 1031.2 nm and scanning the pump beam through the designated wavelength range point by point.

Coating of imaging dish

In experiments where melanoma cell lines were used, imaging dish (MatTEK, P35G-1.5-14-C) was coated with a 2% sterile gelatin solution (Sigma, G1393) for 30 minutes, then the coating solution was removed and the dish was left for air dry for another 30 minutes before using. For U87 and HeLa cell lines, cells were directedly seeded on to the imaging dish without any coating.

Metabolic deuterium labeling

Deuterated glucose RPMI 1640 medium was made by supplying 11.1 mM d_7-glucose (Cambridge Isotope Laboratories, DLM-2062-1) into glucose deficient RPMI 1640 medium (Gibco, 11879020). The solution was then added 10% FBS and 0.2% MycoZap Plus-CL antibiotics. Cultured melanoma cells were seeded onto an imaging dish to optimal confluency. Deuterated glucose DMEM was made by supplying 25 mM d_7-glucose (Cambridge Isotope Laboratories, DLM-2062-1) into glucose deficient DMEM (Gibco). The solution was then added 10% FBS and 1% penicillin-streptomycin.

GPI and cell viability assay

Glycogen phosphorylase inhibitor (Sigma, 361515-1MG) was dissolved in DMSO (ATCC, 4-X) to a concentration of 5 mM before diluting at designated concentrations into cell culture media. To conduct cell viability assay, 3k to 5k cells were seeded into six well dishes (Corning, 3516). After culturing for 2 days, growth medium was replaced with fresh medium containing drugs with indicated concentration, and the incubation continued for another 3 days. For glucose deficiency experiment, the growth medium was replaced with glucose-deficient medium. Cell viability was measured by counting cell numbers of each well. Cell number was normalized by number of cells in normal glucose-containing medium to compute the relative viability.

Ratio image processing and data analysis

Images were analyzed and assigned color by ImageJ. For CD_P/CD_L ratio imaging, a threshold (mask) image was first generated by adjusting threshold using Huang method, then non-zero

values were normalized to one. CD_P images were then divided by the same set of CD_L, and the resulting ratio image multiplied with mask image to create the final CD_P/CD_L ratio image.

Linear combination algorithm for spectral unmixing

To create the linear combination matrix in Fig. 2D, SRS hyperspectral images were acquired for U87 cells. Then spectra of intracellular glycogen, nucleoli, and lipid droplets were averaged. The SRS intensities at 2192 cm^{-1}, 2151 cm^{-1}, and 2123 cm^{-1} were extracted from the spectra and were used as coefficient after normalization to create the 3x3 matrix[23]. For CH channel unmixing, lipid-channel (CH_L) image was processed from a linear combination algorithm of $5\cdot[CH_2] - 0.4\cdot[CH_3]$ from the CH_2 and CH_3 images[24]. Protein-channel (CH_P) image was processed from a linear combination algorithm of $[CH_3] - [CH_2]$ from the CH_2 and CH_3 images[24].

Triton and perchloric acid wash

PBS solution containing 0.5% Triton X-100 (Sigma, T8787), PBS-T solution, was used to wash cells in imaging dish. 1 ml PBS-T detergent solution was gently added into imaging dish and the dish was placed in 4 ^oC for 10 minutes. Then the PBS-T washing solution was removed and the samples were washed with PBS for two times before imaging. Glycogen was removed by incubation in 10% perchloric acid for 5 minutes and washing with PBS.

RNA extraction, library construction, and sequencing

Total RNA was extracted from frozen cells pellets (~ 1 million cells) using the RNeasy Micro Kit (Qiagen, 74004) according to the manufacturer's protocol. Then the RNA sequencing (RNA-seq) was performed using BGISEQ-500 platform at BGI Genomics (Wuhan, China). The library preparation was followed by BGI's standard procedure.

2-NBDG fluorescence and SRS concurrent imaging

HeLa cells were co-incubated with 25mM d_7-glucose for 60 hours and 100μM of 2-NBDG for the last 14 hours. Then fluorescence imaging was conducted with 488 nm excitation laser. Fluorescence was detected at wavelength range 500-600 nm. On the same set of cells, SRS images were taken at pump wavelengths 841 nm (2192 cm^{-1}), 844 nm (2151 cm^{-1}), and 846 nm (2123 cm^{-1}).

Periodic acid acid-Schiff (PAS) staining[7]

HeLa cells incubated with d_7-glucose for three days were fixed using 4% PFA for 15 minutes. After several washing steps using PBS buffer, the cells were then incubated in 1% periodic acid (Sigma, 3951) for 30 minutes at room temperature. After several washing steps using deionized water, the cells were then incubated with Schiff's reagent (Sigma, 3952016) for 30 minutes. The cells were washed multiple times with deionized water before they were imaged under an Olympus microscope (FV3000) installed with a color CMOS camera (Thorlabs, CS165CU).

Immuno-labeling using anti-glycogen antibodies[17]

Fixed cells incubated with d_7-glucose were permeabilized with 2% BSA-0.2% Triton X-100 PBS for 5 minutes on ice. Then non-specific bindings were blocked with 2% BSA-PBS for 1 h at room temperature. The cells were incubated in monoclonal mouse anti-glycogen primary antibody, IV58B6, diluted 1:60 in 2% BSA-PBS at 4 °C overnight. After incubating the cells for 30 minutes in BSA-PBS, the cells were incubated with Alexa Fluor 594-conjugated goat anti-mouse IgM (Invitrogen, A-21044) diluted 1:100 in 2% BSA-PBS for 4 hours at room temperature. The cells were incubated in BSA-PBS for 30 minutes and were washed multiple times in PBS before imaging. Fluorescence imaging was conducted with 561 nm excitation laser. Fluorescence was detected at wavelength range 570-670 nm.

Glycogen extraction using KOH/ethanol[8]

Cells incubated with d_7-glucose were fixed after 3 days. Cell suspension was centrifuged for 5 minutes at 2000 rpm. After removing the supernatant, the cells were incubated in 30% KOH for 30 minutes at 95 °C. After centrifugation and removing the supernatant, pure ethanol was added to precipitate the glycogen. After another round of centrifugation and supernatant removal, white glycogen powder was collected. The powder was then dried on a microscope glass slide before spontaneous spectrum acquisition.

2.4 Results

Identifying Subcellular Glycogen by SRS Microscopy of D_7-glucose Labeling

The coupling of d_7-glucose labeling with SRS imaging is ideal for subcellular visualization of glycogen in cancer cells. Isotope labeling with deuterium is a minimum labeling strategy. D_7-glucose shares almost identical physicochemical properties to glucose and therefore can be metabolized into downstream metabolites. We expected that d_7-glucose, after being transported into cells, will be phosphorylated to d_7-glucose-6-phosphate (G6P) and then be converted to d_7-glucose-1-phosphate (G1P). G1P then reacts with uridine triphosphate (UTP) to synthesize d_7-uridine diphosphate (UDP) glucose **(Fig. 1A)**. This activated glucose metabolite is incorporated into the growing chain of glycogen by glycogen synthase, the key regulatory enzyme in glycogen synthesis. Consequently, all newly synthesized glycogen is composed of repeating units of d_7-glucose monomers **(Fig. 1A)**. Specifically targeting the vibrational frequency of the C-D bonds from glycogen, SRS microscopy could, in principle, map out the intracellular enrichment of glycogen with fine spatial resolution (~ 450 nm) without interference from endogenous cellular background in live cells **(Fig. 1B & Fig. 1C)**. In addition to minimum perturbation, d_7-glucose labeling offers high imaging sensitivity for glycogen. Our detection sensitivity for d_7-glucose solution is determined to be 4 mM[23,24]. Although this number is less satisfying for imaging glucose uptake since the intracellular glucose concentration is about 3-5 mM[19], it is ideal for glycogen imaging with a detection limit as sensitive as 33 nM, since glycogen is a polymer composed of up to 120,000 repeating glucose residues[25]. In contrast, a recently reported alkyne-labeled Raman glucose analogue, 3-OPG, offered a higher detection sensitivity (1.4 mM) for glucose imaging but could not be metabolized via the glycolysis pathway[19,26].

Besides being incorporated into glycogen, d_7-glucose can be converted into deuterated pyruvate, which subsequently enters TCA cycles to produce anabolic precursors including citrate, oxaloacetate, aspartate, and glutamate **(Fig. S1)**. Consequently, macromolecules (e.g. lipids and proteins) synthesized from deuterated precursors are sparsely labelled with deuterium **(Fig. S1)**. The deuterated G6P can also be metabolized through the pentose phosphate pathway for generating sparsely deuterated DNA/RNA **(Fig. S1)**. The labeling patterns for different chemical structures of the macromolecules (i.e. proteins, lipids, DNA/RNA, and glycogen) result in varied Raman C-D peak shapes[23]. Therefore, we reasoned that labeled glycogen could be identified by its unique C-D spectral shape.

Driven by our rationale above, we sought to validate the use of d_7-glucose to label glycogen in both HeLa (cervical cancer) and U87 (glioblastoma) cells, two widely adopted model cancer cell-lines. We cultured both cells in d_7-glucose medium for three days and imaged the cells by targeting the C-D peak at 2151 cm^{-1} by SRS **(Fig. 2A, CD, white-arrowed; Fig. S2)**[23]. Interestingly, we observed highly enriched subcellular C-D signals in the cytoplasm of a subset of cells **(Fig. 2A, CD at 2151 cm^{-1} vs off-resonance at 1836 cm^{-1}, arrowed)**. Such enrichment is distinct from previous reported distributions of lipids, including lipid droplets, and proteins, which yield more diffusive cytosolic patterns present in all the cells cultured in d_7-glucose medium[27]. Since this enrichment pattern resembles the intracellular glycogen pools reported previously by TEM[7], we hypothesized that it originated from glycogen accumulation. To test this, we first compared the CD image with

label-free CH_L and CH_P images, representing pre-existing lipids and proteins, respectively **(Fig. 2A)**. As expected, the enriched C-D pattern (red) does not co-localize with either lipid (green) or protein (blue) distributions in the CH_L and CH_P images from the same cells **(Fig. 2A CD/CH_L/CH_P overlay)**. This suggests that the macromolecules in the accumulated spots are indeed not lipids or proteins but may be glycogen.

Next, we adopted a hyperspectral SRS (hSRS) strategy by acquiring SRS spectra specifically from these bright spots in both HeLa and U87 cells **(Fig. 2A, arrowed)** to spectrally identify the accumulated molecules. The obtained C-D spectra are mountain-like with three characteristic peaks at 2123, 2151, and 2192 cm^{-1} **(Fig. 2B, pink and green)**. The overall spectral shape resembles that directly generated from d_7-glucose solution **(Fig. 2B, black)**, which suggests that the accumulated molecules preserve a similar chemical environment for C-D bond to that of glucose. To confirm whether the bright spots are indeed glycogen, we purified the deuterated glycogen from cells cultured in d_7-glucose using the standard KOH/ethanol glycogen extraction protocol[8]. The spontaneous Raman spectrum from extracted deuterated glycogen closely resembles that of the *in situ* SRS spectrum **(Fig. S3)**. Such high resemblance indicates that the bright glycogen spots, which can be as large as a few μm **(Fig. S2)**, were indeed composed of pure glycogen. A similar spectral shape was previously reported from glycogen extracted from the liver of mice fed with d_7-glucose[23]. In contrast, the C-D spectra **(Fig. 2C, red)** are very different from those generated from lipid droplets **(Fig. 2C, green)** and nucleoli **(Fig. 2C, blue)**. The *in-situ* SRS spectra from deuterated lipid droplets and nucleoli **(Fig. 2A, blue and orange arrowed)** also agreed well with that previous reported from purified lipids and proteins in cells cultured in d_7-glucose[28,29], indicating that the lipid droplets and nucleoli contained close-to-pure newly-synthesized lipids and proteins, respectively. Moreover, this accumulation pattern is retained in paraformaldehyde (PFA) fixed cells, ruling out the possibility of direct clustering of d_7-glucose. Finally, we compared SRS images of d_7-glucose cultured cells with that of the established glycogen staining methods, the periodic acid-Schiff (PAS) staining and the immuno-labeling using anti-glycogen antibody. We confirmed that SRS images present excellent correlation with brightfield images after PAS staining **(Fig. S4)** as well as immunofluorescence images **(Fig. S5)**. We note that PAS also stains glycoproteins and glycolipids which may result in signals in the cytosols **(Fig. S4)**. Together, these data provide direct evidence that the identity of the accumulated molecules is glycogen.

Specific Imaging of Glycogen with a Linear Combination Algorithm

After confirming our imaging capability for intracellular glycogen through d_7-glucose labeling, we then aimed to distinguish deuterated glycogen with other d_7-glucose derived macromolecules to achieve high imaging specificity. Because of the unique C-D spectral shapes of the macromolecules **(Fig. 2C)**, we could generate a linear combination algorithm to specifically retrieve the distribution maps for each C-D labeled metabolic end products. We derived a robust linear-combination algorithm **(Fig. 2D)**, in which SRS signals are the products of normalized cross-section matrix, generated from Fig. 2C, and macromolecule concentrations. A similar strategy was recently adopted for multi-component imaging in mouse liver after starvation[23]. We included glycogen, lipids, and proteins but excluded DNA due to an almost invisible C-D nucleus signal, which suggested minimum

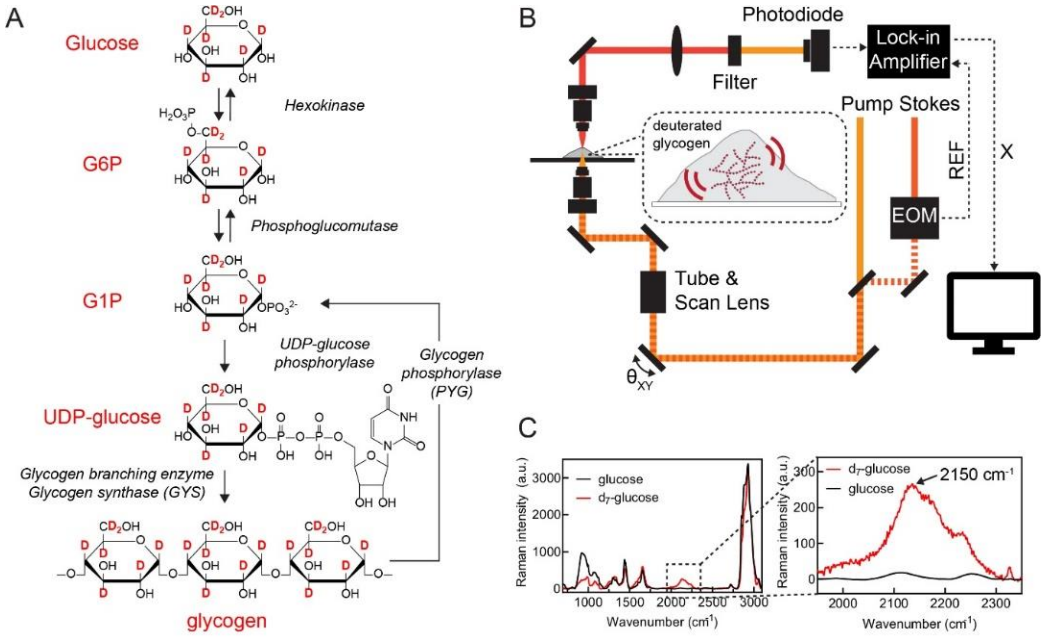

Fig 1. Glycogen mapping by SRS microscopy with d_7-glucose labeling. (A) Metabolic incorporation of d_7-glucose into glycogen through glycogenolysis pathway. G6P: glucose-6-phosphate, G1P: glucose-1-phosphate, UDP: uridine diphosphate. (B) Experimental scheme of SRS microscopy. EOM: electro-optic modulator. REF: reference. (C) Spontaneous Raman spectra of HeLa cells after culturing in regular glucose (black) and d_7-glucose media (red) for 3 days. Zoomed-in spectra of the boxed region show C-D Raman peaks in the cell-silent window.

incorporation of C-D bonds to DNA/RNA in cancer cells. With this matrix, we can construct concentration maps for glycogen, lipids, and proteins metabolically derived from d_7-glucose by acquiring SRS images at three designated frequencies **(Fig. 2D, i.e. 2123, 2151, and 2192 cm^{-1})** without the need of hyperspectral images, which require much longer acquisition time and could lead to motion artifacts for live cells.

We applied the algorithm **(Fig. 2D)** to SRS images acquired from live HeLa and U87 cells cultured in d_7-glucose medium. The same algorithm was also validated on fixed cells to avoid any potential issues from movement of live cells. Our unmixed results successfully distinguished deuterated glycogen, lipids, and proteins **(Fig. 3 & Fig. S6, before vs after unmixing)**. First, CD_G images clearly retrieved the bright subcellular spots. Second, CD_L and CD_P images for newly synthesized lipids and proteins showed high resemblance to those in the CH_L and CH_P channels **(Fig. 3 & Fig. S6, after unmixing, see methods)**. In particular, lipid droplets were shown in both CD_L and CH_L channels; and nucleoli with fast protein turnover are highlighted in both CD_P and CH_P channels. Third, we performed a molecular-specific washing experiment with either triton or perchloric acid to eliminate lipids and glycogen, respectively and then compared the unmixed images before and after wash from the same set of cells. Correspondingly, the resulting images clearly showed the selective removal of lipids in the CD_L channel or glycogen in the CD_G channel (Figs. S7 and S8). This validates our algorithm for unequivocal SRS imaging of glycogen, together with lipids and proteins metabolized from d_7-glucose in both live and fixed cells. We note that, unlike CD_L and CD_P signals that are mostly homogeneous across the cells, CD_G signals are highly localized intracellularly and only appear in a subset of

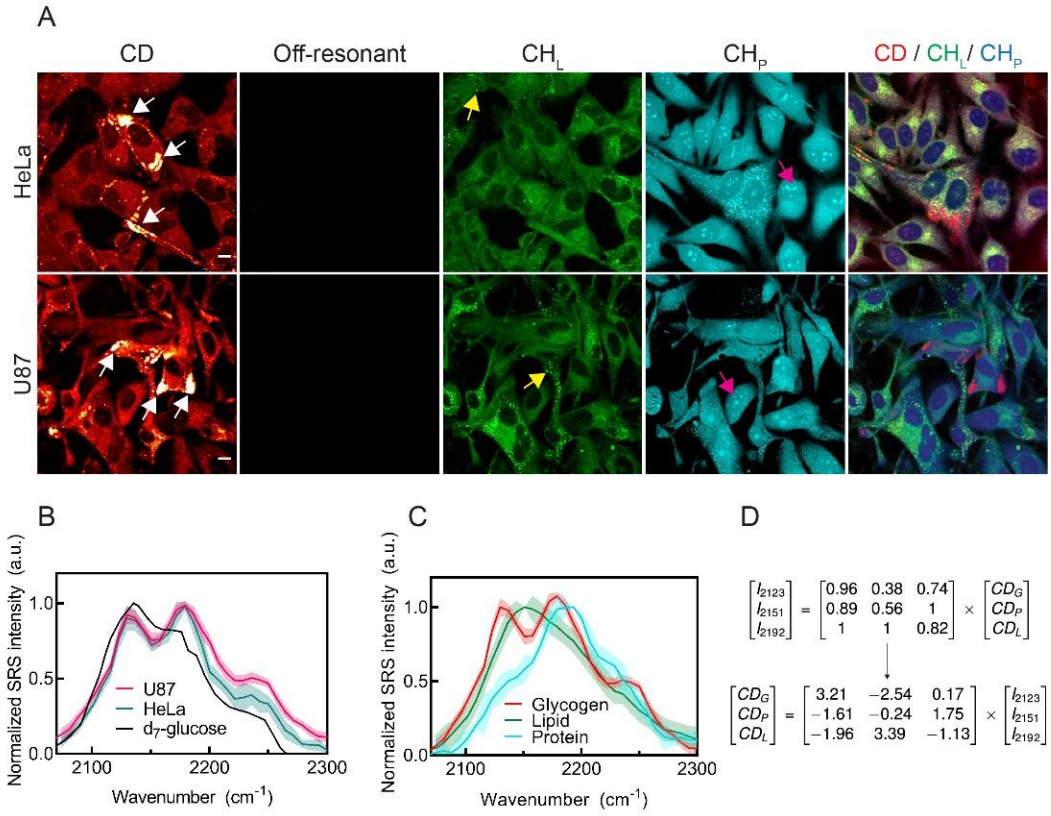

Fig. 2. **Identification of subcellular glycogen by SRS imaging of d_7-glucose labeling.** (A) Live-cell SRS images of HeLa and U87 cells after incubating in d_7-glucose media for 3 days. CD (2151 cm^{-1}) channel shows highly enriched subcellular signals, indicated by white arrows. Off-resonant image (1836 cm^{-1}) of the same cells is background free. CH_L and CH_P images for endogenous lipids and proteins are unmixed from CH images acquired at 2845 cm^{-1} & 2940 cm^{-1} channels using a spectral linear combination algorithm (see Methods for details). Yellow and magenta arrows indicate lipid droplets and nucleoli at which SRS spectra were acquired, respectively. (B) Normalized SRS spectra from the subcellular C-D enriched spots (arrowed in (A)) in U87 (shaded purple), HeLa (shaded pink) cells and 1.1 M d_7-glucose solution (red). (C) Representative glycogen (red), lipid (green), and protein (blue) SRS spectra generated from the subcellular C-D enriched spots (white arrows), lipid droplets (yellow arrows), and nucleoli (magenta arrows) in cells. (D) Linear combination matrix with coefficients derived from (C). Error bar: SD. Scale bars, 10 μm.

cells (~10-20%). Such enrichment signals would have been averaged out in bulk measurement, losing valuable cell-to-cell and subcellular heterogeneity information. This underscores the importance of subcellular imaging in studying glycogen.

After validating high imaging sensitivity and specificity together with metabolic phenotyping using this SRS strategy of d_7-glucose labeling, we compared our results to those from fluorescence imaging of glycogen using 2-NBDG in live cells. 2-NBDG has been reported to be capable of being incorporated into glycogen through glycogenesis[17,18]. We co-incubated HeLa cells with 100 μM of 2-NBDG and 25 mM d_7-glucose and performed correlative fluorescence and SRS imaging. Surprisingly, almost no fluorescence signal from 2-NBDG colocalized with signals from the CD_G channel **(Fig. 4A, Fluorescence (blue) vs CD_G (red), white arrowed).** Instead, the fluorescence image correlated well with the unmixed lipid image **(Fig. 4A, Fluorescence (blue) vs CD_L**

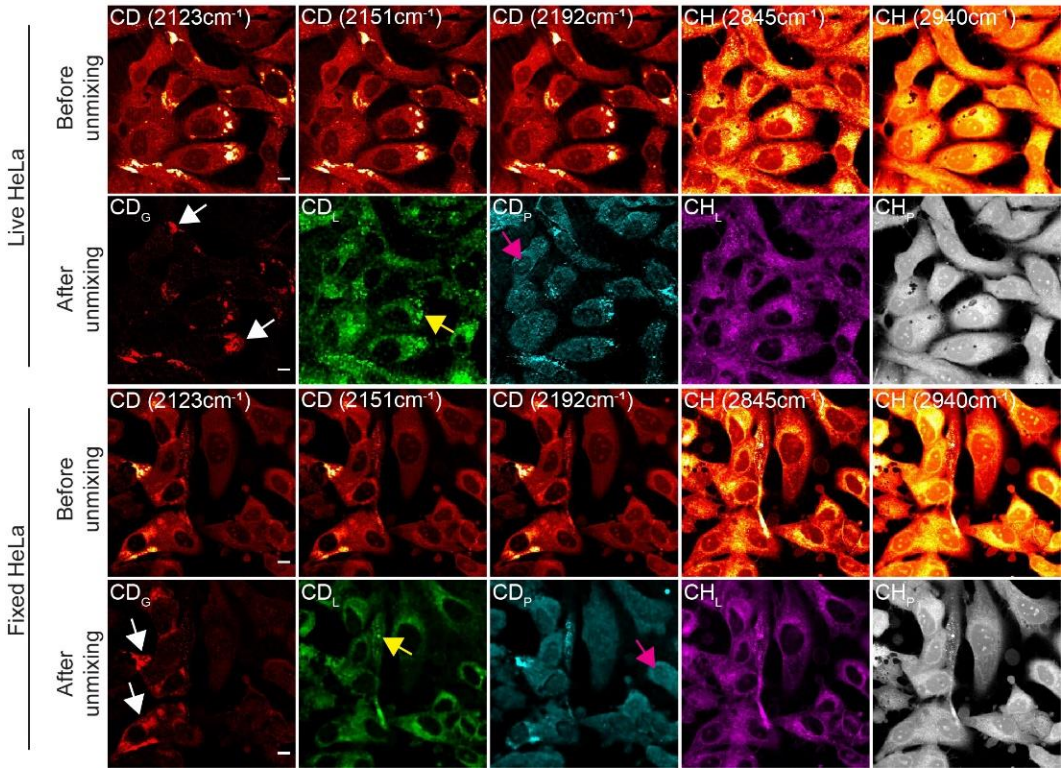

Fig. 3. 5-Channel SRS imaging of newly synthesized glycogen, lipids, proteins with pre-existing lipids, and proteins in live (top) and fixed (bottom) HeLa cells. For both image sets of fixed and live HeLa cells after culturing in d_7-glucose medium: top row (Before unmixing) shows SRS images acquired at C-D channels of 2123, 2151, 2192 cm^{-1} and C-H channels of 2845, 2940 cm^{-1} from the same set of cells; bottom row (After unmixing) shows concentration maps for d_7-glucose-derived glycogen (CD_G, red), lipids (CD_L, green), and proteins (CD_H, blue) unmixed from C-D channel SRS images and concentration maps for pre-existing lipids (CH_L, purple) and proteins (CH_P, gray) unmixed from C-H channel SRS images. White, yellow, and magenta arrows indicate glycogen, lipid droplets, and nucleoli, respectively. Scale bars, 10 μm.

(green), yellow arrowed). Three-channel correlative imaging with SRS imaging of C-D bonds, brightfield imaging of PAS staining and fluorescence imaging from 2-NBDG on the same set of cells was further performed **(Fig. S9)**, as well as two-channel correlative PAS and 2-NBDG on starved cells following a previous reported incubation condition **(Fig. S10)**[17]. Both experiments indicated the raised specificity issue from 2-NBDG. This decreased specificity of 2-NBDG labeling for glycogen may likely due to the increased hydrophobicity of 2-NBDG compared to regular D-glucose from the substitution of the 2-hydroxyl group with large 7-nitobenzofurazan[20,21].

Investigating the Metabolic Dynamics of Glycogen

Leveraging the fine specificity and biocompatibility of SRS and d_7-glucose labeling, we then monitored the glycogenesis and glycogenolysis in live cells with a pulse-chase experiment to characterize their turnover dynamics **(Fig. 4B)**. We first pulse-incubated HeLa cells with d_7-glucose medium for 24, 48, and 72 hours to probe the glycogenesis **(Fig. 4B)**. After 24 hours, glycogen with high C-D enrichment started to emerge in the cytoplasm **(Fig. 4B arrowed, 24 h)**. Longer incubation led to an increase in both C-D signals and

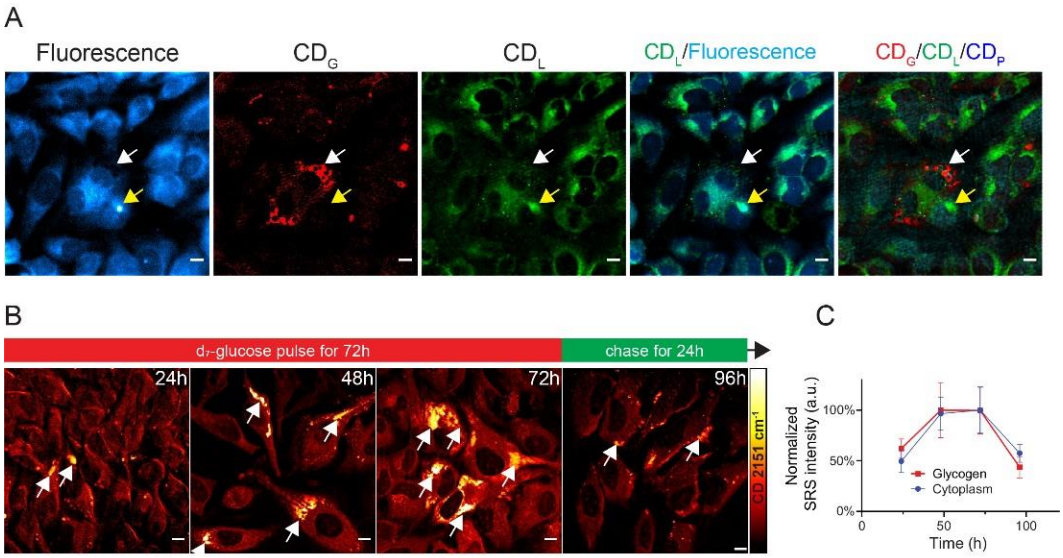

Fig. 4. Correlative and dynamic imaging of glycogen. (A) Colocalization of the fluorescence (cyan) image of 2-NBDG and unmixed SRS images of glycogen (CD_G, red), lipids (CD_L, green), and proteins (CD_P, blue) in HeLa cells co-incubated with 25 mM d_7-glucose and 100 μM of 2-NBDG. White arrows indicate location of glycogen. Yellow arrows indicate enriched lipid region. (B) Pulse-chase imaging of glycogen synthesis and degradation dynamics in live HeLa cells incubated in d_7-glucose medium in the pulse period and replaced with regular glucose medium in the chase period. Arrows indicate the glycogen pools. (C) Normalized SRS CD signals from subcellular enriched glycogen and cytoplasm in (B) (N=20 cells for each time point). Data shown as mean ± SD. Scale bars, 10 μm.

intracellular numbers of glycogen **(Fig. 4B arrowed, 48 h and 72 h)**. The C-D intensity gradually reached a plateau at 72 h **(Fig. 4C, red)**. We then chased the cells by replacing d_7-glucose medium back to regular medium after 72 h of pulse incubation to interrogate the glycogenolysis **(Fig. 4B)**. C-D signals from glycogen were lowered to about 50% after 24 h of chase **(Fig. 4B, 96 h, arrowed & Fig. 4C, red)**. Quantification on signal increase and decrease for both C-D enriched bright spots of glycogen and cytosolic C-D labeled lipids and proteins **(Fig. 4B)** revealed similar turnover dynamics **(Fig. 4C)**. These results suggest a dynamic role of glycogen going beyond static storage sites in cancer cells even under nutrient abundant conditions, which is possibly related to glycogen shunt pathway to maintain metabolic and ATP homeostasis[28].

Metabolic Phenotyping of Glycogen, Lipids, and Proteins in Metastatic Melanoma

We aimed to demonstrate the utility of this technique and the importance of glycogen in a more clinically relevant model. To this end, we investigated a series of patient-derived BRAF mutant melanoma cell-lines that have been extensively characterized at both the genomic and transcriptome levels[29–31]. Melanoma is the most deadly form of skin cancer due to its high metastatic potential[32]. Recently, it has been found that these derived cell-lines exhibit different transcriptional programs and phenotypic behaviors that are associated with degrees of cellular de-differentiation[29–31]. The different melanoma cancer cell phenotypes would likely have varied metabolic programs to meet phenotype-specific energy and growth demands. Thus, we hypothesized that the different cell-lines would

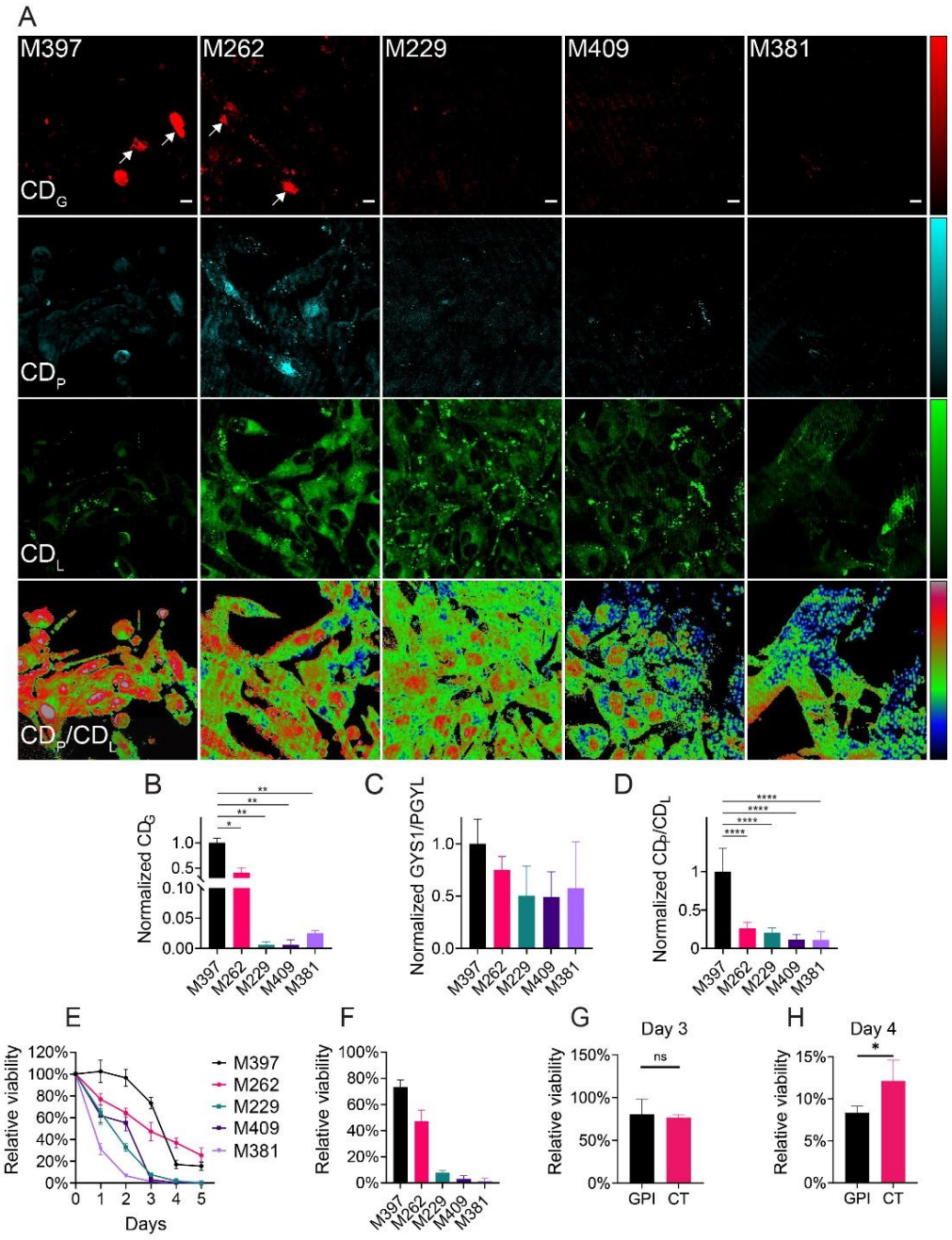

Fig. 5. Metabolic phenotyping of metastatic melanoma. (A) Representative unmixed SRS image sets for glycogen (CD_G, red), lipid (CD_L, green), and protein (CD_P, blue) with ratiometric CD_P/CD_L images across selected melanoma cell-lines (M397 to M381). Each column indicates the representative image set on the same set of cells for one cell-line. Scale bar, 10 μm. (B) Normalized CD_G intensity across melanoma cell-lines. (C) Ratios of gene expression levels between glycogen synthase (GYS1) to glycogen phosphorylase (PGYL). (D) Normalized CD_P/CD_L ratios across cell-lines. (E) Relative viability of melanoma cells cultured in glucose-deficient medium for up to 5 days. (F) Quantification of relative viability across melanoma cell-lines with 3-day glucose deficiency in (E). (G-H) Relative cell viability for M397 cells cultured in glucose-deficient medium (CT) and M397 cells cultured in glucose-deficient medium with 1 μM glycogen phosphorylase inhibitor (GPI) after 3 days (G) and 4 days (H). Statistical significance was determined by unpaired two-tailed t test. ns, not significant ($p>0.05$), *$p < 0.05$, **$p < 0.01$, ****$p < 0.0001$. Data shown as mean ± SD. Scale bars, 10 μm.

exhibit unique accumulation rates and spatial patterns of d_7-glucose derived glycogen, lipids, and proteins.

We selected five melanoma cancer cell-lines representing different de-differentiation status—melanocytic/differentiated (M262), transitory (M397, M229), neural-crest (M409), and undifferentiated (M381)—and cultured them in d_7-glucose medium. We acquired SRS images at the three designated channels **(Fig. S11)** and adopted the linear combination algorithm to construct the concentration maps of C-D labeled lipids, proteins, and glycogen in the corresponding cell-lines **(Fig. 5A)**. To obtain good unmixing results without potential motion artifacts, we started from fixed cells. Interestingly, we found that M397 and M262 cells showed relatively high accumulation of glycogen, whereas the three other cell-lines exhibited almost no evidence of glycogen formation **(Fig. 5A, CD_G, arrowed)**. Quantitatively, the normalized C-D intensity from the glycogen (CD_G) channel of M397 cells is about twice of that in M262 cells, and orders of magnitudes higher compared to the other three cell-lines **(Fig. 5B)**. This suggests that M397 cells have a higher dependence on glycogen-accumulation-associated metabolism. We asked whether this revealed metabolic phenotype is consistent with transcriptomics data. We computed the ratios of expression levels from RNA-sequencing between glycogen synthase (GYS1) to glycogen phosphorylase (PGYL), rate-limiting enzymes for glycogenesis and glycogenolysis, respectively **(Fig. 5C)**. The overall trend of ratios is indeed consistent with our measured CD_G intensities across cell-lines **(Fig. 5B vs 5C)**. The lower magnitude difference in the transcriptomics data likely arises because only a subset of cells presents significantly enhanced glycogen accumulation, and so the effect is smoothed out in bulk measurements. This again highlights the importance of subcellular imaging in uncovering cell-to-cell and subcellular heterogeneities. In addition to single-channel imaging, ratiometric images between different metabolic channels also serve as phenotype indicators. We found that CD_P/CD_L ratios follow a similar trend to that of CD_G signals across cell-lines **(Fig. 5D)**.

Since M397 cells show the most active glycogen accumulation, we examined the spatial pattern of glycogen distribution in M397 cells. We found extensive formation of large (larger than 1 μm) glycogen-enriched extracellular vesicles (EVs) that were only observable in PFA-fixed M397 cells, but not in live cells **(Fig. S12 & S13)**. We performed time-lapse imaging on the same set of M397 cells immediately after PFA addition **(Fig. S14A & S14B)**. We found that the intensity increase of the EVs is accompanied by the intensity decrease of intracellular glycogen, suggesting transportation of intracellular glycogen (up to 80%) to secreted EVs under PFA fixation **(Fig. S14B & S14C)**. This result again highlights the importance of live-cell imaging for glycogen metabolism to rule out potential complications due to PFA fixation.

Observation of Increased Tolerance on Glucose Deficiency for M397 Cells

Since M397 cells present a much-pronounced subcellular glycogen accumulation, we next sought to understand the functional role of glycogen in this cancer cell phenotype. Elevated level of glycogen storage suggests a possible higher tolerance of glucose deficiency. Indeed, many studies report that increased accumulation of glycogen in cancer cells support cancer cell survival in nutrient and oxygen deficient conditions[7,33,34]. To test this potential role of glycogen storage, we cultured the five cell-lines in glucose-deficient medium and

performed time-dependent cell viability assays. Surprisingly, M397 cells showed minimally decreased proliferation even after culturing in glucose-deficient medium for three days **(Fig. 5E & 5F)**. In contrast, the other cell-lines all showed significantly reduced growth **(Fig. 5E & 5F)**. To test whether glycogen is involved in the extended survival, we applied glycogen phosphorylase inhibitor (GPI), which inhibits glycogenolysis to UDP-glucose, to the culture medium during glucose deficiency treatment. We first showed that GPI is non-toxic to cells in normal glucose medium for at least 5 days **(Fig. S15)**. In glucose-deficient condition, the added GPI lowered the viability of M397 after day 3, at which point the glycogenolysis activities may be the most intensive **(Fig. 5G & 5H)**. Our demonstration here hence emphasizes the critical role of glycogen metabolism in specific cancer cell types and may help advance our fundamental biological understanding in elucidating glycogen-related metabolism pathways with further explorations.

2.5 Discussion

The reprogramming of glycogen metabolism in cancer cells is not well understood, and existing probes of glycogen metabolism have a number of limitations[6,13]. We proposed SRS imaging with d_7-glucose labeling as a sub-cellular, minimally perturbative probe for glycogen metabolism in live cancer cells. First, we demonstrated incorporation of d_7-glucose into *de novo* synthesized glycogen, validating the use of d_7-glucose as a probe to label glycogen in cancer cells. Second, highly specific and sensitive imaging of glycogen was shown in live cancer cells using a linear-unmixing algorithm. Third, we surveyed the subcellular glycogen, lipid, and protein metabolism in a series of metastatic melanoma cells and revealed a high glycogen-accumulation phenotype (i.e. M397 cells). This cell-line further showed a high resistance to glucose deficiency. As several recent studies have suggested the critical roles of glycogen metabolism in cancer systems[7–9], this method can help shed light on glycogen function, which is a necessary step towards targeting glycogen metabolism for therapeutic purposes.

Although the above proof-of-concept study already demonstrates the potential of our strategy, further technical improvements may lead to better imaging performance. The speed of SRS imaging can be improved by using techniques such as spectral focusing[35], which can enable much improved speed for hyperspectral imaging. Spectral analysis for hyperspectral images, such as multivariate curve resolution[36], may further reduce mapping errors and allow more sensitive detection of metabolites, such as d_7-glucose derived DNA/RNA. Going beyond cellular studies, this method may also be applicable for *in vivo* research due to the biocompatibility of SRS imaging and d_7-glucose labeling. We envision this technique as a valuable tool in investigating glycogen metabolism and for metabolic phenotyping in both cancer cells and *in vivo*.

2.6 Acknowledgements

We thank Dr. Antoni Ribas for sharing the melanoma cell-lines. We also thank Dr. Otto Baba and Dr. Morita for sharing the anti-glycogen antibodies. We also would like to thank Dr. C. Qian, K. Miao, X. Bi, L. Lin, and Dr. L. Voong for helpful discussions. We acknowledge the following agencies and foundations for support: NIH Grant U01 CA217655 (to J.R.H.) and the WA State Andy Hill CARE Foundation, and an ISB

Innovator Award (Y.S.). L.W acknowledges the support for start-up funds from California Institute of Technology.

2.7 References

1. DeBerardinis, R. J., Lum, J. J., Hatzivassiliou, G. & Thompson, C. B. The Biology of Cancer: Metabolic Reprogramming Fuels Cell Growth and Proliferation. *Cell Metabolism* **7**, 11–20 (2008).
2. Lunt, S. Y. & Vander Heiden, M. G. Aerobic Glycolysis: Meeting the Metabolic Requirements of Cell Proliferation. *Annual Review of Cell and Developmental Biology* **27**, 441–464 (2011).
3. Yan, L., Raj, P., Yao, W. & Ying, H. Glucose Metabolism in Pancreatic Cancer. *Cancers (Basel)* **11**, (2019).
4. Heiden, M. G. V., Cantley, L. C. & Thompson, C. B. Understanding the Warburg Effect: The Metabolic Requirements of Cell Proliferation. *Science* **324**, 1029–1033 (2009).
5. Dauer, P. & Lengyel, E. New Roles for Glycogen in Tumor Progression. *Trends in Cancer* **5**, 396–399 (2019).
6. Zois, C. E. & Harris, A. L. Glycogen metabolism has a key role in the cancer microenvironment and provides new targets for cancer therapy. *J Mol Med* **94**, 137–154 (2016).
7. Favaro, E. *et al.* Glucose Utilization via Glycogen Phosphorylase Sustains Proliferation and Prevents Premature Senescence in Cancer Cells. *Cell Metabolism* **16**, 751–764 (2012).
8. Curtis, M. *et al.* Fibroblasts Mobilize Tumor Cell Glycogen to Promote Proliferation and Metastasis. *Cell Metabolism* **29**, 141-155.e9 (2019).
9. Sun, R. C. *et al.* Nuclear Glycogenolysis Modulates Histone Acetylation in Human Non-Small Cell Lung Cancers. *Cell Metabolism* **30**, 903-916.e7 (2019).
10. Prats, C., Graham, T. E. & Shearer, J. The dynamic life of the glycogen granule. *J. Biol. Chem.* **293**, 7089–7098 (2018).
11. Bak, L. K., Walls, A. B., Schousboe, A. & Waagepetersen, H. S. Astrocytic glycogen metabolism in the healthy and diseased brain. *J. Biol. Chem.* **293**, 7108–7116 (2018).
12. Shulman, R. G., Hyder, F. & Rothman, D. L. Cerebral energetics and the glycogen shunt: Neurochemical basis of functional imaging. *Proceedings of the National Academy of Sciences* **98**, 6417–6422 (2001).
13. Passonneau, J. V. & Lauderdale, V. R. A comparison of three methods of glycogen measurement in tissues. *Analytical Biochemistry* **60**, 405–412 (1974).
14. Zhou, Y. *et al.* Magnetic resonance imaging of glycogen using its magnetic coupling with water. *Proc Natl Acad Sci USA* **117**, 3144–3149 (2020).
15. Witney, T. H. *et al.* A Novel Radiotracer to Image Glycogen Metabolism in Tumors by Positron Emission Tomography. *Cancer Res* **74**, 1319–1328 (2014).
16. Hackett, M. J. *et al.* Concurrent Glycogen and Lactate Imaging with FTIR Spectroscopy To Spatially Localize Metabolic Parameters of the Glial Response Following Brain Ischemia. *Anal. Chem.* **88**, 10949–10956 (2016).
17. Louzao, M. C. *et al.* "Fluorescent glycogen" formation with sensibility for in vivo and in vitro detection. *Glycoconj J* **25**, 503 (2007).

18. Zhu, Y. *et al.* Single-Cell Analysis for Glycogen Localization and Metabolism in Cultured Astrocytes. *Cell Mol Neurobiol* (2019) doi:10.1007/s10571-019-00775-4.
19. Hu, F. *et al.* Vibrational Imaging of Glucose Uptake Activity in Live Cells and Tissues by Stimulated Raman Scattering. *Angewandte Chemie International Edition* **54**, 9821–9825 (2015).
20. Hughes, L. D., Rawle, R. J. & Boxer, S. G. Choose Your Label Wisely: Water-Soluble Fluorophores Often Interact with Lipid Bilayers. *PLOS ONE* **9**, e87649 (2014).
21. Zanetti-Domingues, L. C., Tynan, C. J., Rolfe, D. J., Clarke, D. T. & Martin-Fernandez, M. Hydrophobic Fluorescent Probes Introduce Artifacts into Single Molecule Tracking Experiments Due to Non-Specific Binding. *PLOS ONE* **8**, e74200 (2013).
22. Yamada, K., Saito, M., Matsuoka, H. & Inagaki, N. A real-time method of imaging glucose uptake in single, living mammalian cells. *Nature Protocols* **2**, 753–762 (2007).
23. Zhang, L. *et al.* Spectral tracing of deuterium for imaging glucose metabolism. *Nat Biomed Eng* **3**, 402–413 (2019).
24. Miao, K. & Wei, L. Live-Cell Imaging and Quantification of PolyQ Aggregates by Stimulated Raman Scattering of Selective Deuterium Labeling. *ACS Cent. Sci.* acscentsci.9b01196 (2020) doi:10.1021/acscentsci.9b01196.
25. Fundamentals of Biochemistry: Life at the Molecular Level, 5th Edition | Wiley. *Wiley.com* https://www.wiley.com/en-us/Fundamentals+of+Biochemistry%3A+Life+at+the+Molecular+Level%2C+5th+Edition-p-9781118918401.
26. Long, R. *et al.* Two-color vibrational imaging of glucose metabolism using stimulated Raman scattering. *Chem. Commun.* **54**, 152–155 (2018).
27. Li, J. & Cheng, J.-X. Direct Visualization of De novo Lipogenesis in Single Living Cells. *Sci Rep* **4**, 6807 (2015).
28. Shulman, R. G. & Rothman, D. L. Homeostasis and the glycogen shunt explains aerobic ethanol production in yeast. *PNAS* **112**, 10902–10907 (2015).
29. Su, Y. *et al.* Single-cell analysis resolves the cell state transition and signaling dynamics associated with melanoma drug-induced resistance. *Proc Natl Acad Sci USA* **114**, 13679–13684 (2017).
30. Berger, M. F. *et al.* Integrative analysis of the melanoma transcriptome. *Genome Res.* **20**, 413–427 (2010).
31. Tsoi, J. *et al.* Multi-stage Differentiation Defines Melanoma Subtypes with Differential Vulnerability to Drug-Induced Iron-Dependent Oxidative Stress. *Cancer Cell* **33**, 890-904.e5 (2018).
32. Davies, H. *et al.* Mutations of the BRAF gene in human cancer. *Nature* **417**, 949–954 (2002).
33. Chen, J. *et al.* Gain of Glucose-Independent Growth upon Metastasis of Breast Cancer Cells to the Brain. *Cancer Res* **75**, 554–565 (2015).
34. Liu, J. *et al.* Succinate Dehydrogenase 5 (SDH5) Regulates Glycogen Synthase Kinase 3β-β-Catenin-mediated Lung Cancer Metastasis. *J. Biol. Chem.* **288**, 29965–29973 (2013).
35. Andresen, E. R., Berto, P. & Rigneault, H. Stimulated Raman scattering microscopy by spectral focusing and fiber-generated soliton as Stokes pulse. *Opt. Lett., OL* **36**, 2387–2389 (2011).

36. Zhang, D. *et al.* Quantitative Vibrational Imaging by Hyperspectral Stimulated Raman Scattering Microscopy and Multivariate Curve Resolution Analysis. *Anal. Chem.* **85**, 98–106 (2013).

2.8 Supplementary information

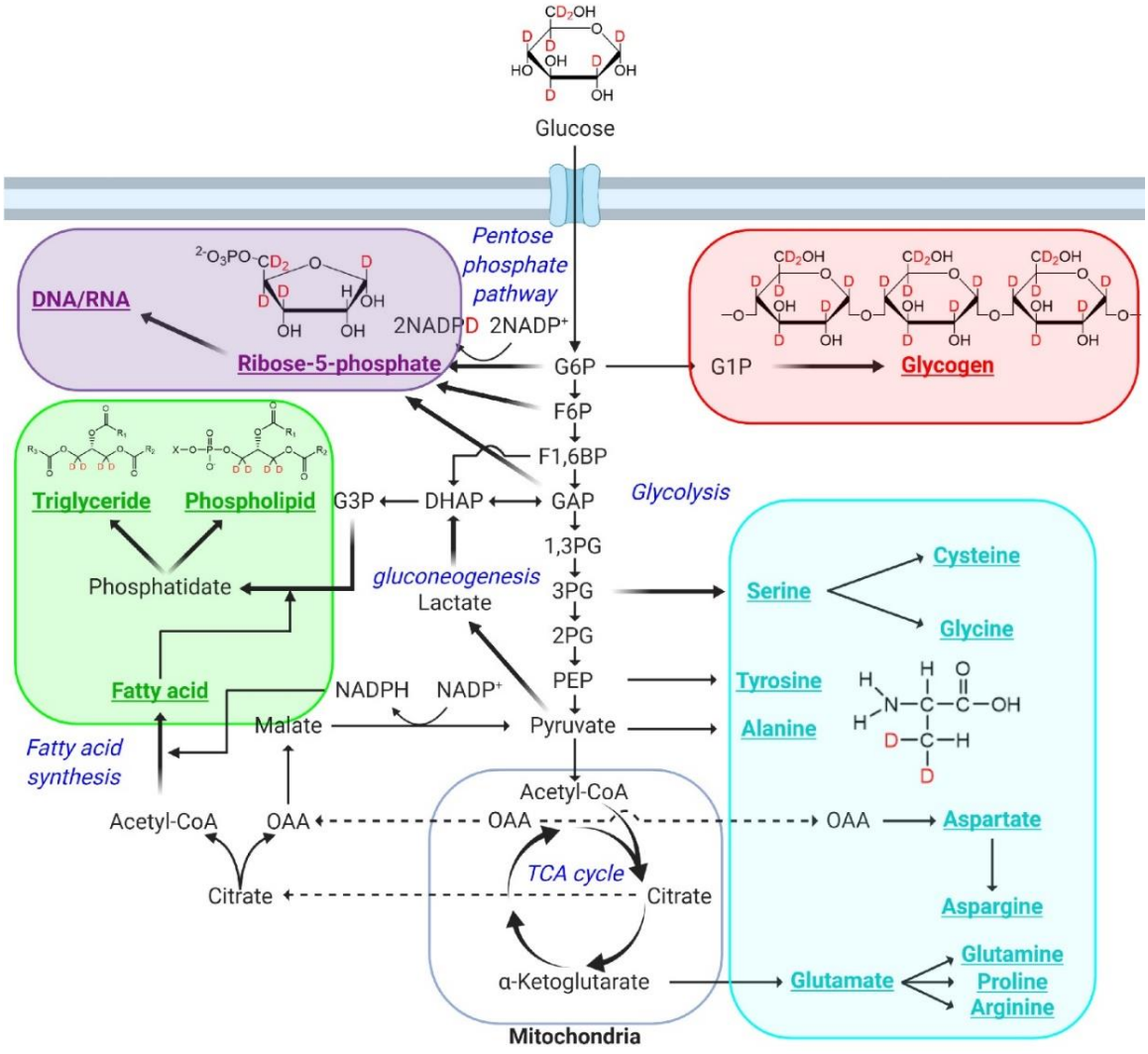

Fig. S1. Sparse C-D labeling of macromolecules (glycogen, DNA/RNA, lipid, and protein) through metabolic pathways branched from glycolysis of d_7-glucose. Glycogen, DNA/RNA, lipid and protein are highlighted in red, purple, green, and cyan, respectively. OAA: oxaloacetate.

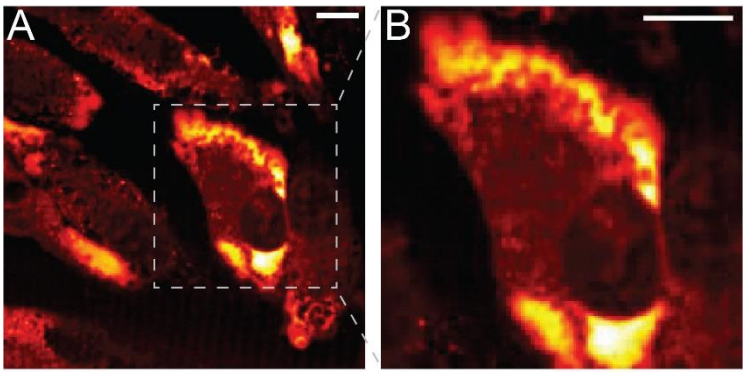

Fig. S2. Higher-magnification image of intracellular glycogen pools. (A) SRS images at 2151 cm^{-1} for HeLa cells after incubating in d_7-glucose media for 3 days. (B) A zoomed-in image of the boxed-region in (A). Scale bars, 10 μm.

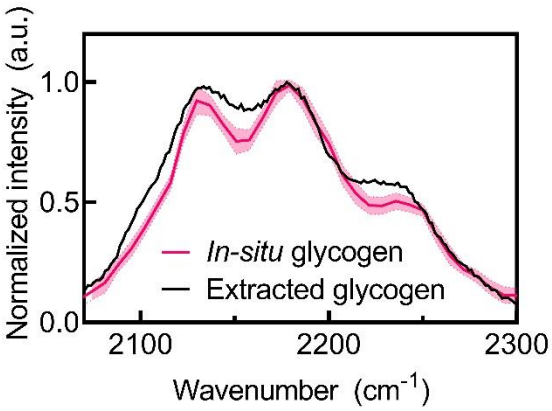

Fig. S3. Comparison between *in-situ* SRS spectra and extracted spontaneous spectra of deuterated glycogen.

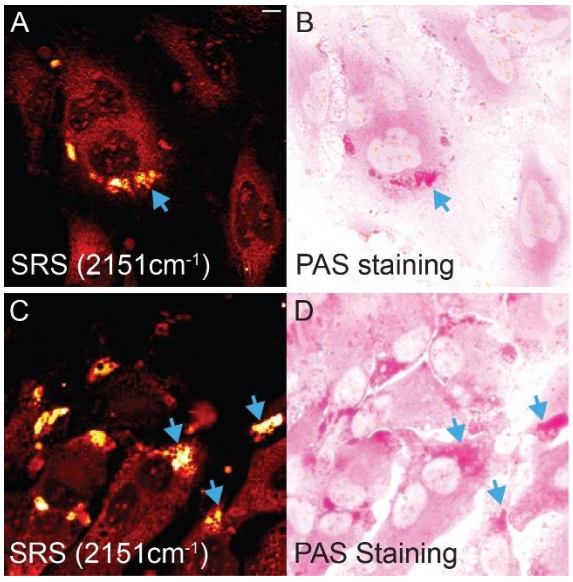

Fig. S4. Two sets of correlative imaging of glycogen. (A) & (C) SRS image of glycogen in HeLa cells incubated with d_7-glucose for three days. (B) & (D) Brightfield image of the same set of cells in (A) and (B), respectively, after PAS staining.

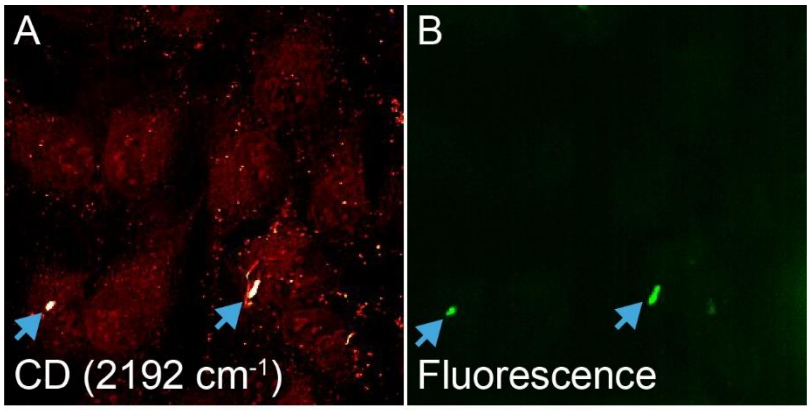

Fig. S5. Correlative imaging of glycogen. (A) SRS image of glycogen in HeLa cells incubated with d_7-glucose for three days and immuno-labeled with anti-glycogen primary antibody and Alexa Fluor 594-conjugated secondary antibodies. (B) Fluorescence image of the same set of cells in (A).

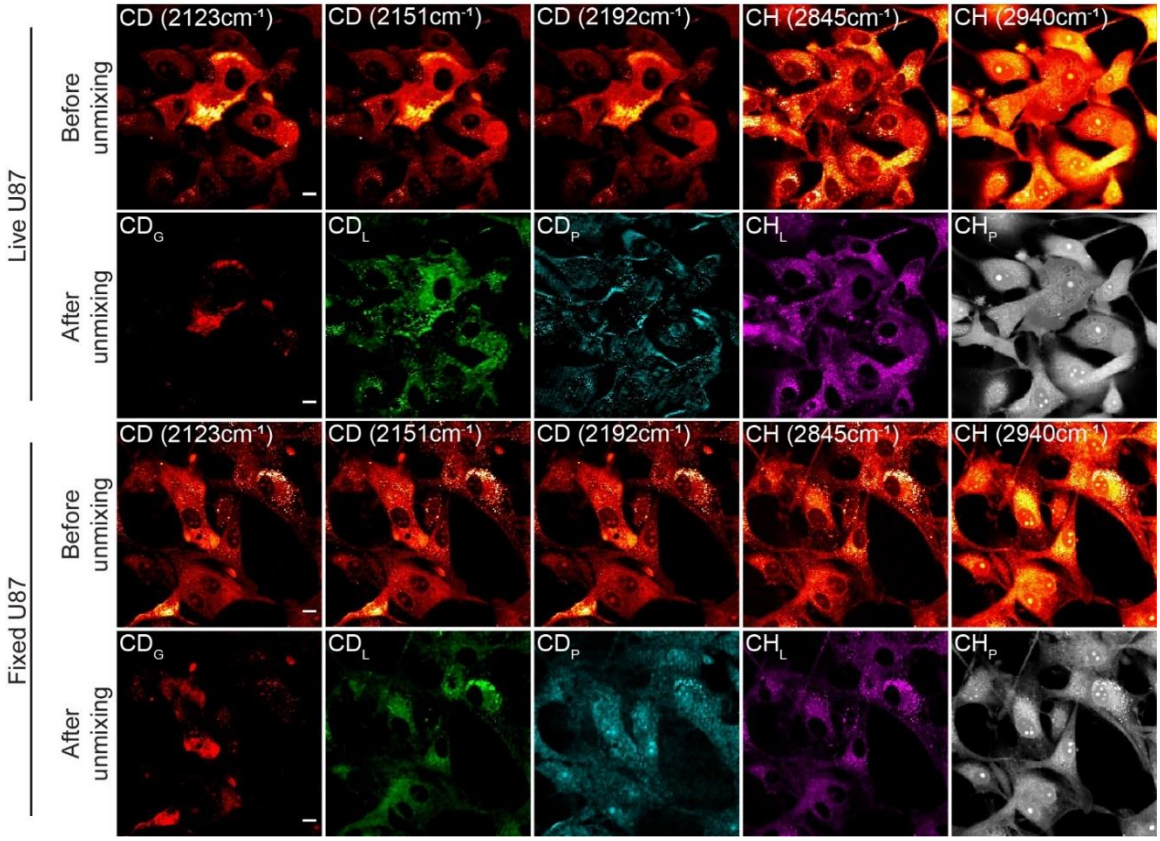

Fig. S6. Spectral unmixing of deuterated glycogen, lipid, and protein macromolecules in live and fixed U87 cells. Concentration maps for d_7-glucose-derived glycogen (CD_G, red), lipids (CD_L, green), and proteins (CD_H, blue) (after unmixing) are spectrally separated from SRS images acquired at channels of 2123, 2151, 2192 cm^{-1} (before unmixing). Pre-existing lipid (CH_L, purple) and protein (CH_P, gray) signals (after unmixing) are unmixed from images collected at 2845, 2940 cm^{-1} (before unmixing). Scale bars, 10 μm.

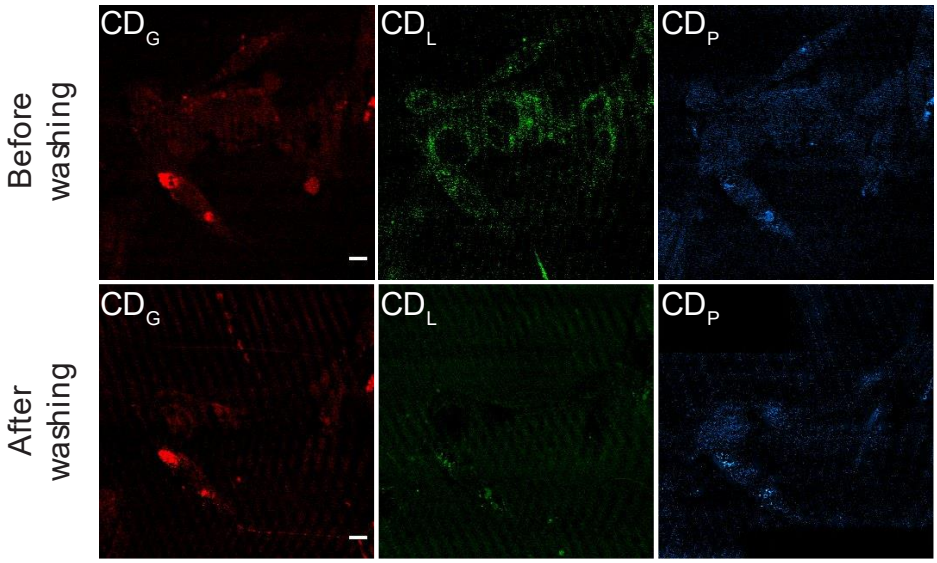

Fig. S7. Unmixed SRS images before and after lipid washing using triton. SRS images collected at 2123, 2151, 2192 cm^{-1} and unmixed into glycogen (CD_G, red), lipid (CD_L, green), and protein (CD_H, blue) signals.

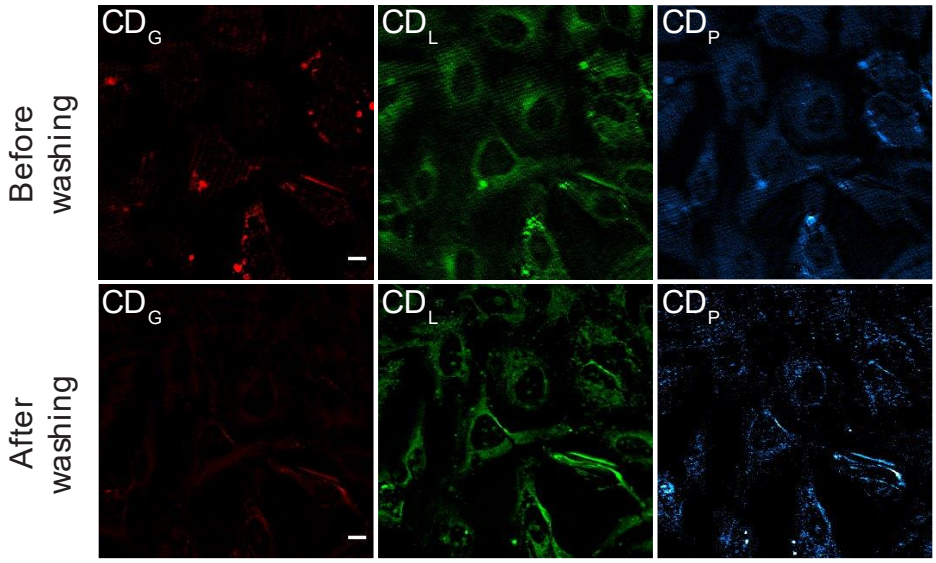

Fig. S8. Unmixed SRS images before and after glycogen washing using perchloric acid. SRS images collected at 2123, 2151, 2192 cm^{-1} and unmixed into glycogen (CD_G, red), lipid (CD_L, green), and protein (CD_H, blue) signals.

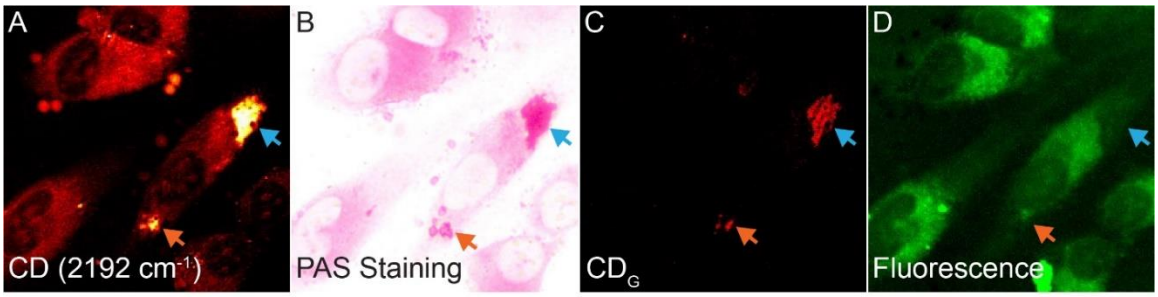

Fig. S9. Correlative imaging of glycogen in fixed HeLa cells co-incubated with d_7-glucose and 2-NBDG. (A) SRS image. (B) Brightfield image on the same set of cells after applying PAS staining. (C) Glycogen SRS channel after spectral unmixing. (D) Fluorescence image of 2-NBDG. Blue arrows indicate regions of high correlation between only SRS image and PAS staining and not fluorescence image. Orange arrow indicate regions of some correlation between all three SRS, PAS, and fluorescence image.

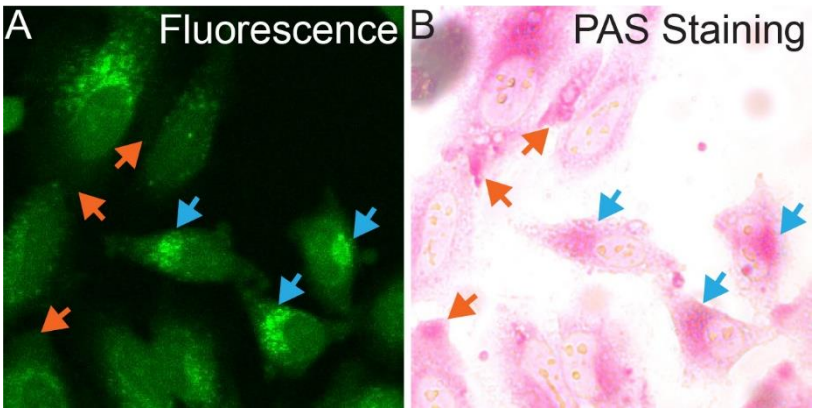

Fig. S10. Non-specific staining of 2-NBDG. (A) Fluorescence image of 2-NBDG. (B) Brightfield image on the same set of cells in (A) after applying PAS staining. Blue arrows indicate regions with correlation. Orange arrows indicate regions with no-correlation. The non-correlation between fluorescence and the PAS image was not due to the z shift, as all the z was checked.

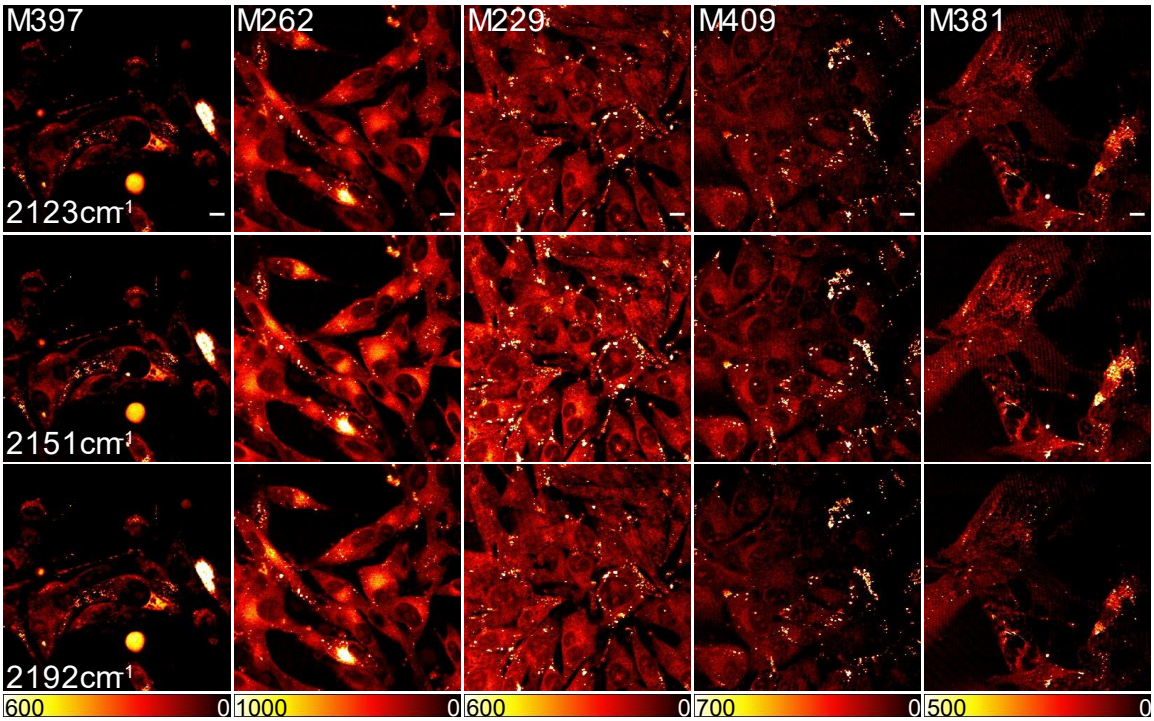

Fig. S11. Representative SRS images of melanoma cell-lines before spectral unmixing. Each column indicates the representative image set on the same set of cells for one cell-line. Scale bar, 10 μm.

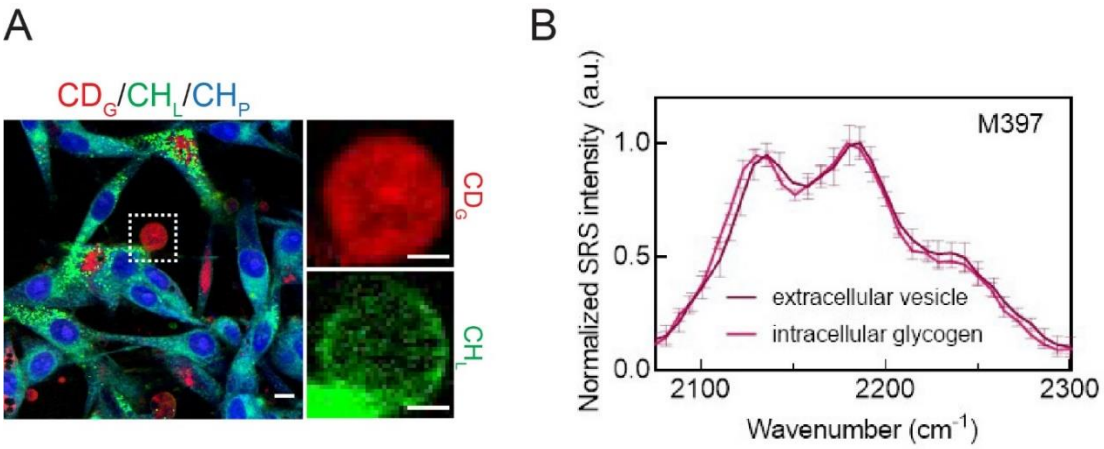

Fig. S12. PFA fixation induces glycogen-enriched extracellular vesicles. (A) Overlay of CH_L, CH_P, and CD_G images for PFA-fixed M397 cells. Scale bar, 10 μm. Zoomed-in images of the dash-boxed region indicate a representative extracellular vesicle enriched with glycogen (CD_G, red) and wrapped by the lipid membranes (CH_L, green). Scale bars, 5 μm. **(B)** Normalized SRS spectra from intracellular glycogen (shaded pink) and extracellular vesicles (shaded purple) in PFA-fixed M397 cells.

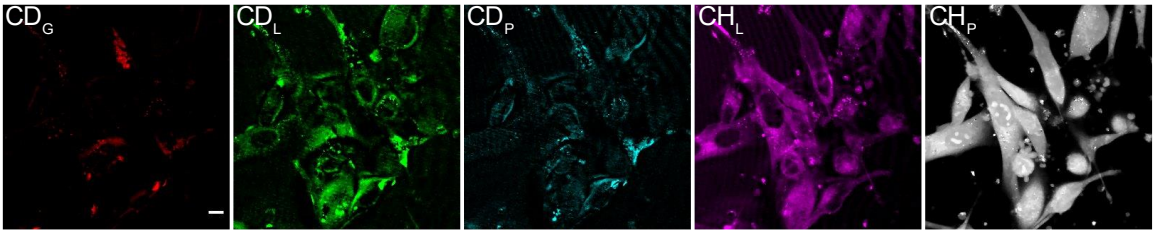

Fig. S13. No glycogen-enriched extracellular vesicles were observed in live M397 cells. Concentration maps for d_7-glucose-derived glycogen (CD_G, red), lipid (CD_L, green), and protein (CD_H, blue) after unmixing. Pre-existing lipid (CH_L, purple) and protein (CH_P, gray) signals (after unmixing) are unmixed from images collected at 2845, 2940 cm^{-1}. Scale bars, 10 μm.

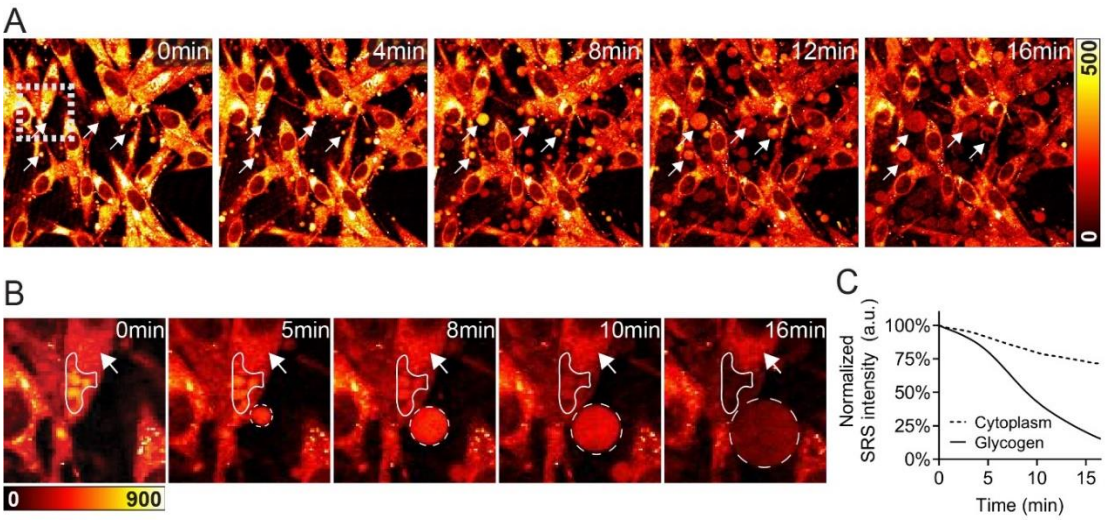

Fig. S14. Observation of glycogen-enriched extracellular vesicles formation and intracellular glycogen loss caused by PFA fixation. (A) Time-lapse SRS images from 0 to 16 minutes immediately after adding PFA to M397 cells. Formation of glycogen-enriched vesicles is indicated by arrows. (B) Zoomed-in images of the boxed-region in (A). Intracellular glycogen is outlined by solid lines. Extracellular vesicles are indicated by dashed circles. Arrows indicate cytoplasm with no glycogen. (C) Quantification of SRS intensities from intracellular glycogen (solid lined) and extracellular vesicles (dashed circled) highlighted in (B). With the secretion of vesicles, the signal levels of intracellularly accumulated glycogen decreased sharply to about only 20% of the original signals, whereas the cytoplasmic signals where glycogen was not present only decreased slightly to about 75%.

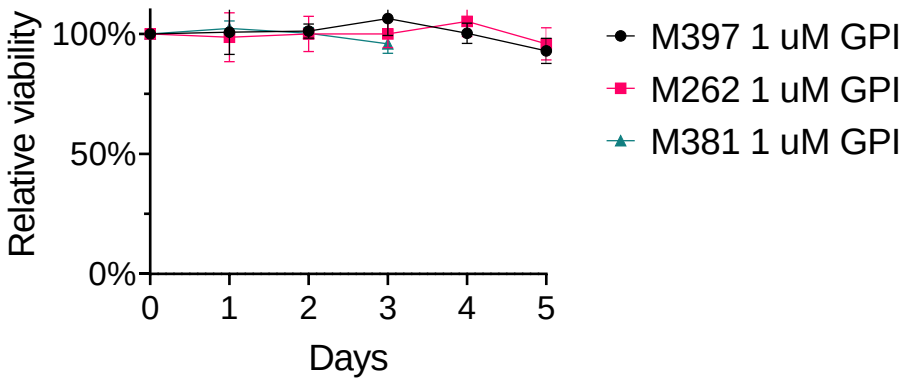

Fig. S15. Non-toxicity from GPI are found in normal glucose containing medium.

Chapter 3

TOWARD PHOTOSWITCHABLE ELECTRONIC PRERESONANCE STIMULATED RAMAN PROBES

Sections of this chapter have been adapted from:
Lee, D.; Qian, C.; Wang, H.; Li, L.; Miao, K.; Du, J.; Shcherbakova, D. M.; Verkhusha, V. V.; Wang, L. V.; Wei, L. Toward Photoswitchable Electronic Pre-Resonance Stimulated Raman Probes. J. Chem. Phys. 2021, 154 (13), 135102. https://doi.org/10.1063/5.0043791

3.1 Abstract

Reversibly photoswitchable probes allow for a wide variety of optical imaging applications. In particular, photoswitchable fluorescent probes have significantly facilitated the development of super-resolution microscopy. Recently, stimulated Raman scattering (SRS) imaging, a sensitive and chemical-specific optical microscopy, has proven to be a powerful live-cell imaging strategy. Driven by the advances of newly developed Raman probes, in particular the pre-resonance enhanced narrow-band vibrational probes, electronic pre-resonance SRS (epr-SRS) has achieved super-multiplex imaging with sensitivity down to 250 nM and multiplexity up to 24 colors. However, despite the high demand, photoswitchable Raman probes have yet to be developed. Here, we propose a general strategy for devising photoswitchable epr-SRS probes. Toward this goal, we exploit the molecular electronic and vibrational coupling, in which we switch the electronic states of the molecules to four different states to turn their ground-state epr-SRS signals on and off. First, we showed that inducing transitions to both electronic excited state and triplet state can effectively diminish the SRS peaks. Second, we revealed that the epr-SRS signals can be effectively switched off in red-absorbing organic molecules through light-facilitated transitions to a reduced state. Third, we identified that photoswitchable proteins with near-infrared photoswitchable absorbance, whose states are modulable with their electronic resonances detunable toward and away from the pump photon energy, can function as the photoswitchable epr-SRS probes with desirable sensitivity (<1 μM) and low photofatigue (>40 cycles). These photophysical characterizations and proof-of-concept demonstrations should advance the development of the novel photoswitchable Raman probes and open up the unexplored Raman imaging capabilities.

3.2 Introduction

Photoswitchable probes are molecules whose signals can be turned on and off reversibly upon irradiation of light. The development of such optical-highlighter probes could greatly expand the range of questions that can be investigated, particularly in biology. For example, the emergence of photoswitchable fluorophores has allowed unique imaging of protein dynamics in cells, sensing of subcellular environment, and optical data writing and storage.[1–5] By precisely activating and deactivating fluorescence in space and time, these probes have

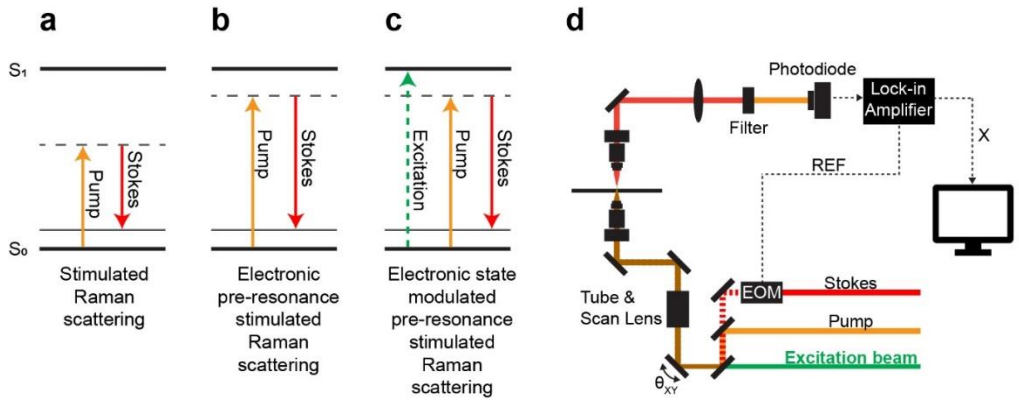

Fig. 1. Principle and design of photoswitchable electronic pre-resonance SRS (epr-SRS) via electronic state transition. (a-c) Energy diagrams of SRS (a), epr-SRS (b), and the proposed electronic-state modulated epr-SRS with an additional electronic excitation laser (green) (c). (d) Experimental scheme of the electronic-state modulated epr-SRS by introducing a third excitation beam (green) to a conventional SRS microscope. EOM, electro-optic modulator; REF, reference. X, in-phase X-output of the lock-in amplifier.

also largely facilitated the development of the ground-breaking super-resolution microscopy, pushing the spatial resolution of optical imaging to tens of nanometers.[6–8] Prominently, utilizing the non-fluorescent states (i.e. the OFF state) of photoswitchable fluorescent proteins, which have much longer lifetime (> ms) compared to the fluorescence lifetime (~ ns) of excited states, RESOLFT (reversible saturable optical fluorescence transitions) has addressed the high-power photo-damage issues in STED (stimulated emission depletion) microscopy and allows an eight-order-of-magnitude smaller illumination intensity than STED for super-resolution live-cell imaging.[9–13]

In addition to fluorescence microscopy, Raman imaging, which targets the vibrational transitions of chemical bonds, has shown its promises to be a powerful biomedical imaging modality that offers complementary information when interrogating biological systems. In particular, stimulated Raman scattering (SRS) microscopy, which harnesses the stimulated emission amplification principle, could accelerate the vibrational transitions by 10^8 times compared to spontaneous Raman **(Fig. 1a)**. Overcoming the low sensitivity issue in conventional spontaneous Raman imaging, SRS has achieved subcellular imaging with speed up to video rate.[14,15] It allows detection of endogenous biomolecules in a label-free fashion and also offers bioorthogonal chemical imaging of small metabolites and drugs in live cells, tissues, and animals with tiny Raman tags.[16–18] However, no photoswitchable Raman probes have been reported so far.

Recently, by bringing the pump photon energy close to, but still slightly detuned away from, the electronic absorption maximum of the red-absorbing dyes, electronic pre-resonance SRS (epr-SRS) has been invented, enhancing the sensitivity of Raman imaging down to 250 nM. Such a sensitivity level is close to that offered by typical confocal fluorescence microscopy.[19,20] Compared to conventional non-resonance SRS **(Fig. 1a)**, epr-SRS obtains an up to 10^5 -fold signal boost while keeping the electronic-resonance-related background to a minimum level **(Fig. 1b)**. With newly developed and synthesized probe

palette, epr-SRS has enabled optical super-multiplex imaging for up to simultaneous 24-color visualization of biological targets.[19] These probes, which incorporate narrow-band and isotope edited nitrile (~11 cm^{-1}) or alkyne (~14 cm^{-1}) moieties to their conjugation systems, share similar electronic absorption peaks, but show distinctly separated Raman bands in the desired cell-silent Raman spectral region (1700 – 2700 cm^{-1}).[19–21]

Herein, we explore and develop the photoswitchable epr-SRS probes. Since epr-SRS probes manifest strong coupling between electronic and vibrational transitions, we use light-induced transitions from one electronic state to another as a general strategy to switch epr-SRS signals on and off. Specifically, we adopt an additional excitation beam to induce electronic state transitions of the molecules **(Fig. 1c, green arrow)**. As the excitation beam depletes the ON state population to the OFF state, the SRS laser pair **(Fig. 1d, Stokes beam fixed at 1031.2 nm and pump beam tunable around 830 - 880 nm for epr-SRS imaging)** is utilized to probe the depleted ON state epr-SRS vibrational modes. In principle, the epr-SRS signals could possibly be switched off and on with and without the excitation from the additional laser, respectively **(Fig. 1c, d)**. One envisioned application with such photoswitchable molecules is super-multiplex (i.e. >10 plex) super-resolution imaging, which has remained as a highly challenging but long sought-after goal.[22] Since epr-SRS probes all share similar absorption peaks, only a single doughnut depletion laser would be required to switch off the periphery signals and leave the spectrally-separated epr-SRS signals in the center **(Fig. S1)**. As a comparison, if STED or RESOLFT were to achieve this goal of super-multiplex super-resolution, an additional pair of excitation and depletion beams are required for each extra color.[9–13] This is highly challenging due to two main reasons. First, the added laser lines and optics would largely increase the complexity for precise instrumentation alignment. Second, the existing color-barrier in fluorescence (i.e. the spectral overlap) would typically limit the number of possible colors to 3-5.[23–25]

Guided by the rationales above, we study the photophysics of different molecular electronic states to evaluate whether they can serve as an OFF state for the ground-state epr-SRS excitations. We first investigated the excited state and the triplet state to implement the ground-state depletion photoswitching strategy. We found that transitions to the first excited state and triplet state result in vanishing epr-SRS peaks, but also induce large electronic background. Guided by the Albrecht A-term pre-resonance approximation equation (Supplementary information Scheme 1), we then revealed that a thiol-promoted long-lived dark state of organic dyes and an absorption-detuned transition state of near-infrared (NIR) proteins could effectively eliminate the epr-SRS signals and serve as the OFF states for cyclic photoswitching. We envision this work to motivate further research in developing and optimizing the photoswitchable epr-SRS probes and to expand the capabilities of optical imaging.

3.3 Results

I. Photoswitching by ground-state-depletion epr-SRS

First, we explored the possibility of harnessing electronic excited states as the OFF state for epr-SRS signals **(Fig. 2a)**. It is known that bond properties (e.g. force constants, bond orders) change between the ground and the excited states.[26] Recent studies have also shown that Raman spectra of molecules in the excited state exhibit shifted peaks compared to those of ground state for certain vibrational modes in the molecules.[27,28] We hence reasoned that

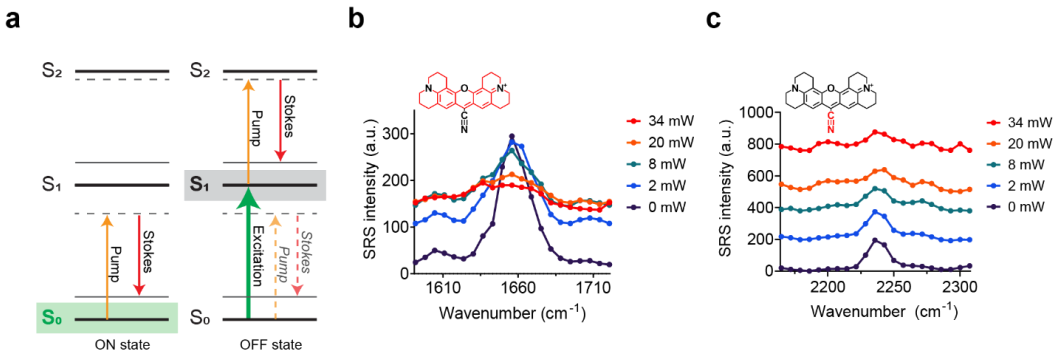

Fig. 2. Photoswitching of epr-SRS signals via transition to the electronic excited state. (a) Energy diagrams of the proposed ON (left, green shade indicates ground state as ON state) and OFF (right, gray shade indicates excited state as OFF state) states for epr-SRS signals. (b) epr-SRS spectra of the conjugated double bond mode (i.e., highlighted red in the molecular structure) of Rh800 at 0, 2, 8, 20, and 34 mW of 660 nm excitation beam irradiation. (c) epr-SRS spectra of the triple bond mode (red colored in the molecular structure) of Rh800 at 0, 2, 8, 20, and 34 mW of 660 nm excitation beam irradiation.

shifting the population to excited state could likely deplete the ground-state Raman signals. To test this for epr-SRS, we adopted Rhodamine 800 (Rh800), a near-infrared-absorbing dye peaked around 680 nm with high and well-characterized epr-SRS signals (the structure shown in Fig. 2b & 2c).[19–21] For electronic excitation, we integrated and aligned a 660 nm continuous wave (CW) laser into the SRS system for steady state excitation **(Fig. 1d)**. We planned to excite Rh800 by the 660 nm excitation beam and simultaneously probe the ground-state epr-SRS signals by the SRS beams **(Fig. 2a, OFF state, dashed laser lines for pump and Stokes)**. We would then compare the resulting epr-SRS spectra with and without 660 nm excitation for signal suppression analysis. To ensure over 80 % excitation of the population from the ground state to the excited state, we applied up to 34 mW of the 660 nm excitation beam (Table S1).

Since excited-state Raman peaks are possibly shifted from those of the ground state, we expected to observe a decrease of epr-SRS signals for electronic pre-resonance enhanced peaks from Rh800 upon 660 nm excitation. We indeed observed a gradual decrease of the epr-SRS peaks for both double bond **(Fig. 2b & Fig. S2a)** and triple bond **(Fig. 2c & Fig. S2b)** of Rh800 with increasing excitation beam powers. However, we simultaneously detected a large increase of the broad background **(Fig. 2b & Fig. 2c)**. The increase of background shows strong resemblance to the SRS spectra in the rigorous resonance regime.[19,20,29] We hence reasoned that the observed background increase should originate from the reduced energy gap between the first electronic excited state (S_1) and the second electronic excited state (S_2) compared to that between the ground state (S_0) and the first electronic excited state (S_1) **(Fig. 2a, OFF state)**. Epr-SRS excitations for the excited-state Rh800 would therefore invoke high rigorous-electronic-resonance-involved background **(Fig. 2a, OFF state, solid laser lines for pump and Stokes)**. In addition to the peak shift that can induce peak decrease at the original epr-SRS frequency channel as we initially hypothesized, there are a few additional possible factors that may likely underlie the decrease of the epr-SRS signals upon 660 nm excitation even without a peak shift. One possibility is the population competition between the epr-SRS excitation and the invoked rigorous-

electronic-resonance-involved four-wave mixing processes.[19] Second, since the frequency-independent K term in the Albrecht A equation include a quadratic dependence on the oscillation strength of the molecular absorption (i.e. σ_{abs}), a smaller σ_{abs} for the S_1-S_2 transition compared to that of the S_0-S_1 transition may also lead to a much-lowered excited-state epr-SRS peaks.

The invoked high electronic background from the excited state would complicate the analysis for the imaging applications. In principle, utilizing a frequency-modulation SRS scheme, which subtracts SRS signals between on-resonance and off-resonance frequencies in real-time[30,31] instead of the intensity-modulation SRS scheme in our setup, should resolve this issue. Nonetheless, it is still desirable to have a high signal-to-background ratio for straightforward imaging interpretations. Since the background is potentially induced by the S_1-S_2 transition, we then aimed to investigate whether the triplet state (T_1) could serve as an OFF state for epr-SRS signals with decreased background **(Fig. 3a)**. To increase the T_1 population, we added potassium iodide (KI) to the dye solution, which is known to accelerate intersystem crossing by the heavy atom induced spin-orbit coupling.[32–34] The increase of triplet state population was confirmed by fluorescence intensity measurements **(Fig. S3)**. Similar to the excited state SRS spectra, the double bond **(Fig. 3b & Fig. S4a)** and triple bond **(Fig. 3c & Fig. S4b)** peaks disappeared when the Rh800 molecules were further shifted to the triplet state in the presence of KI. Surprisingly, while we still detected a large background increase for the triple-bond peaks, we observed a large negative background signal across the double-bond frequency range.

These negative signals indicate an increase of pump photons, since we detected the stimulated Raman loss (i.e. the pump photon loss) as SRS signals (See Methods). Although a complete understanding of the molecular pathways would require further studies, a plausible reason for such increase in pump photons is the population depletion in the presence of Stokes photon due to the excitation competition for the T_1-T_n transitions. Since pump beam wavelength for the triple-bond excitation (i.e. 838 nm) is further blue shifted from that for double bond (i.e. 880 nm) and from the Stokes beam (i.e. 1031.2 nm), it is possible that 838 nm light fall out of the T_1-T_n transition range, and hence do not induce significant negative background. Here, we successfully demonstrated that both the excited state and the triplet state could effectively deprive the epr-SRS signals for both the double and the triple bond of the Rh800 molecules. However, both induced negative and the positive electronic background, which could introduce artifacts in analyzing the epr-SRS images. In addition, inducing transitions to excited and the triplet state would lead to increased photobleaching. We hence continued to explore two other molecular states as the effective OFF state.

II. Photoswitching by modulating the epr-SRS enhancement: organic dyes

The third electronic state we aimed to exploit was the long-lived reversible dark state (~100 ms to s in an oxygenated environment). This photo-reduced state in the presence of electron donors for organic fluorophores has been heavily explored in STORM and d-STORM super-resolution fluorescence microscopy. For example, oxazine and rhodamine dyes are known to form semi-reduced radicals (F·) or leuco (FH) structures in buffers containing primary thiols (RSH) upon irradiations to the triplet state (^{3}F) **(Fig. 4a, gray box, RS- indicates the thiolate anions)**.[35] Similarly, cyanine dyes have also been shown to form a cyanine-thiol

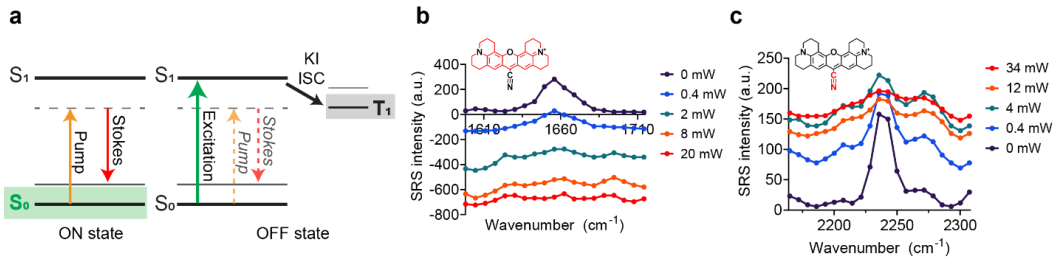

Fig. 3. Photoswitching of epr-SRS signals via transition to the triplet state. (a) Energy diagrams of the proposed ON (left, green shade indicates ground state as ON state) and OFF (right, gray shade indicates triplet state as OFF state) states for epr-SRS signals. (b) epr-SRS spectra of the double-bond mode (red-colored in the molecular structure) of Rh800 at 0, 0.4, 2, 8, and 20 mW of 660 nm excitation beam power in the presence of potassium iodide (KI). (c) epr-SRS spectra of the triple-bond mode (red colored in the molecular structure) of Rh800 at 0, 0.4, 4, 12, and 34 mW of 660 nm excitation beam power in the presence of (KI).

adduct under similar excitation and buffer conditions.[36] A photophysical change associated with this photochemical reduction is the diminishment of the electronic absorption peaks. Since epr-SRS signals strongly depend on the oscillation strength of the molecular absorption (Supplementary information Scheme 1, parameter K),[20,37] the disappearance of absorption peaks in these photo-reduced states indicates that they would be ideal candidates to serve as the OFF state for epr-SRS excitations **(Fig. 4a OFF state, gray box)**.

We tested this hypothesis with ATTO680, a red-absorbing oxazine dye that falls into the desired electronic pre-resonance excitation region under our SRS laser excitation and was reported to undergo light-induced transitions to the above-mentioned long-lived dark state **(Fig. 4a & 4b)**.[35] Exciting ATTO680 solutions containing primary thiol β-mercaptoethylamine (MEA) with a 660 nm excitation beam could indeed transform the color of the solutions into transparent **(Fig. 4c vs 4d, cuvette in the inset, before and after 660 nm illumination)**. Subsequent absorption measurement confirmed the disappearance of corresponding absorption peak for ATTO680 **(Fig. 4c vs 4d)**. The remnant absorption after irradiation **(Fig. 4d)** was due to a layer of unconverted molecules at the interface between the solution and the airspace of the cuvette. After gentle shaking of the cuvette to facilitate dissolution of oxygen in the headspace, both the color and the absorbance peak of the same solution were fully recovered **(Fig. 4e)**, which indicates that the molecules are relaxed back to the ground state ($^1F_0$). These results confirm that the absorption peaks of ATTO680 can be switched on and off, as reported.[38]

We next examined whether the same excitation and oxidation steps can switch the epr-SRS signals on and off. We followed the same excitation procedure but contained the sample solution in a glass chamber typically used for SRS measurement **(Fig. 5a)**. Indeed, we successfully observed reversibly switchable epr-SRS signals targeting the double bond peak of ATTO680 at 1661 cm^{-1} **(Fig. 5b, solid line, red)**. The concurrent switching of the fluorescence over multiple cycles was also observed **(Fig. 5b, solid line, blue)**. The reduced epr-SRS signals could reach as low as to 5% of the original epr-SRS intensity. Control experiments in the absence of MEA showed no effect of such photoswitching **(Fig. 5b, dotted line, red for epr-SRS and blue for fluorescence signals)**. Together, these data confirm that shifting the molecules between the ground state and the photo-reduced dark state could serve as an effective strategy to photoswitch epr-SRS signals.

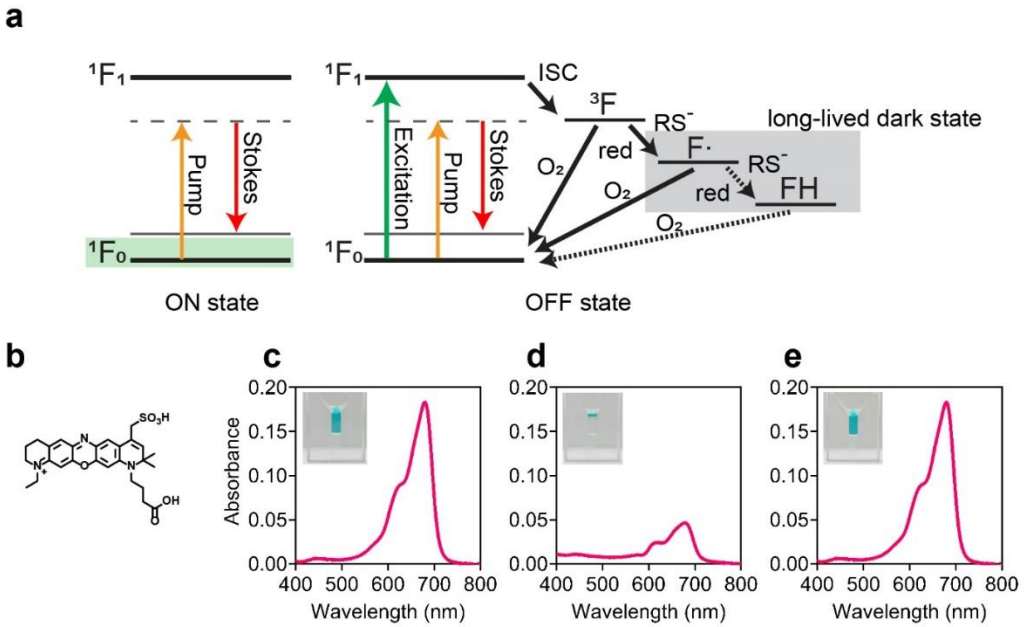

Fig. 4. Proposed strategy to photoswitch epr-SRS signals via transition to the absorption diminished long-lived dark state. (a) Energy diagrams of the proposed ON (left, green shade indicates ground state as ON state) and OFF (right, gray shade indicates long-lived dark state as OFF state) states. $^1F_0$, singlet ground state; $^1F_1$, singlet excited state; ^3F, triplet state; F•, semireduced radical state; FH, fully reduced leuco state; ISC, intersystem crossing; red, reduction. RS$^-$, thiolate anions (b) Molecular structure of ATTO680. (c-e) Absorption spectra of ATTO680 before (c), after (d) irradiating 660 nm excitation beam, and after agitating the cuvette to facilitate oxidation (e). Insets show the images of solution color change in the same cuvette.

Although we have demonstrated the recovery of epr-SRS signals by mechanically accelerating the oxidation through shaking or pipetting the solutions, it is more appealing to utilize light to recover SRS signals for the precise control of the activation kinetics. As the oxidation of semi-reduced radicals is known to be accelerated by irradiation of UV light,[35] we asked whether we could turn the epr-SRS signals on from the dark state by illumination with a 405 nm laser instead. We observed that the 405 nm laser irradiation could increase the epr-SRS signals by 1.7 times compared to that from the OFF state **(Fig. 5c, green vs. pink)**. Fluorescence signals also showed similar level of recovery **(Fig. S5)**. We note that such a recovery was not observed in the absence of the 405 nm activation **(Fig. 5d)**, implying that the recovery was not caused by other processes such as diffusion.

Going beyond the solution characterization, we further confirmed this photoswitching effect in epr-SRS imaging. 5-ethynyl-2′-deoxyuridine (EdU) was incorporated into newly synthesized DNA of dividing HeLa cells and was then click-labeled by ATTO680 azide. The labeled cells immersed in a MEA-containing buffer were subsequently imaged by epr-SRS, targeting the 1661 cm^{-1} peak of ATTO680 **(Fig. 5e)**. After sequential irradiation of the excitation beam and the 405 nm beam, the epr-SRS signals from ATTO680 (1661 cm^{-1}) were first decreased to 50% and then recovered back to 70% of the original signals **(Fig. 5e-h)**. The limited depletion of the SRS signals in cell samples compared to solutions is likely due to the restricted transport of the thiolate anions in cells. We note that the limited recovery of the SRS signals after 405 nm irradiation **(Fig. 5c & 5h, green)** should be due to the fact that ATTO680 has a high electron affinity and accepts

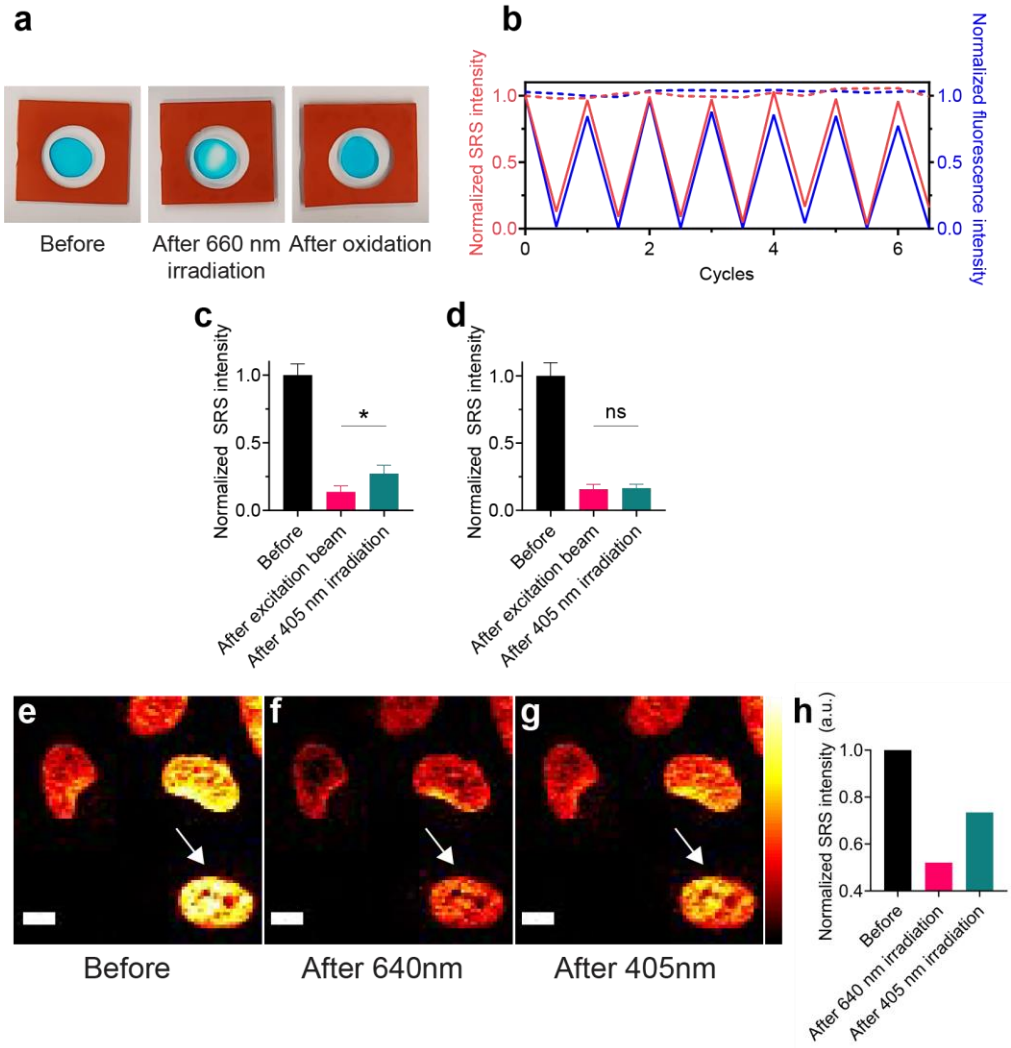

Fig. 5. Photoswitching of epr-SRS signals via transition to the long-lived dark state. (a) A photo of ATTO680 solution containing 0.5 M MEA at pH 9.5 in an SRS imaging chamber before (left), after (middle) excitation beam irradiation, and after oxidation (right). (b) Reversible switching of epr-SRS (red) and fluorescence (blue) signals for multiple cycles of irradiation and oxidation (solid line). No switching was observed in the absence of MEA for both epr-SRS (red) and fluorescence (blue) (dashed line). (c) epr-SRS signals before (black), after (magenta) excitation beam, and after 405 nm activation (green) irradiation. (d) epr-SRS signals of ATTO680 solutions without 405 nm activation. (e-g) Epr-SRS images of ATTO680-click-labeled DNA in HeLa cells before irradiation (e), after excitation beam irradiation (f), and after 405 nm laser irradiation (g). (h) Quantification of epr-SRS signals from the arrowed cell in e-g. Scale bars, 10 μM. In (c-d), statistical significance was determined by unpaired two tailed *t* test. ns, not significant ($p > 0.05$), *$p < 0.05$. Data are shown as mean ± standard deviation (n = 3 replicates for each group).

another electron to form a leuco dye (FH) **(Fig. 4a)**.[38] As this leuco dye is more stable than the semi-reduced radical (F·), the oxidation is not easily facilitated by the 405 nm laser. Screening other rhodamine and oxazine dyes with a stable dark-state in the semi-reduced radical form should further increase the activation efficiency. However, such currently known structures (e.g. ATTO532) mostly fall outside the desired epr-SRS excitation regime (640-790 nm). Shifting the wavelength of SRS lasers to the bluer region, as recently reported, should facilitate screening of better performing photoswitchable epr-SRS probes.[39,40]

III. Photoswitching by modulating the epr-SRS enhancement: photoswitchable proteins

Based on the pre-resonance Raman approximation,[19,20,37] epr-SRS signals are nonlinearly dependent on another photophysical parameter, the detuning between the pump photon energy and the molecular electronic resonance (Supplementary information Scheme 1, parameter $\frac{1}{(\omega_0^2-\omega_{pump}^2)^4}$). The epr-SRS signals would decrease over 10^5 folds when the pump laser energy (ω_{pump}) is detuned away from the molecular electronic transition energy (ω_0).[20] Therefore, molecules with switchable electronic resonances closer to and further away from the pump laser energy could also serve as ON and OFF epr-SRS states respectively, with a decent ON-to-OFF ratio **(Fig. 6a)**.[41] We tested a recently engineered truncated version of a reversibly switchable far-red absorbing soluble bacterial phytochrome photoreceptor (BphP) from *Deinococcus radiodurans*, DrBphP-PCM **(Fig. 6b)**.[42] The absorbing core of the DrBphP-PCM is composed of a photosensory core module (PCM), which is shared by all BphPs, and a covalently attached biliverdin IXa chromophore, which is the enzymatic product of heme catabolism and present in all mammalian cells. Biliverdin undergoes reversible cis-trans isomerization when irradiated with different wavelengths of light, causing BphP transitions between two absorbing states, Pr and Pfr **(Fig. 6b, cis-trans isomerization highlighted in the blue circle)**.[42] With purified DrBphP-PCM solutions, we first confirmed their reversibly switchable absorptions, peaked at 750 nm **(Fig. 6c, magenta, the Pfr state in Fig. 6b)** and 700 nm **(Fig. 6c, black, the Pr state in Fig. 6b)**, upon illumination with 780 nm and 690 nm, respectively.

We next quantified its epr-SRS signal magnitude and reversibility. As the absorption peaks of DrBphP-PCM fall within the desired epr-SRS excitation regime[19,20], DrBphP-PCM in its epr-SRS ON state (i.e. the Pfr state) shows an around 300 times signal magnitude to that of EdU, adopting the recent RIE (relative intensity to EdU) quantification metrics **(Fig. 6d)**.[43] Such a signal size is equivalent to a detection sensitivity below 1 μM for this probe.[44] When switched to the epr-SRS OFF state (i.e. the Pr state) by 780 nm laser, DrBphP-PCM indeed presents a lowered epr-SRS signal for the double bond mode with a Raman peak shifted from 1615 cm^{-1} to 1628 cm^{-1} **(Fig. 6e, magenta and black respectively)**. This peak shift is resulted from the change of cis-trans conformation of the double bond between the ring C and ring D of the biliverdin chromophore **(Fig. 6b)**.[45] Detecting the absolute intensity changes at the 1615 cm^{-1} channel yielded an about 3-fold signal decrease between the epr-SRS ON and the OFF states **(Fig. 6d-e)**. The residual 33% of epr-SRS signals in the OFF state **(Fig. 6d-e)** originates from a combination of the remaining epr-SRS enhancement from the OFF-state Raman peak and a slight electronic background by the pump laser from the relatively broad absorption bands of DrBphP-PCM **(Fig. 6c)**.

After the initial characterization of DrBphP-PCM, we tested the robustness of the photo-switching for epr-SRS signals as the resistance to switching fatigue is an important photophysical parameter in reversibly switchable probes. We first monitored the cycles of reversibility for the DrBphP-PCM fluorescence signals using the sequence of alternating 60 s and 30 s illuminations by the 780 nm **(Fig. 6f, yellow)** and the 640 nm **(Fig. 6f, green)** lasers. The 780 nm laser switches the protein to the Pr state exhibiting weak fluorescence peak at 720 nm,[46] whereas 640 nm laser serves as both the readout laser and the deactivation laser that shifts the protein back to the Pfr non-fluorescent state. We note that the ON and OFF states for fluorescence signals are reversed from those of epr-SRS signals as quantum

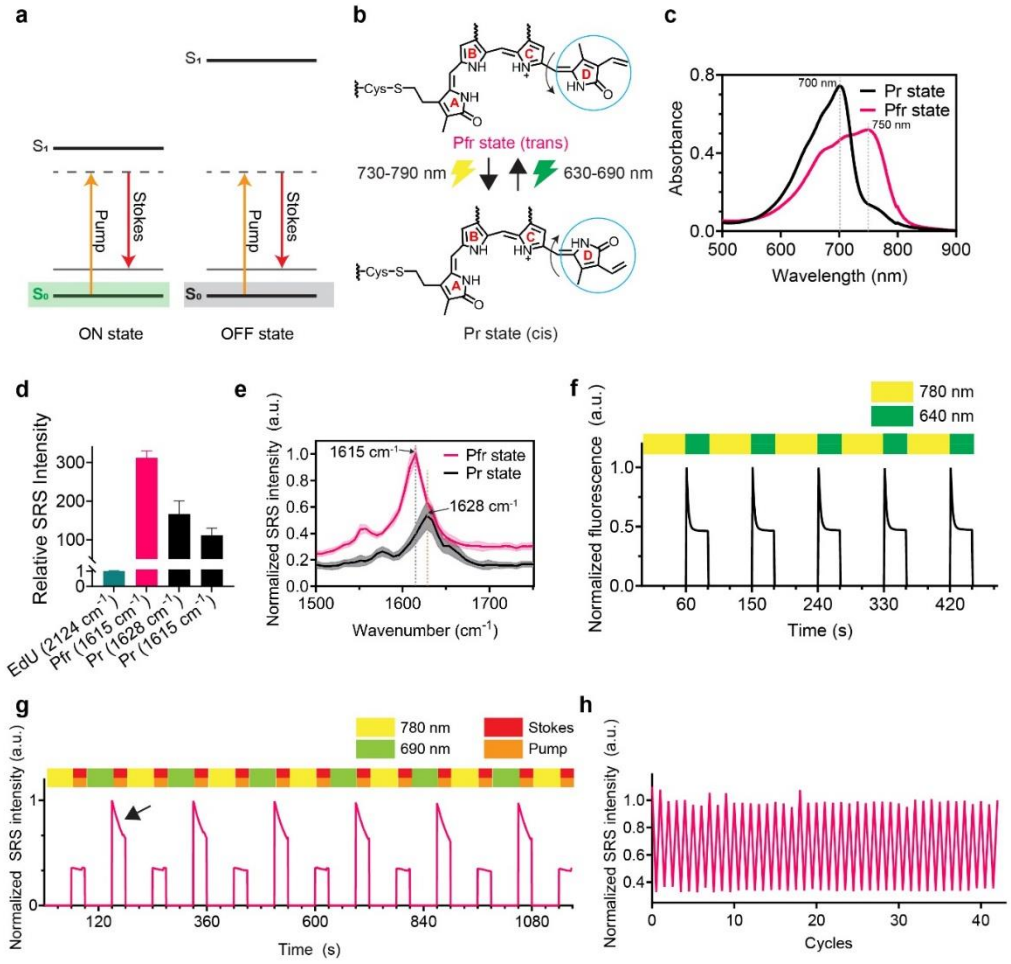

Fig. 6. Photoswitching of the purified near-infrared absorbing DrBphP-PCM protein. (a) Energy diagrams of the proposed ON (left, green shaded) and OFF (right, gray shaded) states. (b) Cis-trans configuration change of the biliverdin chromophore in DrBphP-PCM upon irradiation. (c) Absorption spectra of DrBphP-PCM in the Pr (black) and Pfr (magenta) conformation states. (d) Relative epr-SRS signals of DrBphP-PCM in the Pfr (1615 cm^{-1}, magenta) and Pr (both 1628 cm^{-1}, black; and 1615 cm^{-1}, brown) states compared to the standard SRS signal of EdU (2124 cm^{-1}, green). (e) epr-SRS spectra of DrBphP-PCM in the Pr (black) and Pfr (magenta) states. (f) Cycles of reversible photoswitching of DrBphP-PCM fluorescence, observed in the Pr state. (g) Cycles of reversible photoswitching of DrBphP-PCM epr-SRS signal at 1615 cm^{-1}, the ON state (Pfr state) on-resonance channel. (h) Photoswitching of DrBphP-PCM at 1615 cm^{-1} for over 40 cycles demonstrates no detectable photofatigue.

yields of the Pr and Pfr states are 2.9% and 0%, respectively.[46] Our observed fluorescence depletion and recovery are similar to what were reported previously **(Fig. 6f)**.[42,46]

We then probed the reversibility of the epr-SRS signals. Here, the 780 nm laser was adopted as the deactivation laser, a 690 nm laser was used as the activation laser, and the SRS beams were used as the signal readout laser. Fig. 6g shows the laser sequence and the corresponding epr-SRS ON and OFF intensity. Similar to that for fluorescence, clear photo-switching of epr-SRS signals was observed over multiple cycles **(Fig. 6g)**, whereas the epr-SRS signal levels remained unchanged in the absence of the 690 nm and 780 nm lasers **(Fig. S6a)**. In a separate control experiment, we irradiated the protein solution with Stokes and pump beams for 30 seconds and allowed the molecules to diffuse and replenish for 60

seconds (Fig S6b). However, no SRS recovery was observed **(Fig. S6b, dotted line)**. In contrast, when the protein sample was irradiated by 690 nm activation laser, the SRS signal immediately increased back to the original intensity **(Fig. S6b, green arrow)**. This result indicates that the role of diffusion is minimal and shows that the recovery of SRS signals is not caused by diffusion of the ON molecules into the focal volume, but from activation via 690 nm light.

Interestingly, we observed a decrease in the epr-SRS signals when the DrBphP-PCM solution was irradiated with SRS beams **(Fig. 6g, black arrow)**. We attribute this switching-off effect to pump beam excitation (around 884 nm), which could excite at the very tail of the absorption peak of the Pfr state **(Fig. 6c, magenta)**. We note that this decrease is not due to photobleaching, as epr-SRS signals always recovered back to 100% with 690 nm beam activation **(Fig. 6g)**. We further extended the epr-SRS switchable cycles to more than 40 cycles with minimum photobleaching, demonstrating the robustness of the DrBphP-PCM protein as a photoswitchable epr-SRS probe **(Fig. 6h)**. We reasoned that the minimal photobleaching observed here should likely be due to two reasons. First, the competing switching-off pathway from the SRS beams may have likely helped reduce the potential photobleaching kinetics from either the one-photon or the two-photon excitation by the SRS lasers. Second, the adopted picosecond SRS beams should contribute much less to the higher-order multi-photon excitation induced photobleaching, since their peak power are much smaller compared to that of the femtosecond lasers.

3.4 Discussion

This work presents a series of photophysical characterizations and proof-of-principle observations toward a new type of optical imaging probes, i.e. the photoswitchable epr-Raman probes. We explored the possibilities of four electronic states to serve as the effective OFF state for the epr-SRS signals. In our first two strategies, we induced transitions to the excited state and the triplet states, which led to successful reduction of the epr-SRS peaks. However, robust frequency-modulation SRS techniques are required to remove the large electronic background (both the positive and the negative ones) for further applications.[30,31] Guided by the Albrecht A-term pre-resonance approximation equation (Supplementary information Scheme 1), we subsequently explored another two states, the long-lived dark state with diminished absorption peak from organic dyes and a tunable absorption transition state with modulable detuning to the pump photon energy from photoswitchable proteins. We proved that all four states together with the ground state could serve as the ideal candidates for reversibly photo-switching the epr-SRS signals upon further optimizations through additional engineering and designing of the photoswitchable Raman probes.

As we indicated above, for the red-absorbing organic molecules, extensive screening of rhodamine and oxazine dyes with a stable dark-state in the semi-reduced radical form should help improve the activation efficiency with 405 nm laser. In addition, cyanine dyes with similar cyanine-thiol adduct may also offer new opportunities. In parallel with the dye screening, doubling the frequencies of the SRS lasers as recently demonstrated would offer matching excitation region for molecules across the entire visible absorption range, vastly expanding the pools for photo-switchable epr-SRS probes.[39,40]

We have also demonstrated that the DrBphP-PCM protein shows high promise toward generating a new category of photoswitchable Raman proteins. Further protein

engineering efforts for obtaining larger dynamic ranges of the ON-to-OFF signal ratios are required. This would offer multiplexable epr-SRS peaks and allow genetical encodability for future cell imaging applications. First, slightly blue shifting the absorption peak (e.g. for 30-50 nm) would minimize the electronic background. This would lead to a clearer separation of Raman peaks between the epr-SRS ON and OFF states for easier multiplexing. Second, larger shift in absorption peaks between the epr-SRS ON and OFF states should also contribute to enhancing the dynamic ranges of the ON-to-OFF ratios. Third, mutagenesis of the amino acid residues around the biliverdin binding pocket may shift its double bond vibrational frequency by changing the interacting environment and, hence, creating more colors.[47] Fourth, incorporation of a nitrile bond to the conjugation system of the biliverdin would significantly help expand the epr-SRS color palette owing to the features of the narrow-band and editable nitrile bonds that are ideal for multiplexing. Fifth, the superior property for photoswitchable Raman protein-based probes is their genetic encodability, which is critical for live cell imaging and is not offered by organic dyes. Moreover, it is worth noting that whereas photoswitching of organic dyes frequently require UV light, which is phototoxic for cells, the Raman protein probes derived from BphPs use non-cytotoxic photoswitching far-red and near-infrared light, which penetrates much deeper in biological tissues, thus enabling intravital imaging.[48] Further engineering of distinct BphP-based Raman probes, along with their different intracellular targeting, will allow super-multiplex epr-SRS imaging in live cells.

Ultimately, with successful invention of a new category of photoswitchable epr-SRS probes, super-multiplex super-resolution optical imaging may be implemented, as we rationalized above. Adopting a doughnut set up similar to RESOLFT but with only one additional switching laser, super-multiplex imaging could be brought into the super-resolution regime and offer a valuable new addition to the toolbox of optical imaging in investigating biological activities and functions.

3.5 Methods

Stimulated Raman Scattering Microscopy

A picoEMERALD (Applied Physics and Electronics) system provided the pump (770–990 nm wavelength, 2 ps pulse width, and 80 MHz repetition rate) and Stokes beams (1032 nm wavelength, 2 ps pulse width, and 80 MHz repetition rate). The Stokes beam was modulated by a built-in electro-optic modulator (EOM) at 20 MHz. The pump and Stokes beams were spatially and temporally overlapped within picoEMERALD. To fill the back aperture of a 25× water objective (XLPLN25XWMP, 1.05 NA, Olympus), the two beams were expanded using a telescope and were guided into an inverted multiphoton laser scanning microscope (FV3000, Olympus). The beams were aligned to maximize the SRS signals of deuterium oxide (99.9 at% D, 151882 Aldrich). The beams transmitted through the sample were collected using a high-NA condenser (oil immersion, 1.4 NA, Olympus). Before detection of the stimulated Raman loss using a large area (10 × 10 mm) Si photodiode (S3590-09, Hamamatsu), the Stokes beam was blocked out using a band-pass filter (893/209 BrightLine, 25 mm, AVR Optics). 64V DC bias voltage was used on the photodiode to increase the saturation threshold and reduce the response time. The output current was terminated by a 50 Ω terminator and prefiltered by a 19.2–23.6 MHz band-pass filter (BBP-21.4+, Mini-Circuits) to reduce laser and scanning noise. A lock-in amplifier (SR844, Stanford Research

Systems) demodulated the signals at the modulation frequency. The in-phase X output of the lock-in amplifier was sent to the analog channel of the FV1200 software (FV30-ANALOG). Image acquisition speed was limited by the 30 μs time constant set for the lock-in amplifier. Correspondingly, pixel dwell time is set at 80 μs, yielding a speed of 8.5 s/frame for a 320-by-320-pixel field of view.

SRS spectra were acquired by fixing the Stokes beam at 1031.2 nm and scanning the pump beam through the designated wavelength range for each data point. The total acquisition to record an SRS spectral data cube (40 images) was ~9 min including image acquisition and wavelength tuning. For 1661 cm^{-1} (double bond, ATTO680), 1615 cm^{-1} (double bond, DrBphP-PCM Pfr state), and 1628 cm^{-1} (double bond, DrBphP-PCM Pr state), the wavelengths of the pump laser were 880.4, 884, and 883 nm, respectively. Laser powers on the sample were measured to be 25 mW for the pump beam and 100 mW for the modulated Stokes beam. Laser powers were monitored throughout image acquisition by an internal power meter, and power fluctuations are controlled within 5% by the laser system. Sixteen-bit gray-scale images were acquired by Fluoview software.

Characterization of dye solutions

To characterize photoswitching by transitioning to the first excited state and the triplet state, a solution of 500 μM of Rhodamine 800 dye was prepared without and with 250 mM of potassium iodide (KI), respectively. Figure 1d illustrates the SRS microscopy system used in this study. A 660 nm continuous wave laser (1185057, Coherent), which serves as an excitation beam, was installed and aligned so that it spatially overlapped with the pump and Stokes beam. The alignment precision in all three dimensions was confirmed by measurements on both 1 μm and 200 nm polystyrene beads. The dye molecules were pumped to the excited electronic state by irradiation of 0 mW - 34 mW 660 nm excitation beam on sample concurrently with the pump and Stokes beam. 34 mW power ensures that >80% of the molecules are in the excited state (Table S1).

To test photoswitching by molecular transition to the long-lived dark state, a solution containing 500 μM of ATTO680 and 0.5 M MEA at pH 9.5 was prepared. The pH value was adjusted with 1 M KOH. For absorbance spectra measurement, the solution was loaded into a 100 μL cuvette. The ON state spectrum was measured using a standard spectrophotometer (Cary 500 Scan). To take the OFF state spectrum, the cuvette was illuminated with 100 mW of defocused 660 nm excitation beam for 3 minutes prior to spectrum acquisition. The second ON state spectra was acquired after agitating the same cuvette to facilitate oxidation.

For SRS and fluorescence measurements, the solution was loaded into a glass chamber with a press-to-seal silicone isolator (GBL664501, Sigma) used as a spacer. To measure the epr-SRS/fluorescence signals of the OFF state, the sample solution was illuminated with 100 mW of defocused 660 nm excitation beam for 3-5 seconds prior to SRS/fluorescence measurement. Reactivation was carried out by removing the coverslip, mixing the solution via pipetting up and down, and redepositing the same solution on to a glass slide. The chamber was sealed with a new coverslip for subsequent SRS/fluorescence measurements. For photoswitching experiments shown in Fig. 5b, these depletion and oxidation steps were repeated for multiple cycles on the same solution. To measure the recovery of epr-SRS/fluorescence signals upon irradiation of blue light, the solution sample

after depletion was irradiated with focused 405 nm continuous wave laser (Coherent) at 1.1 mW power for ~8 seconds (15 frames at 0.556 s/frame).

Photoswitching characterization of dyes in cells

HeLa cells were seeded on a coverslip in a Petri dish with DMEM for 20 h, which was then replaced with DMEM medium without FBS for another 20 h for synchronization. 10 μM EdU in fresh DMEM medium was then added to cells for 15 h. Cells were fixed with 4% PFA for 20 min and permeabilized with 0.5% Triton for 30 min. 1 μM ATTO680-azide in Click-iT cell reaction buffer (Invitrogen) was then added to cells to react with EdU for 20 min. Cells were washed twice with PBS before imaging. To turn the epr-SRS signals off, the field-of-view was shined with focused 640 nm laser at 2.2 mW power for 80 seconds (200 frames, 0.412 s/frame). To turn the epr-SRS signals back on, the same field-of-view was shined with 405 nm laser at 1.1 mW power for 20 seconds minutes.

Protein expression and characterization

The protein expression and purification followed the standard protocol from previous report.[1] For absorbance spectra measurement, the purified DrBphP-PCM solution was loaded into a 100 μL cuvette. To take the ON state spectrum, the cuvette was illuminated with a defocused 690 nm laser diode (HL6738MG, Thorlabs Inc.) for 1 minute prior to spectrum acquisition using a standard spectrophotometer (Cary 500 Scan). The OFF state spectra was acquired after illuminating the cuvette with a defocused 780 nm near-infrared LED (M780LP1, Thorlabs Inc) for 1 minute. For SRS and fluorescence measurements, the solution was loaded into a glass chamber typically used for SRS measurements. To measure the epr-SRS signal of the OFF state, the sample solution was illuminated with 11 mW of defocused 660 nm continuous wave laser for 1 minute prior to SRS measurement. To measure the epr-SRS/fluorescence signal of the ON state, reactivation was carried out by shining 140 mW of defocused 780 nm light for 1 minute. For photoswitching experiments shown in Fig. 6g & 6h, the activation and deactivation steps were repeated for multiple cycles on the same solution. For fluorescence measurement, 0.11 mW of focused 640 nm light and emission filter with wavelength range 650-750 nm were used. To acquire SRS spectra of DrBphP-PCM at the Pfr state, 1 minute of 780 nm light was irradiated on the protein samples every 7-10 data points to ensure that all the proteins remain in the Pfr state.

3.6 Acknowledgements

This work was supported by the grants from the National Institutes of Health DP2 GM140919 (to Lu Wei) and R35 GM122567 (to Vladislav Verkhusha) and by the start-up fund from the California Institute of Technology (to Lu Wei).

3.7 References

1. Ando, R., Mizuno, H. & Miyawaki, A. Regulated Fast Nucleocytoplasmic Shuttling Observed by Reversible Protein Highlighting. *Science* **306**, 1370–1373 (2004).
2. Nienhaus, G. U. *et al.* Photoconvertible Fluorescent Protein EosFP: Biophysical Properties and Cell Biology Applications. *Photochemistry and Photobiology* **82**, 351–358 (2006).

3. Lippincott-Schwartz, J. & Patterson, G. H. Photoactivatable fluorescent proteins for diffraction-limited and super-resolution imaging. *Trends in Cell Biology* **19**, 555–565 (2009).
4. Kao, Y.-T., Zhu, X. & Min, W. Protein-flexibility mediated coupling between photoswitching kinetics and surrounding viscosity of a photochromic fluorescent protein. *PNAS* **109**, 3220–3225 (2012).
5. Zhou, X. X. & Lin, M. Z. Photoswitchable fluorescent proteins: ten years of colorful chemistry and exciting applications. *Current Opinion in Chemical Biology* **17**, 682–690 (2013).
6. Klar, T. A. & Hell, S. W. Subdiffraction resolution in far-field fluorescence microscopy. *Opt. Lett., OL* **24**, 954–956 (1999).
7. Betzig, E. *et al.* Imaging Intracellular Fluorescent Proteins at Nanometer Resolution. *Science* **313**, 1642–1645 (2006).
8. Rust, M. J., Bates, M. & Zhuang, X. Sub-diffraction-limit imaging by stochastic optical reconstruction microscopy (STORM). *Nature Methods* **3**, 793–796 (2006).
9. Hofmann, M., Eggeling, C., Jakobs, S. & Hell, S. W. Breaking the diffraction barrier in fluorescence microscopy at low light intensities by using reversibly photoswitchable proteins. *PNAS* **102**, 17565–17569 (2005).
10. Andresen, M. *et al.* Photoswitchable fluorescent proteins enable monochromatic multilabel imaging and dual color fluorescence nanoscopy. *Nature Biotechnology* **26**, 1035–1040 (2008).
11. Sahl, S. J., Hell, S. W. & Jakobs, S. Fluorescence nanoscopy in cell biology. *Nature Reviews Molecular Cell Biology* **18**, 685–701 (2017).
12. Lavoie-Cardinal, F. *et al.* Two-Color RESOLFT Nanoscopy with Green and Red Fluorescent Photochromic Proteins. *ChemPhysChem* **15**, 655–663 (2014).
13. Testa, I., D'Este, E., Urban, N. T., Balzarotti, F. & Hell, S. W. Dual Channel RESOLFT Nanoscopy by Using Fluorescent State Kinetics. *Nano Lett.* **15**, 103–106 (2015).
14. Freudiger, C. W. *et al.* Label-Free Biomedical Imaging with High Sensitivity by Stimulated Raman Scattering Microscopy. *Science* **322**, 1857–1861 (2008).
15. Saar, B. G. *et al.* Video-Rate Molecular Imaging in Vivo with Stimulated Raman Scattering. *Science* **330**, 1368–1370 (2010).
16. Cheng, J.-X. & Xie, X. S. Vibrational spectroscopic imaging of living systems: An emerging platform for biology and medicine. *Science* **350**, (2015).
17. Wei, L. *et al.* Live-Cell Bioorthogonal Chemical Imaging: Stimulated Raman Scattering Microscopy of Vibrational Probes. *Acc. Chem. Res.* **49**, 1494–1502 (2016).
18. Hu, F., Shi, L. & Min, W. Biological imaging of chemical bonds by stimulated Raman scattering microscopy. *Nature Methods* **16**, 830–842 (2019).
19. Wei, L. *et al.* Super-multiplex vibrational imaging. *Nature* **544**, 465–470 (2017).
20. Wei, L. & Min, W. Electronic Preresonance Stimulated Raman Scattering Microscopy. *J. Phys. Chem. Lett.* **9**, 4294–4301 (2018).
21. Xiong, H. *et al.* Stimulated Raman excited fluorescence spectroscopy and imaging. *Nat. Photonics* **13**, 412–417 (2019).
22. Möckl, L. & Moerner, W. E. Super-resolution Microscopy with Single Molecules in Biology and Beyond–Essentials, Current Trends, and Future Challenges. *J. Am. Chem. Soc.* **142**, 17828–17844 (2020).

23. Schermelleh, L. *et al.* Super-resolution microscopy demystified. *Nat Cell Biol* **21**, 72–84 (2019).
24. Bates, M., Dempsey, G. T., Chen, K. H. & Zhuang, X. Multicolor Super-Resolution Fluorescence Imaging via Multi-Parameter Fluorophore Detection. *ChemPhysChem* **13**, 99–107 (2012).
25. Bückers, J., Wildanger, D., Vicidomini, G., Kastrup, L. & Hell, S. W. Simultaneous multi-lifetime multi-color STED imaging for colocalization analyses. *Opt. Express, OE* **19**, 3130–3143 (2011).
26. Wilbrandt, R., Jensen, N. H., Pagsberg, P., Sillesen, A. H. & Hansen, K. B. Triplet state resonance Raman spectroscopy. *Nature* **276**, 167–168 (1978).
27. Rieger, S., Fischedick, M., Boller, K.-J. & Fallnich, C. Suppression of resonance Raman scattering via ground state depletion towards sub-diffraction-limited label-free microscopy. *Opt. Express* **24**, 20745 (2016).
28. Kukura, P., McCamant, D. W. & Mathies, R. A. Femtosecond Stimulated Raman Spectroscopy. *Annual Review of Physical Chemistry* **58**, 461–488 (2007).
29. Shi, L. *et al.* Electronic Resonant Stimulated Raman Scattering Micro-Spectroscopy. *J. Phys. Chem. B* **122**, 9218–9224 (2018).
30. Zhang, D., Slipchenko, M. N., Leaird, D. E., Weiner, A. M. & Cheng, J.-X. Spectrally modulated stimulated Raman scattering imaging with an angle-to-wavelength pulse shaper. *Opt. Express, OE* **21**, 13864–13874 (2013).
31. Fu, D., Yang, W. & Xie, X. S. Label-free Imaging of Neurotransmitter Acetylcholine at Neuromuscular Junctions with Stimulated Raman Scattering. *J. Am. Chem. Soc.* **139**, 583–586 (2017).
32. Chmyrov, A., Sandén, T. & Widengren, J. Iodide as a Fluorescence Quencher and Promoter—Mechanisms and Possible Implications. *J. Phys. Chem. B* **114**, 11282–11291 (2010).
33. Gatzogiannis, E., Zhu, X., Kao, Y.-T. & Min, W. Observation of Frequency-Domain Fluorescence Anomalous Phase Advance Due to Dark-State Hysteresis. *J. Phys. Chem. Lett.* **2**, 461–466 (2011).
34. Widengren, J., Mets, U. & Rigler, R. Fluorescence correlation spectroscopy of triplet states in solution: a theoretical and experimental study. *J. Phys. Chem.* **99**, 13368–13379 (1995).
35. van de Linde, S. *et al.* Direct stochastic optical reconstruction microscopy with standard fluorescent probes. *Nat Protoc* **6**, 991–1009 (2011).
36. Dempsey, G. T. *et al.* Photoswitching Mechanism of Cyanine Dyes. *J. Am. Chem. Soc.* **131**, 18192–18193 (2009).
37. Albrecht, A. C. & Hutley, M. C. On the Dependence of Vibrational Raman Intensity on the Wavelength of Incident Light. *J. Chem. Phys.* **55**, 4438–4443 (1971).
38. van de Linde, S. *et al.* Photoinduced formation of reversible dye radicals and their impact on super-resolution imaging. *Photochem. Photobiol. Sci.* **10**, 499–506 (2011).
39. Xiong, H., Qian, N., Miao, Y., Zhao, Z. & Min, W. Stimulated Raman Excited Fluorescence Spectroscopy of Visible Dyes. *J. Phys. Chem. Lett.* **10**, 3563–3570 (2019).
40. Bi, Y. *et al.* Near-resonance enhanced label-free stimulated Raman scattering microscopy with spatial resolution near 130 nm. *Light Sci Appl* **7**, (2018).

41. Fujioka, H. *et al.* Multicolor Activatable Raman Probes for Simultaneous Detection of Plural Enzyme Activities. *J. Am. Chem. Soc.* (2020) doi:10.1021/jacs.0c09200.
42. Li, L. *et al.* Small near-infrared photochromic protein for photoacoustic multi-contrast imaging and detection of protein interactions in vivo. *Nature Communications* **9**, 2734 (2018).
43. Yamakoshi, H. *et al.* Alkyne-Tag Raman Imaging for Visualization of Mobile Small Molecules in Live Cells. *J. Am. Chem. Soc.* **134**, 20681–20689 (2012).
44. Wei, L. *et al.* Live-cell imaging of alkyne-tagged small biomolecules by stimulated Raman scattering. *Nature Methods* **11**, 410–412 (2014).
45. Kneip, C. *et al.* Protonation State and Structural Changes of the Tetrapyrrole Chromophore during the $P_r \rightarrow P_{fr}$ Phototransformation of Phytochrome: A Resonance Raman Spectroscopic Study †. *Biochemistry* **38**, 15185–15192 (1999).
46. Lychagov, V. V., Shemetov, A. A., Jimenez, R. & Verkhusha, V. V. Microfluidic System for In-Flow Reversible Photoswitching of Near-Infrared Fluorescent Proteins. *Anal. Chem.* **88**, 11821–11829 (2016).
47. Fried, S. D., Bagchi, S. & Boxer, S. G. Extreme electric fields power catalysis in the active site of ketosteroid isomerase. *Science* **346**, 1510–1514 (2014).
48. Shcherbakova, D. M., Stepanenko, O. V., Turoverov, K. K. & Verkhusha, V. V. Near-Infrared Fluorescent Proteins: Multiplexing and Optogenetics across Scales. *Trends in Biotechnology* **36**, 1230–1243 (2018).

3.8 Supplementary information

$$\sigma_{Raman} = K\omega_{pump}\left(\omega_{pump} - \omega_{vib}\right)^3 \left[\frac{\omega_{pump}^2 + \omega_0^2}{(\omega_0^2 - \omega_{pump}^2)^2}\right]^2$$
$$where\ K \sim {\sigma_{abs}}^2$$

Supplementary Scheme 1. Albrecht A-term pre-resonance approximation. ω_{vib} is the vibrational transition energy. ω_0 is the electronic absorption energy. ω_{pump} is the pump photon energy. K is a collection of frequency-independent factors of the Raman dyes. K is proportional to the square of absorption cross-section (σ_{abs}).[2–4]

N_0	N_1	Laser power (mW)
50	50	5.6
20	80	22.2
10	90	50
5	95	105.6
1	99	550.5

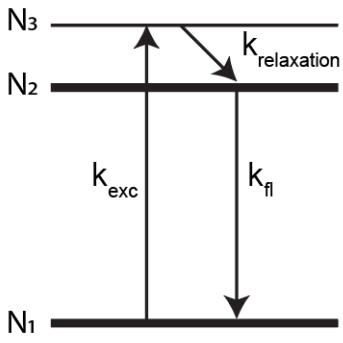

Table S1. Electronic excited state population and required laser power. N_0, ground state population; N_1, excited state population. The molecular transition to the first electronic excited state was modeled as a three-level system. As the vibrational relaxation rate ($k_{relaxation}$) is much faster than the fluorescence emission rate (k_{fl})), the continuous wave excitation at a rate k_{exc} populates the excited state with a steady-state probability $N_1 = k_{exc}/(k_{exc} + k_{fl})$ where $k_{exc} = \sigma I$. k_{fl} is the excited state lifetime, σ is the absorption cross-section at 660 nm, and I is the intensity of the excitation beam. Using k_{fl}= 1/(1.6 ns) and $\sigma = 1.9 \times 10^{-16}$cm^2, I can be solved.

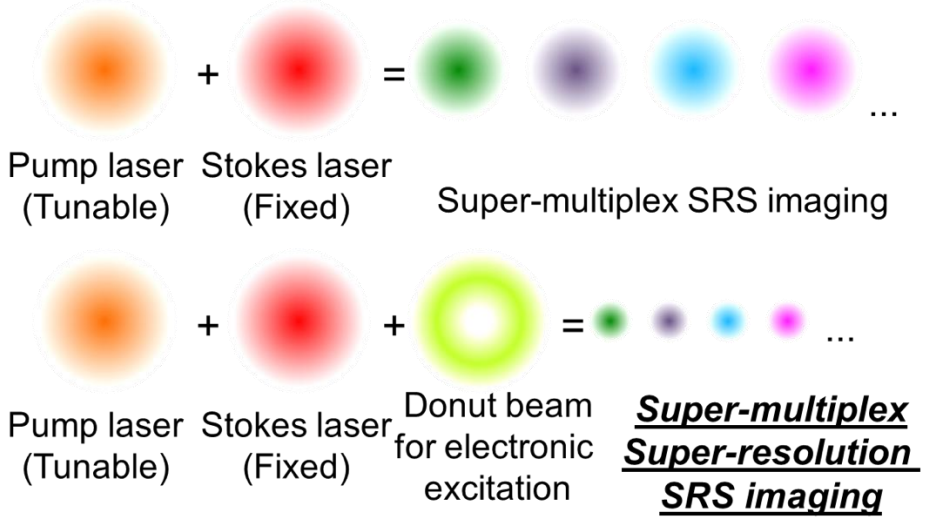

Fig. S1. Proposed scheme of super-multiplex super-resolution epr-SRS imaging. Top: scheme for the existing super-multiplex epr-SRS imaging with a fixed Stokes laser (red) and a tunable pump laser (orange). Bottom: scheme for the proposed super-multiplex super-resolution with photoswitchable epr-SRS probes. With one additional doughnut electronic excitation beam (green) to switch the periphery probes to the OFF state and two SRS lasers (orange and red) to image the multiplexable epr-SRS probes in the ON state at the center, effective super-multiplex super-resolution imaging could be envisioned.

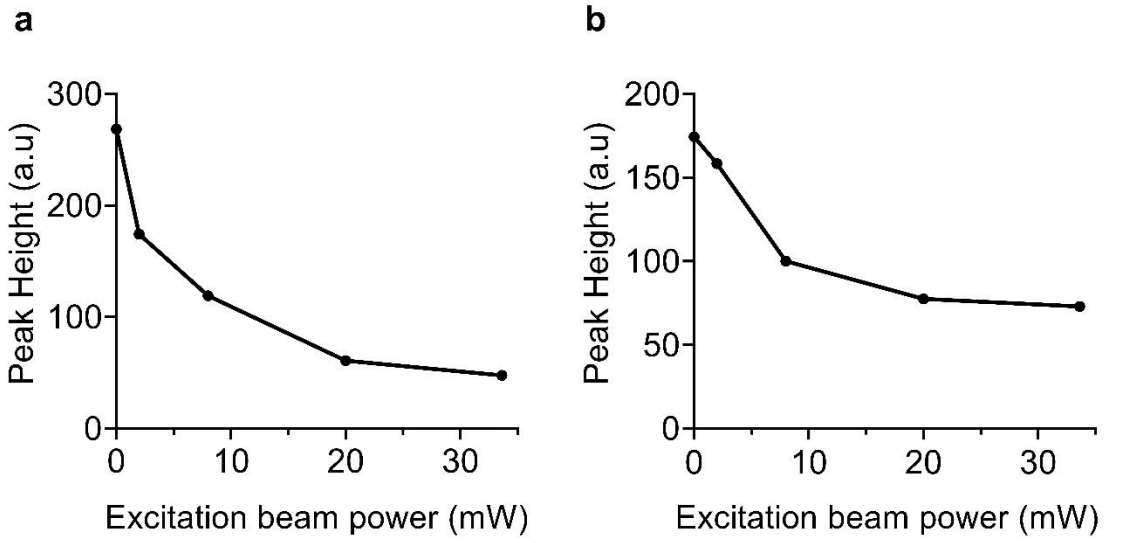

Fig. S2. The remaining epr-SRS signals of Rh800 as a function of 660 nm laser powers used to induce transitions to the electronic excited state. (a) Peak height for double-bond signals of Rh800. (b) Peak height for the triple-bond signals of Rh800. Peak heights were calculated by subtracting the epr-SRS intensity at off-resonance frequency (1694.7 cm^{-1} for double bond, 2278.6 cm^{-1} for triple bond) from on-resonance frequency (1655.9 cm^{-1} for double bond, 2235.7 cm^{-1} for triple bond). The original spectral data is shown in Figs. 2b&c.

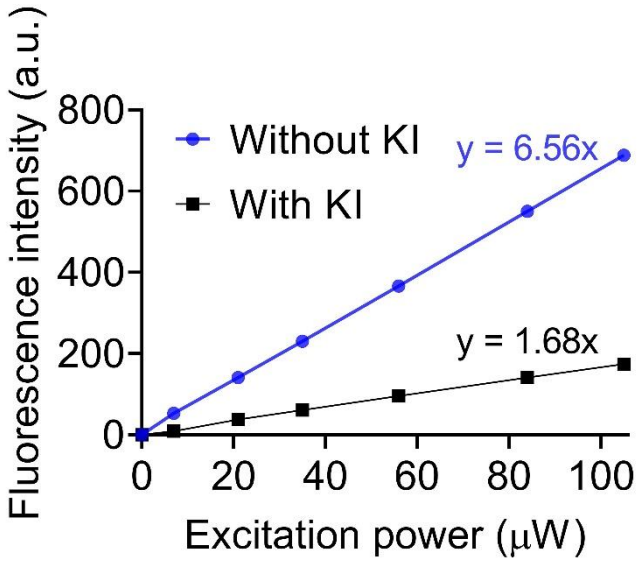

Fig. S3. Comparison of the fluorescence intensities of 500 μM Rh800 solution with (black) and without (blue) KI with 0-100 μW of 640 nm excitation. Although KI is known to induce other transitions including internal conversion from S_1 to S_0 and triplet state quenching by reduction[5–7], k_{ISC} is the most dominant transition at high KI concentration. A factor of 4 decrease in fluorescence intensity with KI indicates an effective shifting of 75% of excited state population to the triplet state compared to that without KI.

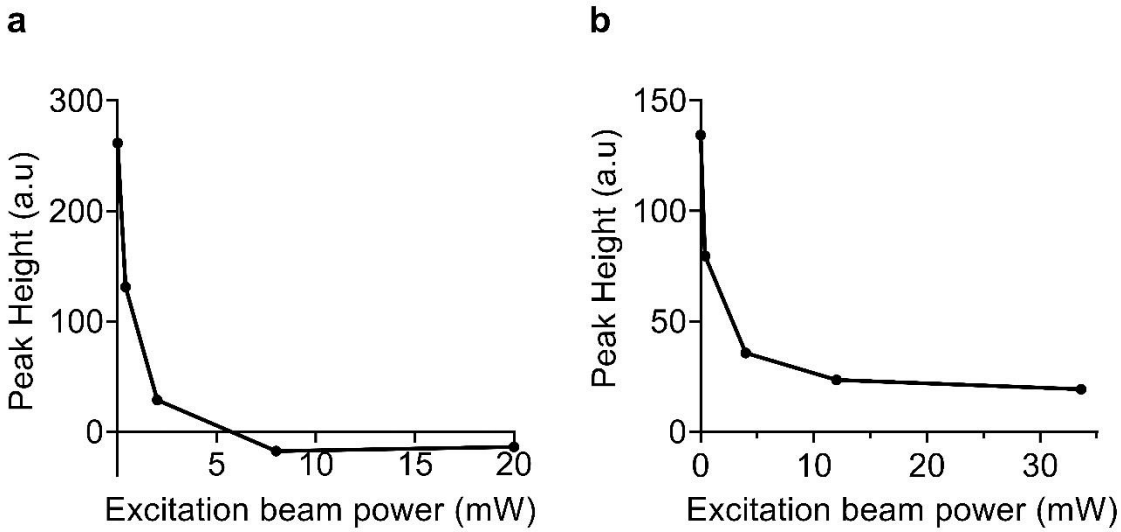

Figure S4. The remaining epr-SRS signals of Rh800 in KI as a function of 660 nm laser powers used to induce transition to the triplet state. (a) Peak height for double-bond signals of Rh800. (b) Peak height was calculated by subtracting the SRS intensity at off-resonance frequency (1694.7 cm^{-1} for double bond, 2278.6 cm^{-1} for triple bond) from on-resonance frequency (1655.9 cm^{-1} for double bond, 2235.7 cm^{-1} for triple bond). The original spectral data is shown in Figs. 3b&c.

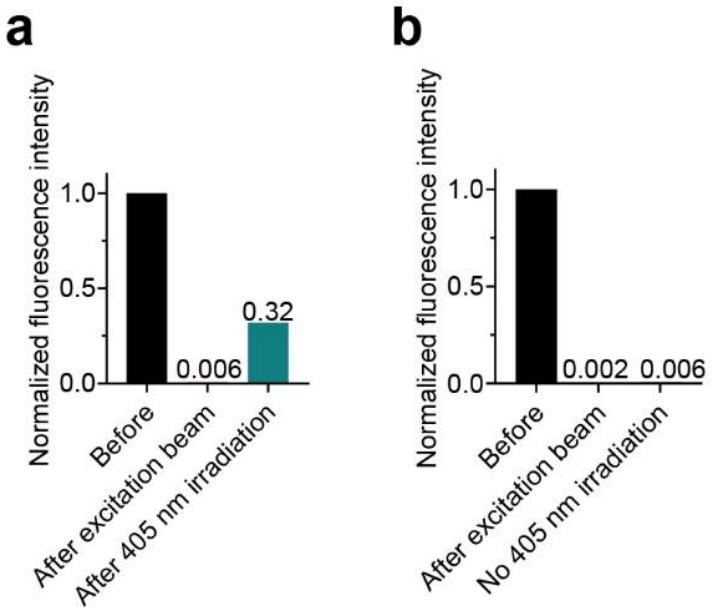

Fig. S5. Photoswitching of fluorescence via transition to the long-lived dark state. a) Fluorescence recovery is observed after 405 nm irradiation. b) Photoswitching is not observed in the absence of the 405 nm laser irradiation.

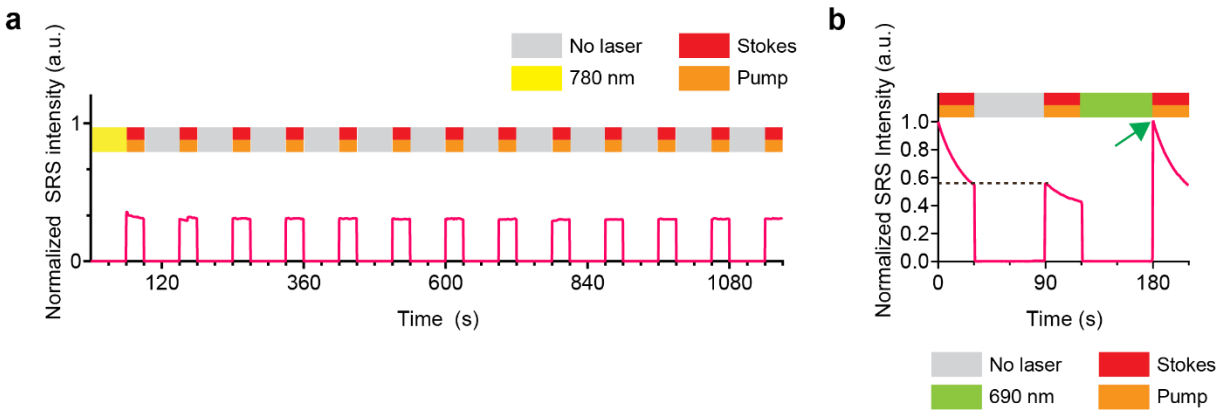

Fig. S6. Characterization of photoswitching properties of DrBphP-PCM. a) Photoswitching is not observed in the absence of the activation and deactivation laser for DrBphP-PCM that started in the epr-SRS OFF state. b) Recovery of the epr-SRS signals are only observed when irradiated with 690 nm laser.

References

(1) Li, L.; Shemetov, A. A.; Baloban, M.; Hu, P.; Zhu, L.; Shcherbakova, D. M.; Zhang, R.; Shi, J.; Yao, J.; Wang, L. V.; Verkhusha, V. V. Small Near-Infrared Photochromic Protein for Photoacoustic Multi-Contrast Imaging and Detection of Protein Interactions in Vivo. *Nature Communications* **2018**, *9* (1), 2734.

(2) Albrecht, A. C.; Hutley, M. C. On the Dependence of Vibrational Raman Intensity on the Wavelength of Incident Light. *J. Chem. Phys.* **1971**, *55* (9), 4438–4443.

(3) Asher, S. A. UV Resonance Raman Studies of Molecular Structure and Dynamics: Applications in Physical and Biophysical Chemistry. 54.

(4) Wei, L.; Min, W. Electronic Preresonance Stimulated Raman Scattering Microscopy. *J. Phys. Chem. Lett.* **2018**, *9* (15), 4294–4301.

(5) Chmyrov, A.; Sandén, T.; Widengren, J. Iodide as a Fluorescence Quencher and Promoter—Mechanisms and Possible Implications. *J. Phys. Chem. B* **2010**, *114* (34), 11282–11291.

(6) Gatzogiannis, E.; Zhu, X.; Kao, Y.-T.; Min, W. Observation of Frequency-Domain Fluorescence Anomalous Phase Advance Due to Dark-State Hysteresis. *J. Phys. Chem. Lett.* **2011**, *2* (5), 461–466.

(7) Widengren, J.; Mets, U.; Rigler, R. Fluorescence Correlation Spectroscopy of Triplet States in Solution: A Theoretical and Experimental Study. *J. Phys. Chem.* **1995**, *99* (36), 13368–13379.

Chapter 4

BOND-SELECTIVE FLUORESCENCE IMAGING WITH SINGLE-MOLECULE SENSITIVITY

Sections of this chapter have been adapted from:
Wang, H.; Lee, D.; Cao, Y.; Bi, X.; Du, J.; Miao, K.; Wei, L. Bond-Selective Fluorescence Imaging with Single-Molecule Sensitivity. Nat. Photon. 2023, 17 (10), 846–855. https://doi.org/10.1038/s41566-023-01243-8

4.1 Abstract

Bioimaging harnessing optical contrasts and chemical specificity is of vital importance in probing complex biology. Vibrational spectroscopy based on mid-infrared (mid-IR) excitation can reveal rich chemical information about molecular distributions. However, its full potential for bioimaging is hindered by the achievable sensitivity. Here, we report bond selective fluorescence-detected infrared-excited (BonFIRE) spectral microscopy. BonFIRE employs two-photon excitation in the mid-IR and near-IR to upconvert vibrational excitations to electronic states for fluorescence detection, thus encoding vibrational information into fluorescence. The system utilizes tuneable narrowband picosecond pulses to ensure high sensitivity, biocompatibility, and robustness for bond-selective biological interrogations over a wide spectrum of reporter molecules. We demonstrate BonFIRE spectral imaging in both fingerprint and cell-silent spectroscopic windows with single-molecule sensitivity for common fluorescent dyes. We then demonstrate BonFIRE imaging on various intracellular targets in fixed and live cells, neurons, and tissues, with promises for further vibrational multiplexing. For dynamic bioanalysis in living systems, we implement a high-frequency modulation scheme and demonstrate time-lapse BonFIRE microscopy of live HeLa cells. We expect BonFIRE to expand the bioimaging toolbox by providing a new level of bond-specific vibrational information and facilitate functional imaging and sensing for biological investigations.

4.2 Introduction

Our understanding of biological processes has been significantly advanced by powerful optical bioimaging techniques that allow visualization of subcellular components with superb specificity, resolution, and sensitivity. Versatile fluorescence strategies with single-molecule sensitivity have generated a profound impact from fundamental biology to translational medicine[1-3]. Complementarily, vibrational imaging, harnessing exquisite chemical contrasts from Raman scattering or mid-infrared (IR) absorption, can uniquely inform the distribution, transformation, and micro-environment of biomolecules and are quickly evolving. While Raman microscopy, such as stimulated Raman scattering (SRS) microscopy, is pushing the boundaries for metabolic imaging and optical super-multiplexing[4,5], IR microscopy has yet to unleash its full potential for modern bioimaging

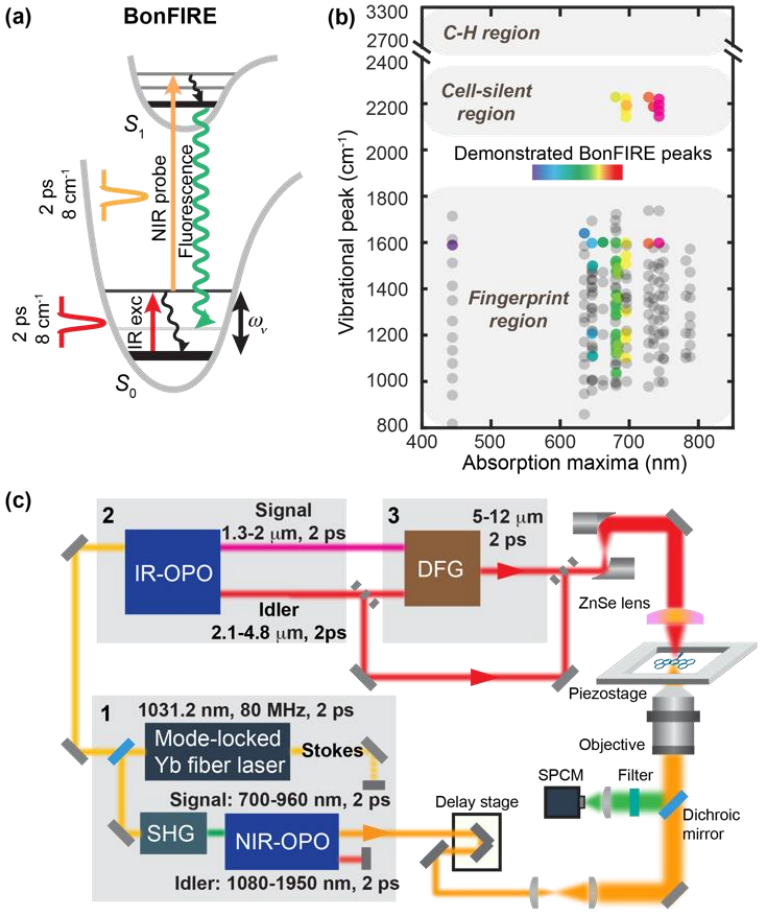

Fig. 1. Principle, setup, and broad spectral coverage of BonFIRE spectro-microscopy. (a) Energy diagram of bond-selective fluorescence-detected IR-excited (BonFIRE) spectroscopy. S_0 and S_1: Ground and first electronic excited states. ω_v: Ground-state vibrational energy. (b) Spectral coverage of BonFIRE. Gray dots are vibrational peaks of 18 dyes measured by FTIR (see **Table S1** and **Extended Data Fig. 3** for details). Rainbow-coloured dots are vibrational peaks that are already detected by BonFIRE. (c) BonFIRE experimental setup. Gray rectangles indicate flip mirrors. Gray-shaded boxes labeled with numbers **1**, **2**, and **3** indicate three interdependent laser modules for generating coherent and tuneable 2-ps near-IR (NIR) and mid-IR pulses in BonFIRE. SHG: second-harmonic generation; OPO: optical parametric oscillator; DFG: difference frequency generation; SPCM: single-photon counting module.

due to inherent limitations, such as coarse spatial resolution, strong water background, and the low detectability of dilute samples. However, IR presents several prominent spectroscopic features over its Raman counterparts[6-9]. IR cross sections (σ_{IR}) are 10^8 to 10^{10} times that of Raman, promising a much-increased sensitivity. Therefore, IR has the potential in fast widefield imaging with high-throughput dynamic analysis. Moreover, as IR and Raman selection rules are complementary, utilizing IR would expand the repertoire of versatile chemical bonds for functional imaging.

Many techniques were developed to address the limitations associated with direct IR imaging utilizing secondary readout schemes[10-12]. For example, mid-IR photothermal (MIP) microscopy[13-16] and ultraviolet (UV)-localized mid-IR photoacoustic microscopy (ULM-PAM)[17] record IR-induced photothermal and photoacoustic responses with short-wavelength visible and UV probes, respectively, detecting biomolecules with sub-IR-diffraction-limited

resolution in cells and clinical tissues. However, the detection sensitivity is still limited to tens of μM to mM, restricting applications of these methods to abundant macromolecules (e.g., proteins and lipids). While single-protein IR detection has been achieved with near-field methods[18], it is not readily applicable to general and quantitative bioimaging.

Here, we report Bond-selective Fluorescence-detected IR-Excited (BonFIRE) spectro-microscopy, an IR-bioimaging approach with a narrowband laser excitation setup suited for quantitative intracellular interrogations with high spatial and spectral resolution and unprecedented single-molecule sensitivity. BonFIRE harnesses a nonlinear double-resonance scheme, encrypting the bond-selective IR spectroscopic features into fluorescence – the most sensitive measurables in bioimaging – with an additional up-conversion probe laser in the near-IR range **(Fig. 1a)**. The resulting fluorescence reports vibrational details with high sensitivity, and achieves subcellular spatial resolution determined by the up-conversion laser. Such IR-promoted double-resonance spectroscopy was introduced in 1975 mainly for vibrational lifetime studies[19-21]. It was recently revisited by utilizing an amplified broadband femtosecond (fs) system in fluorescence-encoded IR (FEIR) spectroscopy (**Fig. S1a**), which demonstrated single-molecule sensitivity in IR-transparent acetonitrile-d_3 solutions[22,23]. However, the excessive peak intensity and low repetition rate of the fs system make FEIR unfeasible for bioimaging due to sample damage and a slow acquisition rate[24,25]. The interferometric detection of FEIR also requires a second IR pulse, adding more complexities to the setup. We also note another recently-introduced Raman-pumped double-resonance scheme, stimulated Raman excited fluorescence[26] (SREF, **Fig. S1b**). However, SREF imposes a strict requirement on the electronic pre-resonance stimulated Raman excitation for optimal signal-to-background (S/B) ratios, restricting the choice of reporter molecules and vibrational modes[27].

In our approach, we chose 2-ps narrowband (~8 cm^{-1}) pulses for both IR and up-conversion probe lasers with wide tunability (**Fig. 1b-c**). This new setup ensures biocompatibility with much lower peak power compared to the fs pulses; efficient up-conversion with matched vibrational relaxation lifetime (~ps, see **Methods** for simulation); explicit bond selectivity for functional and multiplexed imaging; and broad vibrational spectral coverage **(Extended Data Fig. 1)** with flexible BonFIRE dye options (**Fig. 1b**), which greatly outnumber those offered by FEIR or SREF. We first demonstrated BonFIRE spectro-microscopy in fingerprint (800-1800 cm^{-1}) and cell-silent (1800-2800 cm^{-1}) regions. Then, we achieved the first far-field single-molecule IR imaging for conjugated C=C and C≡N bonds. We next applied BonFIRE in targeted imaging with labelled nucleic acids and specific protein species in cells, neurons, and tissues with high spatial resolution and sensitivity, demonstrating vibrational multiplexing beyond what fluorescence alone could offer. For optimal live-cell applications, we implemented a high-frequency modulation scheme for background-free time-lapse imaging. We also benchmarked the unique advantages of BonFIRE, such as super-multiplexing, vibrational lifetime investigation, and widefield imaging over existing techniques. We expect BonFIRE to enable sensitive bond-selective bioimaging that complements fluorescence with rich vibrational information and functions, facilitating novel biological and biophysical discoveries.

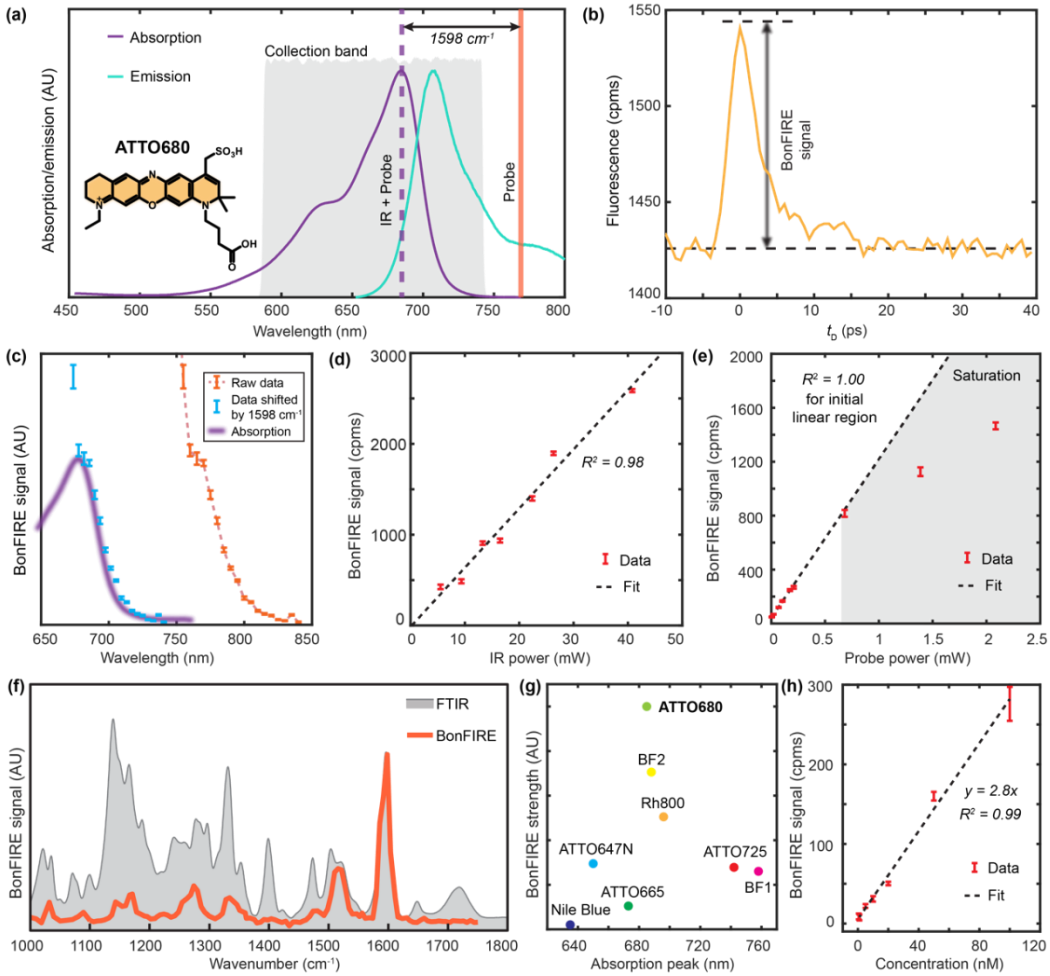

Fig. 2. Double-bond BonFIRE characterizations. (a) Fluorescence absorption/emission spectra of ATTO680 with indicated optimal BonFIRE up-conversion probe wavelength (orange) and collection band (gray), targeting the IR vibrational peak at 1598 cm^{-1}. (b) BonFIRE signal dependence on IR-probe pulse delay. cpms: counts per millisecond. (c) BonFIRE signal dependence on probe wavelength (dashed orange). The BonFIRE excitation profile (orange dots, by horizontally shifting the raw data by adding the IR frequency of 1598 cm^{-1}) is also overplotted with the absorption spectrum of ATTO680 (purple). Data are presented as peak values +/- SD from the background (n = 13). (d-e) BonFIRE signal dependences on IR power (d) and probe power (e) on sample, measured from 10 μM ATTO680 in DMSO. Data are presented as peak values +/- SD from the background (n = 18). (f) Overplot of BonFIRE (red) and FTIR (gray) spectra of ATTO680. (g) Comparison of BonFIRE signals among eight dyes (1 μM in DMSO), targeting the IR excitation for their corresponding C=C bonds around 1600 cm^{-1}, details are provided in **Table S3**. (h) The dependence of BonFIRE signal on the ATTO680 concentration in DMSO. A detection limit of 0.5 nM was obtained with a signal-to-noise ratio (S/N) of 3. Data are presented as mean values +/- SD (n = 3).

4.3 Results

BonFIRE spectroscopy in the fingerprint region

Details of the customized BonFIRE setup **(Fig. 1c)** are in **Methods**. We validated BonFIRE spectroscopy by targeting the skeletal C=C mode at 1598 cm^{-1} of a red dye ATTO680 **(Fig. 2a)**. ATTO680 has high IR ($\sigma_{IR} \sim 1.2 \times 10^{-17}$ cm^2) and absorption cross sections and a quantum yield of 30%, enabling efficient BonFIRE transitions (see **Methods** and **Fig. S2**). A 765-nm up-conversion probe wavelength is chosen **(Fig. 2a, orange line)** so that the

excitation from the combined energy of IR and probe lasers (IR+probe, **Fig. 2a**, dashed purple line) reaches the absorption maximum, while the background excitation from the probe alone is low. We obtained a fluorescence-detected peak as a function of the IR-probe temporal delay (t_D) **(Fig. 2b)**. The time scale of the negative t_D (i.e., the probe is ahead) matches with the temporal overlap profile of the 2-ps lasers. The resulting longer tail toward positive t_D (i.e., the IR is ahead) indicates the vibrational lifetime of C=C bonds[28]. The S/B (peak height/background) is about 8% **(Fig. 2b)**, higher than IR-photothermal-induced fluorescence change[29,30]. Note that the background is much smaller in more IR-transparent solvents **(Extended Data Fig. 2, S/B ~56%)**.

To characterize BonFIRE, we swept the probe wavelength across the excitation range at the red tail of the absorption spectrum (750-850 nm) while fixing the IR excitation at 1598 cm^{-1}. The shifted BonFIRE excitation profile from the combined energy of IR+probe **(Fig. 2c, blue)** overlaps with ATTO680 absorption tail **(Fig. 2c, purple)**, confirming the optimal upconverting wavelength is around 765 nm **(Fig. 2c, dashed curve)**. Tuning the probe wavelength to the bluer side causes reduced S/B and increased noises **(Figs. 2c and S3)**, likely due to other multiphoton processes (e.g., excited-state absorptions). We also confirmed that the BonFIRE signals are linearly dependent on the IR power **(Fig. 2d)** and show a saturated trend on the probe power **(Fig. 2e)**, consistent with the simulation (**Methods** and **Fig. S2**).

We obtained the BonFIRE spectrum of ATTO680 in reference to its FTIR **(Fig. 2f)**. Most fingerprint features were revealed[31]. The intensity mismatch between BonFIRE and FTIR is primarily due to lower Franck-Condon (F-C) constants of less conjugated modes[32]. The correspondence between BonFIRE and FTIR has been confirmed to be explicit for all investigated dyes **(Extended Data Fig. 3)**. We compared eight molecules and identified ATTO680 as the best-performing dye with the highest signal **(Fig. 2g and Table S2)**. Targeting the C=C excitation in ATTO680, the BonFIRE sensitivity reached 0.5 nM **(Fig. 2h)**, well below the calculated single-molecule-equivalent concentration of 5 nM.

Cell-silent BonFIRE spectroscopy

With broad laser tuneability, it is now possible to investigate modes in the cell-silent window, the key spectral region for emerging applications such as super-multiplexing[5,33] and electrostatic sensing[34,35]. So far, no silent-region IR-pumped double-resonance spectroscopy has been demonstrated. Toward this front, we adopted a probe, BF1 **(Fig. 3a, more details in Table S3)**, bearing a C≡N conjugated to the dye resonance structure with strong F-C coupling.[5] We first calculated an optimal upconverting wavelength of 890 nm by matching the combined energy of probe+IR with the absorption peak at 743 nm **(Fig. 3a)**. The resulting BonFIRE signal **(Fig. 3b, blue)** targeting the 2224 cm^{-1} IR excitation for BF1 C≡N is only about 1.2% compared to that of C=C (1598 cm^{-1}, **Fig. 3b**, orange). This is mainly due to a much smaller $\sigma_{IR} \sim 2.7 \times 10^{-19}$ cm^2 of conjugated C≡N (**Table S4**) with a faster vibrational decay (observable from the decay trends in **Fig. 3b**) than that of C=C[28]. Subsequent BonFIRE characterizations **(Extended Data Fig. 4)** confirm the optimal probe wavelength around 890 nm and similar power dependence on IR and probe power to fingerprint-BonFIRE.

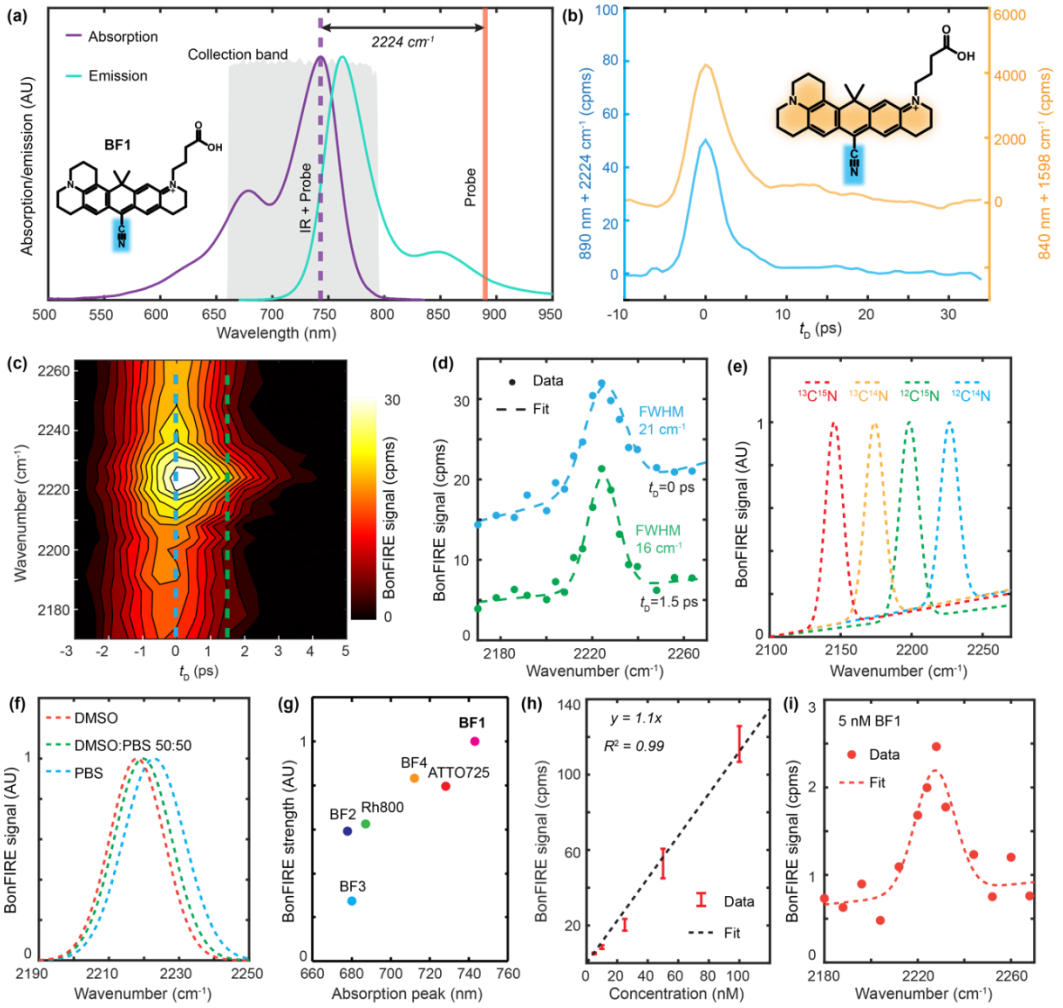

Fig. 3. Cell-silent BonFIRE spectroscopy. (a) Fluorescence absorption/emission spectra of BF1 with optimal BonFIRE up-conversion probe wavelength (orange) and collection band (gray), targeting the IR vibrational peak at 2224 cm^{-1}. (b) BonFIRE signal dependence on IR-probe temporal delay for C=C (yellow) and C≡N (blue) in BF1. Backgrounds were subtracted to compare the BonFIRE peak heights directly. cpms: counts per millisecond. (c) Contour map of C≡N BonFIRE signals as functions of IR frequency (vertical) and IR-probe delay t_D (horizontal). (d) BonFIRE spectra of C≡N extracted at t_D = 0 ps (blue) and t_D = 1.5 ps (green). Data are shown as dots and fittings (Gaussian + linear) are shown as dashed lines. The calculated full width at the half maximum (FWHM) is displayed along each peak. (e) BonFIRE spectra of four C≡N isotopes of BF1. Fitted spectra are shown for clarity. AU: arbitrary unit. (f) Solvatochromism of C≡N measured from 10 μM BF1 in three different PBS/DMSO mixtures. (g) Comparison of BonFIRE signals targeting the triple bonds from six dyes (1 μM in PBS). Details are provided in **Table S4**. (h) Concentration curve of C≡N in BF1 in water. The detection limit was 5 nM with a signal-to-noise ratio (S/N) of 6. Data are presented as mean +/- SD (n = 3). (i) BonFIRE spectrum of 5 nM BF1 in water.

Unlike fingerprint-BonFIRE **(Fig. 2f)**, we observed a background across a broad off-resonance frequency range around the C≡N band **(Fig. 3c, blue dashed line)**. This background is unlikely caused by the excited-state absorption, as it is absent for double-bond BonFIRE and the probe wavelength is at the far red of the excitation tail. We tentatively attribute this background to broadband overtones and combinational modes, as previously reported[36,37]. A more detailed investigation is undergoing. Experimentally, this background

decays faster with t_D detuning than the desired signal. Hence, we chose to extract BonFIRE signal at t_D=1.5 ps **(Fig. 3c, green dashed line)** in all following experiments unless otherwise mentioned, a sweet spot to maintain signal strength and spectral fidelity with diminished background interference **(Fig. 3d)**.

After validating cell-silent BonFIRE spectroscopy, we demonstrated its potential of vibrational super-multiplexing by detecting four C≡N isotopologues of BF1. Four distinct vibrational peaks are resolved **(Fig. 3e, raw data in Fig. S4)**, although the absorption spectra are almost identical **(Fig. S5)**. To confirm the environmental-sensing capability, we proved that BonFIRE could identify the vibrational shift of C≡N bond in solutions with varying hydrogen-bonding conditions. The C≡N peak shifts from 2224 cm^{-1} (in PBS) to 2220 cm^{-1} (in 50:50 PBS/DMSO) and 2218 cm^{-1} (in DMSO) **(Fig. 3f)**. Moreover, to identify the brightest cell-silent BonFIRE probe, we compared six C≡N and C≡C bearing dyes and confirmed that BF1 has the strongest signal **(Fig. 3g)**, which agrees with prediction (**Table S4**). The detection limit targeting C≡N in BF1 reaches the single-molecule level of 5 nM **(Fig. 3h)** with an S/N of 6 and a clearly resolved spectrum **(Fig. 3i)**.

Single-molecule BonFIRE imaging

With the superb sensitivity in solutions for both C=C and C≡N bonds, we aimed to perform single-molecule IR imaging. We first characterized the spatial resolution of BonFIRE microscope on 100-nm fluorescent beads, obtaining lateral and axial resolutions of 600 nm and 1.8 μm, respectively **(Extended Data Fig. 5)**. We then confirmed the quality of the single-molecule samples **(Figs. S6&S7)** prepared following two common approaches (**Methods**).

Single-molecule BonFIRE images were obtained for C=C bonds in ATTO680 and Rh800 **(Fig. 4a-b)**, where the most intense signal appears at the on-resonance frequency of 1598 cm^{-1} and diminishes sharply toward the off-resonance frequencies. The fitted spectra at the single-molecule level **(Fig. 4a-b, right)** closely resemble the bulk spectra **(Fig. S6c)**. We also achieved clear single-molecule imaging and spectroscopy for the weaker C≡N mode in BF1 and isotope-labelled (i.e., $^{13}C\equiv^{15}N$) BF1-conjugated antibodies **(Fig. 4c-d)**. Moreover, BonFIRE can identify multiple isotopologues at the single-molecule level. **Fig. 4e** shows the fluorescence image of a mixture of $^{13}C\equiv^{14}N$, $^{12}C\equiv^{15}N$, and $^{12}C\equiv^{14}N$ labelled BF1 single molecules. The same image is colour-coded **(Fig. 4f)** based on *in-situ* BonFIRE spectra **(Fig. 4g)**. Notably, the co-existence of multiple isotopologues within the same diffraction-limited spot was revealed **(Extended Data Fig. 6)**. To our knowledge, this is the first all-far-field single-molecule IR imaging and spectroscopy. The reproducibility of BonFIRE single-molecule imaging is shown in **Extended Data Fig. 7**, where the S/B ratios of C≡N reach ~3. The imaging results demonstrated here bring the sensitivity of BonFIRE comparable to that of confocal fluorescence.

Bond selective bioimaging by BonFIRE microscopy

With narrow bond selectivity and single-molecule sensitivity, we sought to explore BonFIRE's bio-imaging compatibility. **Fig. 5a** (left) shows a BonFIRE image of ATTO680-azide-click-labelled 5-ethynyl-2′-deoxyuridine (EdU) from newly synthesized DNA in HeLa cells, targeting the C=C vibration at 1598 cm^{-1} for ATTO680. As expected, clear patterns of cell nuclei are highlighted. Tuning the IR to an off-resonant frequency with the same probe

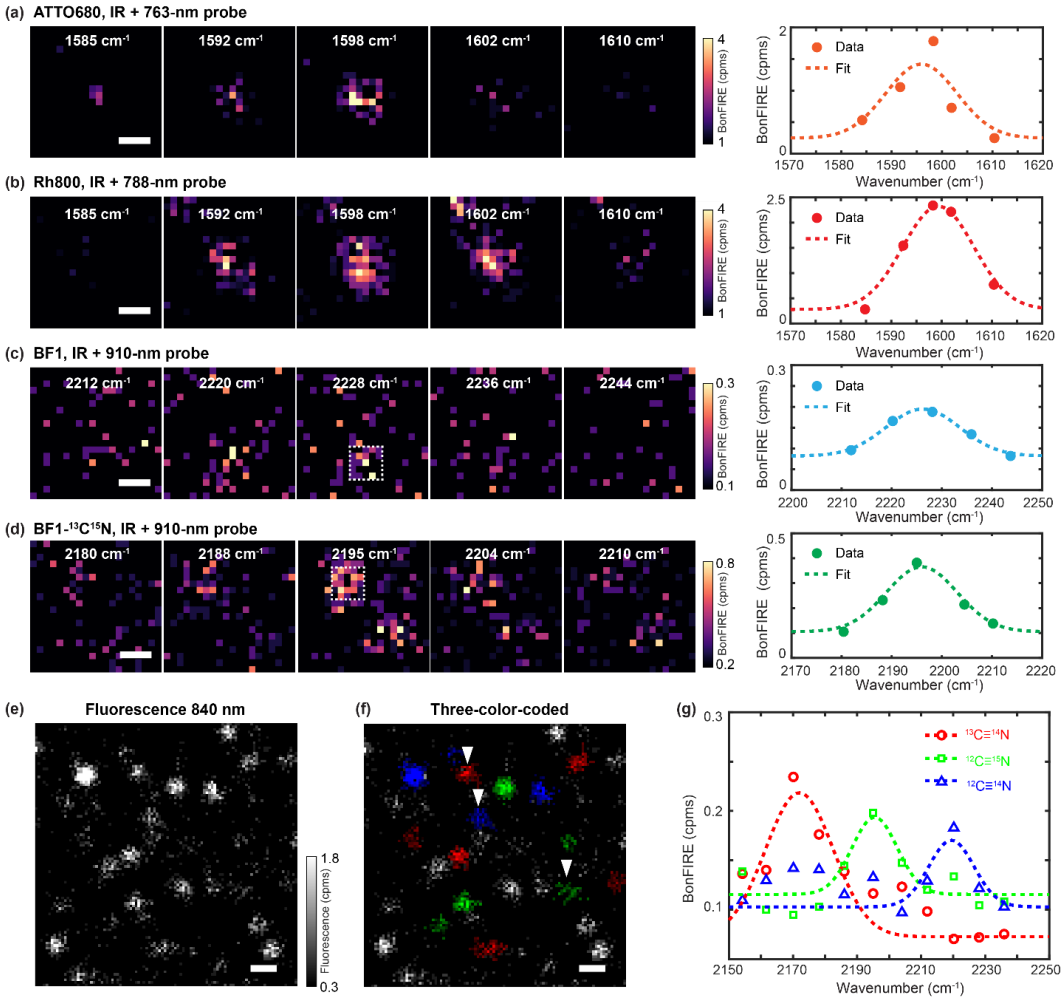

Fig. 4. Single-molecule BonFIRE imaging and spectroscopy. (a-b) Left: single-molecule BonFIRE images of C=C modes in ATTO680 (a) and Rh800 (b) across IR frequencies. The corresponding IR frequencies and the probe wavelengths used are indicated in each image. Right: The spectra with Gaussian fittings are obtained by plotting the average BonFIRE signals within the central 500×500 nm^2 area. (c-d) Left: single-molecule BonFIRE images of C≡N bonds in BF1 (c) and its ^{13}C≡^{15}N isotopologue (d) across IR frequencies. Right: The spectra with Gaussian fittings are obtained by plotting average BonFIRE signals within the 500×500 nm^2 area indicated by white dashed boxes in (c) and (d). Single dye-conjugated antibodies are used. (e-g) Fluorescence image (e) of the single-molecule mixture with three BF1 isotopologues, resolved and colour-coded (i.e., ^{13}C≡^{14}N (red), ^{12}C≡^{15}N (green), and ^{12}C≡^{14}N (blue)) in (f) based on their *in-situ* BonFIRE spectra (g, representative spectra plotted from arrowhead-indicated single molecules from f). Unassigned (gray) dots in (f) are due to either a poor S/N or the existence of more than one colour (**Fig. S12**). Cpms: counts per millisecond. Scale bars: 500 nm (a-d) and 1 μm (e-f).

setting yielded a dark background **(Fig. 5a, 1650 cm^{-1})**, underlining the bond selectivity. Negligible photobleaching in BonFIRE was confirmed by continuously scanning the same area of the ATTO680-labelled EdU over 100 frames with only ~1% signal fluctuations, comparable to that from direct electronic excitation from the probe alone **(Fig. S8)**. To showcase the high spatial resolution, we imaged ATTO680-click-labelled EdU in extracted chromosomes and ATTO680-immunolabelled fibrillarin from nucleoli **(Figs. 5b and 5c, 1598 cm^{-1})**, with spatial contrast close to that of standard confocal fluorescence.

In addition to C=C bonds, we performed cell-silent BonFIRE imaging targeting C≡N bonds. **Fig. 5d** (left) displays the spatial pattern of BF1-immunolabelled α-tubulin targeting its C≡N vibration at 2220 cm^{-1}. Detailed contrast from microtubules in the cytoskeleton of HeLa cells is clearly shown. Such low-abundance delicate cellular structures would not have been detected by mid-IR-photothermal or photoacoustic imaging. BonFIRE signal disappears at an off-resonant frequency, confirming the bond-selectivity **(Fig. 5d, right)**. We also applied the C≡N BonFIRE to map the distribution of MAP2 and GFAP, characteristic marker proteins for mature neurons and astrocytes, respectively, and obtained highly-specific images with BF1 and its $^{13}C\equiv^{14}N$ isotopologue immuno-labelled antibodies in neuronal co-cultures **(Fig. 5e-f)**. Such narrowband resolvability also allows two-colour imaging for BF1-MAP2 neurons and BF1-$^{13}C\equiv^{14}N$-GFAP astrocytes in the same neuronal co-culture **(Fig. 5g)**. BonFIRE also works with tissue imaging, which is exemplified in **Fig. 5h** and a 3D volumetric rendering in **Fig. 5i** of mouse brain tissues. To exploit vibrational super-multiplexed imaging beyond fluorescence "colour barrier",[1,5] we imaged four isotopologues of BF1 through four-colour BonFIRE imaging of labelled and mixed HeLa cells **(Fig. 5j)**. Combining the narrowband selectivity, isotope-edited multiplexed probes, and specific labelling methods, BonFIRE microscopy could encode rich vibrational information into fluorescence, opening new avenues for resolving many biomolecular targets in complex biosystems.

Background-free BonFIRE imaging

The BonFIRE S/B is only 8% for C=C bonds in ATTO680 (DMSO) and 23% for C≡N bonds in BF1 (PBS). Such a high background comprises two major sources: anti-Stokes fluorescence from the thermal population[38] and the IR-induced photothermal modulation of fluorescence, which is absent of vibrational signatures as it mainly comes from the collective solvent/background absorption **(Figs. 6a & S9)**. For the above static BonFIRE images, we retrieved pure signals by subtracting fluorescence images at non-overlapped delays (e.g., t_D = 20 ps and 10 ps for C=C and C≡N) from that at overlapped delays (e.g., t_D = 0 ps and 1.5 ps for C=C and C≡N). However, such subtraction requires two consecutive frames and slows down imaging speed. In addition, subtraction artefacts exist when the sample moves between two consecutive frames **(Fig. S10)**. We reasoned that a fast modulation of the IR beam in the MHz range should significantly remove both backgrounds, given that the photothermal background builds up at the timescale of tens of μs **(Figs. S11&S12)**. An acoustic optical modulator (AOM) is then used to modulate the IR beam **(Fig. 6b)**. The SPCM is correspondingly replaced by a photomultiplier tube (PMT) with an 80-MHz bandwidth for fast signal detection. The demodulated AC signals from a lock-in amplifier are recorded as BonFIRE signals. Although PMT has a lower quantum efficiency than SPCM, the single-molecule sensitivity in solution could still be reached **(Extended Data Fig. 8)**.

Experimentally, we confirmed that background and noise decrease exponentially as modulation frequency increases **(Fig. 6c, insets)**, with S/B and S/N levelling off at approximately 2 MHz **(Fig. 6c)**. Background-free BonFIRE imaging is directly obtained from multiple biomolecule targets without subtraction. **Fig. 6d** shows images from ATTO680-click-labelled-EdU at t_D = 0 ps (left) and 20 ps (right), where signals at 20 ps were turned-off. Similarly, in **Fig. 6e**, BonFIRE images of BF1-$^{13}C\equiv^{15}N$-immuno-labelled α-tubulin of HeLa cells and BF2-click-labelled EdU of extracted chromosomes present clear

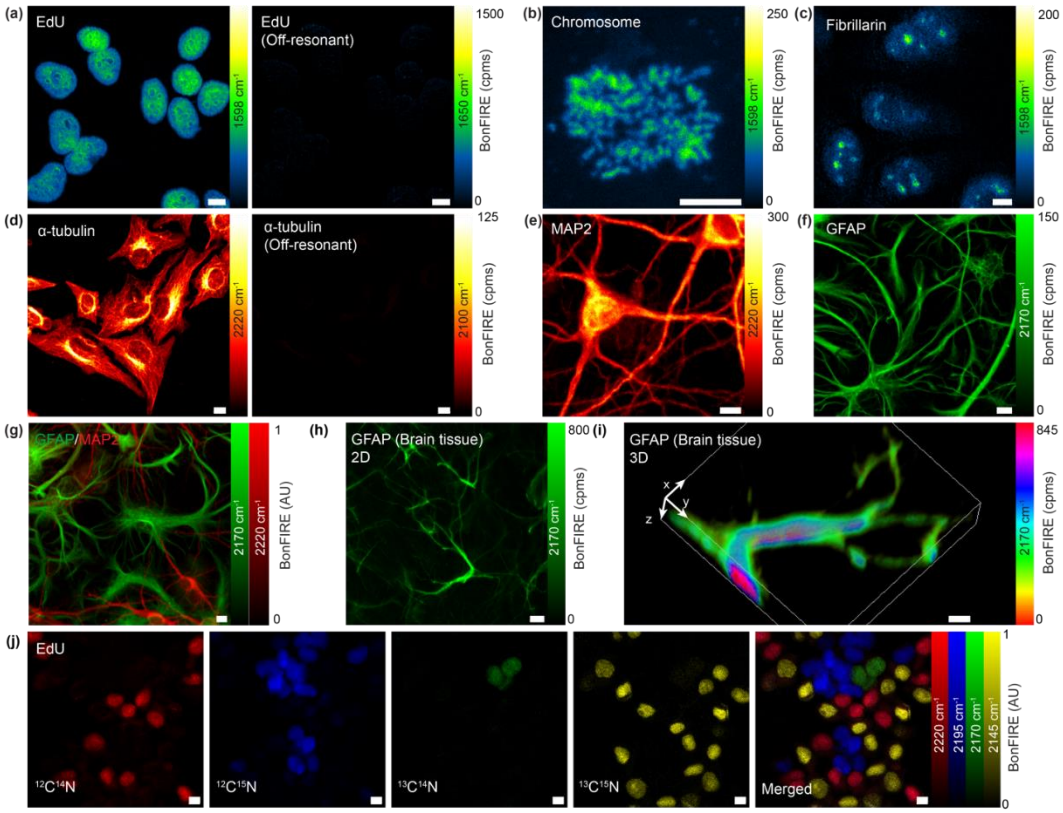

Fig. 5. Bond-selective bioimaging by BonFIRE microscopy. (a) On-resonance (left, 1598 cm^{-1}) and off-resonance (right, 1650 cm^{-1}) BonFIRE images of C=C vibration in ATTO680-click-labeled EdU in nuclei of HeLa cells. (b-c) BonFIRE images targeting C=C vibration in ATTO680-click-labeled EdU in extracted chromosomes (b) and ATTO680-immunolabeled-fibrillarin in nucleoli (c) from HeLa cells. (d) On-resonance (left, 2220 cm^{-1}) and off-resonance (right, 2100 cm^{-1}) BonFIRE images of C≡N vibrations in BF1-immunolabeled α-tubulin in HeLa cells. (e-f) BonFIRE images of $^{12}C{\equiv}^{14}N$ (2220 cm^{-1}, e) in BF1-immunolabeled MAP2 (marker for mature neurons) and $^{13}C{\equiv}^{14}N$ (2170 cm^{-1}, f) in BF1-isotopologue-immunolabeled GFAP (marker for astrocytes) in mouse neuronal co-cultures. (g) Two-colour BonFIRE imaging of $^{13}C{\equiv}^{14}N$ (green, 2170 cm^{-1}) and $^{12}C{\equiv}^{14}N$ (red, 2220 cm^{-1}) in BF1- and BF1-isotopologue-immunolabeled GFAP and MAP2 from the same set of neuronal co-culture. (h-i) 2D (h) and 3D rendering (i) BonFIRE images of BF1-$^{13}C{\equiv}^{14}N$-immunolabeled GFAP in a mouse brain tissue slice. (j) Four-colour BonFIRE images of $^{12}C{\equiv}^{14}N$ (red, 2220 cm^{-1}), $^{12}C{\equiv}^{15}N$ (blue, 2195 cm^{-1}), $^{13}C{\equiv}^{14}N$ (green, 2170 cm^{-1}), and $^{13}C{\equiv}^{15}N$ (yellow, 2145 cm^{-1}) BF1-isotopologue-click-labeled EdU in nuclei of HeLa cells. The merged image is shown to the right. Cpms: counts per millisecond. Scale bars: 10 μm.

spatial resolution with high S/Ns on fine subcellular structures. The elimination of two-frame subtraction allows BonFIRE to image live cells **(Fig. 6f)**. In **Fig. 6g**, the dividing process of Rh800-stained live HeLa cells was time-lapse imaged. The stained mitochondria migrate from peripherals and dividing junction to the whole cell body as the cell goes through telophase to cytokinesis. The background-free BonFIRE is imperative for obtaining spatial and kinetic information in live-cell imaging.

4.4 Discussion

In this work, we designed and developed BonFIRE spectro-microscopy, which realizes the IR-electronic double-resonance excitation with a pair of 2-ps narrowband mid-IR and near-IR pulses. BonFIRE has been demonstrated with high signal fidelity, subcellular spatial resolution, straightforward signal analysis with strict linear concentration dependence,

minimum photobleaching, accurate bond selectivity, and multiplexing with broad spectral coverage. Notably, BonFIRE achieved the first all-far-field single-molecule IR-vibrational imaging without plasmonic enhancements. These features of BonFIRE make it ideal for versatile spatially-resolved functional bio-analysis, including super-multiplexed imaging, live-cell time-lapse imaging, and micro-environment sensing, pushing the boundary of vibrational microscopy one step further to address real-world biological questions.

Admittedly, with the required fluorescence detection scheme, BonFIRE cannot detect nonfluorescent endogenous biomolecules compared to label-free vibrational techniques. However, with proper labelling strategies (e.g., isotope editing, click chemistry, immunolabelling, etc.), BonFIRE can enable multiplexed bioimaging for dilute biomolecules in live cells, which is challenging for label-free methods. With instrument upgrades (e.g., frequency-doubling), we envision that BonFIRE could be applicable to more bio-relevant investigations based on naturally-fluorescent endogenous biomolecules such as chlorophyll, FAD, NADH, as well as fluorescent proteins, such as GFP for genetically-encoded live-cell applications.

With multi-dimensional information, BonFIRE offers unique bioimaging opportunities beyond existing techniques. First, the narrowband and broadly tuneable mid-IR sources allow BonFIRE to investigate many specific bonds of interest for super-multiplexed imaging. In **Extended Data Fig. 9**, BonFIRE images of six vibrational modes of Rh800, ranging from 1100 cm^{-1} to 2860 cm^{-1}, were acquired, greatly exceeding the spectral coverage offered by SREF or FEIR. Second, beyond intensity-based measurement, BonFIRE lifetime imaging microscopy (BLIM) can achieve bond-specific vibrational sensing **(Fig. S13)**. In particular, we found the lifetime of conjugated C≡N is linearly dependent on the hydrogen-bonding abilities and electrostatic fields of solvents **(Fig. S13b)**, and can be used to differentiate the local environment in subcellular compartments **(Fig. S13c-f)**. Interestingly, we found that the BLIM of aromatic C-N (around 1300 cm^{-1} for Rh800) shows high solvatochromism sensitivity and could selectively differentiate the environment between the endoplasmic reticulum (ER) and other structures in the cytoplasm **(Fig. S13g-j)**. This is potentially due to the positive charge from the resonance structure of aromatic C-N, which renders it sensitive to mapping the various charged membrane structures. The vibrational lifetime of C=C, however, lacks environmentally sensitive features in subcellular reporting **(Fig. S13k-n)**. Compared to spectral linewidth or peak shift, the lifetime measured in BLIM is also more sensitive to environmental changes **(Fig. S14)**. Third, widefield BonFIRE has been proven promising in our preliminary data with single-molecule sensitivity **(Fig. S15)**, thanks to the large IR cross section. Such widefield capability is a key step toward localization-based super-resolution imaging and fast widefield mapping for dynamic biological activities (e.g., neuronal firing). These unique advantages in bioimaging distinguish BonFIRE from SREF and FEIR. We summarized the three techniques in **Table S5** for a more detailed comparison.

It is also worth mentioning that each laser module **(Fig. 1c, lasers 1-3)** in BonFIRE setup is commercially available with high stability that ensures day-to-day data reproducibility, which is essential for modern spectroscopic and biological investigations. The current laser system also features an easy conversion to perform state-of-the-art multi-modal vibrational bio-imaging. For example, the signal output from NIR-OPO and the Stokes output **(Fig. 1c, laser 1)** could allow SREF and stimulated Raman scattering (SRS)

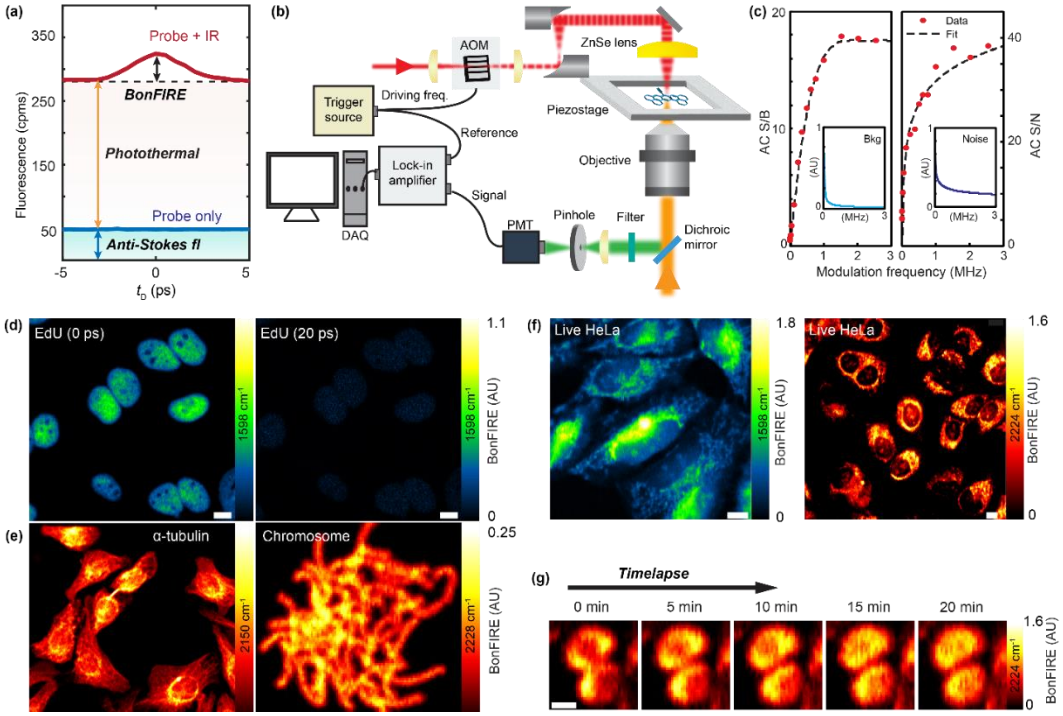

Fig. 6. Background-free BonFIRE microscopy. (a) Two major background sources in BonFIRE: anti-Stokes fluorescence (blue-shaded) and photothermal induced fluorescence (red-shaded). Signals shown are from the C≡N of 10 μM BF1 in PBS. cpms: counts per millisecond. (b) Experimental setup of background-free BonFIRE microscopy with fast modulation. AOM: acoustic optical modulator, PMT: photomultiplier tube, DAQ: data acquisition. (c) Dependence of BonFIRE AC S/B (left) and S/N (right) on the AOM modulation frequency. Reductions of background and noise as modulation frequency increases are shown in the insets. Data shown are extracted from a series of BonFIRE images of neuron cells (not shown). Signals are mean values from an area of 4.7×4.7 μm^2 (n = 400 pixels). Background and noise are from the mean and SD of the same area (n = 400 pixels) in fluorescence images at t_D = 10 ps. Data are fitted and connected by polynomial curves (order = 4). (d) 0-ps delay (left) and 20-ps delay (right) BonFIRE images of C=C in BF1-click-labeled-EdU in nuclei of HeLa cells. (e) BonFIRE imaging of BF1-^{13}C≡^{15}N-immunolabeled α-tubulin in HeLa cells (left, 2150 cm^{-1}) and BF2-click-labeled EdU of extracted chromosomes (right, 2228 cm^{-1}). (f) Background-free live-cell BonFIRE imaging of Rh800-stained HeLa cells in PBS. Left: IR at 1598 cm^{-1}; right: IR at 2224 cm^{-1}. (g) Representative time-lapse BonFIRE imaging (targeting C≡N at 2224 cm^{-1}) for dividing live HeLa cells stained with Rh800 in PBS. Scale bars: 10 μm.

imaging, which we have already achieved in preliminary tests. The upgradability of BonFIRE and smooth integration with other modalities would open new opportunities from fundamental nonlinear optics to biological analysis and beyond.

4.5 Methods

Experimental setup of BonFIRE

As shown in **Fig. 1c**, the BonFIRE system consists of two arms of laser outputs pumped by the primary source of a 2-ps 80 MHz mode-locked Yb fiber laser centered at 1031.2 nm (inside laser **1**). First, mid-IR sources are composed of an optical parametric oscillator (OPO) with IR outputs (Levante IR, APE GmbH, laser **2**) synchronously pumped by the 1031.2-nm laser, and a difference frequency generation (DFG) system (Harmonixx DFG, APE GmbH, laser **3**) fed by the signal and idler from the IR-OPO. The combined 2-ps tunable idler and

DFG outputs cover the range of 800-4800 cm^{-1} (2.1-12 μm) **(Extended Data Fig. 2)**. Second, a separate portion of the 1031.2-nm pump is frequency-doubled to 515.6 nm through a second harmonic generation (SHG) crystal before being used to pump a second OPO with a tunable (700-960 nm, 2 ps) near-IR probe output (PicoEmerald, APE GmbH, laser **1**) for upconverting excitation. The probe beam was guided to a spatial filter with a 70-μm pinhole (P75HK, Thorlabs) to obtain a Gaussian beam profile and then expanded by a pair of lenses by a factor of 4. The IR beam was expanded by a factor of 1.5 through a pair of off-axis parabolic mirrors (Thorlabs). IR and probe beams are then aligned to a customized stage-scan (P-545, PI) confocal microscope in a counter-propagating configuration, with a ZnSe lens (NA = 1) and a water-immersion near-IR-coated objective (25×, NA = 1.05), respectively, for optimal focusing and throughput of each beam. A delay stage (DL325, Newport) is added to the probe beam path for precise temporal overlapping of the two pulse trains. The backward fluorescence is collected by a single-photon-counting module (SPCM) with proper optical filter sets. All data acquisition, stage scanning, and laser tuning are controlled by a home-written LabVIEW program.

Fluorescence signals were separated and collected by a set of a long-pass dichroic mirror and filter through epi-detection and collected by a single-photon counting module (SPCM-AQRH-16, dark count 11 cps, Excelitas). The collected fluorescence was focused by a tube lens (150 mm) onto the 180-μm aperture of the SPCM, ensuring a loose confocal condition. The TTL counts from SPCM were recorded by a multifunctional data acquisition card (PCIe-6351, NI) in the counter mode and read by the customized LabVIEW program. SPCM readings were corrected according to the calibration curve provided by the manufacturer during post-processing. For ATTO680 C=C, the dichroic/filter set was FF738-FDi01/FF01-665/150 (Semrock). For BF1 C≡N, the dichroic/filter set was Di02-R830/FF01-775/140 (Semrock). For single-molecule imaging of BF1 C≡N, double filters (FF731/137 and FF709/167, Semrock) were used to minimize the background.

For background-free BonFIRE, IR modulation was enabled by two AOMs with coatings centered at 4500 nm (GEM-40-4-4500/4mm, Brimrose) for C≡N and 6282 nm (GEM-40-4-6282/4mm, Brimrose) for C=C. The IR was focused on the AOM aperture (4 mm) and collimated by a pair of CaF_2 (LA5255, Thorlabs) or ZnSe (LA7228-E2, Thorlabs) lenses. A 0-5V square wave trigger was generated by a function generator (DG2102, RIGOL) to trigger the AOM. The same trigger was routed to a lock-in amplifier (HF2LI, 50MHz bandwidth, Zurich) for signal demodulation. Fluorescence was detected by a PMT (PMT1002, Thorlabs) installed after a 400-μm confocal pinhole (P400K, Thorlabs). The DC signal from PMT and AC signal from the lock-in amplifier were recorded simultaneously and processed in the customized LabVIEW program.

For widefield BonFIRE microscopy in **Fig. S15**, the SPCM in was replaced by an sCMOS camera (ORCA-Fusion BT, Hamamatsu, with 2304×2304 pixels of 6.5 μm × 6.5 μm each). The same objective and a 200-mm focal length tube lens (AC254-200-B, Thorlabs) were used to achieve a 27.8× magnification, resulting in a 0.23-μm pixel size on the image plane on camera. A ZnSe lens (NA = 1, Edmund) was used to focus the IR beam to a spot of ~ 5 μm diameter to guarantee the maximal IR transition for the single-molecule sensitivity. The illumination area of the probe beam was enlarged to ~10 μm by adjusting the expansion telescope. The field of view (FOV) of BonFIRE was measured to be 5 μm **(Fig.**

S15a) from a Rh800-stained PVA thin film. Each widefield BonFIRE image is the difference between two consecutive fluorescence frames, one at t_D of 0 ps and the other at 20 ps, to remove the background. For single-FOV imaging demonstrated in **Fig. S15g**, 2-ms imaging speed per BonFIRE frame is achieved from the subtraction of the two consecutive fluorescence frames each with ~1 ms exposure. For scanning and stitching individual FOVs to form a large-area image **(Fig. S15h)**, we picked a smaller square FOV with size of 3 μm at the center, where the illumination is uniform. The step size of the piezo sample stage (P-545, PI) was set to match 3 μm during the scan. A customized LabVIEW code was used to synchronize image acquisition with the stage scan. The total time needed for capturing all frames used in **Fig. S15h (**87×87 μm^2, 29×29 FOVs) is 51 s, about 30 times faster than using the point-scan scheme with the same parameters (i.e., pixel size and dwell time). The total time needed for stitching large-area images was mostly dominated by the movement speed of the piezostage and the time needed for the data synchronization between the camera and PC (~ 60 ms per step instead of 2 ms). For biological samples where the single-molecule sensitivity is not necessary, the acquisition time can be further reduced by expanding IR and probe illumination with increased FOV.

For BLIM images, all data were collected based on the background-free BonFIRE setup using IR modulation implemented by a chopper (MC2000B, Thorlabs) at 10 kHz and lock-in demodulation, at multiple t_D steps with small spacings. The signal decay at each pixel is fitted with a single exponential function to extract the 1/e vibrational lifetime.

Modeling of the double-resonance in BonFIRE

Similar to physical modeling in SREF,[1] it is feasible to model the BonFIRE process with a three-level system with populations of N_1, N_2, and N_3 **(Fig. S2a)**. The transition rates between the three states can be written as q_{12} (IR-excitation rate), q_{23} (probe up-conversion rate), and v_{21} (vibrational relaxation rate). The rate equations can be written as follows:

$$\frac{dN_1}{dt} = q_{12}(N_2 - N_1) + v_{21}N_2 \quad (1)$$

$$\frac{dN_2}{dt} = q_{23}(N_3 - N_2) + q_{12}(N_1 - N_2) - v_{21}N_2 \quad (2)$$

$$\frac{dN_3}{dt} = q_{23}(N_2 - N_3) \quad (3)$$

Table S4 summarizes absorption coefficients and calculated F-C factors of six triple-bond bearing dyes. Considering the C≡N bond of BF1 with IR extinction coefficient of 70 M^{-1} cm^{-1} (2.7×10^{-19} cm^2 per molecule). With 100-mW IR power on the sample at 2224 cm^{-1} (4496 nm), there are about 2.8×10^{10} IR photons in one pulse (the laser repetition rate is 80 MHz). The diffraction-limited focal area of IR is $\lambda^2/4 \approx 5.1 \times 10^{-8}$ cm^2. The transition rate q_{12} for a single molecule could be estimated as:

$$q_{12} = \frac{2.8\times10^{10}\times2.7\times10^{-19}}{5.1\times10^{-8}\times2\times10^{-12}} s^{-1} = 7.4 \times 10^{10}\ s^{-1} \quad (4)$$

For the second up-conversion step, we use the extinction coefficient of 1.2×10^5 M^{-1} cm^{-1} at the absorption peak of BF1 as an estimation of the electronic cross section (4.6×10^{-16} cm^2) and use an F-C factor of 0.1.[2] We assume a probe (890 nm) power of 10 mW with 5.6×10^8 photons per pulse. The probe focal area can be estimated from the spatial resolution measurements, which is 3.6×10^{-9} cm^2. Therefore:

$$q_{23} = \frac{5.6\times10^{8}\times4.6\times10^{-16}\times0.1}{3.6\times10^{-9}\times2\times10^{-12}}\,s^{-1} = 3.6\times10^{12}\,s^{-1} \quad (5)$$

Finally, we assume the vibrational lifetime of C≡N to be 0.4 ps, which is estimated from the 13 cm^{-1} linewidth obtained by deconvoluting the Gaussian peak in **Fig. 3d** with 8 cm^{-1} laser bandwidth. Thus, $v_{21} = 2.5\times10^{12}\ s^{-1}$.

Similarly, for BF1 C=C bonds, we can obtain $q_{12} = (3.8\times10^{9}\times1.5\times10^{-17})/(9.8\times10^{-8}\times2\times10^{-12})\ s^{-1} = 3.0\times10^{11}\ s^{-1}$ for 10 mW IR power at 6257 nm (1598 cm^{-1}) and $q_{23} = (5.3\times10^{8}\times4.6\times10^{-16}\times0.1)/(3.6\times10^{-9}\times2\times10^{-12})\ s^{-1} = 3.4\times10^{12}\ s^{-1}$ for 10 mW probe power at 845 nm. We used a longer lifetime of 0.6 ps[2] and $v_{21} = 1.7\times10^{12}\ s^{-1}$ for C=C. Given all these values, we can numerically solve rate equations (1-3) and investigate the properties of BonFIRE signals.

First, changes in N_2 and N_3 are plotted over time in **Figs. S2b&e** for double and triple bonds, respectively. The vibrationally excited-state population of N_2 saturates within the 2-ps duration. The electronic excited-state population N_3, which is proportional to the emitted fluorescence, also starts to level off at the end of the 2-ps duration. The saturated N_3 can be found by arbitrarily extending the pulse duration to 10 ps, and the N_3 from 2-ps excitation is already 82% of the saturated value for C=C and 88% for C≡N. The transition efficiency of BonFIRE could be defined as N_3/N_1. As a result, transition efficiencies are 10.0% and 2.4% for C=C and C≡N, respectively, with 2-ps radiations. Compared to fs pulses, 2-ps pulses reach a balance between the high spectral resolution (~8 cm^{-1}) and sufficient transition efficiency. Note that by updating the used lifetimes of 0.6 ps and 0.4 ps with 1.8 ps and 0.9 ps (experimentally obtained from BLIM), transition rates can increase up to 14.8% and 3.8% for C=C and C≡N, respectively.

In **Figs. S2c-d** and **S2f-g,** N_3 is plotted as the function of transition rates q_{12} and q_{23}, respectively. A monotonic trend, which is linear at the beginning and saturates later, is observed in both curves. This trend successfully reproduces the experimental observations of probe power dependence. Regarding the IR excitation rate, the trend is quite linear within the experimental conditions, agreeing with the linear trend observed in BonFIRE experiments.

Linear unmixing post-processing

BonFIRE signal (S) can be expressed as a multiplication of the normalized cross sections matrix (M) and dye concentrations (C). Using the cross section matrix of C≡N BF1 isotopologues derived from **Fig. 3e**, unmixed images in **Fig 5g&j** were generated via matrix multiplication $C = M^{-1}S$ implemented using MATLAB.

Materials

Dyes. ATTO, Alexa, and cyanine dyes were purchased from ATTO-TEC GmbH, Thermo Fisher, and Lumiprobe. Nile blue and Rh800 were purchased from Sigma Aldrich. All dyes were aliquoted in DMSO as stock solutions (10 mM) upon receiving and stored at -20°C. Synthesis of customized BF dyes and their isotopologues was conducted using published procedures (**Table S3**).

Antibodies. Primary antibodies: Anti-α-tubulin in rabbit (ab18251, Abcam); Anti-GFAP in mouse (3670S, Cell Signaling Technology); Anti-MAP2 in rabbit (ab32454, Abcam). Secondary antibodies: Goat anti-mouse antibody (31160, Invitrogen); Goat anti-rabbit antibody (31210, Invitrogen).

UV-vis absorption, fluorescence emission, and FTIR

UV-vis spectra were obtained from dye solutions with concentrations of 1~10 μM in DMSO or PBS on a Varian Cary 500 Scan UV-Vis near-IR spectrophotometer (Agilent). Fluorescence emission spectra were recorded on an RF-6000 spectrofluorometer (Shimadzu) with dye concentrations of 1~10 μM in DMSO or PBS. FTIR spectroscopy was performed with a VERTEX 80v FTIR spectrometer (Bruker). FTIR were measured from either 10 mM DMSO solution or KBr.

Preparation of single-molecule samples

For the spin-coated samples, a dilute solution of dyes (5-20 pM) in 0.2% PVA was prepared freshly from the stock solution and then deposited on a fresh CaF_2 window by a spin coater (BSC-100, MicroNano Tools) at 5000 rpm for 30 s.[1, 3] For dye-antibody conjugates, the CaF_2 window was first coated with poly-l-lysine by incubating 200 μL of 0.01 mg/mL poly-l-lysine (Sigma) on the surface at room temperature for 1h. Then, the CaF_2 window was rinsed with DI water several times before being incubated with diluted (e.g., 1×10^6 diluted from the stock) dye-antibody solutions for 40 min. Finally, the sample was rinsed with DI water and dried under air at room temperature.[4] The concentrations of BF1-antibody stock solutions for $^{13}C{\equiv}^{14}N$, $^{12}C{\equiv}^{15}N$, and $^{12}C{\equiv}^{14}N$ are 0.93 mg/mL, 0.51 mg/mL, and 1.54 mg/mL with dye: protein ratios of 2.4, 1.7, and 2.6, respectively, confirmed with UV-vis absorption measurements. For the mixed single-molecule sample, the BF1-antibody stock solutions of $^{13}C{\equiv}^{14}N$, $^{12}C{\equiv}^{15}N$, and $^{12}C{\equiv}^{14}N$ were diluted by 0.5×10^6, 1×10^6, and 0.75×10^6 times in PBS and incubated on a poly-l-lysine coated CaF_2 window simultaneously for 30 min.

Preparation of biological samples

HeLa culture. Cultured HeLa-CCL2 (ATCC) cells were seeded onto 0.3-mm thick CaF_2 windows with a density of 1×10^5 cells/mL in 4-well plates with 0.3 mL DMEM culture medium at 37 °C and 5% CO_2. DMEM culture medium was made of 90% Dulbecco's modified Eagle medium (DMEM; 11965, Invitrogen), 10% fetal bovine serum (FBS; 10082, Invitrogen), and 1× penicillin/streptomycin (15140, Invitrogen). For the cells with EdU labelling, DMEM culture medium was then changed to DMEM medium (FBS-free, Gibco) for 20-22 h for cell cycle synchronization. After synchronization, the medium was replaced back to DMEM culture medium and EdU (10 mM stock in H_2O) was simultaneously added with a concentration of 100 μM for 20-24 h. Then 4% PFA was added for 20 min for fixation. After that, DPBS was used to wash away PFA and fixed cells could be stored in DPBS at 4 °C for several days.

Neuron culture. Primary rat hippocampal neurons were isolated from neonatal Sprague–Dawley rat (CD® (Sprague Dawley) IGS Rat, Charles River) pups with a protocol (IA22-1835) approved by Caltech's Institutional Animal Care and Use Committee (IACUC). The

brains were dissected from the skull and placed into a 10 cm petri dish with ice-chilled HBSS (Hanks' Balanced Salt Solution, Gibco). The hippocampus was isolated from the brains under a dissection scope, cut into small pieces (~0.5 mm), and incubated with 5 ml of Trypsin-EDTA (0.25%, Gibco) at 37 °C with 5% CO for 15 min. The Trypsin-EDTA liquid was aspirated and replaced with 2 ml of DMEM containing 10% FBS to stop the digestion. The tissue fragments were changed into 2 mL neuronal culture medium (Neurobasal A medium, B-27 supplement, GlutaMAX supplement, Thermos Fisher, and 1x penicillin-streptomycin) and were dispersed by repeated pipetting several times. The supernatant was collected and further diluted by neuronal culture medium to a final cell density of 9×10^4 cells/mL. A 0.7-ml volume of cell suspension was added to each well of a 24-well plate on the coated CaF_2 windows. For pre-coating, sterile CaF_2 windows were incubated with 100 μg/ml poly-D-lysine (Sigma) solution at 37 °C with 5% CO_2 for 24 h in a 24-well plate. The CaF_2 windows were washed twice with ddH2O and incubated with 10 μg/ml laminin mouse protein (Gibco) solution at 37 °C with 5% CO_2 overnight. Thereafter, the CaF_2 windows were washed twice with ddH_2O and allowed to dry at room temperature inside of biosafety cabinet. Half of the neuron culture medium was replaced with fresh medium every four days. At DIV14, 4% PFA was added for 20 min for fixation. DPBS was used to wash away PFA and fixed cells could be stored in DPBS at 4 °C for several days.

Click-reaction of EdU labelled samples. After permeabilization, the EdU labelled cells were incubated with reaction buffer prepared following the procedure specified in the Click reaction buffer kit (C10269, Thermo Fisher). For the four-colour BonFIRE imaging experiment, four cell suspensions were each clicked-labelled with the four C≡N isotopologues of BF1-azide. Then, a mixture of the clicked-cell suspensions was deposited onto a CaF_2 window.

Spread chromosome preparation. HeLa cells were seeded in a 35-cm dish and labelled with EdU. Cells were incubated with 1 μg/mL colcemid (KaryoMAX™ Colcemid™ Solution in PBS, Gibco) for 4 hours. Cells were trypsinized into single cells with Trypsin-EDTA (0.25%, Gibco). To stop the digestion, 5 mL DMEM containing 10% FBS was added. The cell suspensions were centrifuged at 120 x g for 5 min and the supernatant was aspirated with about 200 μL left in the tube. Clumps were removed by gently tapping the bottom of the tube. 5 mL of ice-cold 0.56% KCl solution was added to the cell suspensions gently. After putting it at room temperature for 10 min, the cell suspensions were centrifuged at 120 x g for 5 min and the supernatant was aspirated with about 200 μl left in the tube. 5 ml of methanol: glacial acetic acid (3:1) fixative solution was added to the cell suspensions gently and slowly. The cell suspensions were centrifuged at 120 x g for 5 min and the cells were resuspended with PBS, after aspirating the supernatant. The cells were then clicked-labelled using the procedure described above. The clicked chromosomes were deposited onto a CaF_2 window and were dried for BonFIRE imaging.

Rh800-stained HeLa cell. Live HeLa cells seeded on 0.3-mm thick CaF_2 windows were incubated in DMEM with 0.5-2 μM Rh800 for 30 min at 37 °C. After incubation, DMEM was replaced with PBS containing 1 μM Rh800 and was transferred to the sample holder.

The CaF_2 window was then sealed using another CaF_2 window with a 12-μm-thick spacer before imaging. For BLIM, fixed HeLa cells were incubated in 10 μM Rh800 (PBS) for 15 min at room temperature and sealed with a 56-μm-thick spacer.

Secondary antibody-dye conjugation. The secondary antibody was diluted to 2 mg/mL using 0.1 M $NaHCO_3$. To reach a final pH of ~8.3, one-tenth volume of 1 M $NaHCO_3$ was added to the diluted antibody solution. To start the conjugation reaction, 3 mM of N-hydroxysuccinimide ester-activated BF1 dye was added at a dye-to-protein ratio of ~30:1. The reaction was incubated in the dark for 1.5 h under slow stirring. Gel permeation chromatography was used to remove the excess dye from the conjugated protein. The Sephadex G-25 was first swelled at 90 °C for 1 h and was used to pack a 1 cm diameter column with >12 cm length. After the reaction, the solution was loaded onto the column and the first eluted dye band was collected. The collected proteins were then concentrated using Amicon ultra-centrifugal filters (UFC501096, EMD, Millipore, 14000 x g for concentrating and 1000 x g for recovering) to a final concentration of 1–2 mg/mL in PBS.

Immuno-staining of fixed HeLa/neurons/brain tissue. Fixed cells were first permeabilized using 0.1% Triton X-100 (T8787, Sigma) for 20 min. After blocking for 1-3 h in 10% goat serum/1% BSA/0.3 M glycine/0.1% PBST, the cells were incubated overnight at 4 °C in 10 μg/mL primary antibody in 3% BSA. After washing with PBS, the cells were blocked using 10% goat serum in 0.1% PBST for 1-3 h, followed by overnight incubation at 4 °C in ~10 μg/mL secondary antibody in 10% goat serum. The cells were blocked with 10% goat serum for 30 min and dried before imaging.

4.6 Acknowledgements

We thank Caltech Beckman Institute Laser Resource Center (BILRC) and Office of Laboratory Animal Resources (OLAR) for research resources. We thank Prof. Mitchio Okumura and Prof. Scott Cushing for kindly sharing research resources. We thank Dr. Xuecheng Tao and Dr. Tomislav Begusic for calculating the Frank-Condon factors and Adrian Colazo for helpful discussions. This work is supported by NIH Director's New Innovator Award, DP2 GM140919-01 for L.W. and the Alfred P. Sloan Research Fellowship for L. W. L.W. is a Heritage Principal Investigator supported by the Heritage Medical Research Institute at Caltech.

4.7 Extended data

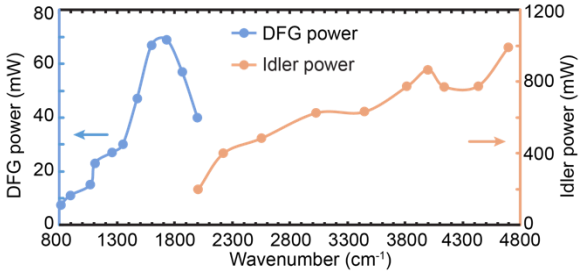

Extended Data Figure 1. Power outputs of the Idler and the DFG IR lasers. The power was measured at the laser outputs using a thermopile power meter (919P-003-10, Newport). All wavenumbers within 800 and 4800 cm^{-1} (2.1~12 μm) are covered. The pulse width is 2 ps with a bandwidth of 8-10 cm^{-1} according to the manufacturer (APE Angewandte Physik & Elektronik GmbH, Berlin, Germany).

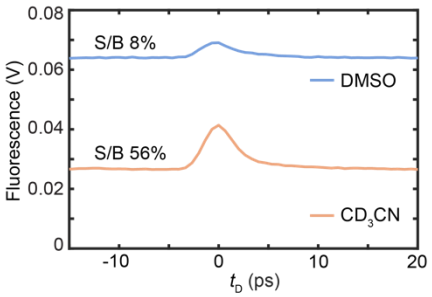

Extended Data Figure 2. Reduced photothermal background in acetonitrile-d_3. The fluorescence vs. IR-probe delay (t_D) of ATTO680 in DMSO (blue) and acetonitrile-d_3 (orange) obtained using 1598 cm^{-1} IR frequency and 765-nm probe wavelength. While the signal-to-background (S/B) ratio is about 8% in DMSO, it increases to 56% in acetonitrile-d_3.

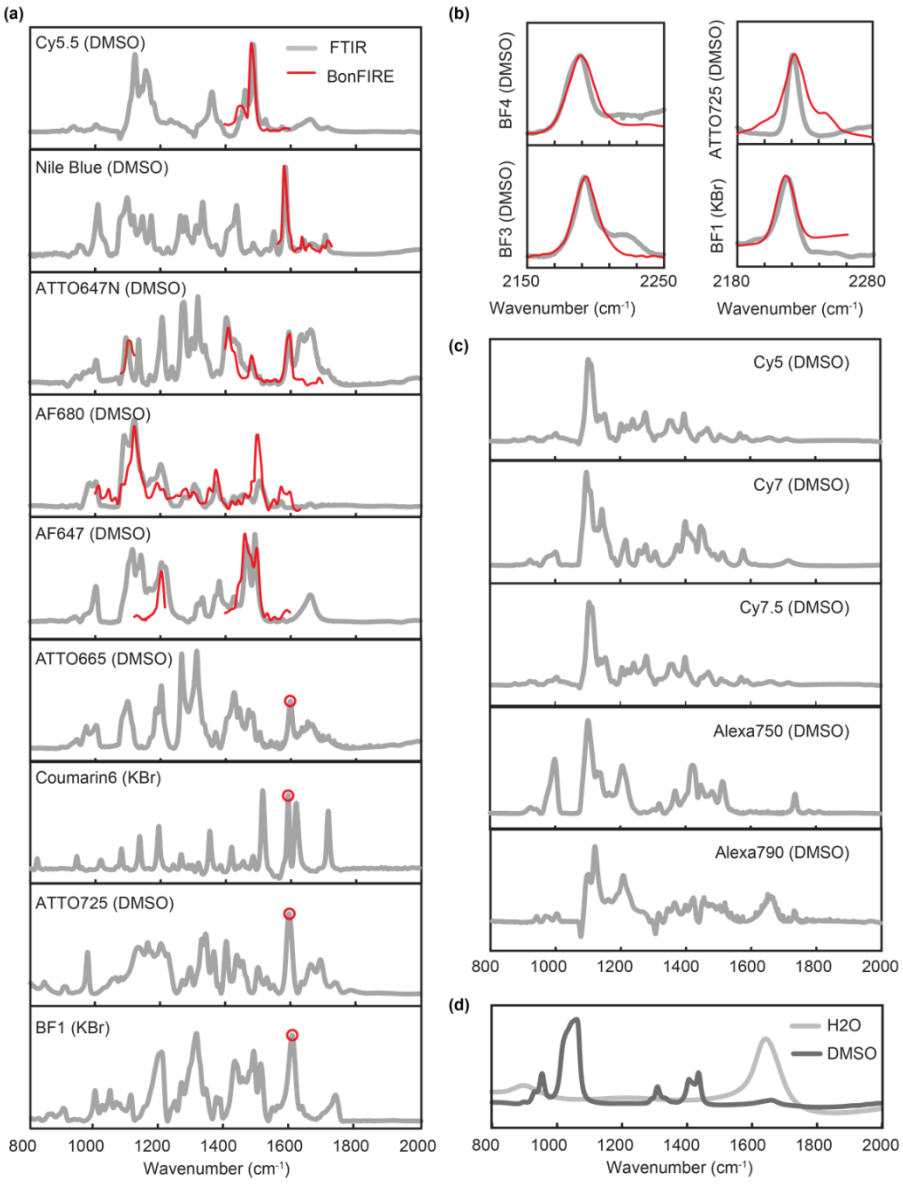

Extended Data Figure 3. Correlation between BonFIRE and FTIR spectra. (a) FTIR (grey) and BonFIRE (red) spectra obtained for dyes in the fingerprint region. The dye and the experimental conditions (either in 10 mM DMSO solutions or in KBr solids) for obtaining FTIR spectrum are indicated in each spectrum. The BonFIRE spectra (red curves) and single-point BonFIRE measurements (red circles, BonFIRE vs. IR-probe delay obtained for the single wavenumber) were scaled and overplotted on top of the FTIR reference for better comparison. (b) FTIR and BonFIRE spectra of four dyes in the cell-silent region. (c) FTIR spectra of other dyes expected to be measured in BonFIRE (for grey dots in **Fig. 1b**). The FTIR spectra in (a) & (c) measured in DMSO are often complicated by the IR absorption of DMSO and water (DMSO is hygroscopic), whose spectra were plotted in (d) for reference. The spectra of ATTO680 and Rh800 are not shown here as they are shown in **Fig. 2f** and **Extended Data Fig. 9**.

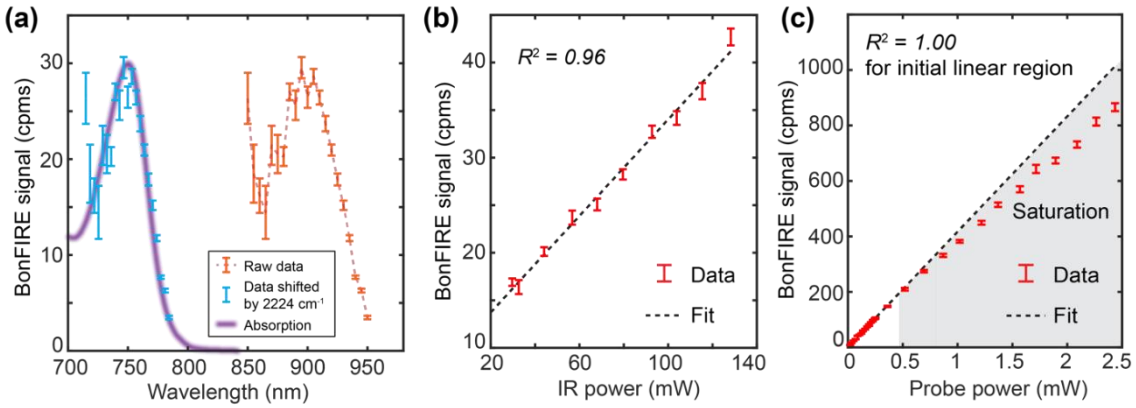

Extended Data Figure 4. Characterization of cell-silent BonFIRE. (a) BonFIRE signal dependence on the probe wavelength (orange). The BonFIRE excitation profile (blue, by horizontally shifting the raw data by adding the IR frequency of 2224 cm^{-1}) is overplotted with the absorption spectrum of BF1 (purple). Data are presented as peak values +/- SD from the background (n = 14). (b-c) BonFIRE signal dependence on the IR power (b) and the probe power (c) on sample, measured from 10 μM BF1 in PBS. The probe power dependence shows good linearity (R^2 = 1.00) at low power levels but quickly saturates. Data are presented as peak values +/- SD from the background (n = 17).

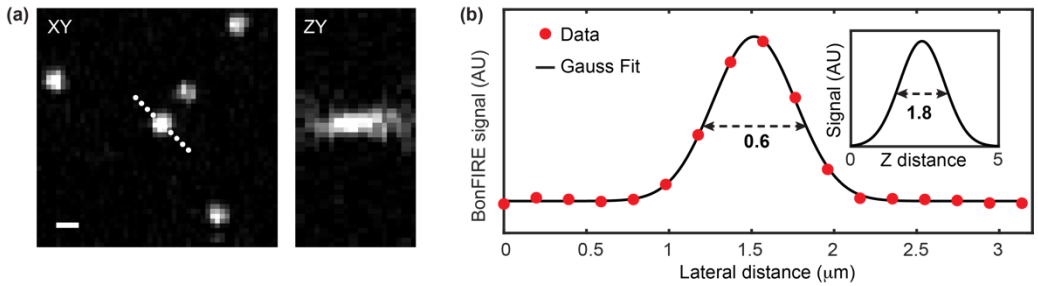

Extended Data Figure 5. Spatial resolution of BonFIRE microscopy. (a) BonFIRE images of 100-nm fluorescent beads (Invitrogen™ FluoSpheres™ carboxylate-modified microspheres, 0.1 μm, 715/755 nm, Fisher Scientific) embedded in PVA film on a CaF_2 substrate. The image was obtained with 1592 cm^{-1} IR (~24 mW on sample) and 815 nm probe (~180 μW on sample). Scale bar is 1 μm. (b) A sectional profile obtained from XY plane from a location indicated by the white dashed line in (a), a lateral resolution (FWHM) of 0.6 μm is obtained from Gaussian fitting. The Z-resolution of 1.8 μm is determined by fitting the sectional profile from the ZY plane (shown as inset).

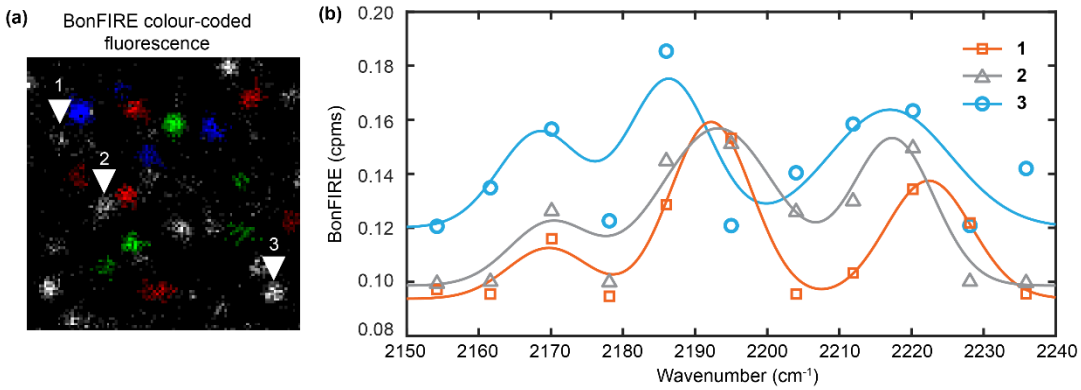

Extended Data Figure 6. Observation of multiple single-molecule isotopologues within the same diffraction-limited spot. (a) Colour-coded fluorescence imaging for a mixture of single-molecule BF1 isotopologues as shown in **Fig. 4i**. Red: BF1-^{13}C≡^{14}N (2170 cm^{-1}); green: BF1-^{12}C≡^{15}N (2195 cm^{-1}); and blue: BF1-^{12}C≡^{14}N (2220 cm^{-1}). (b) *In-situ* BonFIRE spectra obtained from three spots indicated by the corresponding numbered arrowheads in (a). Gaussian fittings (and a linear background) are shown as solid curves. Spectra of spots 1 (orange), 2 (grey), and 3 (blue) contain all three vibrational peaks. Slight variations in peak positions are possibly due to local interactions.[5] These results demonstrate that BonFIRE can resolve multiple vibrational colours within the same diffraction-limited spot at the single-molecule level.

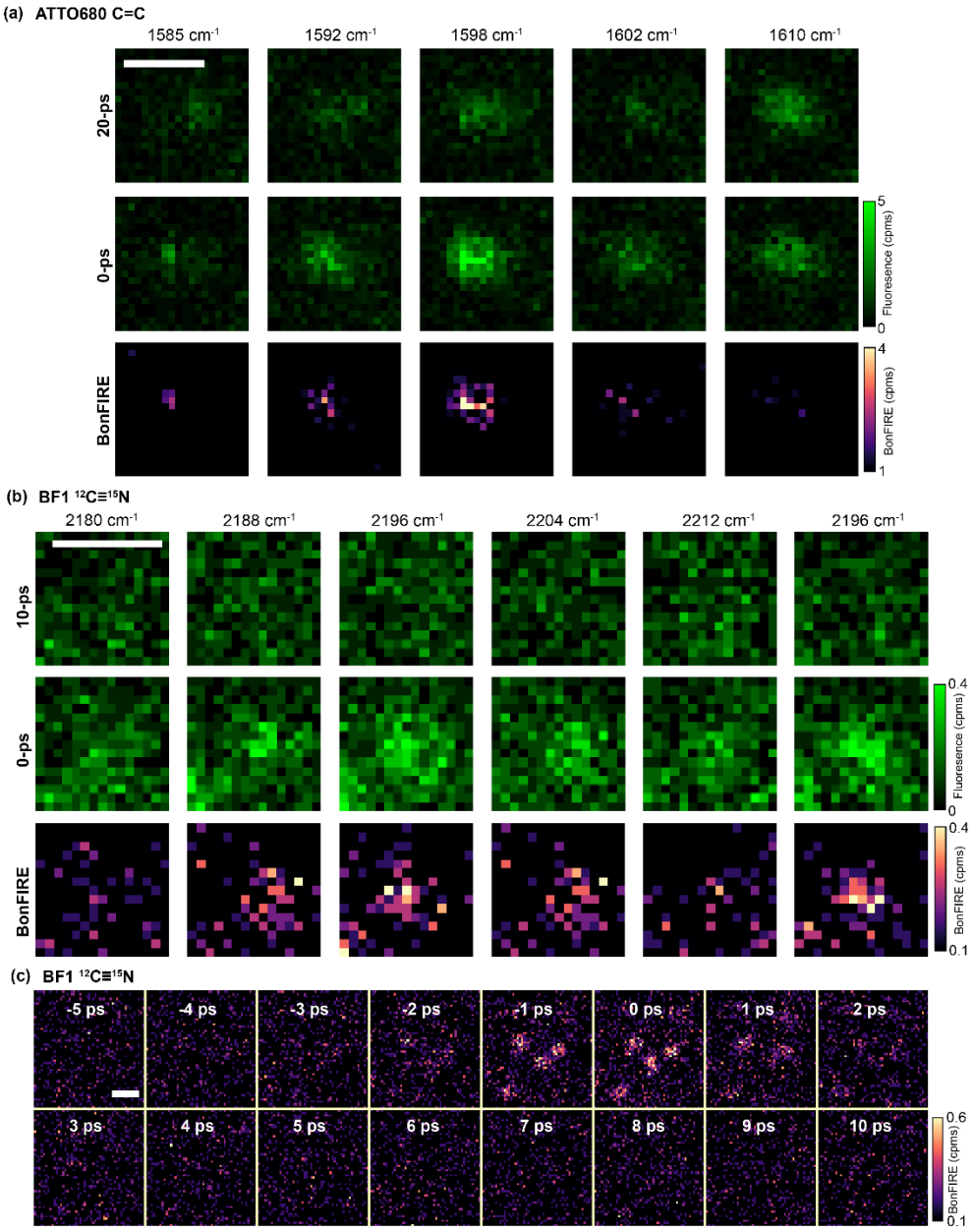

Extended Data Figure 7. Evidence for robust single-molecule sensitivity of BonFIRE. (a) Raw data of single-molecule BonFIRE imaging of ATTO680 C=C in **Fig. 4a**, confirming that BonFIRE data from subtraction are not from single-molecule bleaching or blinking. The S/Bs in (a) reach >100% because of the much-reduced photothermal background of the dilute single-molecule sample and the IR-transparent PVA matrix. (b) Raw data of single-molecule BonFIRE imaging of $^{12}C \equiv {}^{15}N$ labelled BF1, the same sample was used in **Fig. 4e-g**. Repeatable BonFIRE contrast and no photobleaching are confirmed by the continuous scan. (c) Signal vs. IR-probe delay (t_D) of a small region containing multiple single BF1 molecules. The signal on/off as the function of t_D is another evidence of the BonFIRE's single-molecule sensitivity. Scale bars: 1 μm.

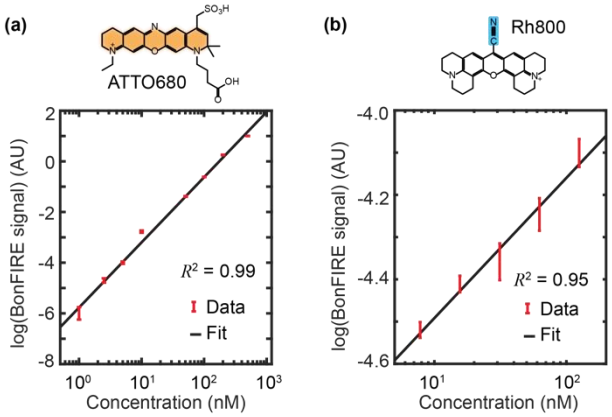

Extended Data Figure 8. BonFIRE concentration curves with PMT AC detection. (a) The concentration curve of C=C in ATTO680 in DMSO. The lowest concentration measured is 1 nM. The probe wavelength is 765 nm, and the IR frequency is 1592 cm^{-1}. Data are presented as peak values +/- SD from the background (n = 9). (b) Concentration curve of C≡N in Rh800 in DMSO. The lowest concentration measured is 8 nM. The probe wavelength is 830 nm, and the IR frequency is 2228 cm^{-1}. Both minimum concentrations are close to or below the calculated single-molecule threshold of 5 nM. Data are presented as peak values +/- SD from the background (n = 22).

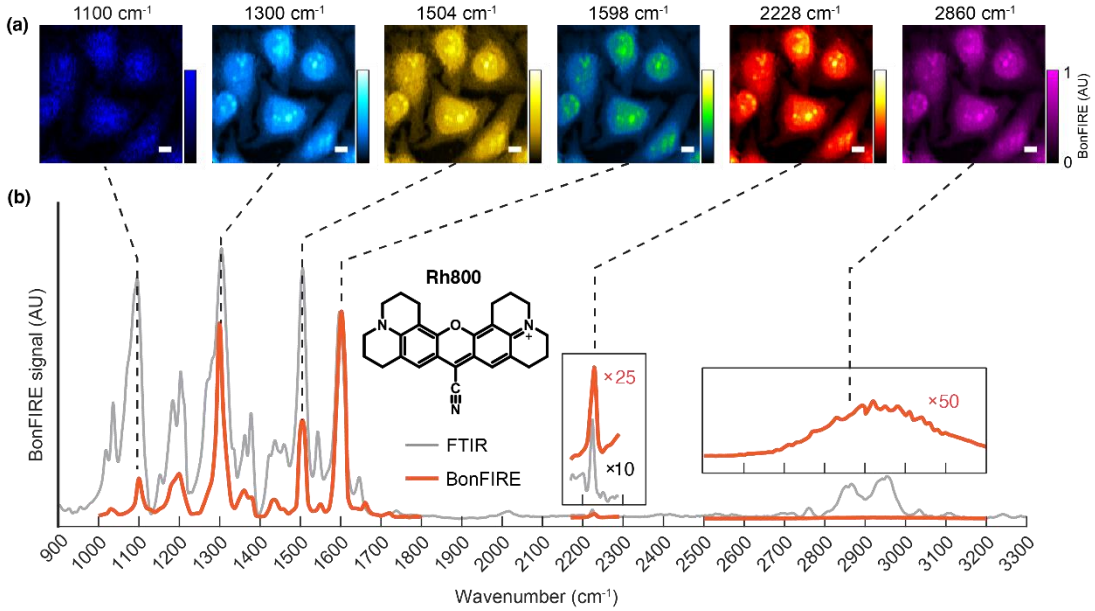

Extended Data Figure 9. Broad spectral coverage of BonFIRE microscopy. (a) BonFIRE images of Rh800-stained HeLa cells targeting six different vibrational modes. Vibrations of phenolic C-O (1100 cm^{-1}), aromatic C-N (1300 cm^{-1}), conjugated C=C (1504 cm^{-1} and 1598 cm^{-1}), conjugated C≡N (2228 cm^{-1}), and C-H stretch (2860 cm^{-1}) can all serve for BonFIRE imaging. Scale bars: 10 μm. (b) BonFIRE spectrum (red) and FTIR spectrum (grey) of Rh800. BonFIRE spectrum is normalized to the most intense peak at 1598 cm^{-1}. The C≡N peak around 2228 cm^{-1} and a weak broad peak of the C-H region (2700 cm^{-1}-3200 cm^{-1}) are enlarged in insets for better comparison.

4.8 References

1 Dean, K. M. & Palmer, A. E. Advances in fluorescence labeling strategies for dynamic cellular imaging. *Nature Chemical Biology* **10**, 512-523 (2014).

2 Möckl, L. & Moerner, W. E. Super-resolution Microscopy with Single Molecules in Biology and Beyond–Essentials, Current Trends, and Future Challenges. *Journal of the American Chemical Society* **142**, 17828-17844 (2020). https://doi.org:10.1021/jacs.0c08178

3 Wu, J., Ji, N. & Tsia, K. K. Speed scaling in multiphoton fluorescence microscopy. *Nature Photonics* **15**, 800-812 (2021). https://doi.org:10.1038/s41566-021-00881-0

4 Cheng, J.-X. & Xie, X. S. Vibrational spectroscopic imaging of living systems: An emerging platform for biology and medicine. *Science* **350**, aaa8870 (2015). https://doi.org:10.1126/science.aaa8870

5 Wei, L. *et al.* Super-multiplex vibrational imaging. *Nature* **544**, 465-470 (2017). https://doi.org:10.1038/nature22051

6 Bhargava, R. Infrared Spectroscopic Imaging: The Next Generation. *Applied Spectroscopy* **66**, 1091-1120 (2012). https://doi.org:10.1366/12-06801

7 Ma, J., Pazos, I. M., Zhang, W., Culik, R. M. & Gai, F. Site-Specific Infrared Probes of Proteins. *Annual Review of Physical Chemistry* **66**, 357-377 (2015). https://doi.org:10.1146/annurev-physchem-040214-121802

8 Ostrander, J. S., Serrano, A. L., Ghosh, A. & Zanni, M. T. Spatially Resolved Two-Dimensional Infrared Spectroscopy via Wide-Field Microscopy. *ACS Photonics* **3**, 1315-1323 (2016). https://doi.org:10.1021/acsphotonics.6b00297

9 Shi, L. *et al.* Mid-infrared metabolic imaging with vibrational probes. *Nature Methods* **17**, 844-851 (2020). https://doi.org:10.1038/s41592-020-0883-z

10 Dazzi, A. & Prater, C. B. AFM-IR: Technology and Applications in Nanoscale Infrared Spectroscopy and Chemical Imaging. *Chemical Reviews* **117**, 5146-5173 (2017). https://doi.org:10.1021/acs.chemrev.6b00448

11 Pleitez, M. A. *et al.* Label-free metabolic imaging by mid-infrared optoacoustic microscopy in living cells. *Nature Biotechnology* **38**, 293-296 (2020). https://doi.org:10.1038/s41587-019-0359-9

12 Bai, Y., Yin, J. & Cheng, J.-X. Bond-selective imaging by optically sensing the mid-infrared photothermal effect. *Science Advances* **7**, eabg1559 (2021). https://doi.org:10.1126/sciadv.abg1559

13 Zhang, D. *et al.* Depth-resolved mid-infrared photothermal imaging of living cells and organisms with submicrometer spatial resolution. *Science Advances* **2**, e1600521 (2016). https://doi.org:10.1126/sciadv.1600521

14 Li, Z., Aleshire, K., Kuno, M. & Hartland, G. V. Super-Resolution Far-Field Infrared Imaging by Photothermal Heterodyne Imaging. *The Journal of Physical Chemistry B* **121**, 8838-8846 (2017). https://doi.org:10.1021/acs.jpcb.7b06065

15 Lim, J. M. *et al.* Cytoplasmic Protein Imaging with Mid-Infrared Photothermal Microscopy: Cellular Dynamics of Live Neurons and Oligodendrocytes. *The Journal of Physical Chemistry Letters* **10**, 2857-2861 (2019). https://doi.org:10.1021/acs.jpclett.9b00616

16 Schnell, M. *et al.* All-digital histopathology by infrared-optical hybrid microscopy. *Proceedings of the National Academy of Sciences* **117**, 3388-3396 (2020). https://doi.org:10.1073/pnas.1912400117

17 Shi, J. *et al.* High-resolution, high-contrast mid-infrared imaging of fresh biological samples with ultraviolet-localized photoacoustic microscopy. *Nature Photonics* **13**, 609-615 (2019). https://doi.org:10.1038/s41566-019-0441-3

18 Ruggeri, F. S., Mannini, B., Schmid, R., Vendruscolo, M. & Knowles, T. P. J. Single molecule secondary structure determination of proteins through infrared absorption nanospectroscopy. *Nature Communications* **11**, 2945 (2020). https://doi.org:10.1038/s41467-020-16728-1

19 Laubereau, A., Seilmeier, A. & Kaiser, W. A new technique to measure ultrashort vibrational relaxation times in liquid systems. *Chemical Physics Letters* **36**, 232-237 (1975). https://doi.org:10.1016/0009-2614(75)87023-0

20 Kryukov, P. G., Letokhov, V. S., Matveets, Y. A., Nikogosyan, D. N. & Sharkov, A. V. Selective two-stage excitation of an electronic state of organic molecules in aqueous solution by picosecond light pulse. *Soviet Journal of Quantum Electronics* **8**, 1405-1407 (1978). https://doi.org:10.1070/qe1978v008n11abeh011337

21 Sakai, M., Kawashima, Y., Takeda, A., Ohmori, T. & Fujii, M. Far-field infrared super-resolution microscopy using picosecond time-resolved transient fluorescence detected IR spectroscopy. *Chemical Physics Letters* **439**, 171-176 (2007). https://doi.org:10.1016/j.cplett.2007.03.035

22 Whaley-Mayda, L., Guha, A., Penwell, S. B. & Tokmakoff, A. Fluorescence-Encoded Infrared Vibrational Spectroscopy with Single-Molecule Sensitivity. *Journal of the American Chemical Society* **143**, 3060-3064 (2021). https://doi.org:10.1021/jacs.1c00542

23 Whaley-Mayda, L., Guha, A. & Tokmakoff, A. Resonance conditions, detection quality, and single-molecule sensitivity in fluorescence-encoded infrared vibrational spectroscopy. *The Journal of Chemical Physics* **156**, 174202 (2022). https://doi.org:10.1063/5.0088435

24 Hopt, A. & Neher, E. Highly Nonlinear Photodamage in Two-Photon Fluorescence Microscopy. *Biophysical Journal* **80**, 2029-2036 (2001). https://doi.org:https://doi.org/10.1016/S0006-3495(01)76173-5

25 Talone, B. *et al.* Phototoxicity induced in living HeLa cells by focused femtosecond laser pulses: a data-driven approach. *Biomed. Opt. Express* **12**, 7886-7905 (2021). https://doi.org:10.1364/BOE.441225

26 Xiong, H. *et al.* Stimulated Raman excited fluorescence spectroscopy and imaging. *Nature Photonics* **13**, 412-417 (2019). https://doi.org:10.1038/s41566-019-0396-4

27 Xiong, H., Qian, N., Miao, Y., Zhao, Z. & Min, W. Stimulated Raman Excited Fluorescence Spectroscopy of Visible Dyes. *The Journal of Physical Chemistry Letters* **10**, 3563-3570 (2019). https://doi.org:10.1021/acs.jpclett.9b01289

28 Kurochkin, D. V., Naraharisetty, S. R. G. & Rubtsov, I. V. A relaxation-assisted 2D IR spectroscopy method. *Proceedings of the National Academy of Sciences* **104**, 14209-14214 (2007). https://doi.org:10.1073/pnas.0700560104

29 Zhang, Y. *et al.* Fluorescence-Detected Mid-Infrared Photothermal Microscopy. *Journal of the American Chemical Society* **143**, 11490-11499 (2021). https://doi.org:10.1021/jacs.1c03642

30 Li, M. *et al.* Fluorescence-Detected Mid-Infrared Photothermal Microscopy. *Journal of the American Chemical Society* **143**, 10809-10815 (2021). https://doi.org:10.1021/jacs.1c03269

31 Watanabe, H., Hayazawa, N., Inouye, Y. & Kawata, S. DFT Vibrational Calculations of Rhodamine 6G Adsorbed on Silver: Analysis of Tip-Enhanced Raman Spectroscopy. *The Journal of Physical Chemistry B* **109**, 5012-5020 (2005). https://doi.org:10.1021/jp045771u

32 Hübner, H. J., Wörner, M., Kaiser, W. & Seilmeier, A. Subpicosecond vibrational relaxation of skeletal modes in polyatomic molecules. *Chemical Physics Letters* **182**, 315-320 (1991). https://doi.org:10.1016/0009-2614(91)80221-I

33 Du, J., Wang, H. & Wei, L. Bringing Vibrational Imaging to Chemical Biology with Molecular Probes. *ACS Chemical Biology* **17**, 1621-1637 (2022). https://doi.org:10.1021/acschembio.2c00200

34 Levinson, N. M. & Boxer, S. G. A conserved water-mediated hydrogen bond network defines bosutinib's kinase selectivity. *Nature Chemical Biology* **10**, 127-132 (2014). https://doi.org:10.1038/nchembio.1404

35 Suydam, I. T., Snow, C. D., Pande, V. S. & Boxer, S. G. Electric Fields at the Active Site of an Enzyme: Direct Comparison of Experiment with Theory. *Science* **313**, 200-204 (2006). https://doi.org:10.1126/science.1127159

36 Seilmeier, A., Kaiser, W. & Laubereau, A. Vibrational combination states of polyatomic molecules investigated by ultrashort two-pulse spectroscopy. *Optics Communications* **26**, 441-445 (1978). https://doi.org:10.1016/0030-4018(78)90242-0

37 Maier, J. P., Seilmeier, A. & Kaiser, W. Population lifetime of CH-stretching modes in medium-size molecules. *Chemical Physics Letters* **70**, 591-596 (1980). https://doi.org:10.1016/0009-2614(80)80132-1

38 Clark, J. L., Miller, P. F. & Rumbles, G. Red Edge Photophysics of Ethanolic Rhodamine 101 and the Observation of Laser Cooling in the Condensed Phase. *The Journal of Physical Chemistry A* **102**, 4428-4437 (1998). https://doi.org:10.1021/jp980589c

4.9 Supplementary information

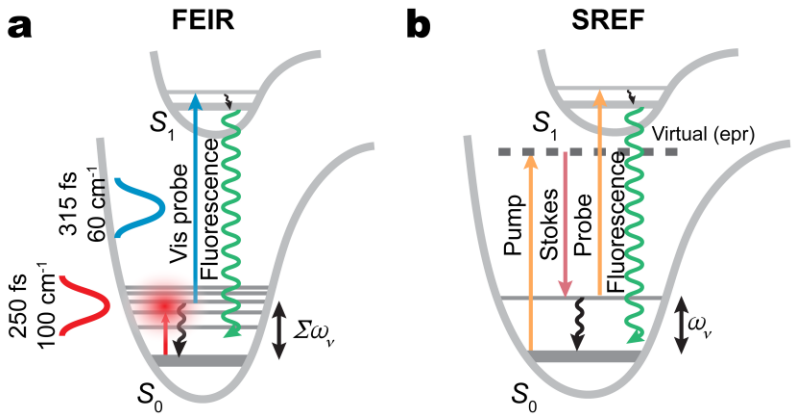

Fig. S1. Energy diagrams of fluorescence-encoded infrared (FEIR, a) and stimulated Raman excited fluorescence (SREF, b). Adapted from refs.[1,2], respectively.

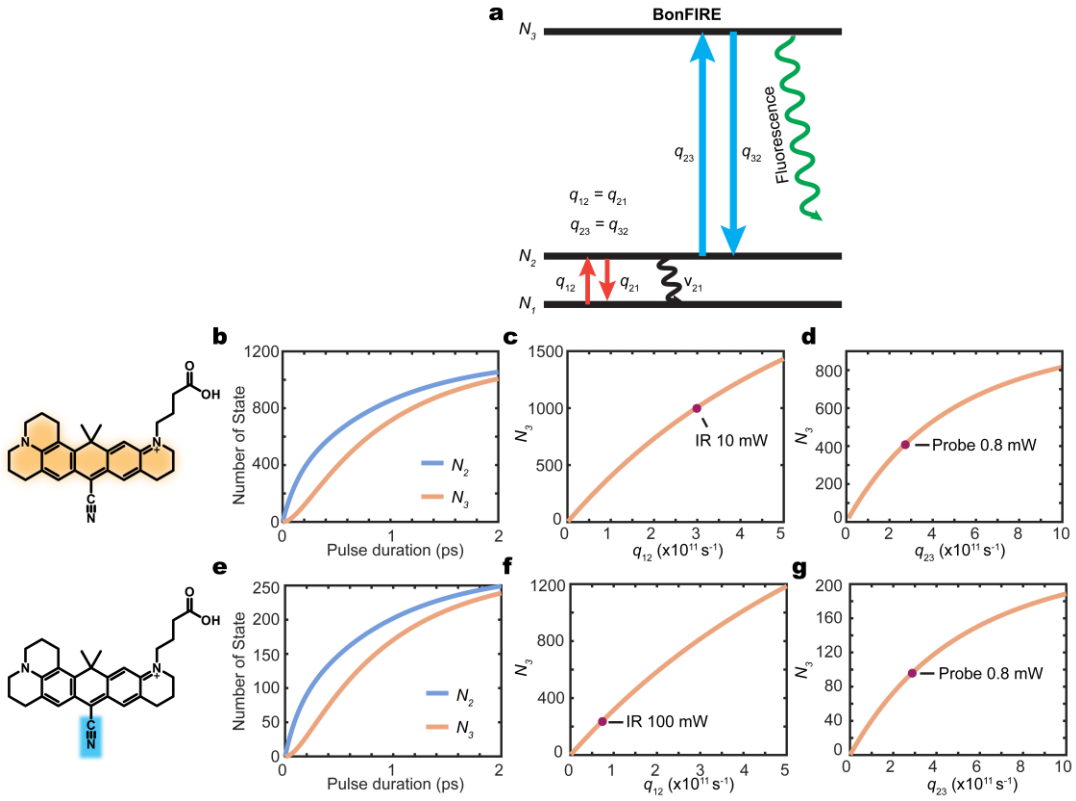

Fig. S2. Simulation of BonFIRE process with a three-level system. a, The energy diagram for the three-level system simulation. Two scenarios – one with C=C excitation (orange-shade highlighted in the second row, **b**-**d**) and the other with C≡N excitation (blue-shade highlighted in the third row, **e**-**g**) in BF1 dye molecule – were numerically simulated. In the simulation, the initial ground-state population (N_1) is set to 10000, and the number of steps of the population evolution is set to 50000, corresponding to 4×10^{-5} ps per step. **b**,**e**, Population changes in N_2 and N_3 during 2-ps pulse duration. **c**,**d**, Electronic excited-state population (N_3) as functions of infrared transition rate of q_{12}. **d**,**g**, N_3 vs. probe transition rate of q_{23}. Fixing all other parameters (pulse duration, wavelength, Franck-Condon constant, etc.), q_{12} and q_{23} are pure functions of infrared and probe powers. infrared powers used for simulation in **b**,**e**, and probe powers reaching the saturation level are indicated by red dots. For the formulae of the simulation, please see the "Modeling of the double-resonance in BonFIRE" in **Methods**.

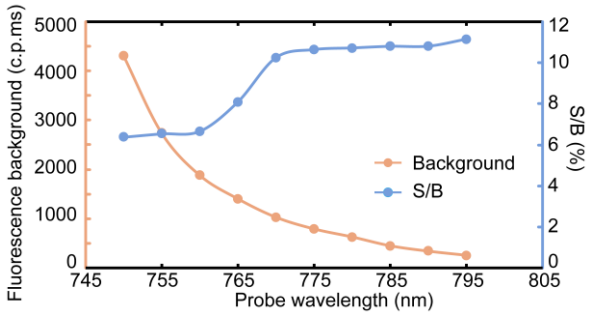

Fig. S3. Dependence of the BonFIRE background and signal-to-background ratios (S/B) on the probe wavelength. The BonFIRE background increases as the combined excitation frequency of the probe and the infrared (at 1598 cm^{-1}) gets closer to the absorption peak (681 nm), leading to a drop in S/B at the probe wavelength lower than 775 nm. To strike a balance between the signal intensity, signal-to-noise ratio (SNR), and S/B, we choose 765 nm for BonFIRE spectroscopy. The sample is 1 μM ATTO680 in DMSO. The on-sample powers are 350 μW of the probe and 40 mW of the infrared (1598 cm^{-1}). SPCM readings (c.p.ms, counts per millisecond) are corrected based on the calibration curve provided by the manufacturer (Excelitas).

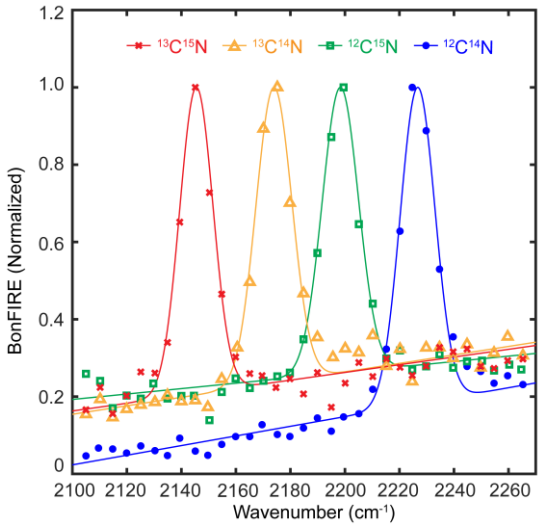

Fig. S4. Raw data and fittings in Fig. 3e. The fittings were performed with a Gaussian function and a linear background for each colour-coded spectrum.

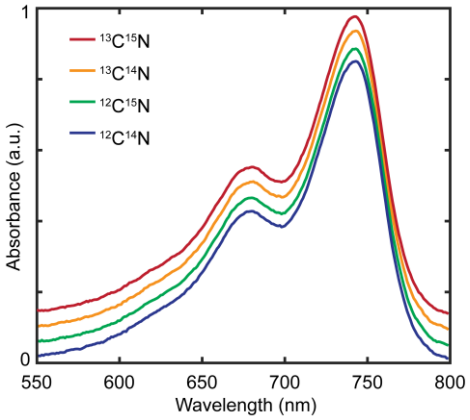

Fig. S5. UV-vis spectra of four BF1 isotopologues. Four absorption spectra and peaks (758 nm) of BF1 dyes with $^{13}C{\equiv}^{15}N$, $^{13}C{=}^{14}N$, $^{12}C{\equiv}^{15}N$, and $^{12}C{\equiv}^{14}N$ are almost identical in 10 μM DMSO solutions. Absorption profiles are vertically shifted for better comparison. a.u., arbitrary unit.

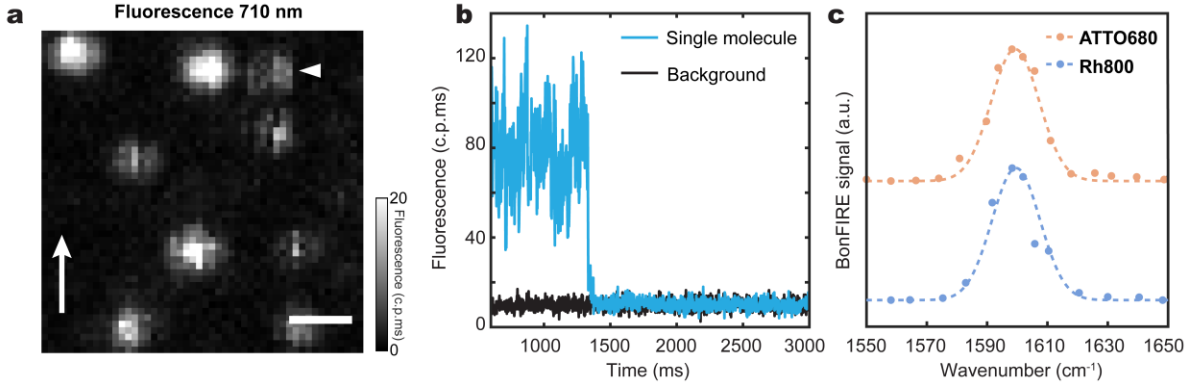

Fig. S6. The single-molecule behaviour and bulk BonFIRE spectra of ATTO680 and Rh800. a,**b**, Representative fluorescence image (**a**) and single-step photobleaching curve (**b**) for confirming the single-molecule sample preparation. In (**a**), the white arrow on the left shows the scan direction, and the white arrowhead indicates the "half-moon" bleach of a single molecule. c.p.ms, counts per millisecond. **c**, BonFIRE spectra of C=C modes in ATTO680 and Rh800 from dried dye/PVA aggregates. Spectra are vertically shifted for better comparison. a.u., arbitrary unit. Scale bar, 1 μm.

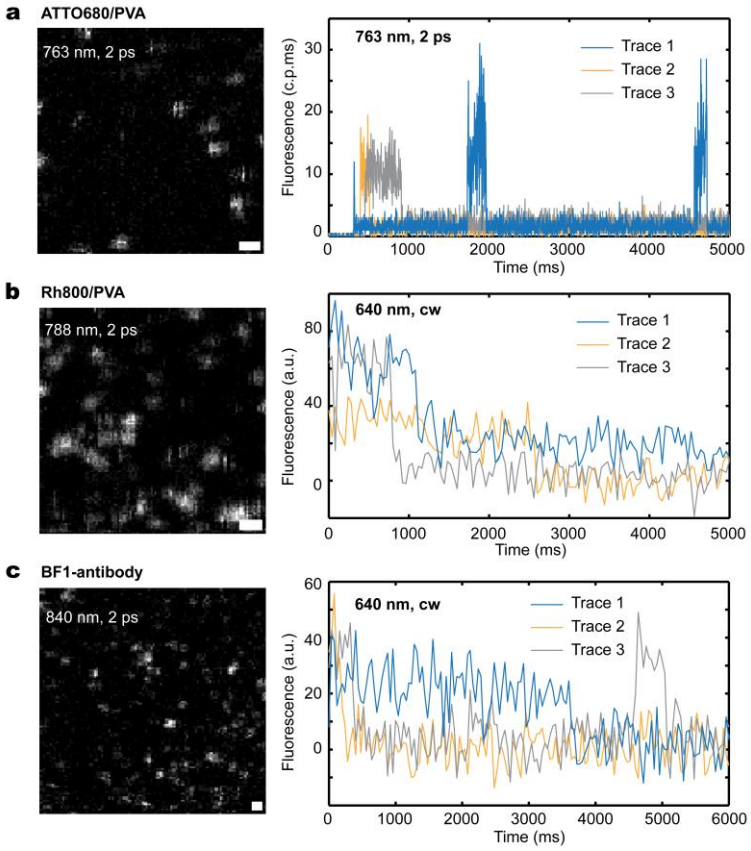

Fig. S7. Representative fluorescence images and photobleaching curves of single-molecule samples. Representative fluorescence images and photobleaching curves (three representative curves for each sample) are obtained for ATTO680 (**a**), Rh800 (**b**), and BF1-antibody conjugates (**c**). Single-step bleach and blinking could be observed in photobleaching curves, indicating the presence of single molecules. For (**a**) and (**b**), single-molecule samples were prepared by spin casting 20 pM ATTO680 or 10 pM Rh800 in 0.2% PVA solution onto a new CaF_2 window using 5000 rpm for 30 s. For (**c**), the single-molecule sample was prepared by incubating dye-antibody conjugates solution (diluted 625000 times in PBS from a 0.5 mg/mL stock solution, the dye:protein ratio is 1.7:1) onto a poly-l-lysine coated CaF_2 window for 30 min, and then dried in air before imaging. For ATTO680 with a high quantum yield (30%), the probe wavelength (763 nm, 2 ps) used for BonFIRE can be directly applied to performing *in-situ* photobleaching, while the fluorescence photon counts were recorded over time through the SPCM with a binning width (temporal step) of 2 ms. For Rh800 and BF1, however, the quantum yield is low (16% and 10%), and the wavelength of BonFIRE probe (788 nm and 840 nm) is too red to obtain reproducible bleach curves. We instead obtained bleach curves of the same samples using a commercial confocal microscope (Olympus FV3000) with a 640-nm cw excitation and detected the fluorescence change over time using PMT. Each step is 40 ms in (**b**) and (**c**). The PMT offset is corrected so that the fluorescence baseline is zero. 0.2 mW at 763 nm for ATTO680 and 5 mW at 640 nm for Rh800 and BF1 were used for obtaining photobleaching curves. c.p.ms, counts per millisecond. a.u., arbitrary unit. Scale bars, 1 μm.

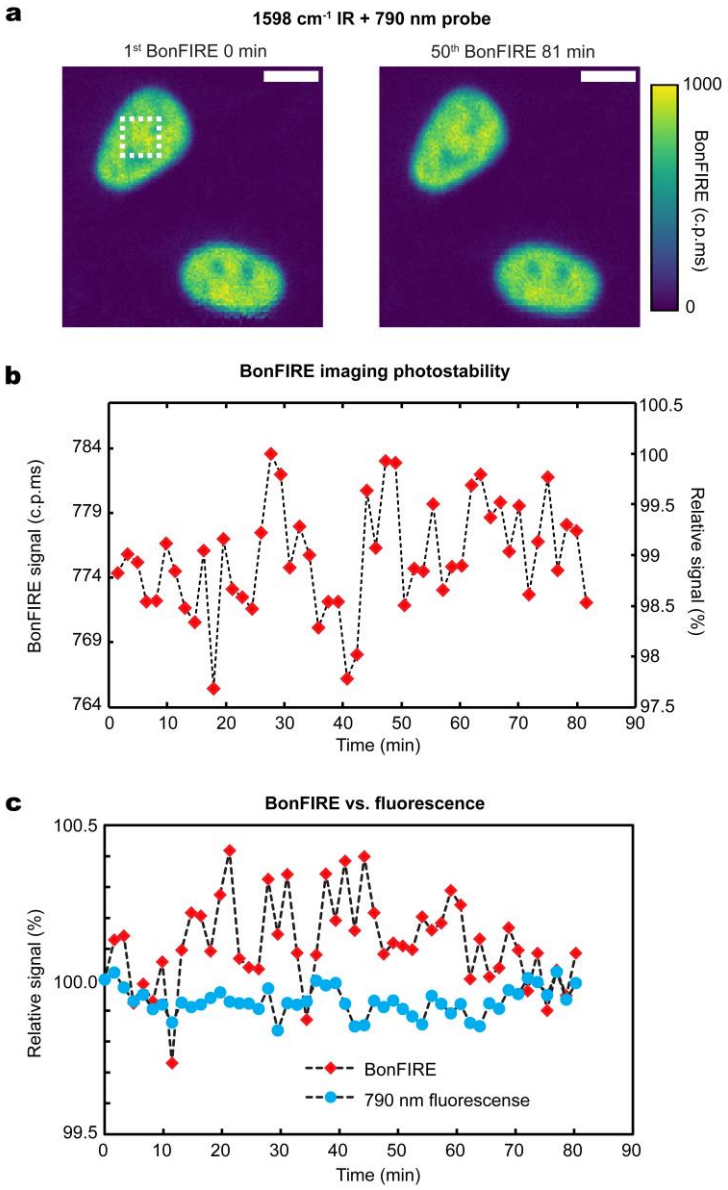

Fig. S8. Photo-stability of biological BonFIRE microscopy. ATTO680-click-labelled-EdU cells on CaF_2 were imaged with on-sample infrared power of 21 mW and probe power of 2 mW over 100-frame consecutive image scans. BonFIRE images were obtained by subtracting two adjacent frames captured at 0-ps and 20-ps infrared-probe delays. **a**, The first and the last (50^{th}) BonFIRE images of ATTO680 C=C showing two cell nuclei. The average signal from a cropped area (indicated by a white dashed box in the first image) is plotted against time in (**b**), where the BonFIRE signal oscillates between 97.5% and 100%. **c**, Comparison of photobleaching between probe-only fluorescence and BonFIRE under the same power and imaging condition, confirming that introducing an additional infrared beam does not increase the photobleaching rate in BonFIRE as compared to that of the probe-only fluorescence. c.p.ms, counts per millisecond. Scale bars, 10 µm.

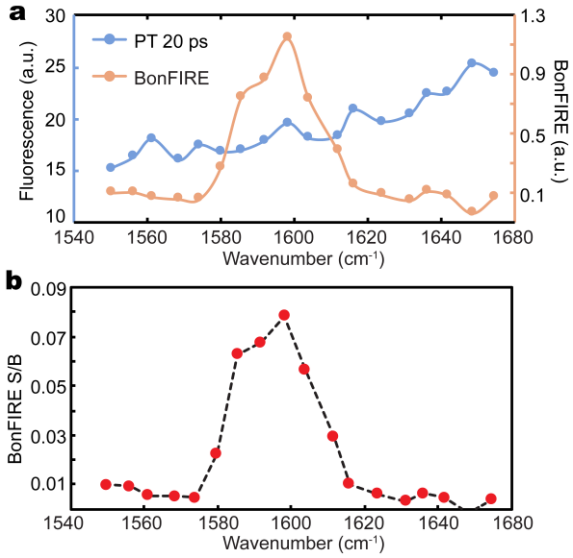

Fig. S9. Comparison between BonFIRE and photothermal (PT) spectra from a 100 µM ATTO680 DMSO solution. While the BonFIRE spectrum shows the 1598 cm^{-1} peak of ATTO680 explicitly, the photothermal spectrum at t_D=20 ps is featureless (**a**). a.u., arbitrary unit. The S/Bs across infrared frequencies are plotted in (**b**).

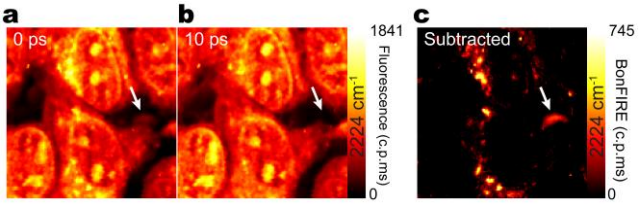

Fig. S10. Sample movement during live-cell imaging. C≡N BonFIRE imaging of Rh800-stained live HeLa cells at infrared-probe delays (t_D) of 0 ps (**a**), 10 ps (**b**), and after subtraction (**c**). The time for capturing each frame was ~40 s. The first two images were acquired consecutively using SPCM. The arrow indicates the subtraction artefact in (**c**) caused by cell movement. c.p.ms, counts per millisecond.

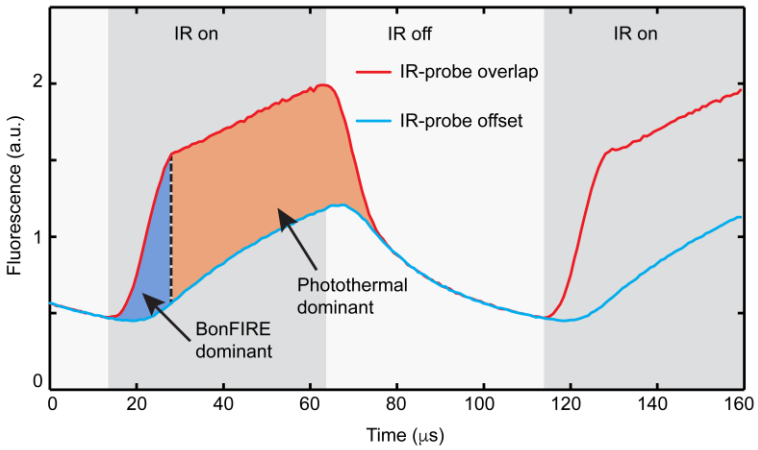

Fig. S11. Characterization for the temporal buildup of the photothermal background. BonFIRE intensity measured by PMT is plotted against time, as the infrared beam is chopped at 10 kHz. When the infrared and probe are temporally overlapped (red curve), a fast-increasing component in the BonFIRE signal (the blue-shaded area) could be observed, followed by a slow-increasing component due to the temperature rise caused by the infrared-photothermal effect. When the infrared and probe are temporally separated (blue curve), only the slow-increasing component is seen, resulting from the pure photothermal effect. The orange-shaded area indicates the photothermal-induced BonFIRE background rises at the time scale of tens of μs, while the initial BonFIRE signal burst stops within several μs (blue-shaded area). Note that the slow increase of BonFIRE-dominant fluorescence signal around 20 μs is mostly caused by the slow chopper movement and data acquisition and does not accurately indicate the temporal generation of BonFIRE signals. a.u., arbitrary unit.

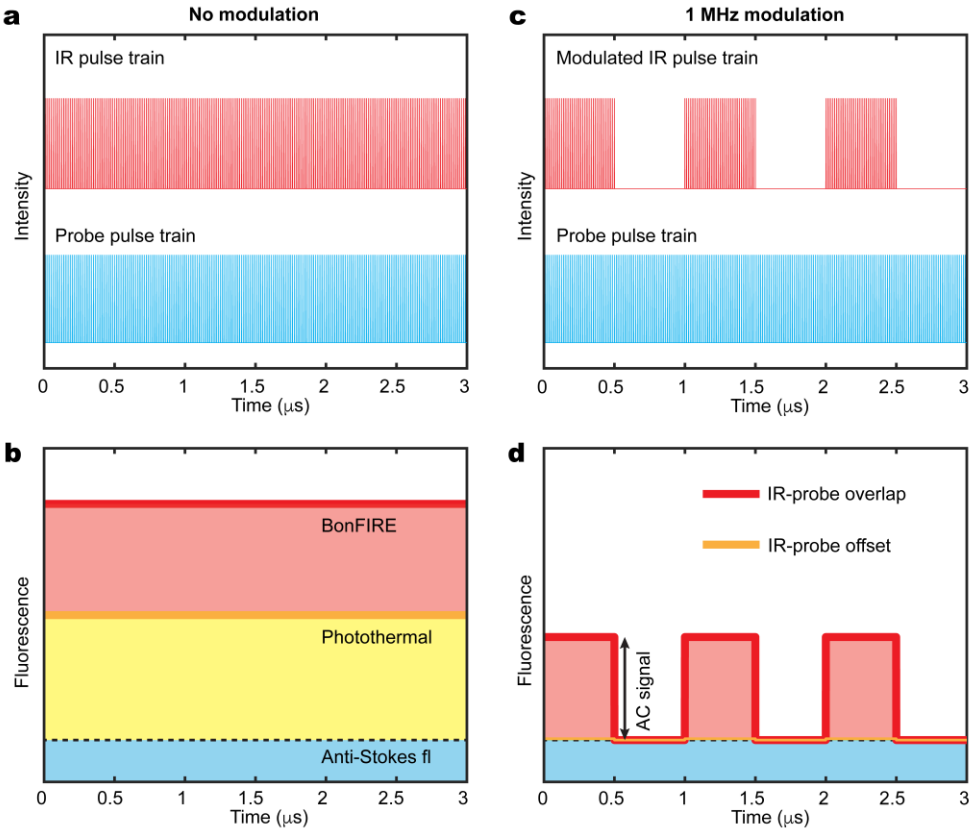

Fig. S12. Modulation scheme of background-free BonFIRE microscopy. a,**b**, Simulated pulse trains (**a**) and the expected total signal (**b**) when infrared pulses are not modulated. The total signal is composed of anti-Stokes fluorescence (blue shaded) detected with probe laser alone, infrared-induced photothermal fluorescence (yellow shaded) detected when infrared and probe are temporally offset, and BonFIRE signal (red shaded) detected when infrared and probe are temporally overlapped. **c**,**d**, Simulated pulse trains (**c**) and the expected signal (**d**) when 80 MHz infrared pulse trains are intensity-modulated by AOM at 1 MHz. The first-order diffraction from AOM completely turns off the infrared throughput and achieves maximal on/off ratios. Due to the high-frequency modulation, the photothermal background has no time to build up (**Supplementary Fig. 11**) and is almost completely suppressed, and the anti-Stokes fluorescence is removed through the lock-in demodulation (**d**).

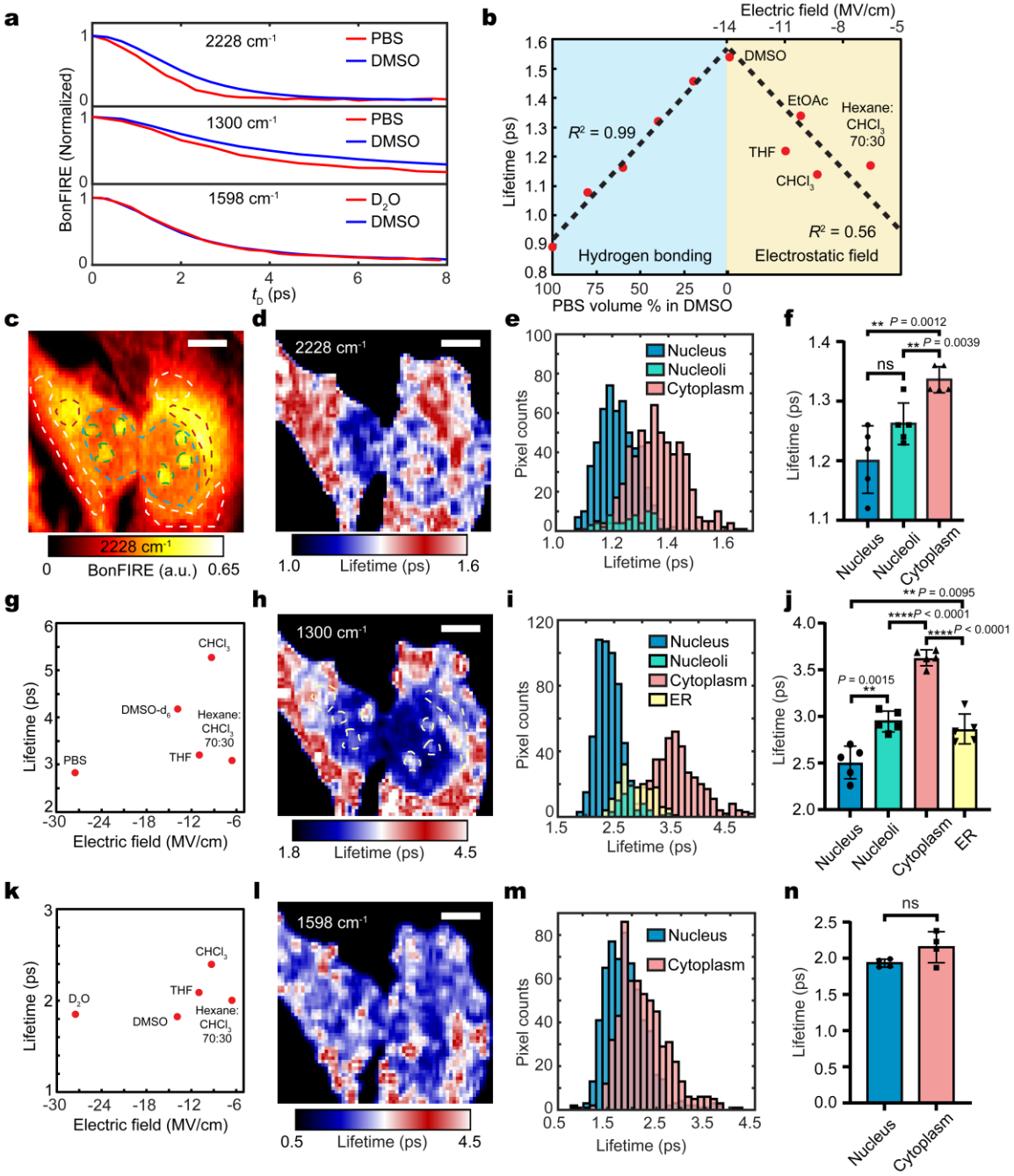

Fig. S13. BonFIRE lifetime imaging microscopy (BLIM). a, BonFIRE signal dependence on infrared-probe temporal delay measured for C≡N (2228 cm^{-1}), aromatic C-N (1300 cm^{-1}), and C=C (1598 cm^{-1}) of Rh800 in water and DMSO environments. While both C≡N and C-N show different lifetimes in water and DMSO, the lifetime of C=C is constant between the two environments. **b**, Solvatochromism of C≡N of Rh800 in PBS:DMSO mixture (left, blue-shaded) and different aprotic solvents with varying electrostatic fields (right, yellow-shaded) calculated from Onsager reaction field theory[3] (field of PBS was adopted from literature[4]). An inverted "V-shape" is observed in (**b**), showing the lifetime of C≡N is an

indicator of the Stark effect (right part) and hydrogen-bonding environment (left part). This finding is consistent with the vibrational Stark effect (VSE) benchmarked with nitrile peak shift,[5] and the opposite trend in PBS:DMSO mixture due to hydrogen-bonding effects.[3,4] **c**, BonFIRE image of Rh800-stained HeLa cells immersed in PBS obtained at 2228 cm^{-1}. Subcellular regions are indicated by dashed green (nucleus and nucleoli), red (endoplasmic reticulum, ER), and white (cytoplasm, excluding ER) enclosures. a.u. arbitrary unit. **d**, BLIM image at 2228 cm^{-1} for C≡N of the same field of view (FOV). Nucleus and cytoplasm (including ER) regions are clearly differentiated. **e**, Histogram of lifetime values in different subcellular regions. **f**, Statistics of lifetime measurements. While the C≡N lifetime can differentiate between the nucleus and cytoplasm (**p = 0.0012 unpaired Student's t-test, two-tailed, n = 5), it cannot distinguish the nucleus from nucleoli. Data are presented as mean values +/- s.d. **g**, Solvatochromism of aromatic C-N (1300 cm^{-1}) lifetime in different solvents. Although a large difference could be found between different solvents (e.g., ~80% increase from PBS to $CHCl_3$), no linear dependence on the electric field could be established, indicating a different sensing mechanism from C≡N. **h**, BLIM image at 1300 cm^{-1}. In addition to the nucleus and cytoplasm, nucleoli and ER (highlighted by white dashed enclosures) could be further distinguished from the nucleus and cytoplasm. **i**, Histogram of lifetime values obtained in different subcellular regions. **j**, Statistics of lifetime measurements. Clear differences could be found between the nucleus and nucleoli (**p = 0.0015 unpaired Student's t-test, two-tailed, n = 5) and between ER and cytoplasm (****p<0.0001 unpaired Student's t-test, two-tailed, n = 5). Compared to C≡N, C-N is more sensitive to differentiating nucleoli from nuclei. Moreover, with a positive charge in the resonant structure, aromatic C-N is likely more sensitive to varied charged membrane environments so that the ER could be distinguished by BLIM. Data are presented as mean values +/- s.d. **k**, Solvatochromism of conjugated C=C (1598 cm^{-1}). The lifetimes are highly close in different solvents, indicating that C=C is less sensitive in sensing. **l**, BLIM image at 1598 cm^{-1}, no clear contrast could be extracted between different subcellular regions. **m**, Histogram of lifetime values obtained in nucleus and cytoplasm, showing a small difference. **n**, Statistics of lifetime measurements. No difference (ns = not significant, unpaired Student's t-test, two-tailed, n = 5) could be found between the nucleus and cytoplasm, indicating the C=C is the least sensitive mode among the three modes. Data are presented as mean values +/- s.d. Scale bars, 10 μm.

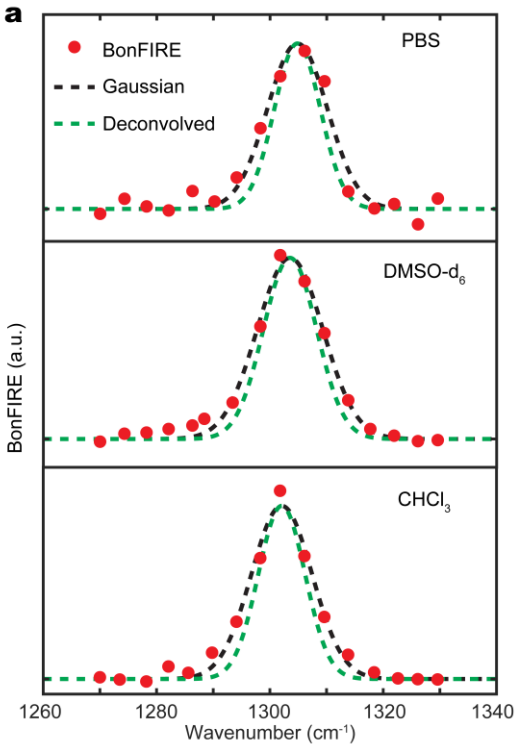

b

Data comparison

Solvent	PBS	DMSO-d_6	$CHCl_3$
Peak position (cm^{-1})	1305	1304	1302
Linewidth (cm^{-1})	9.4	10.8	9.7
Lifetime from linewidth (ps)	0.56	0.49	0.55
Lifetime measured in BLIM (ps)	2.8	4.2	5.3

Fig. S14. Linewidth, peak position, and lifetime measurements of the 1300 cm^{-1} peak for Rh800 in different solvents. a, To fit and extract the linewidth, we oversampled the BonFIRE spectra with a 4 cm^{-1} step size, which is half of the infrared laser bandwidth (8 cm^{-1}). BonFIRE data were obtained from 100 µM Rh800 in each solvent with probe wavelength fixed at 780 nm. The fitted Gaussian peak (black dashed curve) is deconvolved with the laser bandwidth with 8 cm^{-1} full width at the half maximum (FWHM), and the result is shown as the green dashed curve. a.u., arbitrary unit. The peak position, FWHM, lifetime calculated from the FWHM assuming the lifetime-broadening, and lifetime measured directly by BLIM are summarized in (**b**). The lifetime measured by BLIM is significantly longer than that calculated from linewidth, indicating the 1300 cm^{-1} peak of Rh800 is not lifetime-broadened.

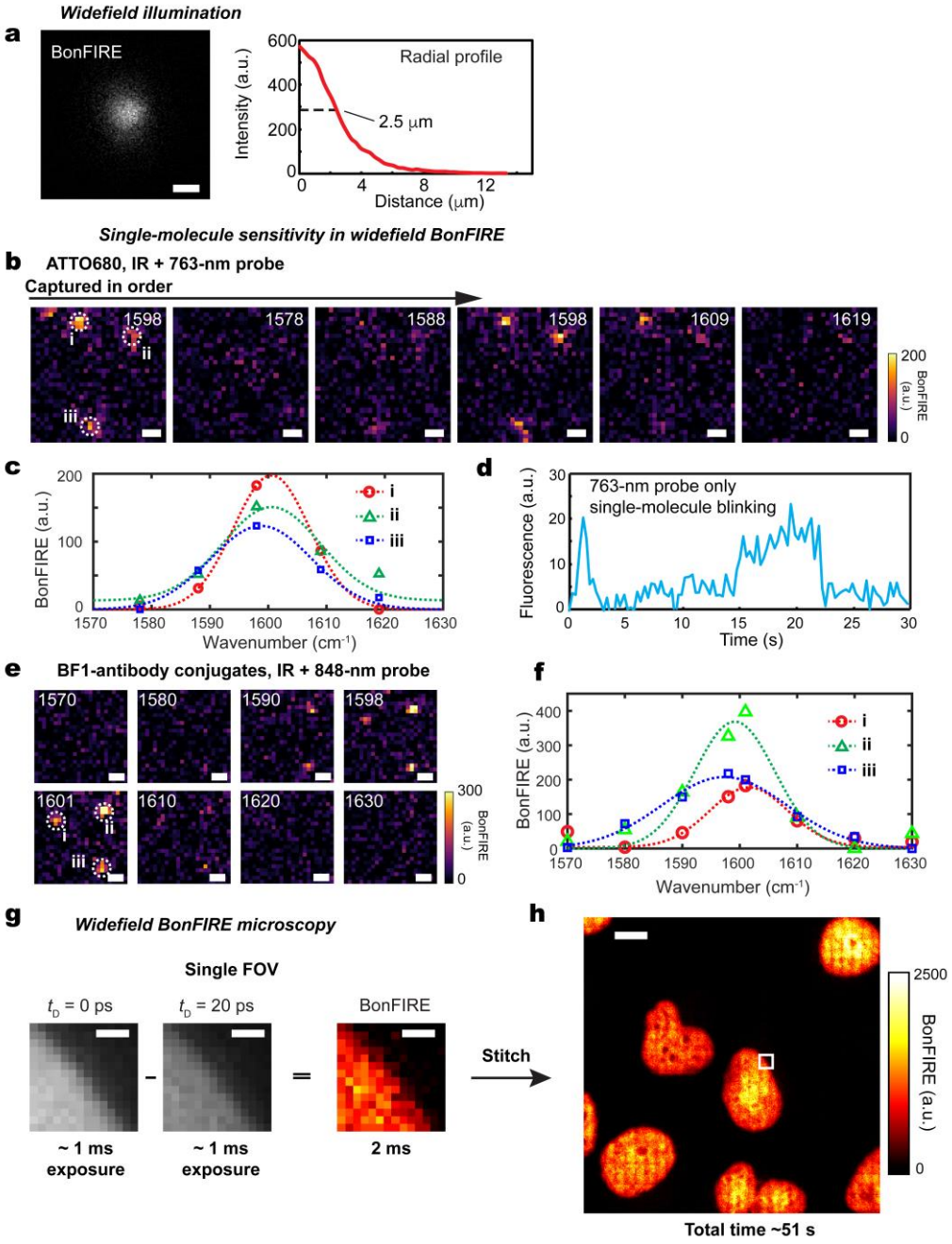

Fig. S15. Widefield BonFIRE microscopy. a, Characterization of illumination area of the widefield BonFIRE microscopy with single-molecule sensitivity. The measured radial profile of BonFIRE indicates a 5 μm BonFIRE spot size. More experimental details in **Methods**. a.u., arbitrary unit. **b**, Widefield BonFIRE images of single ATTO680 molecules embedded in PVA matrix. Each BonFIRE frame is a single field of view (FOV) obtained using widefield illumination and 5 s camera exposure time. The clear contrast between on (1598 cm^{-1}) and off (others) frames indicates the single-molecule sensitivity. Three single molecules (i, ii, and iii) are highlighted with dashed circles in the first on-resonance frame. **c**, *In-situ* BonFIRE spectra and Gaussian fittings obtained from molecules i, ii, and iii. After

the BonFIRE imaging, the same FOV was illuminated with a probe beam with increased power (2 mW on sample) to obtain single-molecule photobleaching curves. **d**, A representative single-molecule blinking time trace obtained from the single molecule i, proving the sample quality. The fluorescence readings were corrected by subtracting the baseline due to the system offset of the sCMOS detector. **e**,**f**, Widefield BonFIRE images of single BF1-conjugated antibodies (**e**) and representative *in-situ* spectra from three single molecules (labelled as i, ii, and iii in the 1601 cm^{-1} frame, **f**). **g**,**h**, Widefield BonFIRE image of ATTO680-EdU-labelled HeLa nucleus at 1598 cm^{-1}. Using an evenly illuminated 3×3 μm^2 BonFIRE FOV, each FOV can be acquired at the video rate (e.g., 2 ms per frame, **g**) and stitched together to form a large-area BonFIRE image (**h**). The stitched large-area (87×87 μm^2) image with 406 × 406 pixels was captured within 51 s, about 30 times faster than using the point-scan scheme with same parameters (i.e., pixel size and dwell time). We note here the imaging speed for the stitching is limited by the movement speed of the piezostage and the time needed for the synchronization between the camera and PC using a customized LabVIEW code (~60 ms per step), not by the imaging acquisition speed (2 ms per frame). The scanning and stitching speed could be further improved by enlarging the FOV. Scale bars, 5 μm (**a**), 1 μm in (**b**,**e**,**g**) and 10 μm (**h**).

Supplementary Table 1. Vibrational peaks of dyes.

Dye	Absorption peak (nm)	Vibrational peaks (cm^{-1})
Coumarin-6	444	817, 941, 1014, 1078, 1134, 1190, 1261, 1350, 1413, 1512, 1589, 1614, 1714
Nile Blue A	635	858, 947, 1008, 1074, 1106, 1171, 1257, 1275, 1332, 1375, 1438, 1549, 1584
Cy5	646	961, 1007, 1106, 1155, 1220, 1298, 1316, 1373, 1407, 1439, 1469, 1496
ATTO647N	646	1003, 1134, 1206, 1274, 1317, 1406, 1439, 1483, 1598, 1693
Alexa Fluor 647	647	1006, 1110, 1145, 1215, 1385, 1470, 1500
ATTO665	662	984, 1004, 1203, 1313, 1429, 1472, 1598
BF2	680	997, 1071, 1160, 1184, 1198, 1258, 1285, 1325, 1340, 1407, 1440, 1515, 1603, 1663, 1695, 2228 ($^{12}C{\equiv}^{14}N$)
Alexa Fluor 680	681	991, 1091, 1122, 1205, 1307, 1374, 1465, 1508, 1576
ATTO680	681	982, 1024, 1038, 1074, 1142, 1168, 1286, 1334, 1402, 1477, 1521, 1598, 1650, 1722
Cy5.5	684	1124, 1157, 1361, 1463, 1489
Rh800	695	1102, 1184, 1208, 1301, 1361, 1379, 1461, 1508, 1544, 1598, 2142 ($^{13}C{\equiv}^{15}N$), 2174 ($^{13}C{\equiv}^{14}N$), 2198 ($^{12}C{\equiv}^{15}N$), 2222 ($^{12}C{\equiv}^{14}N$)
BF3	696	1000, 1079, 1145, 1219, 1314, 1340, 1363, 1445, 1588, 2192 (C≡C)
ATTO725	728	978, 1102, 1165, 1224, 1289, 1341, 1365, 1399, 1456, 1506, 1596, 1738, 2228 ($^{12}C{\equiv}^{14}N$)
BF4	735	1163, 1183, 1222, 1266, 1326, 1358, 1438, 1496, 1577, 2187 (C≡C)
MARS2228 (BF1)	743	998, 1043, 1109, 1203, 1265, 1311, 1371, 1429, 1487, 1508, 1598, 1737, 2145 ($^{13}C{\equiv}^{15}N$), 2170 ($^{13}C{\equiv}^{14}N$), 2195 ($^{12}C{\equiv}^{14}N$), 2220 ($^{12}C{\equiv}^{14}N$)
Alexa 750	749	998, 1100, 1206, 1368, 1516
Cy7	750	1096, 1145, 1217, 1280, 1309, 1401, 1449, 1578
Alexa 790	782	1102, 1121, 1209, 1370, 1522
Cy7.5	788	1106, 1156, 1206, 1242, 1281, 1362, 1400, 1472, 1572

Note: Vibrational peaks were extracted from well-resolved absorption peaks from FTIR spectra of bulk samples or 10 mM solutions in DMSO. Vibrational peaks labelled in red have been experimentally reproduced in BonFIRE spectroscopy, respectively. Except for ATTO680 (data in **Fig. 2f**), Rh800 (data in **Extended Data Fig. 9**), and BF2 (with a structure similar to Rh800, see **Supplementary Table 3**), FTIR and available BonFIRE spectra data can be found in **Extended Data Fig. 3**.

Supplementary Table 2. BonFIRE signal comparison of dyes with C=C modes.

Dye	Absorption peak (nm)	IR frequency (cm^{-1})	Probe wavelength (nm)	Measured BonFIRE strength
Nile Blue A	635	1580	705	0.02
ATTO647N	650	1598	720	0.29
ATTO665	673	1598	740	0.10
ATTO680	685	1598	765	1.00
BF2	688	1598	760	0.71
Rh800	696	1598	775	0.50
ATTO725	742	1598	825	0.28
BF1	758	1598	840	0.26

Note: For Nile Blue A, ATTO647N, and ATTO665, the dichroic/filter set of FF700-Di01/ FF01-650/60 (Semrock) was used; For ATTO680, BF2, and Rh800, the dichroic/filter set of FF738-FDi01/FF01-665/150 was used; For ATTO725 and BF1, the dichroic/filter set of FF801-Di01/FF01-709/167 was used. Absorption peaks were verified with UV-vis and FTIR measurements in DMSO solutions. Probe wavelengths were optimized so that the sum energy of infrared + probe matches the absorption peak (The 705 nm for Nile Blue A was not optimized due to the limitation of the used dichroic mirror). BonFIRE experimental data were taken from 1 μM solutions in DMSO.

Supplementary Table 3. Molecular structures of dyes used in BonFIRE.

Name in the main text	Commercial name	Name in reference	Structure
ATTO680	ATTO680	-	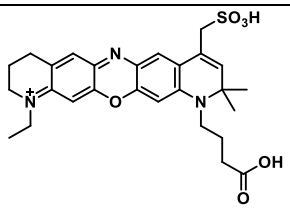
BF1	-	MARS2228[6]	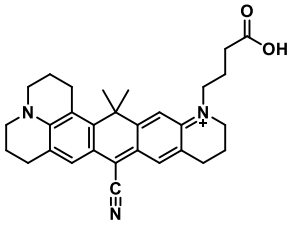
Rh800	Rh800	-	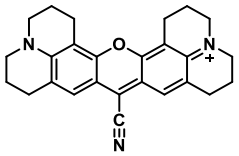
BF2	-	MARS2238[6]	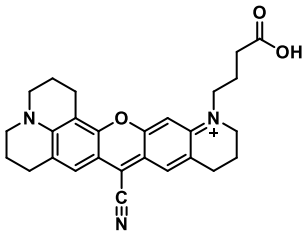
BF3	-	Compound 1a[7]	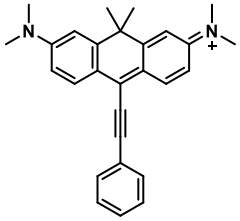
BF4	-	Compound 1b[7]	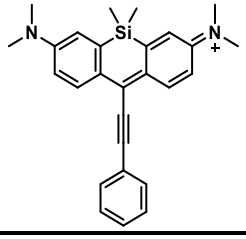

Note: We renamed the dyes to BonFIRE (BF) series, focusing on their infrared properties rather than the Raman counterparts. ATTO dyes were purchased from ATTO-Tec, GmBH. Rh800 was purchased from Sigma Aldrich. Cyanine dyes were purchased from Lumiprobe. Alexa dyes were purchased from Thermo Fisher. BF dyes were synthesized according to the literature cited in the third column. Isotopologues of BF1 and BF2 were synthesized according to ref. [6]. Available structures of other commercially available dyes (ATTO series,

Alexa series, Cyanine series, etc.) used in BonFIRE could be found on the corresponding vendor's websites.

Supplementary Table 4. BonFIRE signal comparison of dyes with C≡C and C≡N modes conjugated to the dye systems.

Dye	Absorption peak (nm)	Absorption coefficient (M^{-1} cm^{-1})	IR frequency (cm^{-1})	IR absorption coefficient (M^{-1} cm^{-1})	Calculated Franck-Condon factor	Quantum yield	Calculated BonFIRE strength relative to BF1	Measured BonFIRE strength
BF2	678	56078	2224 (C≡N)	28	0.08	0.16	0.41	0.59
BF3	680	39811	2194 (C≡C)	307	0.06	0.017	0.25	0.27
Rh800	687	66833	2224 (C≡N)	28	0.078	0.16	0.47	0.63
BF4	712	56234	2188 (C≡C)	351	0.043	0.004	0.07	0.83
ATTO725	728	123423	2224 (C≡N)	63	0.059	0.1	0.93	0.80
BF1	743	120000	2224 (C≡N)	70	0.059	0.1	1.00	1.00
BF1	743	120000	1598 (C=C)	3852	0.036	0.1	34	83

Note: For BF2, BF3, Rh800, and BF4, the dichroic/filter set of FF801-Di01/FF01-709/167 (Semrock) was used; For ATTO725 and BF1, the dichroic/filter set of Di02-R830/FF01-775/140 (Semrock) was used; Absorption peaks and cross sections were verified with UV-vis measurements on dye solutions in PBS. BonFIRE data were obtained from 1 μM PBS solution of each dye. Absorption peaks, coefficients, and quantum yields of BF3 and BF4 were obtained from ref. [7]. ORCA and custom scripts were used to estimate Franck-Condon factors according to ref. [8]. The last row (grey-shaded) of BF1 C=C was added for comparison.

Supplementary Table 5. Comparisons of key parameters of bioimaging between BonFIRE, SREF, and FEIR

Parameter	**BonFIRE**	**FEIR**	**SREF**
Working conditions	$\omega_{\mathrm{vib}} + \omega_{\mathrm{probe}} \approx \omega_{\mathrm{abs}}$	$\omega_{\mathrm{vib}} + \omega_{\mathrm{probe}} \approx \omega_{\mathrm{abs}}$	$\omega_{\mathrm{pump}} - \omega_{\mathrm{Stokes}} = \omega_{\mathrm{vib}}$; $2\omega_{\mathrm{pump}} - \omega_{\mathrm{Stokes}} \approx \omega_{\mathrm{abs}}$; $1400\ \mathrm{cm}^{-1} < \omega_{\mathrm{abs}} - \omega_{\mathrm{pump}} < 4200\ \mathrm{cm}^{-1}$
Laser system	Two OPOs and one DFG	One OPA	One OPO
Repetition rate	80 MHz	1 MHz	80 MHz
Pulse width	2 ps	200~300 fs	~ 2 ps
Laser bandwidth	8 cm^{-1}	120 cm^{-1}	~10 cm^{-1}
Spectral measurement	Laser tuning, bond-selective	Interferometric, broadband	Laser tuning, bond-selective
Laser tunability for optimal Spectral coverage	ω_{vib}: 800 - 4200 cm^{-1} ω_{probe}: 690 - 980 nm	ω_{vib}: demonstrated around 1600 cm^{-1} ω_{probe}: 517 nm, fixed	ω_{vib}: ~ 1600 cm^{-1}; ~ 2200 cm^{-1} ω_{probe}: 700 - 750 nm; 788-834 nm with frequency-doubled idler beam
Objective	25X, NA 1.05	63X, NA 0.8	60X, NA 1.2
Resolution	600 nm	Not available	400 nm
Bioimaging compatibility	Yes	Challenging due to sample damage from high peak powers	Yes
Sensitivity	Single-molecule imaging with bio-compatibility	Single-molecule in acetonitrile-d_3 solution	Single-molecule imaging with bio-compatibility
Widefield compatibility	Yes	N/A	Point-scanning
Lifetime for sensing	Yes, bond-selective	Not demonstrated	Not available
Background source	Anti-Stokes (constant for a fixed ω_{probe}); Photothermal (removable with temporal subtraction)	Anti-Stokes (constant for a fixed ω_{probe}); Photothermal (removable with temporal subtraction)	Anti-Stokes (from both ω_{pump} and ω_{Stokes}, varying for different ω_{vib}); two-photon pump/Stokes combined excitation;
Background-free bioimaging	Demonstrated with fast AC modulation	N/A	Possible with a complex frequency modulation scheme

* We note that the previous vibrational super-multiplexing techniques (e.g., epr-SRS or Carbow) are limited to sensitivities of 250-500 nM, without single-molecule sensitivity for accessing low-abundance biomolecules.

References

1 Whaley-Mayda, L., Guha, A., Penwell, S. B. & Tokmakoff, A. Fluorescence-Encoded Infrared Vibrational Spectroscopy with Single-Molecule Sensitivity. *Journal of the American Chemical Society* **143**, 3060-3064 (2021). https://doi.org:10.1021/jacs.1c00542

2 Xiong, H. *et al.* Stimulated Raman excited fluorescence spectroscopy and imaging. *Nature Photonics* **13**, 412-417 (2019). https://doi.org:10.1038/s41566-019-0396-4

3 Shi, L., Hu, F. & Min, W. Optical mapping of biological water in single live cells by stimulated Raman excited fluorescence microscopy. *Nature Communications* **10**, 4764 (2019). https://doi.org:10.1038/s41467-019-12708-2

4 Deb, P. *et al.* Correlating Nitrile IR Frequencies to Local Electrostatics Quantifies Noncovalent Interactions of Peptides and Proteins. *The Journal of Physical Chemistry B* **120**, 4034-4046 (2016). https://doi.org:10.1021/acs.jpcb.6b02732

5 Bagchi, S., Fried, S. D. & Boxer, S. G. A Solvatochromic Model Calibrates Nitriles' Vibrational Frequencies to Electrostatic Fields. *Journal of the American Chemical Society* **134**, 10373-10376 (2012). https://doi.org:10.1021/ja303895k

6 Wei, L. *et al.* Super-multiplex vibrational imaging. *Nature* **544**, 465-470 (2017). https://doi.org:10.1038/nature22051

7 Pastierik, T., Šebej, P., Medalová, J., Štacko, P. & Klán, P. Near-Infrared Fluorescent 9-Phenylethynylpyronin Analogues for Bioimaging. *The Journal of Organic Chemistry* **79**, 3374-3382 (2014). https://doi.org:10.1021/jo500140y

8 Lee, S.-Y. & Heller, E. J. Time-dependent theory of Raman scattering. *The Journal of Chemical Physics* **71**, 4777-4788 (1979). https://doi.org:10.1063/1.438316

Chapter 5

WIDE-FIELD BOND-SELECTIVE FLUORESCENCE IMAGING: FROM SINGLE-MOLECULE TO CELLULAR IMAGING BEYOND VIDEO-RATE

Sections of this chapter have been adapted from:
Lee, D.; Wang, H.; Kocheril, P. A.; Bi, X.; Naji, N.; Wei, L. 1 Title: Wide-Field Bond-Selective Fluorescence Imaging: From Single-Molecule to Cellular Imaging beyond Video-Rate. Optica. 2025, Accepted

5.1 Abstract

Wide-field (WF) imaging is pivotal for observing dynamic biological events. While WF chemical microscopy offers high molecular specificity, it lacks the sensitivity for single-molecule detection. In contrast, WF fluorescence microscopy provides live-cell dynamic mapping but fails to leverage the rich chemical information necessary for functional interpretations. To address these limitations, we introduce Wide-Field Bond-selective Fluorescence-detected Infrared-Excited (WF-BonFIRE) spectro-microscopy. This technique combines rationally optimized imaging speed and field-of-view (FOV) to achieve single-molecule sensitivity with bond-selective contrast. We demonstrate WF-BonFIRE's capabilities in imaging single molecules, cells, astrocytes, and live neurons, capturing single FOVs up to 50 μm × 50 μm, with further expansion via multi-FOV mosaicking. Additionally, we have implemented a new temporal-delay modulation scheme that allows real-time kilohertz WF-BonFIRE imaging with speeds up to 1500 Hz. We showcase the millisecond temporal resolution through monitoring the random motion of live Escherichia coli. Leveraging its ability to distinguish molecules through distinct narrow-band BonFIRE signals, we further demonstrate multicolor real-time *E. coli* tracking. WF-BonFIRE should significantly broaden the boundary for chemical imaging, enabling high-speed observations at unparalleled sensitivity levels.

5.2 Introduction

Biological processes are inherently heterogeneous and dynamic. Consequently, the ability to image subcellular live-cell activities with high-sensitivity and fast speed has revolutionized our understanding of fundamental biology[1,2]. To this end, point-scanning microscopy configurations face fundamental constraints to achieve high temporal resolution due to serial pixel-by-pixel acquisition[1,3,4]. In contrast, wide-field (WF) microscopy, with down to single-molecule sensitivity, enables the capture of dynamic biomolecular processes, such as those involving RNA, proteins, and metabolites, at video-rate speeds simultaneously across the entire field of view (FOV). This capability is particularly valuable for applications like imaging and tracing neuronal action potentials that occur at millisecond timescales across entire neurons and neighboring cells[2,5]. Furthermore, leveraging the high-sensitivity capabilities of wide-field imaging, advanced functional fluorescence microscopy techniques

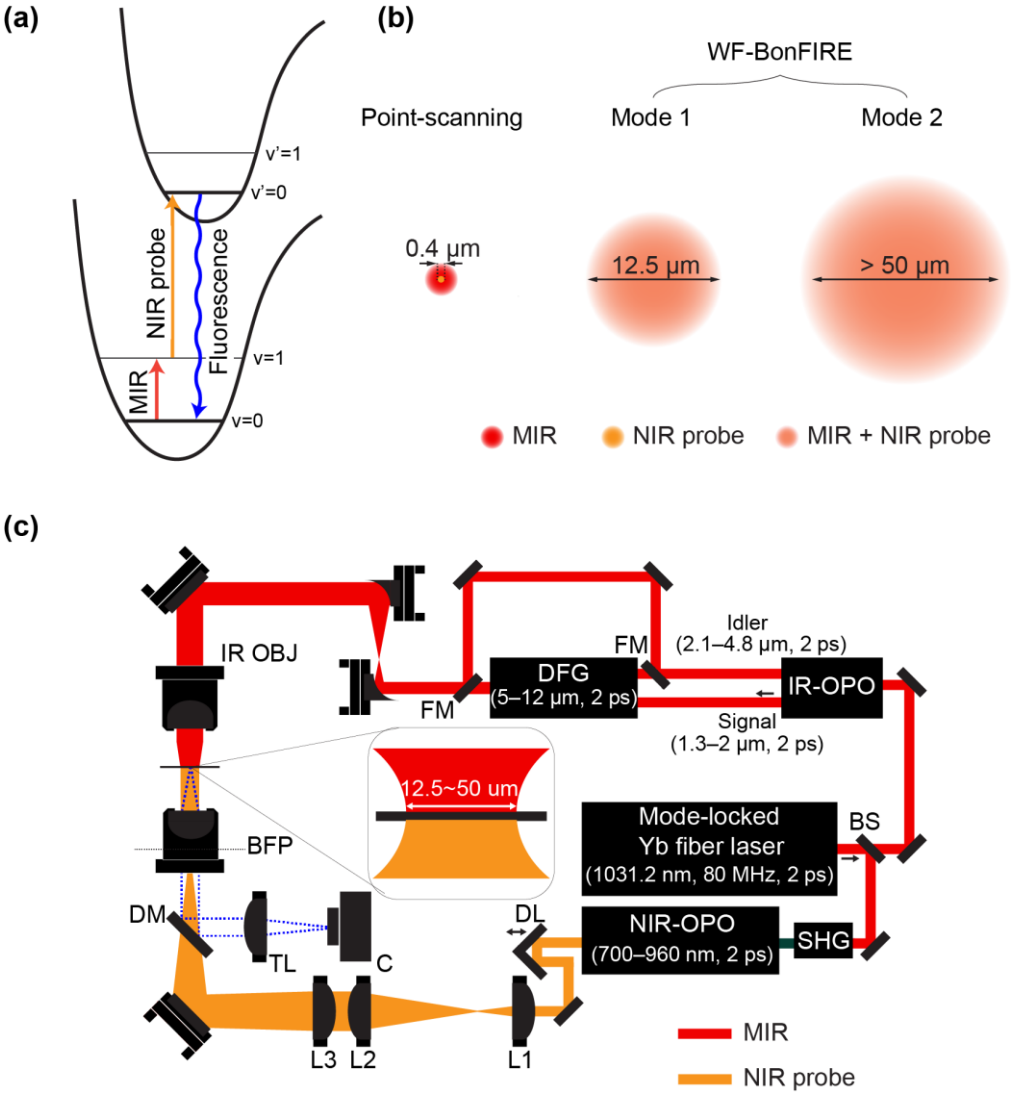

Fig. 1. Principle and design of WF-BonFIRE. (a) Energy diagram of BonFIRE spectroscopy. ν and ν' represent the vibrational states at ground and excited electronic states, respectively. (b) Two implementation modes of WF-BonFIRE (Mode 1 & Mode 2), in comparison to the point-scanning mode. Not drawn to scale. (c) WF-BonFIRE experimental scheme. Dotted blue line indicates fluorescence detection path. OBJ, objective; BFP, back focal plane; DM, dichroic mirror; TL, tube lens; C, camera; L, lens; DL, delay line; BS, beamsplitter; DFG, difference frequency generation; OPO, optical parametric oscillator; SHG, sum frequency generation; FM, flip mirror.

have been developed, including single-molecule localization microscopy (SMLM), single-molecule fluorescence in situ hybridization (smFISH) microscopy, and structured illumination microscopy (SIM), which have significantly advanced our understanding of complex and dynamic biological phenomena to unprecedented levels[6–9].

Over the past two decades, chemical imaging techniques have dramatically advanced, offering high molecular specificity and detailed bond-selective information crucial for biological research[10]. Despite these advances, achieving single-molecule sensitivity in WF chemical imaging remains a formidable challenge. Raman scattering suffers from inherently small cross-sections of vibrational transitions, ranging from 10^{-30} to 10^{-28} cm^2, more than ten

orders of magnitude smaller than the visible absorption cross-sections in fluorescence spectroscopy[11]. Nonlinear Raman techniques, such as stimulated Raman scattering (SRS), address this limitation with up to 10^8 stimulated emission amplification with two simultaneous pulsed lasers[12]. However, the reliance on tightly-focused nonlinear excitation limits the scope of WF biological imaging, even with the most recent advances of electronic pre-resonance SRS (epr-SRS) and stimulated Raman-excited fluorescence (SREF)[13–16]. Conversely, mid-infrared (MIR) spectroscopy, with its substantially larger linear MIR absorption cross-sections (10^{-22} – 10^{-17} cm^2), enhances the feasibility of high-speed WF imaging[17–19]. Recently, MIR photothermal microscopy have achieved significant advances, in both laser-scanning and wide-field imaging modes[20–22]. To enhance sensitivity, wide-field fluorescence-detected photothermal microscopy (WF-F-MIP) was developed[23]. It measures the modulation in fluorescent quantum yield of the reporter fluorophores, induced by local thermal changes from the MIR vibrational excitation of nearby target non-fluorescent molecules. This scheme increased the sensitivity by up to 100-fold. However, these photothermal-based methods still remain considerably far from single-molecule sensitivity for universal probing of low-copy biological targets.

To advance toward single-molecule detectability, a seemingly similar but fundamentally different approach has proven to be effective. Building on the pioneering work of Kaiser and co-workers in 1975[24], recent efforts focused on exploiting a nonlinear double-resonance fluorescence detection scheme mediated by MIR-excited vibrational states, through the adoption of various laser excitation and detection strategies[25–28]. The successfully achieved single-molecule detection and spectroscopy is expected to open the door for many new applications from biological imaging to single-molecule catalysis[25,26]. However, current demonstrations remain challenging for wide-field imaging with down to single molecule sensitivity and up to video-rate while maintaining superb biocompatibility[27,28].

Implemented with picosecond (ps) excitation pulses, we recently demonstrated bond-selective fluorescence-detected infrared-excited (BonFIRE) microscopy[26]. BonFIRE achieves single-molecule sensitivity while capturing mid-infrared chemical information for live biological imaging, representing a significant leap in bio-imaging capabilities[26,29]. Employing a 2-ps pair of MIR and near-infrared (NIR) lasers for bond-selective double-resonance excitation, BonFIRE transfers the rich MIR-excited vibrational information into fluorescence signals for highly sensitive detection **(Fig. 1(a))**. The initial design of BonFIRE utilized a point-scanning (PS) mode with tightly focused beams of both the MIR and the NIR lasers to ensure single-molecule detectability across the wide fingerprint and cell-silent regions (1300 cm^{-1} – 2400 cm^{-1}) for double- and triple- bond vibrational modes[26]. However, the serial-acquisition PS-BonFIRE is limited by its temporal resolution, making it challenging to capture rapid dynamic processes.

Here, we report wide-field (WF)-BonFIRE **(Fig. 1(b))**. Through carefully balanced design and simulations of sensitivity against laser power, we push the imaging speed and the FOV limits of WF-BonFIRE to its maximum while achieving single molecule sensitivity **(Table S1)**. Such a design facilitates up to 10,000-fold faster frame acquisition compared to PS-BonFIRE, under the same number of pixels and SNR. In addition, we demonstrate exceptional WF-BonFIRE imaging performance in cells, astrocytes, and in live neurons, capturing intricate structural details and networks with robust signal-to-noise ratios (SNRs).

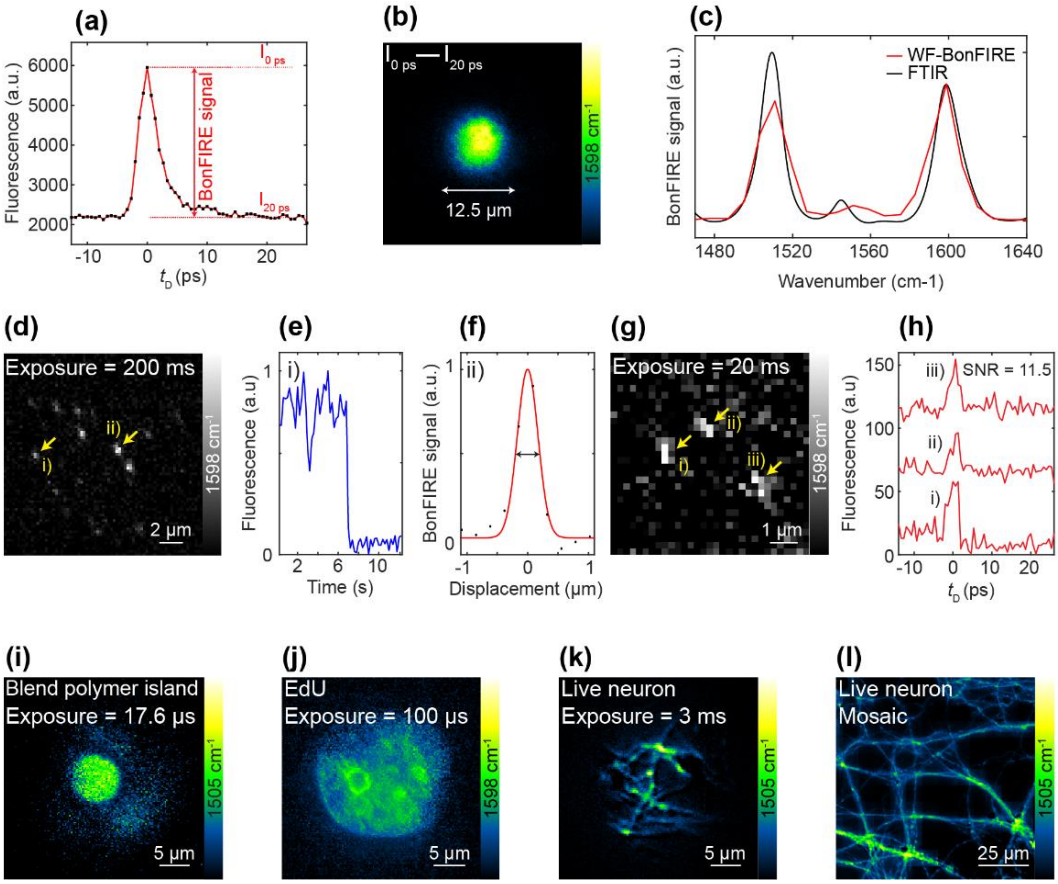

Fig. 2. Characterization of WF-BonFIRE (Mode 1) spectroscopy and imaging performance. (a) WF-BonFIRE signal of Rh800 polymer film as a function of temporal delay (t_D). (b) WF-BonFIRE image of Rh800 polymer film generated by subtracting two images acquired at temporal delays 0 ps and 20 ps ($I_{0\ ps}$ and $I_{20\ ps}$ shown in (a)). (c) Overlay of WF-BonFIRE (red) and FTIR (black) spectra of Rh800. (d) Single-molecule WF-BonFIRE image of Rh800 at 1598 cm^{-1}. Exposure time: 200 ms. (e) Exemplary single-step photobleaching curve of a single molecule i) in (d) for confirming single-molecule detection. (f) Cross-section profile of a single molecule ii) in (d). (g-h) Short-exposure (20 ms) WF-BonFIRE image (g) of single-molecule Rh800, with corresponding temporal profiles (h) for single molecules of i), ii), and iii) in (g). SNR = 11.5 (N = 3). (i) WF-BonFIRE images of Rh800 blend polymer island at on-resonance (1505 cm^{-1}). Exposure time: 17.6 μs. (j) WF-BonFIRE image targeting C=C vibration in ATTO680-click-labelled EdU in the nuclei of HeLa cells at on-resonance (1598 cm^{-1}). (k-l) Single FOV (k) and mosaic (l) WF-BonFIRE images of Rh800-labelled mitochondria in live mouse neuronal cultures acquired at on-resonance (1505 cm^{-1}). Exposure time: 3 ms. Acquisition area in (l): 100 × 100 μm^2.

To further achieve kilohertz frame rate, we implement a new temporal-delay modulation scheme that obtains up to 1500 frames per second (FPS) for WF-BonFIRE. We showcase the performance of temporal-delay modulation by tracking the random motion of live Escherichia coli (*E. coli*). Furthermore, by distinguishing fluorophores with overlapping electronic spectra but distinct bond-selective MIR peaks, WF-BonFIRE enables precise multicolor differentiation in real time. We anticipate that WF-BonFIRE will significantly push the boundaries of both chemical imaging and fluorescence imaging, facilitating high-speed and high-throughput imaging at the single-molecule level **(Fig. 1(c))**.

5.3 Results

Rational design and simulation of WF-BonFIRE.

We first rationalize the feasibility of WF-BonFIRE especially in the single molecule regime. Contrary to conventional virtual-state mediated two-photon imaging techniques such as two-photon fluorescence and SRS microscopy, which face challenges in high-sensitivity WF implementation due to high photon-flux requirements, BonFIRE is a real vibrational state-mediated non-degenerate two-photon excitation process. Employing 2-ps laser excitation achieves a balance between bond-selectivity and efficient vibrational excitation, which competes with the picosecond vibrational relaxation lifetime **(Fig. S1)**. The up-conversion step is also highly efficient due to the large electronic absorption cross section. These efficient excitation steps hence alleviate the high photon flux requirement, thus allowing picosecond laser pulses to spread over a wider focal area. In addition, in PS-BonFIRE **(Fig. 1(b), Point-scanning)**, the diffraction-limited MIR spot is significantly larger than that of the NIR probe laser, which results in more than 50% of MIR photons not being utilized for signal generation. Given the excess power of the NIR probe laser, the most straightforward design of WF-BonFIRE is to expand the NIR probe beam to match with the diffraction-limited spot of the MIR beam, thereby optimizing the utilization of MIR photons with opportunities for additional area expansion.

To quantitatively model the optimal FOVs, we next calculated the achievable signals and SNRs as a function of FOV using a high-sensitivity sCMOS camera **(Fig. S2, Eq S1-S3)**. At a 12.5 μm FOV, the achievable WF-BonFIRE signal from a single Rhodamine 800 (Rh800) molecule is estimated to reach 1 photon/ms with a SNR of 3, under a short camera exposure time of 25 ms. In situations where single-molecule sensitivity is not essential, the FOV can be further expanded. Hence, we investigated the maximum FOV for higher concentration samples. To this end, we introduced a pixel rate ratio, R (Eq. S4-S5), for comparing speeds between WF-BonFIRE and PS-BonFIRE. At the upper limit of R=1 where WF-BonFIRE theoretically matches the speed of PS-BonFIRE, FOV of WF-BonFIRE extends to 620 μm. However, reaching such large FOV results in reduced detection sensitivity, due to the inverse quadratic relationship between laser intensity and the illumination size for each beam **(Fig. S3)**.

Based on the above simulation, we implemented WF-BonFIRE in two modes, each providing optimal combination of sensitivity, speed and FOV for different biological applications. In Mode 1 **(Fig. 1(b))**, we expanded and matched the sizes of the NIR probe and the MIR beams to a diameter of 12.5 μm for fast single-molecule imaging applications, paving the way toward WF-BonFIRE SMLM. In Mode 2 **(Fig. 1(b))**, both beams are expanded and matched to 50 μm, sufficient to cover an entire mammalian cell while achieving an optimal balance between SNR and speed. At 50 μm FOV, the imaging speed of WF-BonFIRE is estimated to be over 150 times faster than PS-BonFIRE **(Fig. S3, R>150)**. The smaller pixel rate ratio R at 50 μm FOV (Mode 2) compared to that at 12.5 μm FOV (Mode 1) is due to the quadratic reduction in photon flux across both MIR and NIR beams **(Fig. S3)**. When a larger FOV is needed, a parallel mosaicking approach is applied by precisely moving the piezo stage. Experimentally, we focused the probe beam onto the back focal plane of the objective to ensure uniform illumination **(Fig. 1(c))**. Simultaneously, the MIR beam underwent expansion using a lower numerical aperture (NA) MIR objective to

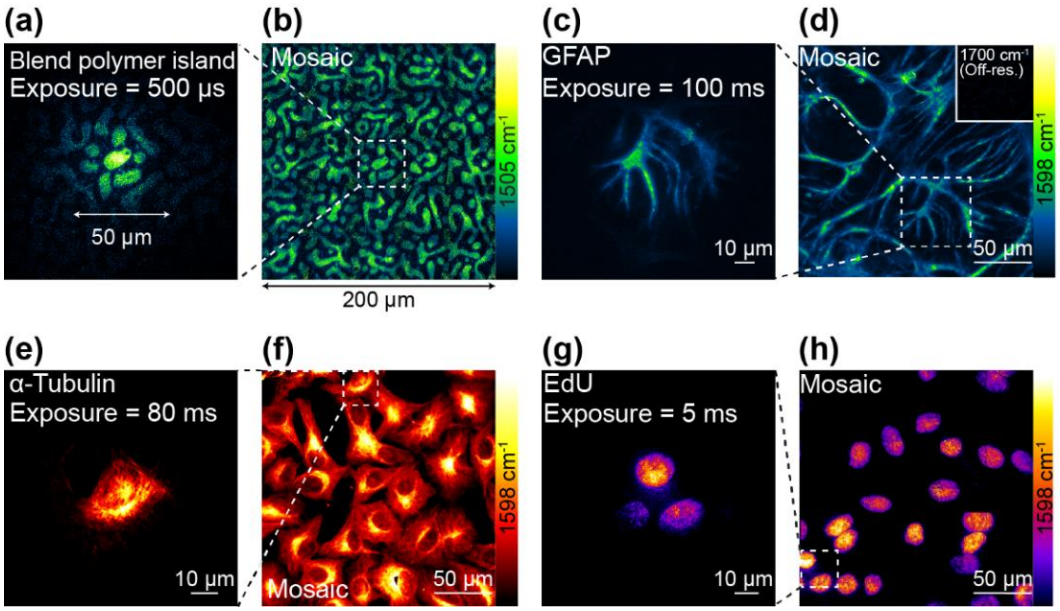

Fig. 3. Large FOV WF-BonFIRE imaging (Mode 2). (a-b) Single FOV (a) and mosaic (b) WF-BonFIRE images of Rh800 blend polymer film acquired at 1505 cm^{-1}. Exposure time: 500 µs. Acquisition area in (b): 200 × 200 $µm^2$. (c-h) Single FOV (c, e, g) and mosaic (d, f, h) WF-BonFIRE images targeting C=C vibration (1598 cm^{-1}) for ATTO680-immunolabeled GFAP in mouse neuronal co-cultures (c & d. Exposure time: 100 ms. Acquisition area in (d): 200 × 200 $µm^2$); ATTO680-immunolabelled α-tubulin in HeLa cells (e & f. Exposure time: 80 ms. Average: 5 frames. Acquisition area in (f): 200 × 200 $µm^2$); and ATTO680-click-labelled EdU in the nuclei of HeLa cells (g & h. Exposure time: 5 ms. Average: 16 frames. Acquisition area in (h): 200 × 200 $µm^2$).

align its spot size with that of the probe beam. System magnification was carefully determined to meet the requirements of the Nyquist theorem **(Fig. S4)**.

Characterization of WF-BonFIRE (Mode 1) spectroscopy and imaging performance

We first validated WF-BonFIRE (Mode 1) by targeting the C=C bond (1598 cm^{-1}) of Rh800, a NIR fluorescent molecule with an absorption peak at 696 nm **(Fig. S5)**. We tuned the NIR probe wavelength to 788 nm to achieve a sum frequency of NIR and MIR lasers that matches the absorption peak maximum **(Fig. S5)**. The WF-BonFIRE signal of Rh800-embedded spin-coated polymer film was generated by subtracting an image captured with a 20 ps temporal delay between MIR and NIR pulses from that with overlapping pulses (t_D=0 ps) **(Fig. 2(a) & (b))**. Minimal photobleaching was observed over 60 consecutive frames, as indicated by the flat baseline. The background from temporally separated laser pulses is attributed to anti-Stokes fluorescence and photothermal signal, resulting from local temperature increases from the environment, both of which are constant across the temporal profile **(Fig. S6)** and exhibit no vibrational characteristics from the target molecules[26]. The authenticity of the BonFIRE signal was further verified by the WF-BonFIRE spectrum, obtained by scanning the MIR laser wavelength, which closely aligns with the FTIR spectra from Rh800 in solution **(Fig. 2(c))** featuring prominent peaks at 1505 cm^{-1} and 1598 cm^{-1}, and by the linear power dependence on both MIR and NIR laser powers **(Fig. S7)**. The difference in relative amplitude between FTIR and BonFIRE is due to the extra Franck-Condon factor involved in the BonFIRE vibronic excitation step. Slight spectral broadening observed in the WF-

BonFIRE spectrum is primarily due to the laser broadening with MIR pulse bandwidth of 10 cm^{-1}. Additional difference in peak shift may have resulted from molecular aggregation effect due to high concentrations (millimolar) required for FTIR measurements but not in BonFIRE which can perform spectral measurement with nM solution concentration.

To demonstrate the high sensitivity of WF-BonFIRE (Mode 1), single molecules of Rh800 were imaged with robust SNRs (> 48). This was achieved under an exposure time of 200 ms **(Fig. 2(d) & Fig. S8)** and even as short as 20 ms **(Fig. 2(g) & (h))**, which is consistent with the predictions in **Fig. S2**. For single molecule measurements, the imaging speed of WF-BonFIRE exceeds that of PS-BonFIRE by over 200 times, underscoring its potential use in advanced super-resolution microscopy techniques like SMLM. Standard single-step photobleaching and blinking curves were observed throughout, indicating single-molecule nature of the sample **(Fig. 2(e) & Fig. S8)**[30–32]. Here our single-molecule BonFIRE reaches a high signal-to-background ratio of 5. By utilizing a single molecule as a point source, the spatial resolution of our WF-BonFIRE was next characterized to be 400 nm **(Fig. 2(f))**, confirming its diffraction-limited performance.

We then applied WF-BonFIRE (Mode 1) to rapidly image various samples ranging from blend polymer films to live neurons. An exposure time of 17.6 μs was achieved when imaging a Rh800-labeled blend polymer film, consisting of phase-separated polystyrene and polymethylmethacrylate segments **(Fig. 2(i))** with high bond-selectivity **(Fig. S9a)**. The imaging speed was indeed 10,000 times faster than PS-BonFIRE, closely aligning well with our earlier predictions **(Fig. S3)**. In these experiments, a single polymer island was captured, which was approximately the size of small mammalian cells (~10 μm). Additionally, we imaged a single nucleus of a HeLa cell using microsecond-level exposure time **(Fig. 2(j) & Fig. S9b, 100 μs)**, using ATTO680 click-labeled 5-ethynyl-2'-deoxyuridine (EdU) in newly synthesized DNA. The short exposure time demonstrates the high sensitivity of WF-BonFIRE, which is critical for enabling potential biological imaging at kilohertz speeds in temporally-modulated systems, as illustrated later in **Fig. 4**, a feat challenging for existing chemical-selective imaging modalities. Leveraging its high sensitivity and speed, WF-BonFIRE further demonstrated live neuron imaging at an exposure time of 3 ms, revealing distributions of mitochondria labeled with Rh800 **(Fig. 2(k) & (l), & Fig. S9c)**. Such speeds fulfill the necessary requirements for resolving fast dynamics in cells, such as voltage imaging in neurons. Additionally, by mosaicking single FOV WF-BonFIRE images, a network of live neurons was captured within ~30 seconds, enabling extensive imaging of a large area (100 x 100 μm^2) of live cells **(Fig. 2(l))**.

Large FOV WF-BonFIRE imaging (Mode 2)

We then explored the expanded FOV capabilities of WF-BonFIRE (Mode 2), which more effectively captures a larger area for biological samples at 50 μm. Imaging of a Rh800 blend polymer sample is achieved at an exposure time of 500 μs **(Fig. 3(a))**. Additionally, a 200 x 200 μm^2 area was acquired within 1.3 s using mosaicking **(Fig. 3(b))**. Although Mode 2 lacks single-molecule sensitivity, it effectively imaged a wide variety of biological targets, including low-abundance proteins at micromolar concentrations and below **(Fig. 3(c)-(h))**. Using ATTO680-immuno-labeled GFAP, a key marker protein for astrocytes, we obtained an exposure time of 100 ms for single FOV WF-BonFIRE (Mode 2) imaging that targeted the 1598 cm^{-1} of the C=C vibration **(Fig. 3(c) & (d))**. This enabled capturing a 200 x 200

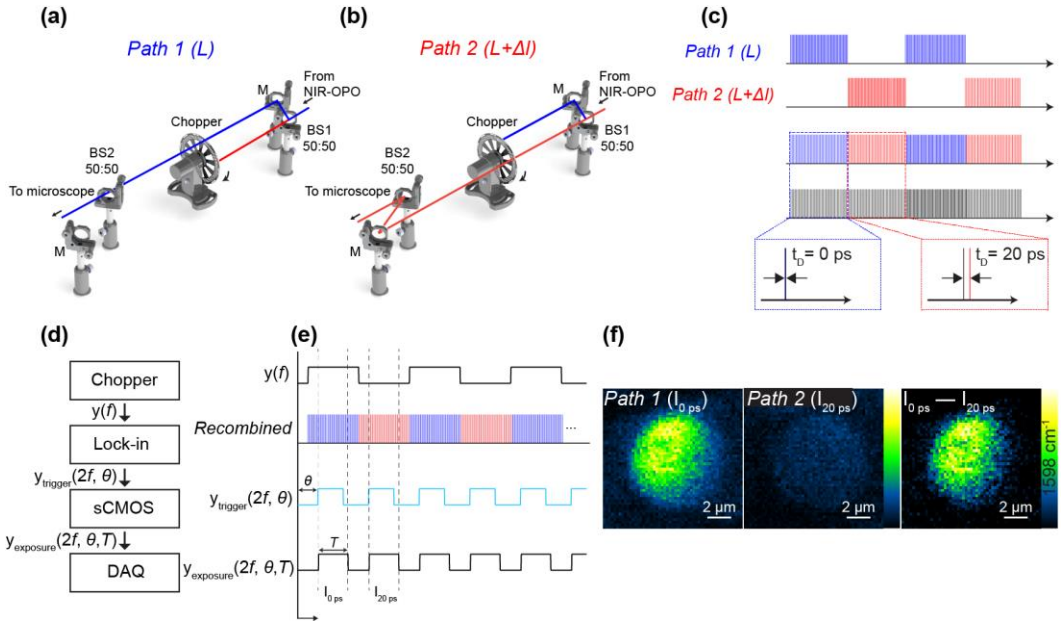

Fig. 4. Kilohertz WF-BonFIRE imaging using temporal-delay modulation using Mode 1 (FOV = 12.5 μm). (a-c) Experimental set-up of temporal-delay modulation scheme. NIR laser pulses, divided into Path 1 (a, blue) and Path 2 (b, red), which have the exact same intensity but with different path lengths (Δl), introduce different temporal delays (0 ps and 20 ps) relative to the pulse trains of the MIR pulses after recombination at BS2 (c). A chopper is precisely aligned and synchronized to ensure that only one path of NIR pulse trains reach the sample at any given time. BS: Beam splitter. (d) Wiring diagram for camera-chopper synchronization. (e) Synchronization timing chart. (f) Kilohertz (FPS, 1500 Hz) WF-BonFIRE image ($I_{0\ ps} - I_{20\ ps}$) acquired using temporal-delay modulation, through subtraction of subsequent camera frame images, where one image is from Path 1 pulse trains (Path 1 ($I_{0\ ps}$)) and the other image is from Path 2 pulse trains (Path 2 ($I_{20\ ps}$)).

um^2 area within 10 s **(Fig. 3(d), Mosaic)**, with high bond-selectivity **(Fig. 3(d), inset)**. Similarly, ATTO680-labeled α-tubulin **(Fig. 3(e) & (f))** and EdU **(Fig. 3(g) & (h))** were imaged with WF-BonFIRE (Mode 2). The high SNR enabled resolving clear tubulin **(Fig. 3(e))** and nuclei **(Fig. 3(g))** structures, providing detailed insights into their spatial organization. Here, a single FOV image successfully captured an entire HeLa cell **(Fig. 3(e))** and multiple nuclei **(Fig. 3(g))**.

Kilohertz WF-BonFIRE imaging with newly-developed temporal-delay modulation

A major advantage of WF microscopy is its ability to perform live-cell dynamic imaging at kilohertz frame rates surpassing video-rate FPS, which is valuable for applications such as tracking bacterial movement or mapping the neuronal action potentials. Although WF-BonFIRE achieved microsecond acquisition speed for a single image, a bottleneck to reaching kilohertz framerate is the requirement to subtract subsequent images between the temporal on (t_D=0 ps) and off states (t_D=20 ps) to effectively remove the flat photothermal background, which accumulates over a slower timescale[26]. The adjustment of the temporal delay involves tuning a delay stage, which requires an additional 0.2-second mechanical settling **(Fig. S10)**, thereby hindering the achievement of real-time dynamic imaging. High frequency modulation of the MIR proved to be an effective approach in removing photothermal background in PS-BonFIRE[26]. However, such approach is challenging with

high-sensitivity wide-field camera detection with such high-frequency modulation (beyond 1 MHz).

To address this challenge, we developed a temporal-delay modulation scheme that allows instantaneous modulation of pulse delays without relying on the physical position of the mechanical delay line **(Fig. 4(a) & (b))**. To achieve this, the NIR probe beam was split into two pulse trains of equal intensity using a beam splitter **(Fig. 4(a) & (b), BS1)**. The equal intensity for each beam arm was carefully calibrated using a continuously variable neutral density (ND) filter. One path was deliberately lengthened by Δl relative to the other **(Fig. 4(b))**, introducing an additional delay (t_D) of about 20 ps compared to the pulse trains from the shorter path with t_D=0 ps **(Fig. 4(a))**. To synchronize imaging, a chopper rotating at half the frequency of camera frame rate was employed to alternately allow pulse trains from only one path to reach the sample at a time, while blocking the other **(Fig. 4(a) & (b), Chopper)**. These two beams were then recombined using a second beam splitter **(Fig. 4(a) & (b), BS2)** and directed towards the sample, producing pulse trains with alternating temporal delays **(Fig. 4(c), Recombined at BS2)**. The chopper was precisely synchronized with the camera, ensuring that one image was captured with only the first pulse train at t_D = 0 ps, followed by another image with the second pulse train at t_D = 20 ps, **(Fig. 4(d) & (e))**.

In Figure 4d, we present a wiring diagram for control signals that govern camera and lock-in synchronization within the system. The reference output from the chopper (y(*f*)) is doubled in frequency by a lock-in amplifier, and this digital output ($y_{trigger}(2f, \theta)$) serves as the trigger for the sCMOS camera's exposure **(Fig. 4(d) & (e), $y_{exposure}(2f, \theta, T)$)**. The critical elements for achieving precise synchronization are the camera's exposure timing output and the recombined alternating pulse train **(Fig. 4(e))**. To ensure seamless coordination, adjustments are made to the lock-in phase (θ) to account for the chopper's rise and fall times, during which the beam partially obstructs. Moreover, the exposure duration (T) is set to approximately 60% of the reciprocal of the doubled chopper frequency ($1/2f$).

Utilizing the temporal-delay modulation scheme, we performed real-time WF-BonFIRE imaging on a Rh800 blend polymer sample **(Fig. 4(f))**. Subsequent camera frames corresponding to Path 1 ($I_{0\ ps}$) and Path 2 ($I_{20\ ps}$) delays were captured according to the chopper's modulation frequency **(Fig. 4(e))**. Consequently, a background-free WF-BonFIRE image **(Fig. 4(f), $I_{0\ ps}$-$I_{20\ ps}$)** was directly obtained through subtraction. As a control, dark images were consistently confirmed by setting the time delays of Path 1 and Path 2 to the temporal-off position, indicating the absence of artifacts or power difference between the two paths **(Fig. S11)**. Using the temporal-delay modulation, we achieved kilohertz real-time WF-BonFIRE imaging at 1500 FPS **(Fig. 4(f))**. To demonstrate WF-BonFIRE's dynamic imaging capabilities beyond video rate, we applied it to track the random motion of Rh800-stained *E. coli* —a critical aspect of microbial behavior in liquid environments. The diffusion coefficient of *E. coli* has been experimentally measured to range from 10 to 100 $\mu m^2/s$ in aqueous buffers and polymeric solutions[33]. Furthermore, *E. coli* exhibit rapid rotational and tumbling motions [34]. To effectively capture and analyze this rapid microscopic motion, high-speed microscopy with frame rates exceeding several tens of frames per second is required. We acquired WF-BonFIRE images at 150 FPS. In **Fig. 5(a)**, eight consecutive frames within 50 milliseconds are displayed, confirming that WF-BonFIRE can precisely track the rapid movement of *E. coli* without motion artifacts **(Fig. 5(a) & (b), Movie S1)**.

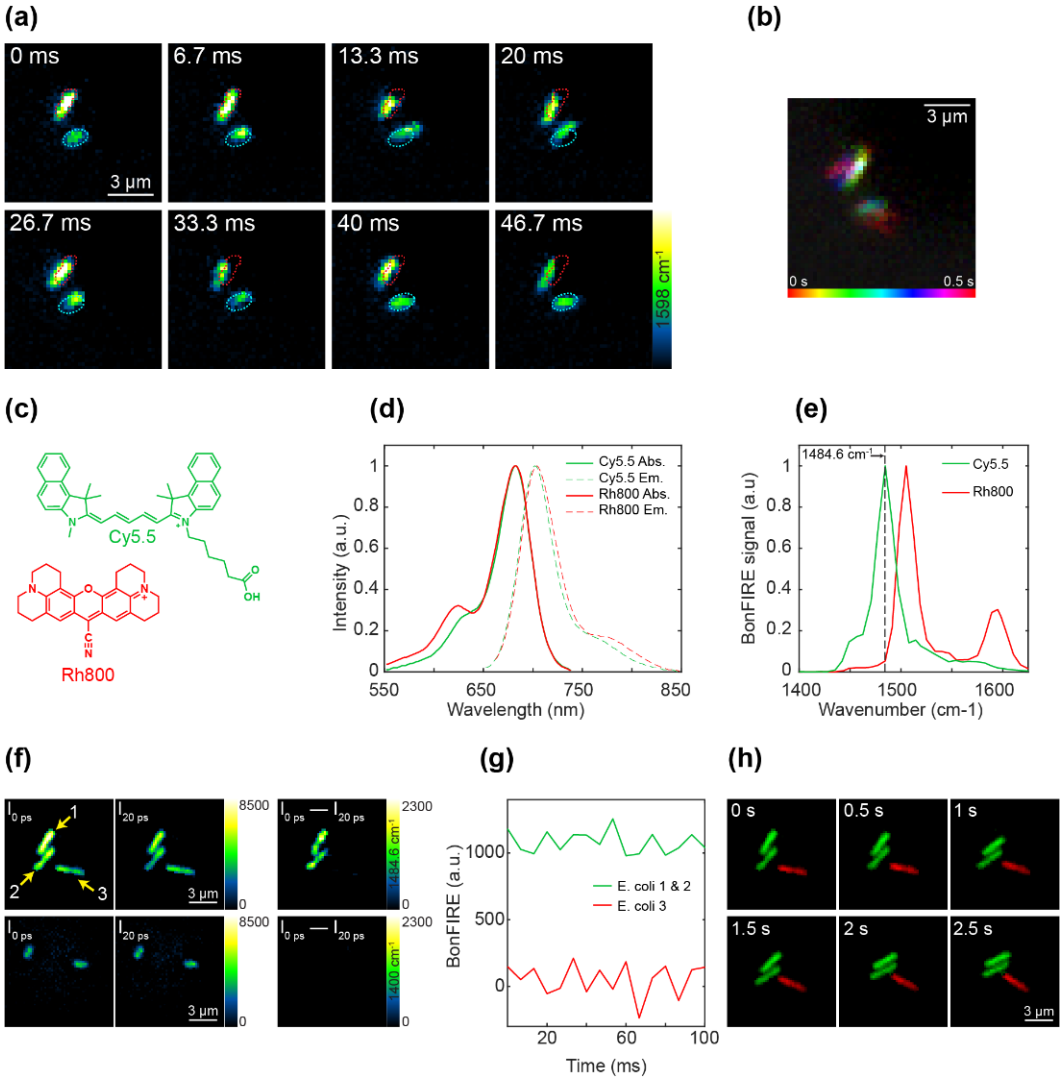

Fig 5. High-speed WF-BonFIRE imaging with real-time and multicolor visualization of fluorophore-stained *E. coli* at 150 frames per second (FPS) using temporal-delay modulation. (a-b) Single-color WF-BonFIRE imaging (a) of Rh800-stained *E. coli* at sequential time points. Red and blue dotted profiles indicate the positions of the Rh800-stained *E. coli* at t = 0 ms frame. FPS: 150 Hz. Temporal color-coded image (b) showing the moving trajectory of *E. coli* over a period of t = 0 to 0.5 s. (c-h) Multicolor WF-BonFIRE imaging at 150 FPS. Chemical structures (c), absorption (solid) and emission (dashed) spectra (d) in PBS, and the BonFIRE spectra (e) of two dyes Cy5.5 (green) and Rh800 (red). WF-BonFIRE images (f, $I_{0\ ps} - I_{20\ ps}$) of *E. coli* mixtures separately stained with Cy5.5 and Rh800 imaged at 1484.6 cm^{-1} (top row, 1484.6 cm^{-1}) and at off-resonance (bottom row, 1400 cm^{-1}) frequencies acquired using temporal-delay modulation. BonFIRE signal (g) of *E. coli* 1 & 2 and 3 indicated in f at 1484.6 cm^{-1} as a function of time. Color-coded images (h) at different representative time points (Cy.5.5, *E. coli* 1 & 2, green and Rh800, *E. coli* 3, red), based on the chemically sensitive WF-BonFIRE signal (g).

Multicolor tracking of E. coli using temporal-delay modulation

Leveraging the unique advantage of high-speed (at 150 FPS) and chemically sensitive WF-BonFIRE imaging, we sought to achieve multicolor imaging at the same frame rate. To test this, we used widely used fluorophores Rh800 and Cy5.5 **(Fig. 5(c))**. Despite the nearly identical emission and absorption spectra of these dyes **(Fig. 5(d))**, which make them difficult to distinguish using fluorescence alone, their distinct chemical structures result in

resolvable BonFIRE peaks **(Fig. 5(e))**, enabling clear differentiation of the two molecules in the BonFIRE channel. By employing temporal-delay modulation, we captured successive camera frames at Path 1 ($I_{0\ ps}$) and Path 2 ($I_{20\ ps}$) delays at 300 Hz, corresponding to a WF-BonFIRE frame rate of 150 FPS. At 1484.6 cm^{-1}, strong WF-BonFIRE signal was observed in single-color *E. coli* stained with Cy5.5, while no WF-BonFIRE signal was detected in those stained only by Rh800 **(Fig. S12, Movie S2 & S3)**. We then mixed two populations of *E. coli*, each stained separately with Rh800 and Cy5.5, and imaged at 1484.6 cm^{-1} and 150 FPS. Although a single fluorescence channel showed no distinguishable differences between the three *E. coli* cells **(Fig. 5(f), $I_{0\ ps}$ & $I_{20\ ps}$)**, our WF-BonFIRE channel **(Fig. 5(f), $I_{0\ ps}$ - $I_{20\ ps}$, 1484.6 cm^{-1})** clearly differentiated them: *E. coli* containing Cy5.5 exhibited a strong BonFIRE signal, while those with Rh800 showed essentially no signal at 1484.6 cm^{-1}, but a detected fluorescence at $I_{20\ ps}$ **(Fig. 5(g) & Fig. S13)**. As a control, tuning the MIR laser excitation to 1400 cm^{-1}, where both dyes are vibrationally off-resonant, resulted in no BonFIRE signal for any *E. coli* entering the field of view, monitored by fluorescence at $I_{20\ ps}$ **(Fig. 5(f), 1400 cm^{-1})**. The color-coded images **(Fig. 5(h), Movie S4 & Fig. S14)**, based on chemically sensitive WF-BonFIRE signal **(Fig. 5(g))**, effectively captured the real-time movement of *E. coli*, enabling multicolor tracking at speeds far exceeding the standard video rate.

5.4 Discussion

In this manuscript, we present wide-field bond-selective fluorescence imaging that achieves high sensitivity and speed. This advancement is attributed to the efficient vibronic transitions of WF-BonFIRE, which reduce the typically high photon flux requirements of multiphoton microscopy. We demonstrate significant increases in imaging speed using WF-BonFIRE compared to PS-BonFIRE, for both polymer films at high concentrations and single-molecule samples. Key results include achieving a 20-millisecond exposure time for single-molecule WF-BonFIRE imaging with robust SNRs, and rapid WF-BonFIRE acquisition to capture fine structures in live neurons and cells at low concentrations. This method achieved large FOV imaging (200x200 μm^2) within several seconds, exceeding point-scanning capabilities. Moreover, by introducing a temporal-delay modulation scheme, WF-BonFIRE achieved imaging kilohertz speed up to 1500 FPS, far exceeding video rates. This development enables the multiplexed tracking of random motion in *E. coli*, which requires millisecond-level temporal resolution, and offers potential to capture other rapid dynamic processes such as neuronal firing.

Imaging speed is influenced by the SNR, which is primarily determined by the photon flux of MIR and NIR probe lasers where detection shot noise is the limiting factor **(Fig. S15 & Table S2)**. In scenarios where the available laser power exceeds necessity, increasing the FOV by a factor of M (in one dimension) improves imaging speed by M^2. However, our system primarily operates in a source-limited regime where an increased FOV decreases photon flux and signal, resulting in a net decrease in overall imaging speed despite gains from spatial multiplexing. For this reason, we have implemented two distinct operational modes to accommodate various application needs. Mode 1 is utilized for situations that demand high photon flux, including single-molecule imaging and fast dynamic imaging. Mode 2 is selected for simultaneous detection across larger areas, suited for relatively more abundant molecular targets. Additionally, using a larger FOV reduces the

number of stage steps needed to cover a large acquisition area (e.g. 200x200 μm^2). As an outlook, adopting a higher-power laser could enable larger FOVs beyond 50 μm. Achieving speeds beyond 1500 FPS is mostly limited by the current camera technology and frequency constraints of chopper rotation. For instance, the sCMOS camera used in our experiments is limited to a maximum speed of ~3500 FPS with external triggering, and the chopper's maximum speed is limited to 10 kHz. Nonetheless, employing electro-optic modulators (EOM) and quartz crystals could provide a solution by enabling temporal-delay modulation at significantly higher frequencies, potentially overcoming these limitations[35].

WF-BonFIRE offers unique advantages over conventional wide-field fluorescence imaging by integrating bond-selectivity with enhanced speed, enabling fast vibrational lifetime imaging in live cells. This makes local environment sensing more accessible, quantitative, and physically interpretable in biological systems. For example, WF-BonFIRE holds exciting potential for electric field sensing, a critical task in molecular biology for characterizing enzyme active sites and mapping hydration[36–38]. Recently, we demonstrated that nitrile vibrational lifetimes can detect local electric fields in a physically interpretable manner, a task challenging for fluorescence due to its complex response to applied fields[29].

In addition to local environment sensing, WF-BonFIRE enables high-speed multiplexed imaging by leveraging the narrow linewidths of vibrational peaks. This capability allows for simultaneous monitoring of multiple molecular targets, providing insights into microbial behavior, live-cell processes, and complex biological interactions in real time [39]. Moving forward, we aim to expand these multiplexing capabilities by targeting additional vibrational peaks in both the fingerprint and cell-silent regions, further broadening the palette of BonFIRE-compatible dyes for high-content imaging (**Fig. S16)**.

Furthermore, WF-BonFIRE presents significant opportunities for super-resolution bond-selective imaging, overcoming limitations faced by existing fluorescence-based methods. In chemical imaging, achieving sub-100 nm spatial resolution has been challenging due to limited SNR[40–43]. Combining chemical imaging with techniques such as STED and RESOLFT often results in photobleaching and limits multiplexing capabilities. In contrast, the sensitivity and speed of WF-BonFIRE offer considerable opportunities for super-resolution bond-selective imaging, especially using single-molecule localization microscopy (SMLM), which could substantially minimize photobleaching effects[44]. When combined with SMLM, WF-BonFIRE could enable highly multiplexed super-resolution microscopy with local environment sensing[29], addressing a challenge for current fluorescence techniques.

5.5 Methods

Materials

ATTO dyes were purchased from ATTO-TEC. Rhodamine 800 was purchased from Sigma Aldrich. All dyes were aliquoted in DMSO as stock solutions (10 mM) upon receipt and stored at −20 °C. The following primary antibodies were used: anti-α-tubulin in rabbit (ab18251, Abcam) and anti-GFAP in mouse (3670S, Cell Signaling Technology). The following secondary antibodies were used: goat anti-mouse antibody (31160, Invitrogen) and goat anti-rabbit antibody (31210, Invitrogen).

Experimental setup of WF-BonFIRE

The laser sources for WF-BonFIRE are identical to that of PS-BonFIRE1. A 1.8 ps, 80 MHz, 1031.2 nm mode-locked Yb fiber laser (aeroPULSE PS10, NKT Photonics, Copenhagen, Denmark) was used as a seed laser for both NIR and MIR optical parametric oscillators (OPOs), providing wide wavelength turnabilities. The frequency doubled beam was used to pump the NIR-OPO (picoEmerald, Applied Physics and Electronics), which tunes from 700-960 nm. IR-OPO (Levante IR, Applied Physics and Electronics, Berlin, Germany) generates an idler beam that tunes from 2.1-4.8 μm (2083-4762 cm-1). Differential frequency generation (HarmoniXX DFG, Applied Physics and Electronics) inputs signal and idler beams of the IR-OPO to generate MIR wavelengths from 5-12 μm (833-2000 cm-1). The bandwidth of NIR and MIR pulses is 10 cm-1. NIR power of 1-50 mW and MIR power of 50 mW on sample were used for all Mode 1 and Mode 2 imaging.

For wide-field illumination, the NIR beam was focused onto the back focal plane of the NIR objective (XLPLN25XWMP2, Olympus) using plano-convex lens to ensure homogeneous illumination. The average power density of the NIR beam focused at the back focal plane was < 2.5 kW/cm^2, below the manufacturer's general damage threshold guideline. The location of the back focal plane was confirmed by monitoring the collimation of the beam after the objective at varying lens position. A 2000 mm (LA1258-B-ML, Thorlabs) and 500 mm (LA1908-B-ML, Thorlabs) focal length lens were used to achieve 12.5-μm (Mode 1) or 50-μm (Mode 2) FOVs, respectively. The MIR beam was loosely focused onto the sample plane using a 6.35 mm (39-469, Edmund optics) or a 20 mm (LA7733, Thorlabs) focal length lens to achieve 12.5-μm (Mode 1) and 50-μm (Mode 2) FOVs, respectively. The lenses used for MIR illumination in Mode 1 and Mode 2 are not optimized for large MIR wavelength ranges, and thus chromatic aberration needs to be considered. To assess the extent of chromatic aberration, we generated chromatic focal shift curves using Code V. These simulations revealed focus shifts of 0.11 μm/cm^{-1} and 0.27 μm/cm^{-1} for these lenses respectively. To compensate for this, the z-position of the lens was optimized for each IR frequency using a focusing module. This ensures that the MIR density profile at the sample plane remains consistent, minimizing spectral distortion caused by chromatic aberration. For the imaging path, a sCMOS camera (C15440-20UP, Hamamatsu Photonics) was installed at the focal plane of the tube lens with focal length of 200 mm. The magnification of the imaging system was 200 mm/7.2 mm = 27.78x, confirmed by measuring the effective pixel size. Fluorescence was separated from excitation using a dichroic mirror (FF738-FDi01, AVR optics) and bandpass filter (FF01-665/150, AVR optics). A custom LabVIEW program was used for all data acquisition, including stage scan, delay line movement, and camera capture.

For temporal-delay modulation, a pair of pellicle beamsplitters (BP145B2, Thorlabs) were used to divide the beam into two paths. To ensure equal power in both beams, a continuously variable neutral density (ND) filter (NDL-10C-2, Thorlabs) was placed in one of the paths and adjusted until the fluorescence signals measured using a photomultiplier tube (PMT1002, Thorlabs) from both paths were identical. The XY translation stage of the chopper (MC2000B, Thorlabs) was then fine-tuned to make both beams equidistant from the chopper's center. The optimal position of the chopper was found by minimizing the demodulated anti-stokes fluorescence signal at the chopper frequency. The reference output from the chopper was frequency-doubled using a lock-in

amplifier (HF2LI, 50-MHz bandwidth, Zurich), which was then used to trigger the sCMOS camera. To achieve perfect synchronization between the chopper and the camera, the phase of the lock-in output was adjusted. This setup ensured that only the pulse trains from a single path reached the sample at any given time. For 1500 Hz WF-BonFIRE imaging, the camera was operated at 3000 FPS, capturing consecutive frames alternating between two temporal delays. Each frame consisted of 60 × 60 pixels, corresponding to a field of view (FOV) of 14 μm × 14 μm, sufficient to capture the FOV of Mode 1. The BonFIRE imaging frame rate, therefore, is effectively 1500 FPS. The camera speed is determined by the camera's operation mode and the number of rows acquired. Using external triggering and ~60 × 60 pixels, we verified experimentally that the fastest speed that can be achieved by the sCMOS camera is 3480 FPS. This was done by counting the number of frames acquired within a known time window.

For mosaic acquisitions, the unevenness of the beam was addressed by performing a nonlinear background correction, which involved: (1) averaging the frames to generate a background image, (2) fitting the background image with a two-dimensional polynomial, and (3) dividing each frame by the fitted polynomial to correct for power variations.

Preparation of single-molecule and polymer samples

For single molecule samples, PVA (363138, Sigma) solution of 2.7 mg/mL in H2O was used to dilute Rh800 (83701, Sigma) solution in DMSO to 1 pM. Rh800-PVA solution was spin coated onto a CaF2 window (CAFP10-0.35, Crystran) at 5000 RPM for 30 seconds. For blend polymer film sample, 12 mg/mL polystyrene (430102, Sigma) and 18 mg/mL PMMA (200336, Sigma) in toluene were mixed. After dissolving Rh800 with the mixture to reach a final concentration of 100 μM, Rh800-PS-PMMA solution was spin coated (BSC-100, MicroNano Tools) onto a CaF2 window at 1200 RPM for 30 seconds.

Preparation of fixed HeLa cell samples

HeLa-CCL2 (ATCC) cells were seeded onto 10 mm diameter 0.35-mm-thick CaF2 windows at a cell density of 105 cells/mL and were cultured in Dulbecco's modified Eagle medium (DMEM) at 37 °C with 5% CO2. The DMEM mixture was composed of 90% DMEM (11965, Invitrogen), 10% fetal bovine serum (FBS; 10082, Invitrogen), and 1× penicillin/streptomycin (15140, Invitrogen). For HeLa cells with EdU labeling, the medium was switched to FBS-free DMEM (Gibco) for 20–22 hours to synchronize the cell cycle. After synchronization, the medium was reverted to the original DMEM and EdU (10 mM stock in H2O) was added at a concentration of 200 μM for 20–24 hours. The cells were then fixed with 4% paraformaldehyde (PFA) for 20 min, and the PFA was removed using Dulbecco's phosphate-buffered saline (DPBS). For click reaction labeling of EdU incorporated cells, the cells underwent permeabilization using 0.2% X-100 (T8787, Sigma) for 20 min. They were then washed with 2% BSA in PBS. Subsequently, the cells were incubated in a reaction buffer containing 10 μM of ATTO680, prepared as specified in the click reaction buffer kit (Thermo Fisher, C10269). After a 30-minute incubation at room temperature, the cells were washed again with 2% BSA in PBS prior to imaging.

Preparation of live and fixed neuron culture samples

For neuron culture, primary hippocampal neurons were isolated from neonatal Sprague–Dawley rat pups using a Caltech-approved protocol (IA22-1835) by the Institutional Animal Care and Use Committee (IACUC). The brains were removed and immersed in ice-chilled Hanks' balanced salt solution (Gibco) in a 10-cm Petri dish. Under a dissection microscope, the hippocampi were separated, finely minced to approximately 0.5 mm pieces, and digested in 5 mL of 0.25% Trypsin-EDTA (Gibco) at 37°C in a 5% CO2 incubator for 15 min. After aspiration of the Trypsin-EDTA, the tissue was quickly neutralized with 2 mL of DMEM containing 10% FBS. The tissue pieces were then gently moved into 2 mL of neuronal culture medium (Neurobasal A, B-27 and GlutaMAX supplements, Thermo Fisher, with 1× penicillin-streptomycin) to dissociate the cells. The resultant cell suspension was further diluted to a final density of 9 × 104 cells/mL using the same medium. Each well of a 24-well plate, containing pre-coated CaF2 windows, received 0.7 mL of this suspension. The CaF2 windows had been prepared by incubating them with 100 μg/mL poly-d-lysine (Sigma) at 37°C and 5% CO2 for 24 hours, followed by a laminin mouse protein (Gibco) layer at 10 μg/mL, also at 37°C and 5% CO2 overnight. After rinsing twice with ddH2O and drying in a biosafety cabinet at room temperature, the neurons were maintained with a half-medium exchange every four days. At day 14 in vitro (DIV14), neurons were fixed with 4% paraformaldehyde (PFA) for 20 min, washed with DPBS, and could be stored in DPBS at 4 °C for several days. For live neuron samples, the neurons were incubated in DMEM containing 5 μM Rh800 for 30 minutes at 37°C in a 5% CO2. After incubation, the DMEM was replaced with D2O-PBS before proceeding to imaging.

Immunolabeling of fixed HeLa and neurons

Fixed cells were first permeabilized using 0.1% Triton X-100 (T8787, Sigma) for 20 min. After blocking for 1–3 h in 10% goat serum/1% BSA/0.3 M glycine/0.1% PBST, the cells were incubated overnight at 4 °C in 10 μg mL−1 primary antibody in 3% BSA. After washing with PBS, the cells were blocked using 10% goat serum in 0.1% PBST for 1–3 h, followed by overnight incubation at 4 °C in ~10 μg mL−1 secondary antibody in 10% goat serum. The cells were blocked with 10% goat serum for 30 min and dried before imaging.

Preparation of live E. coli sample

E. coli BL21 was cultured in LB broth overnight at 37°C. The *E. coli* culture was centrifuged, and the supernatant was removed. The bacterial pellet was then incubated for 3-10 minutes in PBS containing 0.5 μM Cy5.5 or Rh800. After another centrifugation and removal of the supernatant, the cells were resuspended in D2O before imaging. For two-color *E. coli* samples, the dye-stained *E. coli* solutions were mixed prior to imaging.

5.6 Acknowledgements

We thank Dr. Ryan Leighton for proofreading of the manuscript. L. W. acknowledges the support of an Alfred P. Sloan Research Fellowship. L.W. is a Heritage Principal Investigator supported by the Heritage Medical Research Institute at Caltech.

5.7 References

1. Yang, W. & Yuste, R. In vivo imaging of neural activity. *Nat. Methods* **14**, 349–359 (2017).
2. Ji, N., Freeman, J. & Smith, S. L. Technologies for imaging neural activity in large volumes. *Nat. Neurosci.* **19**, 1154–1164 (2016).
3. Papagiakoumou, E., Ronzitti, E. & Emiliani, V. Scanless two-photon excitation with temporal focusing. *Nat. Methods* **17**, 571–581 (2020).
4. Wu, J. *et al.* Kilohertz two-photon fluorescence microscopy imaging of neural activity in vivo. *Nat. Methods* **17**, 287–290 (2020).
5. Dodt, H.-U. *et al.* Ultramicroscopy: three-dimensional visualization of neuronal networks in the whole mouse brain. *Nat. Methods* **4**, 331–336 (2007).
6. Möckl, L. & Moerner, W. E. Super-resolution Microscopy with Single Molecules in Biology and Beyond–Essentials, Current Trends, and Future Challenges. *J. Am. Chem. Soc.* **142**, 17828–17844 (2020).
7. Skinner, S. O., Sepúlveda, L. A., Xu, H. & Golding, I. Measuring mRNA copy number in individual Escherichia coli cells using single-molecule fluorescent in situ hybridization. *Nat. Protoc.* **8**, 1100–1113 (2013).
8. Chen, K. H., Boettiger, A. N., Moffitt, J. R., Wang, S. & Zhuang, X. Spatially resolved, highly multiplexed RNA profiling in single cells. *Science* **348**, aaa6090 (2015).
9. Gustafsson, M. G. L. *et al.* Three-Dimensional Resolution Doubling in Wide-Field Fluorescence Microscopy by Structured Illumination. *Biophys. J.* **94**, 4957–4970 (2008).
10. Hu, F., Shi, L. & Min, W. Biological imaging of chemical bonds by stimulated Raman scattering microscopy. *Nat. Methods* **16**, 830–842 (2019).
11. Min, W., Freudiger, C. W., Lu, S. & Xie, X. S. Coherent Nonlinear Optical Imaging: Beyond Fluorescence Microscopy. *Annu. Rev. Phys. Chem.* **62**, 507–530 (2011).
12. Freudiger, C. W. *et al.* Label-Free Biomedical Imaging with High Sensitivity by Stimulated Raman Scattering Microscopy. *Science* **322**, 1857–1861 (2008).
13. Wei, L. *et al.* Super-multiplex vibrational imaging. *Nature* **544**, 465–470 (2017).
14. Xiong, H. *et al.* Stimulated Raman excited fluorescence spectroscopy and imaging. *Nat. Photonics* **13**, 412–417 (2019).
15. Heinrich, C., Bernet, S. & Ritsch-Marte, M. Wide-field coherent anti-Stokes Raman scattering microscopy. *Appl. Phys. Lett.* **84**, 816–818 (2004).
16. Fantuzzi, E. M. *et al.* Wide-field coherent anti-Stokes Raman scattering microscopy using random illuminations. *Nat. Photonics* 1–8 (2023) doi:10.1038/s41566-023-01294-x.
17. Shi, L. *et al.* Mid-infrared metabolic imaging with vibrational probes. *Nat. Methods* (2020) doi:10.1038/s41592-020-0883-z.
18. Yeh, K. *et al.* Infrared spectroscopic laser scanning confocal microscopy for whole-slide chemical imaging. *Nat. Commun.* **14**, 1–12 (2023).
19. Zhang, D. *et al.* Depth-resolved mid-infrared photothermal imaging of living cells and organisms with submicrometer spatial resolution. *Sci. Adv.* **2**, e1600521 (2016).
20. Bai, Y. *et al.* Ultrafast chemical imaging by widefield photothermal sensing of infrared absorption. *Sci. Adv.* **5**, eaav7127 (2019).

21. Ishigane, G. *et al.* Label-free mid-infrared photothermal live-cell imaging beyond video rate. *Light Sci. Appl.* **12**, 174 (2023).
22. Yin, J. *et al.* Video-rate mid-infrared photothermal imaging by single-pulse photothermal detection per pixel. *Sci. Adv.* **9**, eadg8814 (2023).
23. Zhang, Y. *et al.* Fluorescence-Detected Mid-Infrared Photothermal Microscopy. *J. Am. Chem. Soc.* (2021) doi:10.1021/jacs.1c03642.
24. Laubereau, A., Seilmeier, A. & Kaiser, W. A new technique to measure ultrashort vibrational relaxation times in liquid systems. *Chem. Phys. Lett.* **36**, 232–237 (1975).
25. Whaley-Mayda, L., Guha, A., Penwell, S. B. & Tokmakoff, A. Fluorescence-Encoded Infrared Vibrational Spectroscopy with Single-Molecule Sensitivity. *J. Am. Chem. Soc.* (2021) doi:10.1021/jacs.1c00542.
26. Wang, H. *et al.* Bond-selective fluorescence imaging with single-molecule sensitivity. *Nat. Photonics* **17**, 846–855 (2023).
27. Sakai, M., Kawashima, Y., Takeda, A., Ohmori, T. & Fujii, M. Far-field infrared super-resolution microscopy using picosecond time-resolved transient fluorescence detected IR spectroscopy. *Chem. Phys. Lett.* **439**, 171–176 (2007).
28. Yan, C. *et al.* Multidimensional Widefield Infrared-Encoded Spontaneous Emission Microscopy: Distinguishing Chromophores by Ultrashort Infrared Pulses. *J. Am. Chem. Soc.* **146**, 1874–1886 (2024).
29. Kocheril, P. A., Wang, H., Lee, D., Naji, N. & Wei, L. Nitrile Vibrational Lifetimes as Probes of Local Electric Fields. *J. Phys. Chem. Lett.* 5306–5314 (2024) doi:10.1021/acs.jpclett.4c00597.
30. Dempsey, G. T., Vaughan, J. C., Chen, K. H., Bates, M. & Zhuang, X. Evaluation of fluorophores for optimal performance in localization-based super-resolution imaging. *Nat. Methods* **8**, 1027–1036 (2011).
31. Roy, R., Hohng, S. & Ha, T. A practical guide to single-molecule FRET. *Nat. Methods* **5**, 507–516 (2008).
32. Zhang, H. & Guo, P. Single molecule photobleaching (SMPB) technology for counting of RNA, DNA, protein and other molecules in nanoparticles and biological complexes by TIRF instrumentation. *Methods* **67**, 169–176 (2014).
33. Patteson, A. E., Gopinath, A., Goulian, M. & Arratia, P. E. Running and tumbling with E. coli in polymeric solutions. *Sci. Rep.* **5**, 15761 (2015).
34. Darnton, N. C., Turner, L., Rojevsky, S. & Berg, H. C. On Torque and Tumbling in Swimming *Escherichia coli*. *J. Bacteriol.* **189**, 1756–1764 (2007).
35. Hill, A. H., Munger, E., Francis, A. T., Manifold, B. & Fu, D. Frequency Modulation Stimulated Raman Scattering Microscopy through Polarization Encoding. *J. Phys. Chem. B* **123**, 8397–8404 (2019).
36. Suydam, I. T. Electric Fields at the Active Site of an Enzyme: Direct Comparison of Experiment with Theory. *Science* **313**, 200–204 (2006).
37. Zheng, C., Ji, Z., Mathews, I. I. & Boxer, S. G. Enhanced active-site electric field accelerates enzyme catalysis. *Nat. Chem.* **15**, 1715–1721 (2023).
38. Shi, L., Hu, F. & Min, W. Optical mapping of biological water in single live cells by stimulated Raman excited fluorescence microscopy. *Nat. Commun.* **10**, 4764 (2019).
39. Valm, A. M. *et al.* Applying systems-level spectral imaging and analysis to reveal the organelle interactome. *Nature* **546**, 162–167 (2017).

40. Xiong, H. *et al.* Super-resolution vibrational microscopy by stimulated Raman excited fluorescence. *Light Sci. Appl.* **10**, 87 (2021).
41. Shou, J. *et al.* Super-resolution vibrational imaging based on photoswitchable Raman probe. *Sci. Adv.* **9**, eade9118 (2023).
42. Fu, P. *et al.* Super-resolution imaging of non-fluorescent molecules by photothermal relaxation localization microscopy. *Nat. Photonics* **17**, 330–337 (2023).
43. Gong, L., Zheng, W., Ma, Y. & Huang, Z. Higher-order coherent anti-Stokes Raman scattering microscopy realizes label-free super-resolution vibrational imaging. *Nat. Photonics* **14**, 115–122 (2020).
44. Jungmann, R. *et al.* Multiplexed 3D cellular super-resolution imaging with DNA-PAINT and Exchange-PAINT. *Nat. Methods* **11**, 313–318 (2014).

5.8 Supplementary information

Table S1. Summary of speed and sensitivity of emerging bond-selective imaging modalities

Table of Reported Imaging Speeds*							
Modality	Configuration	Labels	Source	Pixel dwell time (μs)	X dimension	Y dimension	FPS
MIP[1]	Point-scanning	Label-free	Fig. 3A	2	150 pixels	100 pixels	20
MIP[2]	Point-scanning	Label-free	Fig. 3A	1000	-	-	0.033
			Fig. 4C	500	-	-	0.067
			Fig. 5A	500	-	-	0.067
SRS[3]	Point-scanning	Vibrational tags	All imaging	100	-	-	0.33
BonFIRE[4]	Point-scanning	Exogenous label	Fig. 5c	3000	-	-	0.011
SREF[5]	Point-scanning	Exogenous label	Fig. 5a	1000	-	-	0.033
epr-SRS[6]	Point-scanning	Exogenous label	Fig. 1c	4	-	-	8.3
			Fig. 2c	200	-	-	0.17
WF-MIP[7]	Wide-field	Label-free	Fig. 5b	-	87 μm	87 μm	50
MD-WISE[8]	Wide-field	Exogenous label	Fig. 5F	-	30 μm	30 μm	0.1 - 2
WF-F-MIP[9]	Wide-field	Exogenous label	Fig. 5b	-	70 μm	40 μm	20
WF-BonFIRE	Wide-field	Exogenous label	Fig. 5	-	12.5 μm	12.5 μm	150

* As a summary, the state-of-the-art acquisition speed and sensitivity reported from biological sample measurements for bond-selective imaging modalities employing exogenous dye labels, including WF-BonFIRE, are listed. Their counterpart modalities for label-free or small vibrational tags are also included as references. The imaging speeds listed refer exclusively to imaging of biological samples. When the FPS was not explicitly stated for the point-scanning system, it was calculated based on 150 × 100 pixel dimensions.

Table of Reported Sensitivity				
Modality	Configuration	Labels	Source	Detection limit (nM)
MIP[10]	Point-scanning	Label-free	Fig. 2e, 2f	5000
MIP[2]	Point-scanning	Label-free	Fig. 2B	10,000
SRS[3]	Point-scanning	Label-free	Fig. 1b	200,000
BonFIRE[4]	Point-scanning	Exogenous dye	Fig. 2h	0.5
SREF[11]	Point-scanning	Exogenous dye	Fig. 2g	8
epr-SRS[6]	Point-scanning	Exogenous dye	Fig. 1b	250
WF-MIP[7]	Wide-field	Label-free	Estimated	10,000 – 1,000,000
MD-WISE[8]	Wide-field	Exogenous dye	Not reported	
WF-F-MIP[9]	Wide-field	Exogenous dye	Estimated	100
WF-BonFIRE	Wide-field	Exogenous dye	Fig. 2(d), 2(g)	Single-molecule level

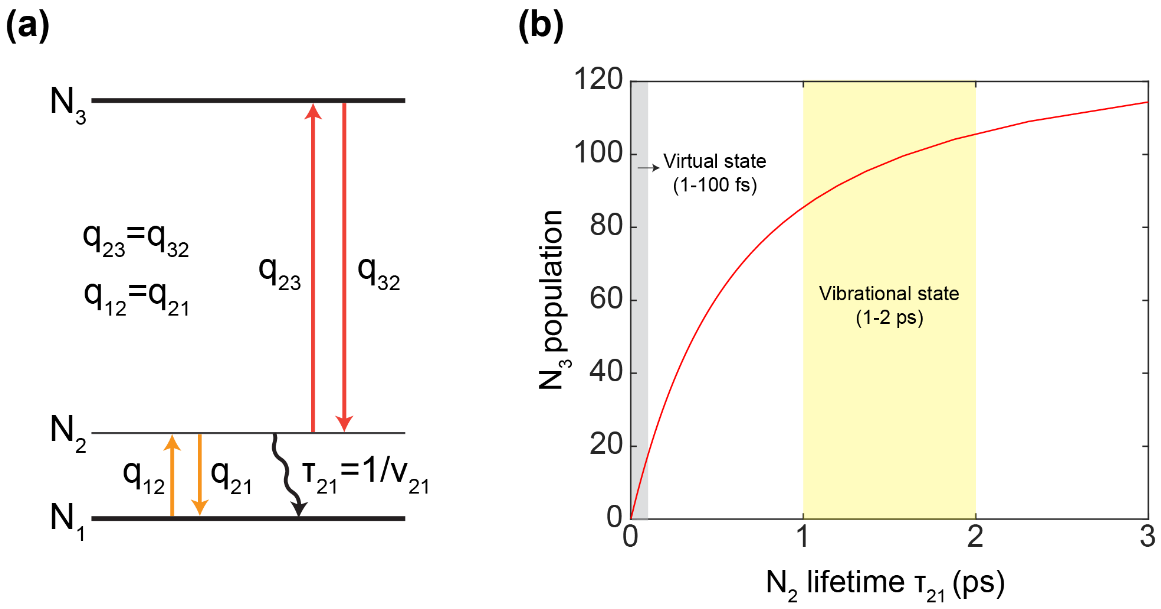

Fig. S1. BonFIRE signal calculation with varying lifetimes of intermediate state. (a) The energy diagram of a three-level system used for the simulation. N_1 and N_3 indicate the ground and excited electronic state; N_2 indicates the intermediate state, which is either a virtual state or vibrational state in our analysis. **(b)** N_3 state population as a function of vibrational lifetime of N_2 state (τ_{21}) calculated from the three-level rate equation simulations[4]. On-sample laser powers: NIR Probe=0.1 mW and MIR=10 mW. The pulse duration is 2 ps for both lasers. Gray and yellow highlights the relevant temporal regions for typical lifetimes of virtual states (1-100 fs, gray) and vibrational states (1-2 ps, e.g., double bonds and nitriles, yellow). Significant increase in N_3 population is observed as intermediate state lifetimes shifts from virtual (gray) to vibrational state (yellow), indicating efficient vibronic excitation.

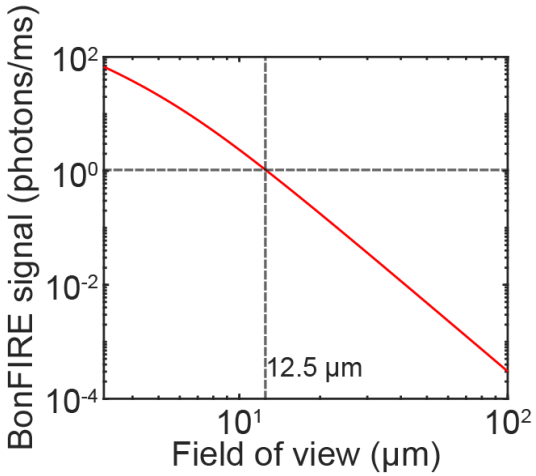

Fig. S2. WF-BonFIRE signal estimation at varying field-of-view (FOV) size using Rh800. Three-level rate equations were used to calculate the BonFIRE signal (photons/ms)[4]. On-sample MIR (50 mW) and NIR probe powers (25 mW) were used for the simulation. The pulse duration is 2 ps. At FOV of 12.5 μm, BonFIRE signal was computed to be 1 photon/ms. Signal-to-noise ratio (SNR) can be computed by the following equations:

$$SNR = \frac{QE \cdot N \cdot t}{\sqrt{\sigma^2_{shot\ noise} + \sigma^2_{read\ noise} + \sigma^2_{dark\ noise}}} \quad \text{(S1)}$$

$$\sigma_{shot\ noise} = \sqrt{QE \cdot N \cdot t} \quad \text{(S2)}$$

$$\sigma_{dark\ noise} = \sqrt{I_d \cdot t} \quad \text{(S3)}$$

where QE is quantum efficiency, N is number of photons per pixel per millisecond, t is exposure time, and I_d is dark current. At 12.5 μm FOV, SNR of 3 can be achieved with exposure times of 25 ms, indicating single-molecule sensitivity while achieving wide-field detection. We note that at single-molecule concentrations and in IR-transparent systems, background shot noise is negligible.

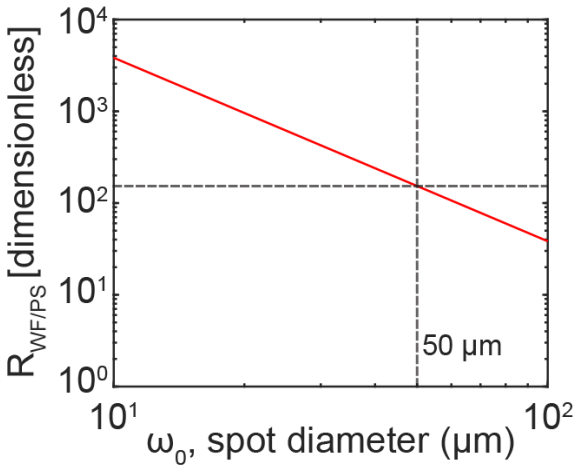

Fig. S3. WF-BonFIRE speed estimation relative to PS-BonFIRE as a function of FOV. FOV is indicated as the spot diameter of the laser beams, ω_0. Due to the quadratic reduction in photon flux across both probe and IR beams, WF-BonFIRE signal is expected to diminish quickly with increasing FOV. Although this would make single molecule detection infeasible, it should offer superior speed than the PS-BonFIRE for bio-imaging applications that do not require single-molecule sensitivity. Theoretically, the upper limit of FOV for WF-BonFIRE is when the imaging acquisition speed of WF-BonFIRE becomes equal (R=1) and then slower comparing to PS-BonFIRE. To perform the comparison, we followed a previous report that defined a pixel rate and pixel rate ratio R as follows[12]:

$$pixel\ rate\ \equiv \left(\ total\ acquisition\ time\ normalized\ by\ number\ of\ pixels\ and\ SNR^2\right)^{-1} \tag{S4}$$

$$R_{WF/PT} \equiv \frac{pixel\ rate\ for\ widefield}{pixel\ rate\ for\ point\ scanning} = \frac{\left(\frac{t_{WF}}{n_{WF}\cdot SNR_{WF}^2}\right)^{-1}}{\left(\frac{t_{PS}}{n_{PS}\cdot SNR_{PS}^2}\right)^{-1}} = \frac{n_{WF}}{n_{PS}}\frac{t_{PS}}{t_{WF}}\left(\frac{SNR_{WF}}{SNR_{PS}}\right)^2 \tag{S5}$$

where n is the number of pixels, t_{PS} is the pixel dwell time, t_{WF} is the camera exposure time, and SNR is the signal-to-noise ratio. Assuming the system shot noise is the dominant noise source, Equation (S1) is simplified to:

$$SNR\ = \sqrt{QE\cdot C\cdot\left(k\cdot\sigma\cdot I_{IR}\cdot I_{probe}\right)\cdot t} \tag{S6}$$

where QE is quantum efficiency, C is concentration, k is a scaling constant, σ is the BonFIRE cross-section, I is the peak intensity, and t is the acquisition time. Combining Equations S5 and S6 gives:

$$R_{WF/PS} = \frac{n_{WF}}{n_{PS}}\frac{t_{PS}}{t_{WF}}\cdot\left(\frac{\sqrt{QE\cdot C\cdot\left(k\cdot\sigma\cdot I_{IR_{WF}}\cdot I_{probe_{WF}}\right)\cdot t_{WF}}}{\sqrt{QE\cdot C\cdot\left(k\cdot\sigma\cdot I_{IR_{PS}}\cdot I_{probe_{PS}}\right)\cdot t_{PS}}}\right)^2 \tag{S7}$$

where QE is quantum efficiency, C is concentration, k is a scaling constant, σ is the BonFIRE cross-section, I is the peak intensity, and t is the acquisition time. Here k includes factors like quantum yield of the fluorophore and collection efficiency, but cancelled out between the PS- and WF- BonFIRE for pixel rate ratio $R_{WF/PT}$ that gives:

$$R_{WF/PS} = \frac{n_{WF}}{n_{PS}} \frac{t_{PS}}{t_{WF}} \cdot \frac{(I_{IR_{WF}} \cdot I_{probe_{WF}}) \cdot t_{WF}}{(I_{IR_{PS}} \cdot I_{probe_{PS}}) \cdot t_{PS}} \tag{S8}$$

Substituting peak intensity $I = P/A$, where P is peak power and A is spot area:

$$R_{WF/PS} = \frac{n_{WF}}{n_{PS}} \frac{t_{PS}}{t_{WF}} \cdot \frac{\frac{P_{IR_{WF}}}{A_{IR_{WF}}} \cdot \frac{P_{probe_{WF}}}{A_{probe_{WF}}} \cdot t_{WF}}{\frac{P_{IR_{PS}}}{A_{IR_{PS}}} \cdot \frac{P_{probe_{PS}}}{A_{probe_{PS}}} \cdot t_{PS}} \tag{S9}$$

Rearranging the above equation:

$$R_{WF/PS} = \frac{n_{WF}}{n_{PS}} \cdot \frac{P_{IR_{WF}}}{P_{IR_{PS}}} \cdot \frac{P_{probe_{WF}}}{P_{probe_{PS}}} \cdot \frac{A_{IR_{PS}}}{A_{IR_{WF}}} \cdot \frac{A_{probe_{PS}}}{A_{probe_{WF}}} \tag{S10}$$

We note that the photon flux of the IR laser is limited in both point-scanning and wide-field configuration, whereas the photon flux of the probe laser is in excess. This is simply because of the large spot size of the IR beam caused by longer wavelengths and lower numerical aperture of the IR objective. Hence, in both cases, maximum MIR laser powers are used resulting in $P_{IR\_WF} = P_{IR\_PT}$. Equation S10 thus simplifies to:

$$R_{WF/PS} = \frac{n_{WF}}{n_{PS}} \cdot \frac{P_{probe_{WF}}}{P_{probe_{PS}}} \cdot \frac{A_{IR_{PS}}}{A_{IR_{WF}}} \cdot \frac{A_{probe_{PS}}}{A_{probe_{WF}}} \tag{S11}$$

The number of pixels in wide-field can be described as total wide-field area divided by the pixel area:

$$n_{WF} = \frac{A_{WF}}{(pixel\ size_{WF})^2} \tag{S12}$$

while n_{PS} equal to 1 in point-scan.

The area of the focused probe in point-scanning can be approximated by 4 times the pixel area, assuming the Nyquist criterion is satisfied (i.e., a pixel size of 200 nm was used in PS-BonFIRE for a diffraction-limited probe spot size of 400 nm):

$$A_{probe_{PS}} = (pixel\ size_{PS})^2 \cdot 4 \tag{S13}$$

In wide-field, the spot size the IR and probe are matched, where ω_0 is the spot diameter of the wide-field FOV:

$$A_{WF} = A_{IR_{WF}} = A_{probe_{WF}} = \pi \left(\frac{\omega_0}{2}\right)^2 \tag{S14}$$

Combining Equation S11, S12, and S13:

$$R_{WF/PS} = \frac{A_{WF}}{(pixel\ size_{WF})^2} \cdot \frac{P_{probe_{WF}}}{P_{probe_{PS}}} \cdot \frac{A_{IR_{PS}}}{A_{WF}} \cdot \frac{(pixel\ size_{PS})^2 \cdot 4}{A_{WF}} \tag{S15}$$

With our current magnification in WF and diffraction-limited spot size in PS, the pixel sizes in WF and PS are roughly equal (~200 nm) and thereby cancel out. After substitution using Equation S14:

$$R_{WF/PS} = \pi\left(\frac{\omega_0}{2}\right)^2 \cdot P_r \cdot \frac{A_{IR_{PS}}}{\pi\left(\frac{\omega_0}{2}\right)^2} \cdot \frac{4}{\pi\left(\frac{\omega_0}{2}\right)^2} \; where \; P_r \equiv \frac{P_{probe_{WF}}}{P_{probe_{PS}}} \tag{S16}$$

$$R = \frac{16}{\pi} \cdot \frac{A_{IR_{PS}} \cdot P_r}{\omega_0^2} \; where \; P_r \equiv \frac{P_{probe_{WF}}}{P_{probe_{PS}}} \tag{S17}$$

where $A_{IR_{PS}}$ is diffraction-limited area at MIR wavelength, ω_0 is spot diameter, and P_r is the ratio of the probe power used for wide-field and point-scanning. P_r is determined by various factors (e.g. SNR, concentration of the sample, saturation) and experimentally determined to be ~5000 for many biological samples. Using Equation (S17), R is calculated to be 153 at $\omega_0 = 50$ μm and P_r = 5000, achieving more than two orders of magnitude increase in imaging speed compared to point-scanning. In theory, the FOV reaches 620 μm when R = 1, at which wide-field is the same speed compared to point-scanning. However, such large FOV would significantly sacrifice the detection sensitivity as reasoned above. We hence choose to perform Mode 2 WF-BonFIRE at $\omega_0 = 50$ μm to target both high sensitivity and fast speed. The key takeaway for Mode 2 here is that despite the parallel acquisition advantage of wide-field ($\propto \omega_0^2$), capturing multiple pixels simultaneously, the reduced photon flux for both IR and probe beam results in decrease of signal ($\propto \omega_0^{-4}$), and therefore decrease of imaging speed with increasing FOV ($\propto \omega_0^{-2}$).

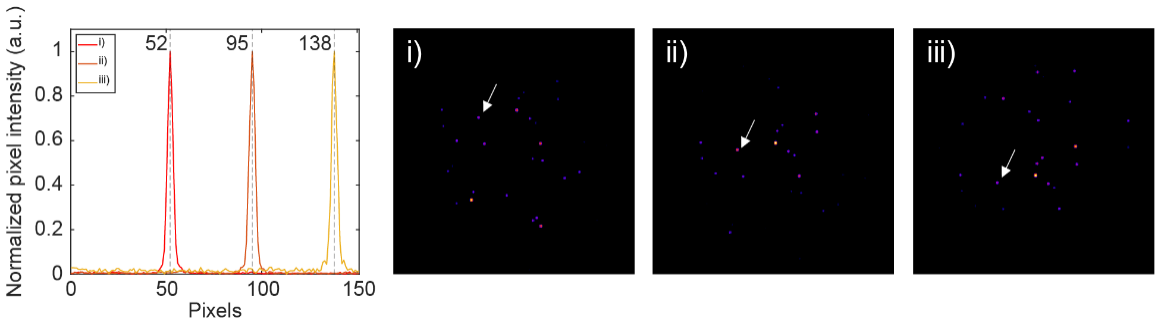

Fig. S4. System magnification characterization. Profiles of 100 nm beads that were imaged at different stage position i) X = 0 µm, ii) X = 10 µm, iii) X = 20 µm. The resulting pixel size and magnification are 10 µm /(95-52)= 0.233 µm and 6.5 µm/0.233 µm = 27.9 x, which agrees with the theoretical magnification determined by the effective focal lengths of the objective and the tube lens (200 mm/7.2 mm = 27.8x).

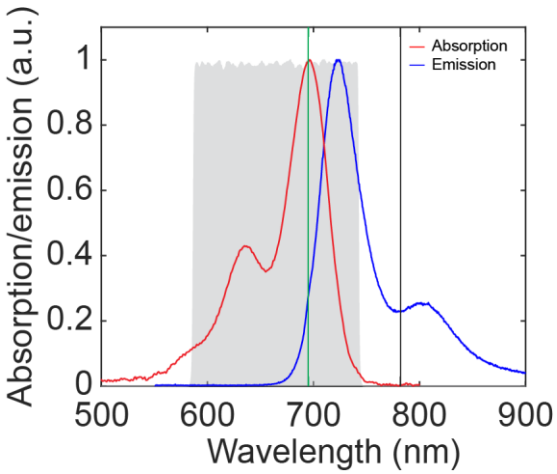

Fig. S5. Absorption and emission spectra of Rh800. The gray indicates collection window, whereas the green and black lines indicate sum frequency (MIR+NIR) and NIR probe wavelength, respectively.

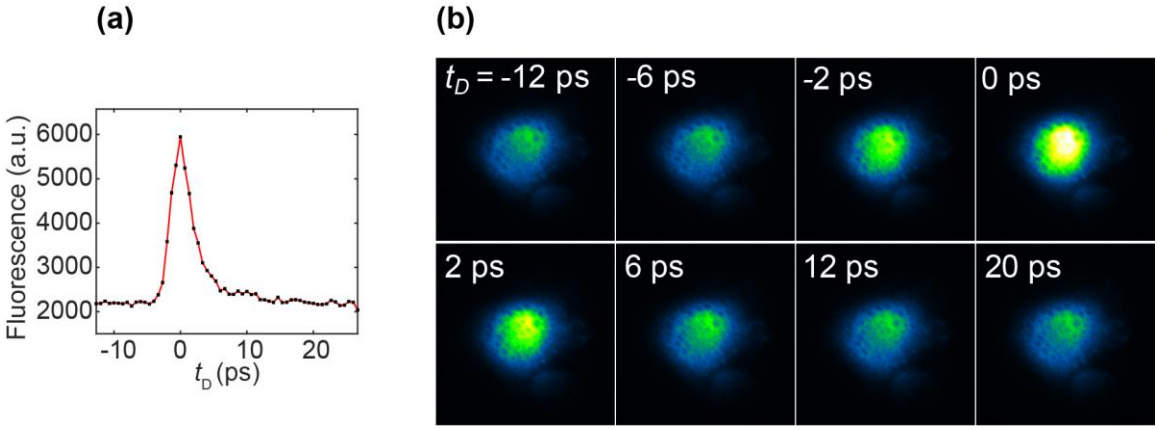

Fig. S6. Temporal profile characterization of Rh800 polymer sample (a) Temporal profile characterization of Rh800 stained polymer sample (same as shown in Fig. 2a). **(b)** Fluorescence images corresponding to different temporal delays t_D between the MIR and the NIR probe lasers ($t_D > 0$ or $t_D < 0$ indicates MIR or NIR probe pulses arriving first on sample, respectively; $t_D = 0$ indicates both laser pulses arriving the sample simultaneously). Here the background contribution is mostly due to the anti-stokes fluorescence since the polymer films is IR-transparent at this frequency region that renders minimal ambient photothermal effect, which yielded a signal-to-background (S/B) of ~200% for Rh800 in polymer film compared to that in the hygroscopic DMSO solution (S/B ~8%). However, we note that this S/B is still much smaller than expected from Boltzmann distribution analysis. Such observed higher thermal population was shown in previous reports [13], and requires further investigations.

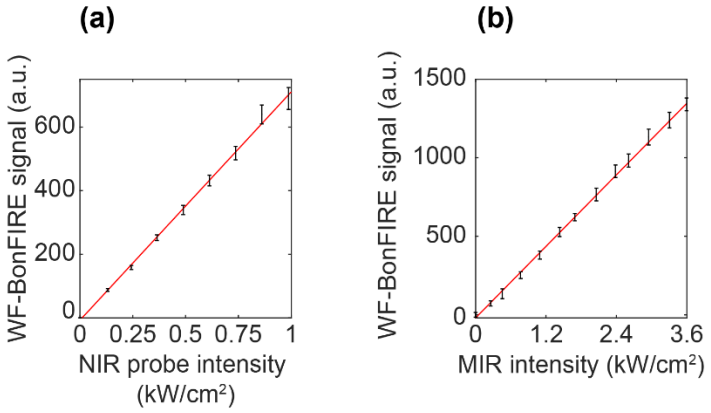

Fig. S7. Power dependence of WF-BonFIRE. (a-b) WF-BonFIRE signal dependence on the NIR probe power (a, MIR power was fixed at 4 mW on sample); and on the MIR power (b, NIR power was fixed at 50 mW on sample).

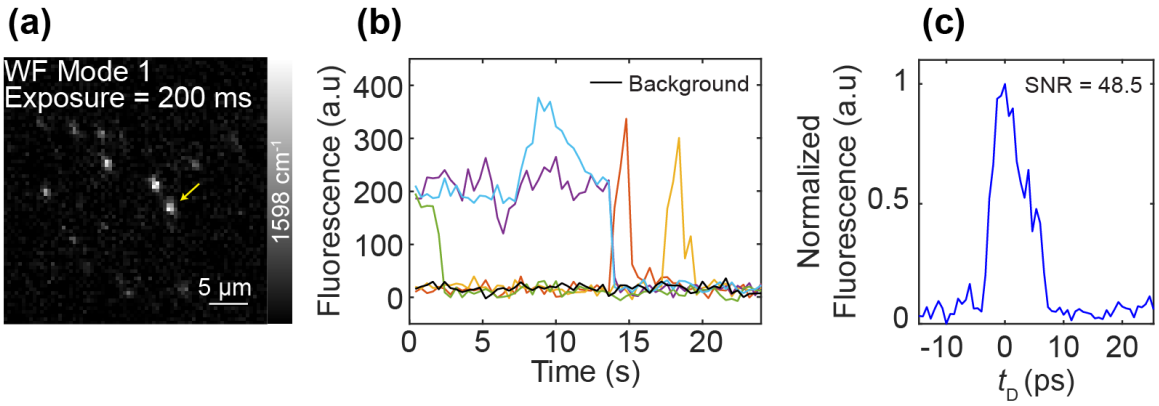

Fig. S8. Single-molecule WF-BonFIRE image at 200 ms exposure time. (a) WF-BonFIRE image of single-molecule sample at 200 ms exposure time (same as shown in Fig. 2a). **(b)** Representative single-step photobleaching and blinking curves from molecules shown in (a), confirming that the signal acquired is indeed from single molecules. **(c)** Representative temporal sweep of a molecule (yellow-arrowed in (a)) for SNR characterization.

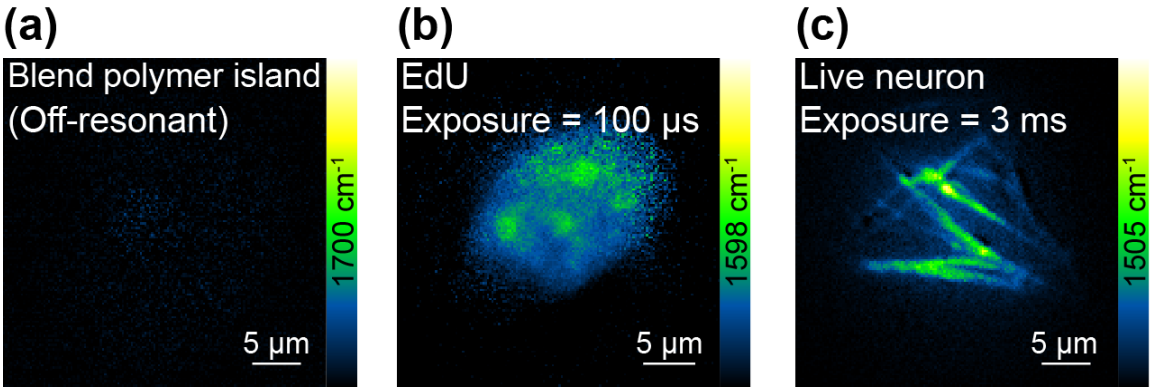

Fig. S9. WF-BonFIRE imaging (Mode 1) of various samples. (a) WF-BonFIRE image of Rh800 blend polymer island at off-resonance (1700 cm^{-1}). Exposure time: 17.6 μs. **(b-c)** WF-BonFIRE image targeting C=C vibration in ATTO680-click-labelled EdU in the nuclei of HeLa cells (b, 1598 cm^{-1}. Exposure time: 100 μs) and in Rh800-labelled mitochondria in live mouse neuronal cultures (c, 1505 cm^{-1}. Exposure time: 3 ms).

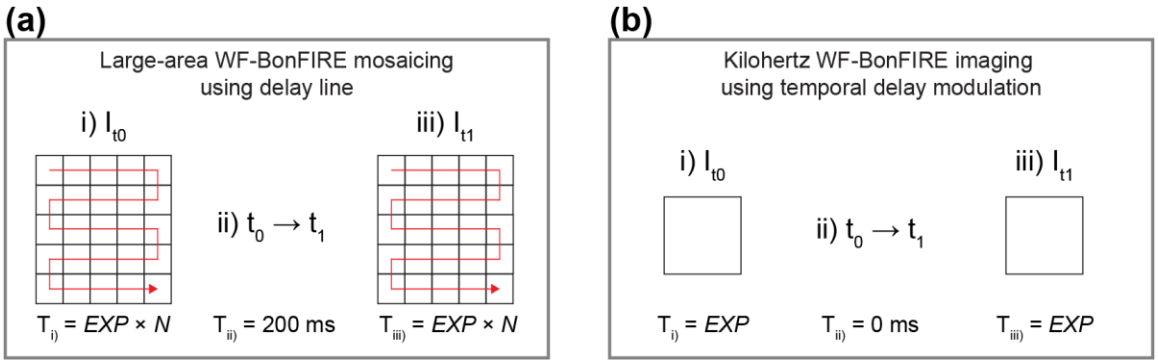

Fig. S10. Temporal delay modulation eliminates mechanical settling time of the delay line enabling real-time kilohertz WF-BonFIRE imaging. (a) Large-area WF-BonFIRE mosaicking using delay line. N is the number of FOVs acquired in a mosaic. $T_{i)}$ and $T_{iii)}$ are the image acquisition time for the designated FOV for t_D =0 and t_D = 20 ps. $T_{ii)}$ designates the delay line stabilization time. Mosaic images (I_{t0} and I_{t1}) were acquired at two different temporal positions with delay line being moved between the two mosaic acquisitions. Here the settling time $T_{ii)}$ is negligible in large-area WF-BonFIRE imaging because $T_{i)}$ and $T_{iii)}$ are much longer. (b) Kilohertz WF-BonFIRE imaging using temporal-delay modulation. $T_{ii)}$ of 200 ms is no longer negligible, as $T_{i)}$ and $T_{iii)}$ are sub-millisecond timescale to achieve kilohertz imaging speed. Temporal-delay modulation scheme is introduced to reduce $T_{ii)}$ to near 0 ms.

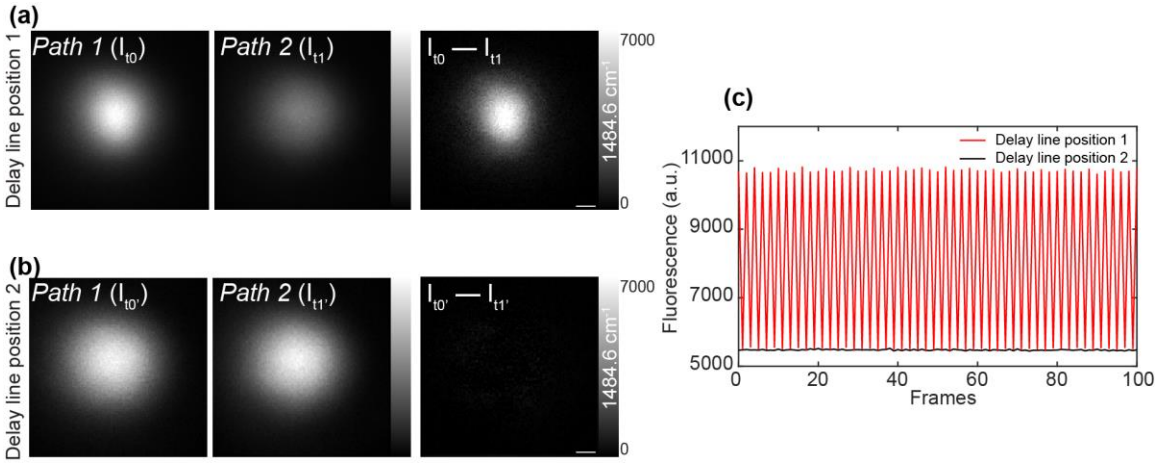

Fig. S11. Alignment characterization of the temporal-delay modulation scheme using 20 μM Cy5.5 solution in DMSO-d_6. (a-b) WF-BonFIRE images (a, $I_{t0} - I_{t1}$) and (b, $I_{t0'} - I_{t1'}$) generated by subtracting successive camera frames from Path 1 and Path 2 at delay line positions 1 and 2, respectively. At delay line position 1, temporal delay t_0 corresponds to a temporal overlap between MIR and NIR pulses (t_D =0), while t_1 indicates temporal misalignment. At delay line position 2, both temporal delays $t_{0'}$ and $t_{1'}$ represent the temporal misalignment of MIR and NIR pulses. (c) Continuous camera-frame acquired fluorescence intensities at delay line position 1 (red) and delay line position 2 (black) in (a, b). The average fluorescence modulation ($I_{t0} - I_{t1}$), i.e. the BonFIRE signal, at delay line position 1 is 5200, whereas the average modulation ($I_{t0'} - I_{t1'}$) at delay line position 2 is 20, indicating negligible signal fluctuation (0.4%), and confirming the robustness of temporal-delay modulation.

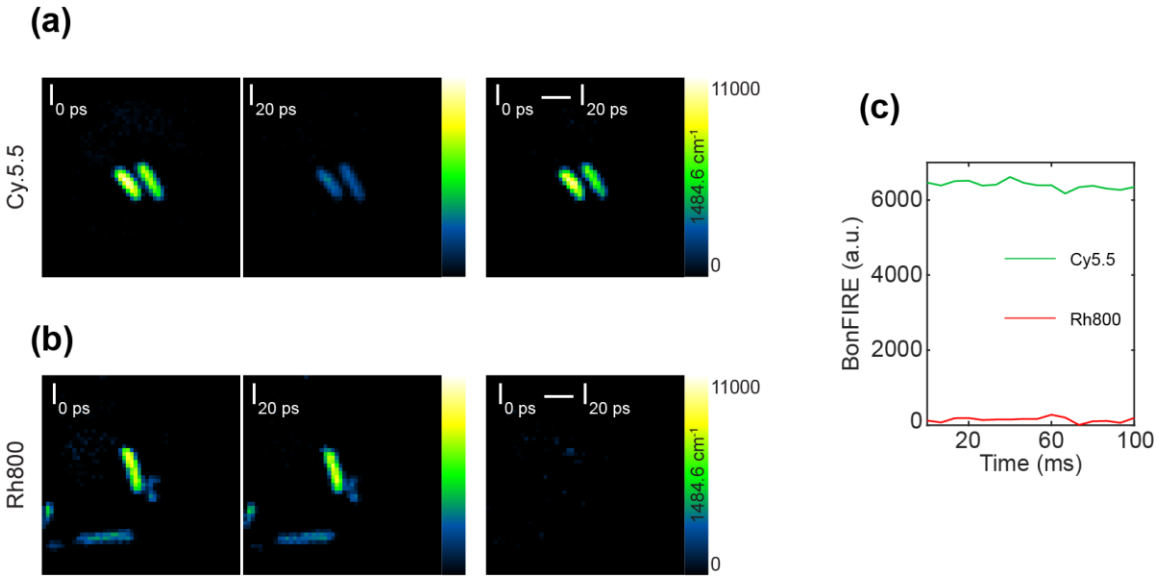

Fig. S12. Chemical-selective WF-BonFIRE imaging capturing random motion of fluorophore-stained *E. coli* at 150 frames per second (FPS) using temporal-delay modulation. (a-b) WF-BonFIRE imaging at 1484.6 cm^{-1} of Cy5.5-stained (on-resonance) *E. coli* (a, $I_{0\ ps} - I_{20\ ps}$) and Rh800-stained (off-resonance) *E. coli* (b, $I_{0\ ps} - I_{20\ ps}$) acquired using temporal-delay modulation, where one image is from Path 1 pulse trains ($I_{0\ ps}$) and the other image is from Path 2 pulse trains ($I_{20\ ps}$). (c) Average BonFIRE intensity of *E. coli* in (a) and (b) over the timespan of 100 ms, indicating bright signal for Cy5.5-stained *E. coli* (green), but dark signal for Rh800-stained *E. coli* (red) at 1484.6 cm^{-1}.

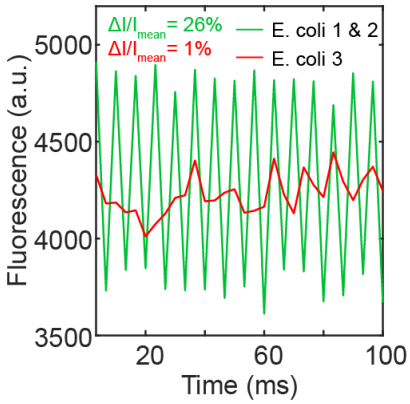

Fig. S13. Average fluorescence intensity of *E. coli* corresponding to Fig. 5f at 1484.6 cm^{-1}. *E. coli* 1 and 2 demonstrated significant fluorescence intensity modulation ($\Delta I/I_{mean}$=26%) corresponding to their WF-BonFIRE signal, whereas *E. coli* 3 showed minimal modulation ($\Delta I/I_{mean}$)=1%), confirming strong BonFIRE signals in *E. coli* 1 and 2 and the absence of BonFIRE signal in *E. coli* 3. Fluorescence intensities were calculated by applying Huang's threshold for segmentation and averaging the pixel intensities within the segmented regions.

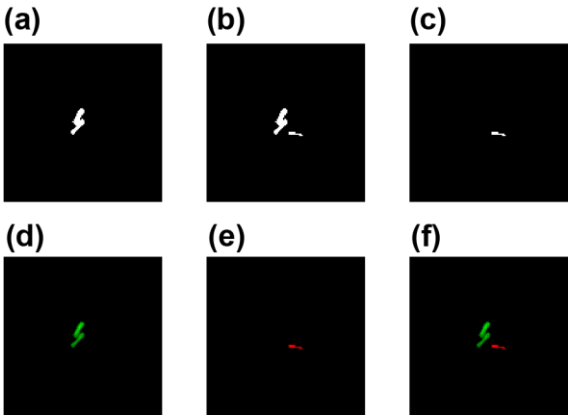

Fig. S14. Processing steps for two-color *E. coli* images. (a) Mask generated from the BonFIRE image by subtracting consecutive images acquired at different temporal delays ($I_{0\ ps} - I_{20\ ps}$). (b) Mask generated from the fluorescence image acquired at $I_{0\ ps}$. (c) Mask created by applying an XOR operation to the masks in (a) and (b). (d) Fluorescence image highlighting *E. coli* containing Cy5.5, generated by multiplying the mask in (a) with the fluorescence image at $I_{0\ ps}$. (e) Fluorescence image highlighting *E. coli* containing Rh800, generated by multiplying the mask in (c) with the fluorescence image at $I_{0\ ps}$. (f) Composite image combining (d) and (e). The two-color images were generated using an automated process in Fiji instead of manual picking, detailed as follows:

1. Mask generation for BonFIRE signal: A BonFIRE image was created by subtracting the images captured at two temporal delays (0 ps and 20 ps) to highlight regions containing *E. coli* labeled with Cy5.5. A mask was then generated to select these regions using the Huang method for thresholding (Fig. S14(a)).
2. Mask generation for fluorescence signal: A fluorescence image ($I_{0\ ps}$) was used to identify regions containing *E. coli* labeled with either Cy5.5 or Rh800. A mask was generated to select these regions (Fig. S14(b)).
3. Differentiation of fluorophores: An XOR operation was applied to the two masks to create a new mask specifically selecting regions containing *E. coli* labeled with Rh800 (Fig. S14(c)).
4. Segmentation of original images: Each mask was multiplied with the raw fluorescence image to generate separate images for *E. coli* labeled with Rh800 and Cy5.5, respectively (Fig. S14(d) and Fig. S14(e)).
5. Merging of segmented images: The segmented images were combined to produce the final two-color image (Fig. S14(f)).
6. Implementation across all time points: These steps were repeated for each time point in the dataset.

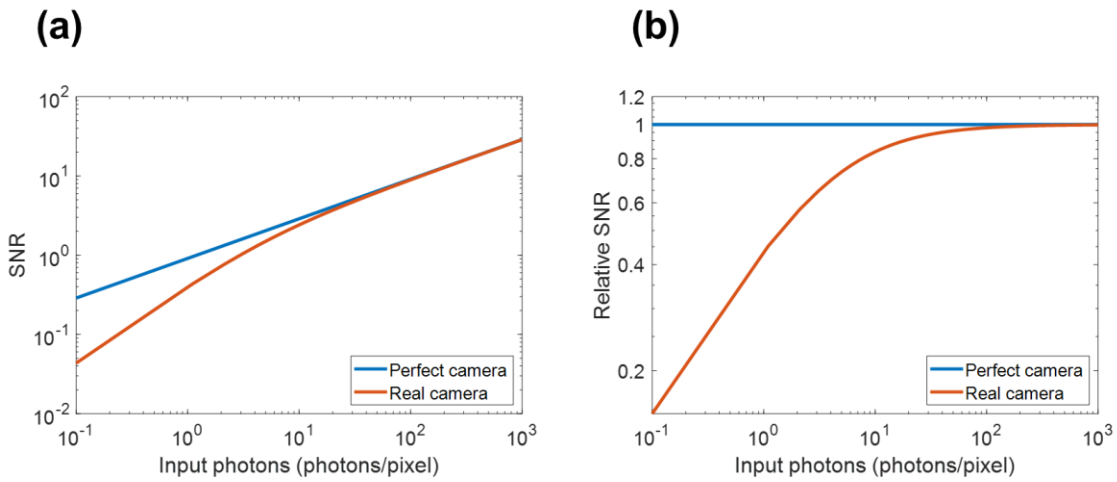

Fig. S15. Impact of camera noise to SNR. (a) SNR as a function of input photons (photons/pixel), calculated using Equations S1–S3. The "Perfect camera" (blue) assumes a quantum efficiency of 0.83 with zero read noise and dark noise. The "Real camera" (red) assumes a quantum efficiency of 0.83, read noise of 1.6 electron, and dark noise of 1 electron/s, as specified by the camera manufacturer. (b) Relative SNR plot, showing the SNR of the real camera normalized to the SNR of the perfect camera. Although the number of photons detected in fluorescence imaging is much smaller compared to stimulated Raman scattering, the photon counts are still large enough that the dominant source of noise is shot noise. Using Equations S1–S3, the SNR of the camera was computed as a function of input photons. At low light levels below 10 photons/pixel, dark noise and read noise dominate. However, as input photons increase beyond 10 photons/pixel, the system becomes shot-noise limited, converging close to the SNR curve of a perfect camera with zero dark noise and read noise. Since most fluorescence samples provide more than 10 photons/pixel, imaging is typically in the shot-noise-limited regime[14–16]. This was also found to be the case for BonFIRE. Table S2 below summarizes the BonFIRE signal, total noise, and individual noise contributions.

Fig.	BonFIRE signal [e-]	Camera noise [e-]	Shot noise [e-]	Total noise [e-]	Full well capacity usage [%]
Fig. 2(d)	114.5	4.7	10.7	11.7	0.8
Fig. 2(j)	1465.0	2.6	38.2	38.4	9.8
Fig. 2(k)	592.1	5.6	24.3	25.0	3.9
Fig. 3(c)	264.0	11.1	16.2	19.7	1.8
Fig. 3(e)	1015.7	4.4	31.8	32.2	6.8
Fig. 3(g)	212.2	0.7	14.5	14.6	1.4

Table S2. Summary of WF-BonFIRE signal and noise contributions. Camera noise was measured by acquiring an image with the laser turned off and calculating the standard deviation. Shot noise was estimated as the square root of the BonFIRE signal.

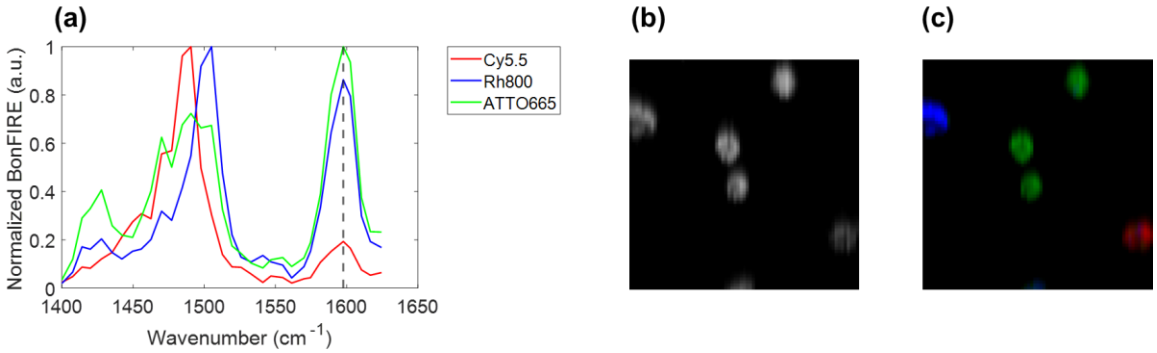

Fig. S16. Three-color BonFIRE imaging. (a) BonFIRE spectra of Cy5.5 (red), Rh800 (blue), and ATTO665 (green) acquired from individually stained cells. (b) BonFIRE image at 1598 cm^{-1} indicated as vertical dotted line in (a). (c) Unmixed three-color BonFIRE image after applying LASSO unmixing. To demonstrate the multiplexing capabilities of BonFIRE, we utilized the full spectral information and applied standard least absolute shrinkage and selection operator (LASSO) unmixing, an approach commonly used for robust spectral decomposition in stimulated Raman scattering microscopy [17]. Compared to simple linear unmixing, the LASSO algorithm offers improved performance in handling overlapping spectra. For this demonstration, we acquired a hyperspectral BonFIRE image of fixed HeLa cells labeled with three BonFIRE dyes—Cy5.5, Rh800, and ATTO665—over the spectral range of 1400 cm-1 to 1624 cm-1. To prepare the sample, live HeLa cells were incubated with 10 μM concentrations of the three dyes for 30 minutes, followed by trypsinization, fixation, mixing, and deposition onto a CaF_2 window. Despite the spectral overlap among the three dyes (Fig. S16(a)), LASSO unmixing successfully decomposed the hyperspectral data (Fig. S16(b)) into distinct chemical concentration maps (Fig. S16(c)), demonstrating the potential of BonFIRE for high-multiplexed imaging in the fingerprint region. Moving forward, we aim to expand these multiplexing capabilities by targeting additional vibrational peaks in both the fingerprint and cell-silent regions, further broadening the palette of BonFIRE-compatible dyes for high-content imaging.

Movie S1. WF-BonFIRE imaging capturing random motion of Rh800-stained *E. coli* at 1598 cm^{-1} using temporal-delay modulation. FPS: 150 Hz. Scale bar: 3 μm.

Movie S2. Chemical-selective WF-BonFIRE imaging capturing random motion of Cy5.5 -stained *E. coli* at 1484.6 cm^{-1} using temporal-delay modulation. FPS: 150 Hz. Scale bar: 3 μm.

Movie S3. Chemical-selective WF-BonFIRE imaging capturing random motion of Rh800-stained *E. coli* at 1484.6 cm^{-1} using temporal-delay modulation. FPS: 150 Hz. Scale bar: 3 μm.

Movie S4. Multicolor WF-BonFIRE tracking of Cy5.5 (green) and Rh800-stained (red) *E. coli* using temporal-delay modulation. FPS: 150 Hz. Scale bar: 3 μm.

References

1. Yin, J. *et al.* Video-rate mid-infrared photothermal imaging by single-pulse photothermal detection per pixel. *Sci. Adv.* **9**, eadg8814 (2023).
2. Zhang, D. *et al.* Depth-resolved mid-infrared photothermal imaging of living cells and organisms with submicrometer spatial resolution. *Sci. Adv.* **2**, e1600521 (2016).
3. Wei, L. *et al.* Live-cell imaging of alkyne-tagged small biomolecules by stimulated Raman scattering. *Nat. Methods* **11**, 410–412 (2014).
4. Wang, H. *et al.* Bond-selective fluorescence imaging with single-molecule sensitivity. *Nat. Photonics* **17**, 846–855 (2023).
5. Xiong, H. *et al.* Super-resolution vibrational microscopy by stimulated Raman excited fluorescence. *Light Sci. Appl.* **10**, 87 (2021).
6. Wei, L. *et al.* Super-multiplex vibrational imaging. *Nature* **544**, 465–470 (2017).
7. Ishigane, G. *et al.* Label-free mid-infrared photothermal live-cell imaging beyond video rate. *Light Sci. Appl.* **12**, 174 (2023).
8. Yan, C. *et al.* Multidimensional Widefield Infrared-Encoded Spontaneous Emission Microscopy: Distinguishing Chromophores by Ultrashort Infrared Pulses. *J. Am. Chem. Soc.* **146**, 1874–1886 (2024).
9. Zhang, Y. *et al.* Fluorescence-Detected Mid-Infrared Photothermal Microscopy. *J. Am. Chem. Soc.* (2021) doi:10.1021/jacs.1c03642.
10. He, H. *et al.* Mapping enzyme activity in living systems by real-time mid-infrared photothermal imaging of nitrile chameleons. *Nat. Methods* **21**, 342–352 (2024).
11. Xiong, H. *et al.* Stimulated Raman excited fluorescence spectroscopy and imaging. *Nat. Photonics* **13**, 412–417 (2019).
12. *Spectrochemical Analysis Using Infrared Multichannel Detectors*. (Wiley, 2005). doi:10.1002/9780470988541.
13. Clark, J. L., Miller, P. F. & Rumbles, G. Red Edge Photophysics of Ethanolic Rhodamine 101 and the Observation of Laser Cooling in the Condensed Phase. *J. Phys. Chem. A* **102**, 4428–4437 (1998).
14. Li, X. *et al.* Real-time denoising enables high-sensitivity fluorescence time-lapse imaging beyond the shot-noise limit. *Nat. Biotechnol.* **41**, 282–292 (2023).

15. Wilt, B. A., Fitzgerald, J. E. & Schnitzer, M. J. Photon Shot Noise Limits on Optical Detection of Neuronal Spikes and Estimation of Spike Timing. *Biophys. J.* **104**, 51–62 (2013).
16. Garini, Y., Gil, A., Bar-Am, I., Cabib, D. & Katzir, N. Signal to noise analysis of multiple color fluorescence imaging microscopy. *Cytometry* **35**, 214–226 (1999).
17. Lin, H. *et al.* Microsecond fingerprint stimulated Raman spectroscopic imaging by ultrafast tuning and spatial-spectral learning. *Nat. Commun.* **12**, 3052 (2021).

Appendix: Theory of light matter interaction process

Classical description of IR absorption. The classical description of IR absorption can be useful as it provides intuitive understanding of the process. Therefore, it is briefly summarized here[1-4]. Light-matter interaction is modeled as a charged particle interacting with an oscillating electric field, inducing motion that leads to absorption phenomena. In essence, this induced motion causes induced polarization, which generates re-emitted electric field that destructively interferes with the incident electric field, resulting in decreased transmitted light.

The electric dipole moment $p(t)$ describes the separation of positive and negative charges in the molecule:

$$p(t) = qx(t) \tag{1}$$

where $x(t)$ is the displacement of the nuclei with respect to their equilibrium position and q is the effective charge. In a macroscopic sample of N molecules, the total dipole moment per unit volume is the polarization $P(t)$.

$$P(t) = Np(t) = Nqx(t) \tag{2}$$

The polarization responds to the applied electric field and can be described by defining the susceptibility:

$$P(t) = \epsilon_0 \chi^{(1)}(t) E(t) \tag{3}$$

where $\chi^{(1)}$ is the linear dielectric susceptibility. The susceptibility describes how easily the macroscopic response of the material (polarization) changes to the applied electric field. Combing equation with Equation (2) and (3), susceptibility $\chi^{(1)}$ can be expressed as a function of $x(t)$:

$$\chi^{(1)}(t) = \frac{Nq}{\epsilon_0 E(t)} x(t) \tag{4}$$

We model the molecular vibration as a driven harmonic oscillator under the influence of the oscillating electric field $E(t)$. The equation of motion for the nuclear displacement $x(t)$ is:

$$\frac{d^2x}{dt^2} + 2\gamma \frac{dx}{dt} + \Omega_R^2 x = \frac{F(t)}{\mu} \tag{5}$$

where $\mu = \frac{m_A m_B}{m_A + m_B}$ is reduced mass, γ is the damping factor, Ω_R is the resonant frequency of the harmonic oscillator, and $F(t)$ is the force generated by the electric field to the vibrating mass. The driving force is proportional to the external oscillating electric field:

$$F(t) = qE(t) = qE_0 e^{-i\omega t} \quad (6)$$

where ω is the angular frequency. The solution to Equation (5) is:

$$x(t) = x(\omega)e^{-i\omega t} \quad (7)$$

where

$$x(\omega) = \frac{-\frac{qE_0}{2\Omega_R \mu}}{(\omega - \Omega_R) + i\gamma} \quad (8)$$

assuming close to resonance ($\omega \approx \Omega_R$) and small damping coefficient ($\gamma \ll \Omega_R$). The following observations can be made for different ranges of ω

1. At $\omega \ll \Omega_R$, the amplitude of the displacement is small. The phase is close to zero;
2. At $\omega = \Omega_R$, the amplitude of the displacement is large. The phase is π/2, which means that the oscillation lags 90 degrees than the incident field;
3. At $\omega \gg \Omega_R$, the amplitude of the displacement is small. The phase is π, which means that the oscillation lags 180 degrees than the incident field,

when $\omega = \Omega_R$, $x(\omega)$ is maximized, and energy is efficiently transferred from the electric field to the molecular vibration. The absorbed energy corresponds to a quantum transition between vibrational states, where the photon energy matches the vibrational energy gap. Combining Equation (4), (7), and (8),

$$\chi^{(1)}(\omega) = \frac{-\frac{Nq^2}{2\epsilon_0 \mu \Omega_R}}{(\omega - \Omega_R) + i\gamma} \quad (9)$$

Note that the change in the dipole moment $\frac{\partial p}{\partial x} = q$ should be non-zero for the susceptibility to be non-zero and the molecule to be IR active. The susceptibility is relevant because it can be related to the physical properties. The imaginary part of the susceptibility is related to absorption coefficient, and the real part is related to the refractive index[3].

$$\alpha = kIm(\chi^{(1)}) \quad (10)$$

$$n = \frac{1}{2} Re\left(\chi^{(1)}\right) + 1 \quad (11)$$

The induced polarization described by oscillation $x(t)$ in Equation (2) result in emitted field that interferes with the incident light. The resulting total electric field $E(z,t)$ that is transmitted can be derived by solving the Maxwell's equation[3], using the slow varying envelope approximation, resulting in the following equation:

$$\frac{\partial E_0}{\partial z} = \frac{ik}{2\epsilon_0} P_0 \quad (12)$$

where $E(z,t) = E_0(z)e^{i(kz-wt)}$ and $P(z,t) = P_0(z)e^{i(kz-wt)}$. Note that the re-emitted field ΔE_0 has a 90-degree phase shift with respect to the polarization. The following observations can be made for different range of ω.

1. At $\omega \ll \Omega_R$, the oscillation lags 90 degrees than the incident field.
2. At $\omega = \Omega_R$, the oscillation lags 180 degrees than the incident field.
3. At $\omega \gg \Omega_R$, the oscillation lags -90 degrees than the incident field.

Hence, at resonance, the re-emitted field destructively interferes, resulting in reduced intensity for the transmitted light. Solving Equation (12),

$$E_0(z) = E_0(0)\mathrm{e}^{\frac{ik}{2}\chi^{(1)}z} \tag{13}$$

Combining Equation (11), (12), and (13),

$$E(z,t) = E_0(0)e^{\left(-\frac{\alpha}{2}z\right)}e^{i(nkz-\omega t)} \tag{14}$$

Taking the (time-averaged) square of Equation (14),

$$I(z) = I(0)\exp\left(-\alpha z\right) \tag{15}$$

which is the Beer's law.

Classical description of spontaneous Raman scattering. Raman scattering is related to the polarizability $p(t)$ which describes how easily the electron cloud responds to an external electric field.

$$p(t) = \alpha(t)E(t) \tag{16}$$

Since the nuclei and electrons are coupled, the position of the nuclei x influences the electronic structure, and therefore the polarizability. Thus, $\alpha = \alpha(x)$ where x presents the displacement of the nuclei from their equilibrium positions during a vibration. The nuclear displacement x in vibrational motion is usually small compared to the equilibrium bond length. This allows us to approximate $\alpha(x)$ about its equilibrium value ($x = 0$) using a Taylor series.

$$\alpha(x) = \alpha_0 + \left(\frac{\partial\alpha}{\partial x}\right)_{x=0} x + \cdots \tag{17}$$

where α_0 is the equilibrium polarizability of the molecule when the nuclei are at their equilibrium position ($x = 0$). This term describes the baseline response of the electron cloud. The $\left(\frac{\partial\alpha}{\partial x}\right)_{x=0}$ term represents the first order change in polarizability due to the

displacement x. This term quantifies how sensitive the polarizability is to nuclear motion. For Raman scattering, this coupling determines whether a vibrational mode is Raman active. The higher order terms account for nonlinear effects in polarizability but are typically negligible for small displacements.

The nuclear displacement $x(t)$ oscillates harmonically due to vibrations:

$$x(t) = x_0 \cos(\Omega_R t) \tag{18}$$

where x_0 is the amplitude of the nuclear vibration, and Ω_R is the resonant frequency of the vibrational mode. The incident electric field is oscillatory

$$E(t) = E_0 \cos(\omega_P t) \tag{19}$$

where ω_P is the angular frequency of the incident pump beam. Combining the equations (16), (17), (18), and (19),

$$P(t) = Np(t) = N\alpha(t)E(t) = N\left(\alpha_0 + \left(\frac{\partial \alpha}{\partial x}\right)_{x=0} x(t)\right)E(t) \tag{20}$$

Combining equations

$$P(t) = N\left(\alpha_0 + \left(\frac{\partial \alpha}{\partial x}\right)_{x=0} x_0 \cos(\Omega_R t)\right)E_0 \cos(\omega_P t) \tag{21}$$

$$P(t) = N\alpha_0 E_0 \cos(\omega_P t) + \frac{N\left(\frac{\partial \alpha}{\partial x}\right)_{x=0} x_0 E_0}{2} \cos((\omega_P - \Omega_R)t) + \frac{N\left(\frac{\partial \alpha}{\partial x}\right)_{x=0} x_0 E_0}{2} \cos((\omega_P + \Omega_R)t) \tag{22}$$

The first term corresponds to Rayleigh scattering at the same frequency as the incident light, and therefore is elastic scattering. The second and third term are inelastic scattering corresponding to Stokes ($\omega_S = \omega_P - \Omega_R$) scattering and anti-stokes ($\omega_{AS} = \omega_P + \Omega_R$) scattering, respectively, occurring because energy is transferred between light to molecular vibration.

Classical description of coherent Raman scattering. In coherent Raman scattering, two beams—the Stokes beam and the pump beam, with frequencies ω_S and ω_P, respectively—are involved. The total electric field can be expressed as:

$$E(z,t) = A_P e^{i(k_P z - \omega_P t)} + A_S e^{i(k_S z - \omega_S t)} + c.c. \tag{23}$$

where c.c. denotes the complex conjugate. The pump and Stokes fields are individually given as $E_P(z,t) = A_P e^{i(k_P z - \omega_P t)}$ and $E_S(z,t) = A_S e^{i(k_S z - \omega_S t)}$, respectively. The

coherent Raman signals are calculated from the principles outlined earlier for IR absorption and spontaneous Raman scattering. The nuclear displacement $x(\Omega)$ is obtained by solving the equation of motion for a driven damped harmonic oscillator (Equation (5)), where the driving force $F(t)$ is derived from Equation (23). The displacement is given by:

$$x(\Omega) = \frac{-\left(\frac{\epsilon_0}{2m\Omega_R}\right)\left(\frac{\partial\alpha}{\partial x}\right)_{x=0} A_P A_S^*}{(\Omega-\Omega_R)+i\gamma} \tag{24}$$

where $\Omega = \omega_P - \omega_S$. The induced polarization is calculated using Equation (20), but now the electric field involves both the pump and Stokes using Equation (23). This results in polarization terms $\left(P(\omega_{AS}), P(\omega_{CS}), P(\omega_P), P(\omega_S)\right)$ that are nonlinear with respect to the electric field, leading to contributions at four distinct frequencies $\omega_{AS} = 2\omega_P - \omega_S$, $\omega_{CS} = 2\omega_S - \omega_P$, ω_P, and ω_S, corresponding to coherent anti-Stokes Raman scattering (CARS), coherent Stokes Raman scattering (CSRS), Stimulated Raman Loss (SRL), and Stimulated Raman Gain (SRG) processes. The nonlinear polarization terms for these frequencies are expressed as follows:

$$P(\omega_P) = N\epsilon_0 \left(\frac{\partial\alpha}{\partial x}\right)_{x=0} x(\Omega) A_S e^{ik_p z} \tag{25}$$

$$P(\omega_S) = N\epsilon_0 \left(\frac{\partial\alpha}{\partial x}\right)_{x=0} x^*(\Omega) A_P e^{ik_S z} \tag{26}$$

$$P(\omega_{AS}) = N\epsilon_0 \left(\frac{\partial\alpha}{\partial x}\right)_{x=0} x(\Omega) A_P e^{i(2k_p - k_S)z} \tag{27}$$

$$P(\omega_{CS}) = N\epsilon_0 \left(\frac{\partial\alpha}{\partial x}\right)_{x=0} x^*(\Omega) A_S e^{i(2k_S - k_P)z} \tag{28}$$

The induced polarization P can also be expressed in terms of the third order susceptibility, resulting in the following equations:

$$P(\omega_P) = 6\epsilon_0 \chi_R^{(3)}(\omega_P)|A_S|^2 A_P e^{ik_P z} \tag{29}$$

$$P(\omega_S) = 6\epsilon_0 \chi_R^{(3)}(\omega_S)|A_P|^2 A_S e^{ik_S z} \tag{30}$$

$$P(\omega_{AS}) = 3\epsilon_0 \chi^{(3)}(\omega_{AS})|A_P|^2 A_S^* e^{i(2k_P - k_S)z} \tag{31}$$

$$P(\omega_{CS}) = 3\epsilon_0 \chi^{(3)}(\omega_{CS})|A_S|^2 A_P^* e^{i(2k_S - k_P)z} \tag{32}$$

The coefficient 3 CARS and CSRS terms arises due to symmetry, as these processes involve two identical fields. From this point forward, we focus on SRL process, which is measured as the SRS signal throughout this thesis.

The third order susceptibility can be computed from Equations (24) and (25), and (29) as:

$$\chi_R(\omega_P) = \frac{-\frac{N\epsilon_0}{6\mu\Omega_R}\left(\frac{\partial\alpha}{\partial x}\right)^2_{x=0}}{(\Omega-\Omega_R)+i\gamma} \tag{33}$$

where $\Omega = \omega_P - \omega_S$.

The SRL process can be thought of as interference between the incident electric field $E_P = A_P e^{i(k_{Pz}-\omega_P t)}$ and the re-emitted electric field $E_P^{(3)} = A_P^{(3)} e^{i(k_{Pz}-\omega_P t)}$ caused by the nonlinear polarization $P(\omega_P)$, as the two are at the same frequency and are coherent. This inference can be described as:

$$I_P \propto \left|A_P + A_P^{(3)}\right|^2 \propto |A_P|^2 + \left|A_P^{(3)}\right|^2 + 2\left|A_P + A_P^{(3)}\right|^2 \cos\left(\phi(A_P) - \phi\left(A_P^{(3)}\right)\right) \quad (34)$$

The induced $P(\omega_P)$ has a 90-degree phase lag compared to the incident E_P (similar to Equation (12)), leading to the phase:

$$\phi\left(A_P^{(3)}\right) = \frac{\pi}{2} + \phi(P(\omega_P)) = \frac{\pi}{2} + \phi(A_P) + \phi\left(\chi_{\mathrm{R}}^{(3)}\right) \quad (35)$$

At resonance, $\phi\left(\chi_{\mathrm{R}}^{(3)}\right)$ is $\frac{\pi}{2}$, derived from Equation (33). This results in the phase difference of:

$$\phi\left(A_P^{(3)}\right) - \phi(A_P) = \pi \quad (36)$$

This phase difference leads to destructive interference, which causes the stimulated Raman loss (SRL), represented by the second term in Equation (37):

$$I_P \propto |A_P|^2 + 2\left|A_P A_P^{(3)}\right| \cos(\pi) \propto I_P - 2\sqrt{I_P I_P^{(3)}} \quad (37)$$

The re-emitted light from the induced polarization can be computed as in Equation (12), yielding the final result:

$$\Delta I_P = SRL \approx -Im\left(\chi_R^{(3)}\right) I_S I_P \quad (38)$$

The SRL signal is proportional to the $Im\left(\chi_R^{(3)}\right)$, which is why SRS spectrum matches well with the spontaneous Raman spectrum. This behavior is distinct from CARS where the signal is:

$$I_{AS} \propto \left|\chi^{(3)}(\omega_{AS})\right|^2 L^2 sinc^2\left(\frac{\Delta kL}{2}\right) I_P^2 I_S \quad (39)$$

were $\chi^{(3)}(\omega_{AS}) = \chi_R^{(3)} + \chi_{NR}^{(3)}$. The CARS signal includes non-resonant background due to $\chi_{NR}^{(3)}$.

References

1. Cheng, J.-X.; Xie, X. S. Coherent Raman Scattering Microscopy; Series in cellular and clinical imaging; CRC press: Boca Raton (Fla.), 2013.
2. Rigneault, H. Coherent Raman Scattering Processes. In Stimulated Raman Scattering Microscopy; Elsevier, 2022; pp 3–20. https://doi.org/10.1016/B978-0-323-85158-9.00004-X.
3. Boyd, R. W. Nonlinear Optics (Third Edition); Boyd, R. W., Ed.; Academic Press: Burlington, 2008; pp 473–509. https://doi.org/10.1016/B978-0-12-369470-6.00010-1.
4. Butcher, P. N.; Cotter, D. The Elements of Nonlinear Optics, 1. paperback ed., repr.; Cambridge studies in modern optics; Cambridge Univ. Pr: Cambridge,